

University of Windsor

Scholarship at UWindor

Electronic Theses and Dissertations

Theses, Dissertations, and Major Papers

11-26-2015

Analysis and Improvement of Aerodynamic Performance of Straight Bladed Vertical Axis Wind Turbines

Mojtaba Ahmadi-Baloutaki
University of Windsor

Follow this and additional works at: <https://scholar.uwindsor.ca/etd>

Recommended Citation

Ahmadi-Baloutaki, Mojtaba, "Analysis and Improvement of Aerodynamic Performance of Straight Bladed Vertical Axis Wind Turbines" (2015). *Electronic Theses and Dissertations*. 5625.
<https://scholar.uwindsor.ca/etd/5625>

This online database contains the full-text of PhD dissertations and Masters' theses of University of Windsor students from 1954 forward. These documents are made available for personal study and research purposes only, in accordance with the Canadian Copyright Act and the Creative Commons license—CC BY-NC-ND (Attribution, Non-Commercial, No Derivative Works). Under this license, works must always be attributed to the copyright holder (original author), cannot be used for any commercial purposes, and may not be altered. Any other use would require the permission of the copyright holder. Students may inquire about withdrawing their dissertation and/or thesis from this database. For additional inquiries, please contact the repository administrator via email (scholarship@uwindsor.ca) or by telephone at 519-253-3000ext. 3208.

**Analysis and Improvement of Aerodynamic Performance
of Straight Bladed Vertical Axis Wind Turbines**

By

Mojtaba Ahmadi-Baloutaki

A Dissertation

Submitted to the Faculty of Graduate Studies
through the Department of Mechanical, Automotive and Materials Engineering
in Partial Fulfillment of the Requirements for
the Degree of Doctor of Philosophy
at the University of Windsor

Windsor, Ontario, Canada

© 2015 Mojtaba Ahmadi-Baloutaki

**Analysis and Improvement of Aerodynamic Performance
of Straight Bladed Vertical Axis Wind Turbines**

By

Mojtaba Ahmadi-Baloutaki

APPROVED BY:

H. M. Hangan, External Examiner
University of Western Ontario

T. Bolisetti
Department of Civil & Environmental Engineering

G. Rankin
Department of Mechanical, Automotive & Materials Engineering

R. Balachandar
Department of Mechanical, Automotive & Materials Engineering

R. Carriveau, Co-Advisor
Department of Civil & Environmental Engineering

D. Ting, Co-Advisor
Department of Mechanical, Automotive & Materials Engineering

12 November 2015

Declaration of Co-Authorship / Previous Publication

I. Co-Authorship Declaration

This thesis includes six original papers that have been previously published/submitted for publication in peer-reviewed journals, as follows:

Thesis chapter	Publication title/Full citation	Publication status
Chapter 2	Ahmadi-Baloutaki, M., Carriveau, R., Ting, D.S.-K., SB-VAWT rotor design guide based on aerodynamic performance and loading analysis, Proceedings of the Institution of Mechanical Engineers, Part A: Journal of Power and Energy, 2014; 228(7): 742-759, Winner of the Best Paper Award of the Year.	Published
Chapter 3	Ahmadi-Baloutaki, M., Ting, D.S.-K., Carriveau, R., The role of free-stream turbulence on flow evolution in the wake of a VAWT blade, Wind Engineering, 2013; 37(4): 401-420.	Published
Chapter 4	Ahmadi-Baloutaki, M., Carriveau, R., Ting, D.S.-K., An experimental study on the interaction between free-stream turbulence and a wing-tip vortex in the near-field, Aerospace Science and Technology, 2015; 43: 395-405.	Published
Chapter 5	Ahmadi-Baloutaki, M., Carriveau, R., Ting, D.S.-K., Performance of a vertical axis wind turbine in grid generated turbulence, Sustainable Energy Technologies and Assessments, 2015; 11: 178-185.	Published
Chapter 6	Ahmadi-Baloutaki, M., Carriveau, R., Ting, D.S.-K., A wind tunnel study on the aerodynamic interaction of vertical axis wind turbine arrays, Renewable Energy, Under review.	Under review
Appendix	Ahmadi-Baloutaki, M., Carriveau, R., Ting, D.S.-K., Effect of free-stream turbulence on flow characteristics over a transversely-grooved surface, Experimental Thermal and Fluid Science, 2013; 51: 56-70.	Published

In all papers listed above, the key ideas, primary contributions, literature survey, computational analysis, experimental designs, data analysis and interpretation, and manuscript

preparations were performed by the author. Contributions of the co-authors were primarily in the supervision or editorial level.

I am aware of the University of Windsor Senate Policy on Authorship and I certify that I have properly acknowledged the contribution of other researchers to my dissertation, and have obtained permission from each of the abovementioned co-authors to include the above materials in my dissertation. I certify that, with the above qualification, this dissertation, and the research to which it refers, is the product of my own work.

II. Declaration of Previous Publication

I certify that I have obtained a written permission from the copyright owners to include the above published materials in my thesis. I certify that the above material describes work completed as a graduate student at the University of Windsor.

I certify that, to the best of my knowledge, my thesis does not infringe upon anyone's copyright nor violate any proprietary rights and that any ideas, techniques, quotations, or any other material from the work of other people included in my thesis, published or otherwise, are fully acknowledged in accordance with the standard referencing practices. Furthermore, to the extent that I have included copyrighted material that surpasses the bounds of fair dealing within the meaning of the Canada Copyright Act, I certify that I have obtained a written permission from the copyright owner(s) to include such material(s) in my thesis.

I declare that this is a true copy of my thesis, including any final revisions, as approved by my thesis committee and the Graduate Studies office, and that this thesis has not been submitted for a higher degree to any other University or Institution.

Abstract

Vertical axis wind turbines (VAWTs) with straight blades are attractive for their relatively simple structure and aerodynamic performance. Their commercialization, however, still encounters many challenges. A series of studies were conducted in the current research to improve the VAWTs design and enhance their aerodynamic performance. First, an efficient design methodology built on an existing analytical approach is presented to formulate the design parameters influencing a straight bladed-VAWT (SB-VAWT) aerodynamic performance and determine the optimal range of these parameters for prototype construction. This work was followed by a series of studies to collectively investigate the role of external turbulence on the SB-VAWTs operation. The external free-stream turbulence is known as one of the most important factors influencing VAWTs since this type of turbines is mainly considered for urban applications where the wind turbulence is of great significance. Initially, two sets of wind tunnel testing were conducted to study the variation of aerodynamic performance of a SB-VAWT's blade under turbulent flows, in two major stationary configurations, namely two- and three-dimensional flows. Turbulent flows generated in the wind tunnel were quasi-isotropic having uniform mean flow profiles, free of any wind shear effects. Aerodynamic force measurements demonstrated that the free-stream turbulence improves the blade aerodynamic performance in stall and post-stall regions by delaying the stall and increasing the lift-to-drag ratio. After these studies, a SB-VAWT model was tested in the wind tunnel under the same type of turbulent flows. The turbine power output was substantially increased in the presence of the grid turbulence at the same wind speeds, while the increase in turbine power coefficient due to the effect of grid turbulence was small at the same tip speed ratios. The final section presents an experimental study on the aerodynamic interaction of VAWTs in arrays configurations. Under controlled flow conditions in a wind tunnel, the counter-rotating configuration resulted in a slight improvement in the aerodynamic performance of each turbine compared to the isolated installation. Moreover, the counter-rotating pair improved the power generation of a turbine located downstream of the pair substantially.

Dedication

This research is dedicated to the future wind turbines. I hope this work and other researchers' work in this field would accelerate the global development of wind power generation.

Acknowledgements

I wish to express my deep appreciation and gratitude to my research supervisors, Dr. David Ting and Dr. Rupp Carriveau for their leadership, knowledge, and support throughout this exciting course of study. Your passion for research is contagious and you have made my PhD program a memorable experience. I would also like to thank the members of my PhD committee, Dr. Tirupati Bolisetti, Dr. Gary Rankin and Dr. Ram Balachandar for all of their support and critical feedback throughout my PhD dissertation. As well, I would like to extend my sincerest thanks to my external examiner, Dr. Horia Hangan, for taking time out of a busy schedule to be a part of this work. The contribution of Dr. Kemal Tepe to my PhD defense as the session chair is also greatly appreciated.

Additionally, I would like to take this opportunity to acknowledge the University of Windsor, the Natural Sciences and Engineering Research Council (NSERC) of Canada, Ontario Centres of Excellence (OCE) for providing research funding, and the Ontario Ministry of Training, Colleges and Universities for providing me the Ontario Graduate Scholarship (OGS) which allowed me to pursue the current research projects. The financial support of Great Lakes Energy Inc. during the work on Chapters 2 and 3 is also greatly appreciated. I would also like to thank the Atmospheric Boundary Layer Wind Tunnel Laboratory of the Western University for providing the facility for conducting experiments presented in Chapter 6. Finally, I would like to thank my family for all of their support throughout my entire life especially during my PhD program.

Table of Contents

Declaration of Co-Authorship / Previous Publication	iii
Abstract.....	v
Dedication	vi
Acknowledgements	vii
List of Tables	xii
List of Figures.....	xiii
Nomenclature	xvii
Chapter 1: Introduction	1
1.1 Background.....	1
1.2 Methodology.....	7
1.3 References.....	9
Chapter 2: Straight bladed vertical axis wind turbine rotor design guide based on aerodynamic performance and loading analysis.....	12
2.1 Introduction.....	12
2.2 Analytical modeling.....	14
2.2.1 Local flow parameters	14
2.2.2 Double-Multiple Streamtube model	16
2.2.3 Refinement of the analytical model	18
2.2.4 Code validation.....	22
2.3 Aerodynamic performance	25
2.3.1 Rotor solidity factor.....	26
2.3.2 Blade aspect ratio.....	28
2.3.3 Rotor swept ratio.....	29

2.4 Aerodynamic loading.....	30
2.4.1 Number of blades.....	32
2.4.2 Blade profile	32
2.4.3 Blade-supporting-arm interaction.....	33
2.4.4 Blade dimensions and material.....	34
2.4.5 Supporting arms.....	35
2.4.6 Rotor interaction with electrical devices	36
2.4.7 Cut-in and cut-out wind speeds	37
2.4.8 Self-starting challenge	38
2.5 Design flowchart.....	38
2.6 Conclusion	40
2.7 References.....	41
 Chapter 3: The role of free-stream turbulence on flow evolution in the wake of a VAWT blade.....	45
3.1 Introduction.....	45
3.2 Experimental apparatus.....	46
3.3 Results and discussion	49
3.3.1 Aerodynamic forces.....	50
3.3.2 Wake profiles.....	52
3.3.3 Frequency analysis.....	65
3.4 Conclusion	67
3.5 References.....	67
 Chapter 4: An experimental study on the interaction between free-stream turbulence and a wing-tip vortex in the near-field	71
4.1 Introduction.....	71
4.2 Experimental setup and data measurement.....	73
4.2.1 Apparatus	73
4.2.2 Instrumentation and measurement details	75

4.2.3 Uncertainty	77
4.3 Results and discussion	78
4.3.1 Aerodynamic loads	78
4.3.2 Mean velocity data.....	81
4.3.3 Vortex trajectory	85
4.3.4 Turbulence intensity	86
4.3.5 Circulation	88
4.4 Conclusion	91
4.5 References.....	91
Chapter 5: Performance of a vertical axis wind turbine in grid generated turbulence	95
5.1 Introduction.....	95
5.2 Experimental setup	97
5.2.1 Model description	97
5.2.2 Instrumentation	99
5.3 Results and discussion	101
5.3.1 Free-stream turbulence characteristics	101
5.3.2 Wind turbine performance testing	104
5.4 Conclusion	108
5.5 References.....	109
Chapter 6: A wind tunnel study on the aerodynamic interaction of vertical axis wind turbines in array configurations.....	111
6.1 Introduction.....	111
6.2 Experimental apparatus.....	113
6.2.1 Wind tunnel and VAWT model.....	113
6.2.2 Data acquisition and processing	117
6.3 Results and discussion	118
6.3.1 Two-VAWT arrays.....	118

6.3.2 Three-VAWT arrays	122
6.4 Conclusion	130
6.5 References.....	131
Chapter 7: Conclusions and Recommendations	135
7.1 Research outcomes	135
7.2 Recommendations for future works.....	137
Appendix A: Effect of free-stream turbulence on flow characteristics over a transversely-grooved surface	139
A.1 Introduction.....	140
A.2 Experimental details.....	142
A.3 Results and discussion	146
A.3.1 Uncertainty analysis.....	147
A.3.2 Velocity profiles	147
A.3.3 Turbulence moments.....	151
A.3.4 Turbulence length scales.....	159
A.4 Conclusion	165
A.5 References.....	166
Appendix B: Uncertainty analysis.....	169
Appendix C: Scaling analysis.....	170
C.1 Flow similarity	170
C.2 Flow around a single blade	170
C.3 Flow over a VAWT.....	171
Appendix D: Wind turbine generator electrical losses.....	173
Appendix E: Permissions for previously published works	174
Vita Auctoris.....	176

List of Tables

Chapter 2

Table 1: Equations used for SB-VAWT formulation15

Table 2: The specifications of candidate SB-VAWT studied in Section 2.431

Chapter 4

Table 1: Fitted coefficients of the current data using analytical expressions90

Chapter 6

Table 1: Geometrical parameters of current SB-VAWT and their optimum range..114

Table 2: Description of different configurations of wind turbine arrays studied115

Appendix A

Table 1: Free-stream values of different parameters at nine streamwise sections ...144

List of Figures

Chapter 1

Figure 1: Schematic of a SB-VAWT for illustration purposes.....	3
Figure 2: Schematic of a counter-rotating VAWT configuration.....	5

Chapter 2

Figure 1: A typical SB-VAWT with its three main parts	14
Figure 2: Schematic illustration of VAWTs operation.....	16
Figure 3: The double-multiple streamtube conceptual schematic	18
Figure 4: Lift and drag coefficients of a NACA0015 blade	19
Figure 5: Variation of local blade parameters in one complete revolution of a SB-VAWT	21
Figure 6: Power coefficient comparison of current DMS model with experimental data.....	23
Figure 7: Comparison of current DMS method with experiment.....	24
Figure 8: A typical performance curve of a SB-VAWT.....	26
Figure 9: Effect of rotor solidity factor on the performance of a SB-VAWT	28
Figure 10: Effect of blade aspect ratio on the performance of a SB-VAWT	29
Figure 11: Effect of rotor aspect ratio on the performance of a SB-VAWT	30
Figure 12: Aerodynamic forces as a function of azimuthal angle	32
Figure 13: Bending stress distribution along the blade length of a SB-VAWT	34
Figure 14: Effect of supporting arms geometry on SB-VAWT performance	36
Figure 15: Flow diagram of the design methodology for SB-VAWTs	40

Chapter 3

Figure 1: A schematic of the VAWT blade in wind tunnel	47
Figure 2: Orificed perforated plate photo and cross-section.....	48
Figure 3: A schematic of experimental apparatus	49
Figure 4: Coefficients of lift and drag for smooth flow.....	51

Figure 5: Effect of FST on aerodynamic coefficients of the VAWT blade	52
Figure 6: Effect of FST on the wake mean velocity profiles.....	55
Figure 7: Similarity check for wake mean velocity profiles.....	57
Figure 8: Effect of FST on the wake thickness.....	58
Figure 9: Effect of FST on the wake turbulence intensity profiles.....	60
Figure 10: Effect of FST on the wake turbulence <i>rms</i> velocity profiles.....	62
Figure 11: Turbulence <i>rms</i> velocity contours and colormaps.....	63
Figure 12: Effect of FST on the wake turbulence strain rate profiles.....	65
Figure 13: Energy spectrum of the streamwise velocity fluctuation component	67

Chapter 4

Figure 1: A schematic of experimental fixture	74
Figure 2: Sketch of the experimental arrangement in the wind tunnel test section showing the coordinate system	76
Figure 3: Aerodynamic coefficients of the NACA 0015 wing.....	79
Figure 4: Effect of FST on the wing aerodynamic coefficients.....	81
Figure 5: Contours of crossflow velocity	83
Figure 6: Effect of FST on circumferential velocity variations.....	84
Figure 7: Comparison of circumferential velocity with analytical solutions.....	85
Figure 8: Location of vortex center vs. streamwise distance.....	86
Figure 9: Contours of streamwise turbulence intensity	88
Figure 10: Effect of FST on the circulation within the vortex.....	89
Figure 11: Comparison of circulation data with analytical solutions	91

Chapter 5

Figure 1: A schematic illustration of the experimental fixture including the grid turbulence generator and VAWT.....	97
Figure 2: Airfoil profile of the VAWT blades.....	98
Figure 3: Schematic illustrations of the orificed perforated plate	99
Figure 4: The variation of turbulence intensity and integral length scale with streamwise distance from grid generator	102

Figure 5: Turbulence characteristics of the flow downstream of the grid	103
Figure 6: Effect of FST on VAWT output parameters	105
Figure 7: Wind turbine total power output and performance curves at several free-stream turbulence levels.....	106

Chapter 6

Figure 1: A schematic of a SB-VAWT.....	114
Figure 2: Schematic of the wind tunnel test section showing a three-VAWT array in a triangular configuration	116
Figure 3: Mean velocity and turbulence intensity profiles of the incoming flow in low free-stream turbulence case	119
Figure 4: Performance parameters for Array 1 (counter-rotating pair)	121
Figure 5: Performance parameters for Array 2 (co-rotating pair)	122
Figure 6: Mean velocity and turbulence intensity profiles of the incoming flow in high free-stream turbulence case	123
Figure 7: Performance parameters for Array 3 (three-VAWT configuration) and the effect of streamwise distance of the downstream turbine.....	126
Figure 8: Performance parameters for Array 4 (three-VAWT configuration) and the effect of turbine spacing	128

Appendix A

Figure 1: Schematic of experiment layout and the designed fixture	143
Figure 2: Grooved area and geometry on the aluminum plate	144
Figure 3: Orificed perforated plate photo and cross-section.....	145
Figure 4: Effect of FST and transverse grooves on velocity profiles	148
Figure 5: Comparison of velocity profiles for smooth and grooved surfaces	150
Figure 6: Boundary layer thickness for smooth and grooved surfaces.....	151
Figure 7: Effect of FST and transverse grooves on turbulence intensity profiles	153
Figure 8: Effect of FST and transverse grooves on skewness factor.....	155
Figure 9: Effect of FST and transverse grooves on flatness factor.....	156
Figure 10: PDF of velocity fluctuation and velocity fluctuation variation.....	159
Figure 11: Energy dissipation rate variations for smooth and grooved surfaces.....	161

Figure 12: Kolmogorov microscale profiles for smooth and grooved surfaces	162
Figure 13: Integral length scale variations for smooth and grooved surfaces	164
Figure 14: Energy cascade span for smooth and grooved surfaces	165

Appendix D

Figure 1: Wind turbine generator electrical losses	173
----------------------------------------------------------	-----

Nomenclature

A_r	rotor frontal area, $A_r = DH$
A_p	blade planform area, $A_p = cH$
AC	aerodynamic center of airfoil section
AR	blade aspect ratio, $AR = H^2/A = H/c$
a_0	slope of the lift curve for an airfoil profile
B	blockage ratio
b	supporting arm width (Chapter 2)
b	wake thickness; distance between two locations on lower and upper parts of wake where the velocity deficit reaches half of the maximum velocity deficit (Chapter 3)
b	wing semi-span length (Chapter 4)
b	streamwise distance from a pair of turbines (Chapter 6)
C_d	drag coefficient
C_l	lift coefficient
C_n	normal aerodynamic force coefficient
C_p	power coefficient of the wind turbine, $C_p = P/(0.5\rho A_r U_\infty^3)$
C_t	tangential aerodynamic force coefficient
c	blade chord length
D	diameter of the rotor (Chapter 2,5,6)
D	diameter of the grid turbulence generator holes (Chapter 4)
E_u	energy spectrum of the streamwise velocity fluctuation component
F	aerodynamic force (Chapter 2)
F	flatness (Chapter 5)
f	frequency
H	blade length
I	electrical current
$l_{0.5}$	wake flow length scale; distance from wake center where the velocity deficit reaches half of the maximum velocity deficit
M	bending moment
m	mass
N	number of the blades (Chapter 2,5,6)
N	number of sample points in hot-wire measurements (Chapter 3,4)

O	origin of xyz coordinates
O'	vortex center
P	output power
Q	aerodynamic torque
R	radius of the rotor (Chapter 2,5,6)
R	electrical resistance (Chapter 5,6)
R_u	auto-correlation function
r	radial distance from the vortex center
Re	local Reynolds number based on blade's chord length, $Re = Uc/\nu$
Re_θ	local Reynolds number at each azimuthal angle, $Re_\theta = Wc/\nu$
Re_∞	free-stream Reynolds number based on blade's chord length, $Re_\infty = U_\infty c/\nu$
S	skewness
s	spacing between a pair of turbines
TE	trailing edge
Tu	turbulence intensity, $Tu(\%) = 100 * u_{rms}/U_{mean}$
t	time
U	streamwise velocity component
\bar{U}	time-averaged velocity
U_{cf}	crossflow velocity, $U_{cf} = \sqrt{V^2 + W^2}$
U_i	instantaneous velocity
U_{rt}	rated wind velocity; the velocity at which turbine produces the maximum power
U_∞	free-stream wind velocity
U_θ	circumferential velocity, $U_\theta = V\sin\theta - W\cos\theta$
u	axial induction factors (Chapter 2)
u	streamwise velocity fluctuation component; $u = U_i - U_{mean}$
u_{rms}	root mean squared of the velocity fluctuations
V	local induced velocity (Chapter 2)
V	velocity in y direction (Chapter 4)
V	electrical voltage (Chapter 5)
W	relative wind velocity (Chapter 2)
W	velocity in z direction (Chapter 4)
w	blade span length (Chapter 3)

w	turbine distance from wind tunnel wall (Chapter 6)
X	streamwise distance from the grid turbulence generator
x	wake streamwise coordinate
y	vertical position from the blade trailing edge (Chapter 3)
y	spanwise distance from wing tip in inboard direction (Chapter 4)
z	coordinate in the direction of lift (Chapter 4)

Abbreviations

AEP	Annual Energy Production
AOA	Angle Of Attack
CCW	Counter Clockwise
CW	Clockwise
DMS	Double-Multiple Streamtube
FST	Free-Stream Turbulence
HAWT	Horizontal Axis Wind Turbine
OPP	Orificed Perforated Plate
PDF	Probability Density Function
PSD	Power Spectral Density
RPM	Rotation Per Minute
SB-VAWT	Straight Bladed Vertical Axis Wind Turbine
STP	Standard Temperature and Pressure
TSR	Tip Speed Ratio
VAWT	Vertical Axis Wind Turbine

Subscripts

a	arm
c	centrifugal direction
d	design point
e	equilibrium region between two semitubes
l	load
n	normal direction
opt	optimum

r	radial direction (Chapter 2)
r	rectifier (Chapter 5)
rt	rated (power)
rms	root mean squared
s	single (installation)
t	tangential direction
w	winding

Greek letters

α	angle of attack
Γ	circulation
γ	turbulence strain rate, $\gamma = u_{rms}/\lambda$
θ	azimuthal angle (Chapter 2)
θ	angular coordinate measured from y to z axis (Chapter 4)
Λ	turbulence integral length scale
λ	blade tip speed ratio, $\lambda = R\omega/U_\infty$ (Chapter 2,5,6)
λ	Taylor microscale (Chapter 3)
μ	blade aspect ratio, $\mu = H/c$ (Chapter 2)
μ	statistical mean of a sample data (Chapter 5)
ϑ	kinematic viscosity
ρ	density
σ	rotor solidity factor, $\sigma = Nc/R$ (Chapter 2,5,6)
σ	standard deviation (Chapter 5)
ω	rotational speed of rotor

Chapter 1: Introduction

1.1 Background

Vertical axis wind turbines (VAWT) have been considered as a potential choice in the wind industry in the recent decade [1-3]. Although VAWTs predate horizontal axis wind turbines (HAWTs), HAWTs have received more attention in the wind turbine industry [3]. From a historical viewpoint, modern VAWTs were patented in 1920s, but were then mainly ignored until the oil embargo of the early 1970s. This renewed interest in VAWTs was delayed again until the late 1980s as significant research and development investment in HAWTs has led to maturity in large scale electricity generation at relatively higher efficiencies in these machines [3,4]. In spite of this, a revival of interest has emerged in the VAWT technology in recent years (since late 2010s) for applications where VAWTs are likely to be more appropriate [1-3].

Compared to the horizontal design, VAWTs claim several advantages. The main advantage of VAWTs is that they can harness wind energy from any direction without yawing [5]. They also operate with lower aerodynamic noise emissions and integrate better into architectural projects [5]. In addition, vertical axis design offers better accessibility in that the generator, gearbox, and primary bearings can be located conveniently at or close to the ground [3]. On the other hand, this type of turbine has some challenges including self-starting requirement, large blade bending stresses, and oscillating loadings of the supporting structure that may result in fatigue failure due to severe vibrations [6].

It is also commonly stated that the efficiency of vertical axis machines is lower than horizontal ones for a given rotor area, however such an argument must be taken in proper context. In fact, it has been recently shown that VAWTs can perform more efficiently than HAWTs in certain environmental conditions; Pope et al. [7] conducted research on the influence of energy quality on wind turbines performance, and concluded that HAWTs can achieve higher efficiencies than VAWTs, only if the wind's energy quality is high. They [7] stated that the performance of a horizontal axis machine could be influenced negatively by several environmental factors such as wind turbulence or wind directional variability, while VAWTs can operate smoothly with no significant deterioration in such conditions [7]. HAWTs also need a great amount of land outside of urban areas to be installed, while VAWTs could be installed in small areas, building rooftops for instance [8]. Considering the aforementioned remarks, it can be

concluded that VAWTs are more appropriate for urban applications, water pumping, as well as off-grid and low power production [2,3,8,9].

Although VAWTs have relatively simple structure, their aerodynamic analysis still faces many challenges mainly due to the complex flowfield around and inside the rotor [10]. The complex aerodynamics exhibited by VAWTs can be attributed to the rapid and unsteady changes in angle of attack and the resultant wind velocity (hence the local Reynolds number); which are experienced as the blades rotate. Also, dynamic stall which occurs at low tip speed ratios along with tip vortices create a complicated three-dimensional flowfield [10,11]. Furthermore, the interactions between each turbine blade with either its own wake or with the vorticity field developed downstream of the other blades, generate an impulsive aerodynamic loading on the blades [12].

Various configurations of VAWTs evolved over many years can be broadly divided into two major categories of Savonius and Darrieus turbines [4]. A Savonius rotor which is driven by drag force consists of two half cylinders or cups attached to a rotating vertical shaft in opposing directions. The difference in drag on the two sides produces a torque for most but not all orientations to the wind [13]. Savonius turbines have some drawbacks including relatively large and heavy rotors, requirement of massive supporting structures to withstand storms, and low aerodynamic efficiency compared to other kind of wind turbines. In fact, the power coefficient of Savonius turbines can only reach up to 0.25 [3,13], while typical values of maximum power coefficient for other types of wind turbines vary between 0.3 to 0.45. It has been concluded in the literature that Savonius rotors are not cost-effective and only suitable for wind speed instruments or an auxiliary rotor to provide starting torque for rotors of the Darrieus turbines [3,10].

The Darrieus type VAWTs are driven by aerodynamic lift and consist of two or more airfoil shape blades connected to a central shaft. This configuration includes two popular designs, namely straight bladed and curved bladed VAWTs. The straight bladed-VAWTs (SB-VAWTs) which have relatively simple structure are reported to demonstrate higher aerodynamic performance than curved bladed or beater type VAWTs [3,13]. However, the bending moments encountered on curved bladed turbines are smaller than those of straight bladed machines [3,10,13]. But whether the blades are curved or straight, if they are of fixed pitch the VAWT typically develops little or no torque at low speeds, and therefore suffers from self-starting problem [10,13]. SB-VAWTs have gained much more attention in the wind industry, primarily due to their relatively simple structure and aerodynamic performance. A typical SB-VAWT is

depicted in Fig. 1. This research focuses on Darrieus type SB-VAWTs even if not specified specifically in the text.

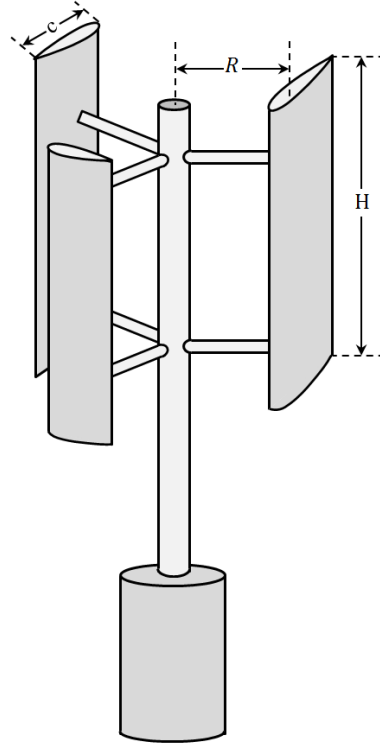


Figure 1: Schematic of a typical SB-VAWT for illustration purposes; R : rotor radius, H : blade height, c : blade chord length

Understanding the fundamental aspects of VAWT aerodynamics is crucial for a successful design. Numerous efforts have been made in the literature in order to better comprehend VAWTs flowfield via utilizing different analytical, numerical, and experimental approaches. Despite all research on different aspects of VAWTs, a straightforward design procedure is still lacking for such turbines. Because of this, several VAWT designs reported in the literature are not as efficient as they should be due to poor parameter selection [3,13]. The current research tries to address the design criteria on the most important parameters affecting VAWT performance. The knowledge gathered from the literature and an analytical aerodynamic analysis are utilized to provide a comprehensive design methodology for VAWTs.

Among the external parameters that can influence the aerodynamic performance of a wind turbine, free-stream turbulence is of great importance [14-15]. The turbulence intensity can also increase mechanical stresses on turbine components [16] and reduce the fatigue life of the

turbine structure [17]. The impact of wind turbulence is especially crucial for small wind turbines since they are typically installed near to ground where obstacles such as buildings, trees, etc. can result in high levels of free-stream turbulence [18]. Moreover, wind turbulence approaching small wind turbines in urban areas can be greater than that of a rural wind farm [19]. VAWTs which play an important role in the small wind turbine market can be highly affected by free-stream turbulence.

Despite the importance of the wind turbulence in VAWTs' power generation, the available literature on the topic is relatively scarce. Only a few researchers studied the influence of free-stream turbulence on the operation of horizontal [20-23] and vertical [23-25] axis wind turbines. Despite, there is no concrete agreement in their results on the effect of wind turbulence as different trends for the turbine output power with respect to the turbulence intensity have been reported in the literature. This may be partially due to the different turbulent flow types studied by different researchers, complicated by varying amounts of wind shear and unsteady wind [19,24,26]. This highlights the need for systematic performance testing under controlled turbulent flows with uniform and steady wind conditions. To achieve better experimental control, it would be advantageous to start with the simplest form of inflow turbulence, isotropic turbulence. To this end a grid turbulence generator has been employed to generate isotropic turbulence. Therefore, the influence of free-stream turbulence intensity on the aerodynamic performance of a SB-VAWT was studied in the presence of steady quasi-isotropic turbulent winds. Moreover, the variation in aerodynamic performance of a SB-VAWT's blade in a stationary installation under the effect of quasi-isotropic turbulent flows was measured in two series of wind tunnel testing. In these two fundamental studies, a SB-VAWT's blade was tested in two major flow configurations around a blade, namely two- and three-dimensional flows around a blade having closed- and free-ends, respectively.

Another subject of interest in VAWT design is the aerodynamic interaction of a group of turbines. The wind turbine wake losses in a wind farm can result in a substantial reduction in the total power output [27]. Therefore, finding the best possible way of positioning the turbines in the wind farm is an important stage in designing a wind farm. To avoid the wind and power reductions as well as to reduce the structural vibrations and fatigue loads, wind turbines are always spaced far apart occupying large areas of land [4]. For HAWTs, all turbines shed wakes or wind trails which reduce the turbine performance up to 40% [28,29]. In a HAWT farm, to maintain 90% of the performance of isolated HAWTs, the turbines must be spaced 3-5 turbine diameters apart in the cross-wind direction and 6-10 diameters apart in the downwind direction

which needs a relatively wide land area [29]. On the other hand, it has been suggested in the literature [30,31] that arranging VAWTs in specific layouts could enable them to extract energy from adjacent wakes. In particular, it has been shown that the output power from the whole farm exceeds the simple sum of the individual machine outputs [31]. The fundamental aspect of this idea is to optimally place counter rotating machines such that the wake shed by each is combined and accelerated in a common downstream direction, as displayed in Fig. 2. According to the literature, when two counter-rotating VAWTs are placed closely, the flow induced by each turbine is oriented in the same direction, resulting in reduced turbulence and vortex shedding [30,31].

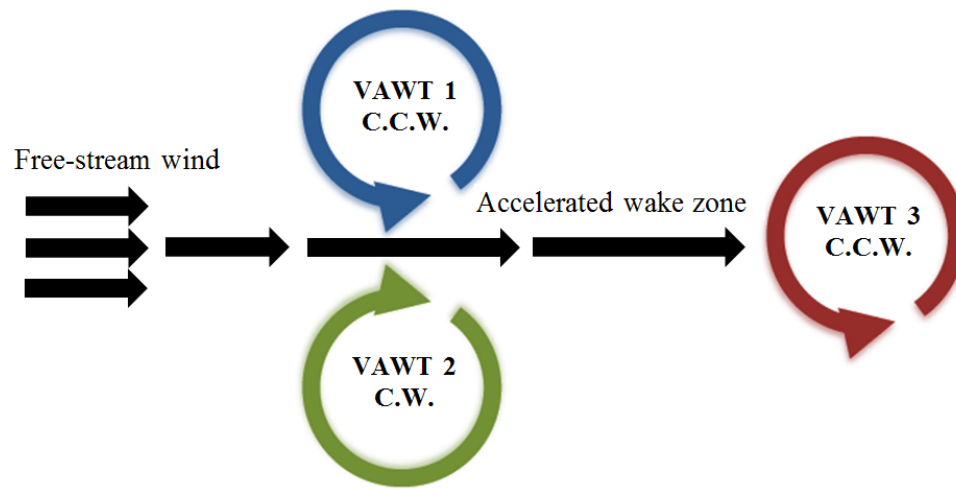


Figure 2: Schematic top view of a three-VAWT configuration with two counter-rotating turbines;
CW: clockwise, CCW: counter clockwise

While there are many studies on the optimal positioning of HAWTs in a wind farm, the aerodynamic interaction of VAWTs, particularly counter-rotating machines, has been investigated only in a handful of researches. The idea of employing counter-rotating VAWTs was first patented by Thomas in 2002 [30]. He claimed that putting a pair of VAWTs in a counter-rotating configuration can result in aerodynamic efficiency enhancement of the pair through vortex interaction between the two adjacent rotors [30]. Two series of full-scale field measurement of counter-rotating VAWTs under natural wind conditions in a wind farm was reported in two separate studies by Dabiri [31] and Kinzel et al. [32]. In the testing of a two counter-rotating VAWT configuration, Dabiri [31] found an increase, even though small, in the counter-rotating turbines' performance compared to that of isolated installation. In his array testing, Dabiri [31] reported the performance of the turbine located downstream of a counter-

rotating pair recovered to within 5% of the isolated turbine performance when the streamwise distance increased to four turbine diameters. Kinzel et al. [32] also studied the flowfield of counter-rotating VAWT arrays in the same wind farm as in Dabiri's study [31]. They [32] found the flow velocities return to 95% of the undisturbed wind within 6D downstream of a counter-rotating pair. In a full-scale numerical study on a pair of counter-rotating VAWTs, Korobenko et al. [33] reported a slight drop in the predicted aerodynamic torque of the pair compared to the single turbine. They [33] attributed this reduction to the small separation distance between the turbines (0.32D) that caused the turbines' blades encountering the wake of the blade from other neighboring turbine.

As briefly reviewed, all recent works on counter-rotating VAWTs are either field measurements [31,32], analytical [30], or numerical simulations [33,34]. Although these studies provide valuable information regarding the aerodynamic interaction of a group of wind turbines, they have some limitations to completely investigate this phenomenon. Field measurements are subject to the various terrain effects, stochastic nature of wind and varying meteorological conditions, making the repetition of the observation improbable if not impossible [29,35]. Numerical simulations still suffer from the lack of accuracy in turbulence modelling especially in separated flow regions [36], and analytical solutions use many simplifications which make them suitable mostly for engineering applications [37]. Wind tunnel testing, on the other hand, provides controlled conditions to systematically investigate the phenomenon. Therefore, one objective of this study is to analyze the aerodynamic interaction of counter-rotating VAWT arrays using a series of wind tunnel measurements under controlled flows with uniform and steady wind conditions.

To sum up, this thesis attempts to contribute to the understanding of the VAWT aerodynamics and tackle a few unaddressed challenges in this field. The research objectives of this thesis are as follows:

- To formulate the design parameters influencing a SB-VAWT aerodynamic performance and find the optimal range of these parameters,
- To study the influence of external turbulence on the aerodynamic performance of SB-VAWTs, and
- To investigate the aerodynamic interaction of counter-rotating SB-VAWTs in array configurations under controlled flow conditions.

1.2 Methodology

In order to address the unresolved challenges of the VAWT aerodynamics, formulating and analysis of parameters affecting a VAWT design seems imperative. The equations governing the VAWT flows were formulated to determine the turbine aerodynamic performance using a fast and cost effective analytical approach, introduced in Chapter 2. The double-multiple streamtube (DMS) method along with implementing a few refinements was formulated numerically in order to analyze the flow parameters affecting a SB-VAWT performance. The efficiency of this method was examined by comparing its results with experimental data from the literature. Several geometric parameters concerned with the design of a SB-VAWT have been optimized with respect to the turbine aerodynamic performance. These parameters include rotor solidity factor, blade aspect ratio, and rotor aspect ratio. Moreover, aerodynamic forces acting on the turbine rotor have been examined at several turbine operating conditions, and the critical loading conditions have been determined.

For understanding the effect of free-stream turbulence on VAWTs' performance, it is important that the performance of a single blade is examined under turbulent free-stream conditions first. The turbulent flows discussed in this thesis were generated using a grid in the shape of an orificed perforated plate with circular holes. It was shown the turbulent flows generated downstream of this grid are quasi-isotropic having uniform mean flow profiles, free of any wind shear effects. The level of turbulence intensity of these turbulent flows was controlled by varying the location of the grid upstream of the test model. Chapters 3 and 4 include two fundamental studies on the free-stream turbulence effect on the aerodynamic performance of a VAWT's blade in two different stationary installations. The two-dimensional aerodynamic testing of a single VAWT blade was performed in a wind tunnel at two levels of free-stream turbulence to characterize the aerodynamic performance of the blade's airfoil profile, discussed in Chapter 3. Two dynamic force transducers were used to measure the aerodynamic loading of the blade at a range of angles of attack as the blade was spanning the entire wind tunnel section width. Hot-wire anemometry technique was also employed to quantify several flowfield parameters in the wake of the blade at different flow conditions.

While two-dimensional aerodynamic testing provides the fundamental behavior of a blade airfoil profile, it is necessary to carry out three-dimensional testing of the turbine blade to simulate conditions based on the real application. Chapter 4 focused on the performance testing of a single VAWT blade under three-dimensional flow scenario having two levels of free-stream turbulence. The wing section spanned approximately half height of the wind tunnel section and

fixed vertically to the load cell at the base. The aerodynamic forces and wake flow parameters were measured and discussed in this chapter. The so-called wing-tip vortex that rolls up around the free ends of finite-length lifting surfaces was also captured and discussed in chapter 4.

Having completed two fundamental studies of the external turbulence effect on a single turbine blade in Chapters 3 and 4, Chapter 5 is devoted to examine the influence of free-stream turbulence on a SB-VAWT operation. This was carried out experimentally via wind tunnel testing by generating turbulent flows using the same turbulence generator grid. The turbulence parameters of the flow were characterized using the hot-wire anemometry technique. The turbine's aerodynamic performance at different levels of free-stream turbulence intensity was quantified by measuring its power output and rotational speed.

The aerodynamic interaction of SB-VAWTs was studied by conducting a series of wind tunnel measurements, discussed in Chapter 6. Several configurations of two- and three-turbine arrays were tested and their results were compared with that of the isolated installation case. Two pairs of counter-rotating and co-rotating VAWTs were tested where the free-stream wind was perpendicular to the line connecting the turbines center. Several measurements were also performed for three-turbine arrays with different spacing where a turbine was operating downstream of a counter-rotating pair and the free-stream wind was perpendicular to the pair. A series of testing was also performed to find the optimum range for the spacing parameters in the three-turbine arrays.

Another related topic studied in this thesis is investigating the turbulence characteristics of a flow over a transversely grooved surface under low and high levels of external turbulence, discussed in Appendix A. This was done with the goal of finding an efficient and inexpensive way to improve the aerodynamic performance of a lifting surface. Surface modification by using grooves is a well-known flow control approach to control the flow separation. In fact, transverse grooves can serve as vortex generators introducing vortices and increasing the momentum of boundary layer regions [38]. The added energy from vortex generated geometries enables near-wall fluid particles to resist and delay separation. Generally it is desirable to postpone separation so that form drag is reduced, stall is delayed, lift is enhanced, and pressure recovery is improved [39]. The outcome of this study may be generalized for efficiency improvement of any aerodynamic surfaces including VAWT blades.

The studies performed in this thesis have the common goal of improving the aerodynamic efficiency of VAWTs. Further research is still required to uncover the underlying physics of VAWT aerodynamics and improve the current designs. More detailed performance testing as well

as high-accuracy numerical simulations can add value in this regard. The design guide presented in this thesis can be an efficient tool to assist future researchers in primary design phase of SB-VAWTs. Moreover, the experimental data presented here can be a benchmark for future studies to investigate the challenges discussed in the current research in a more efficient way.

1.3 References

- [1]. Bedon, G., Castelli, M.R., Benini, E., Optimization of a Darrieus vertical-axis wind turbine using blade element - momentum theory and evolutionary algorithm, *Renewable Energy*, 2013; 59: 184-192.
- [2]. Tjiu, W., Marnoto, T., Mat, S., Ruslan, M.H., Sopian, K., Darrieus vertical axis wind turbine for power generation I: Assessment of Darrieus VAWT configurations (Review), *Renewable Energy*, 2015; 75: 50-67.
- [3]. Aslam Bhutta, M.M., Hayat, N., Farooq, A.U., Ali, Z., Jamil, Sh.R., Hussain, Z., Vertical axis wind turbine - a review of various configurations and design techniques, *Renewable and Sustainable Energy Reviews*, 2012; 16(4): 1926-1939.
- [4]. Spera, D.A., *Wind turbine technology: Fundamental concepts in wind turbine engineering*, 2nd Ed, ASME, New York, 2009.
- [5]. Battisti, L., Zanne, L., Dell'Anna, S., Persico, G., Paradiso, B., Aerodynamic measurements on a vertical axis wind turbine in a large scale wind tunnel, *Journal of Energy Resources Technology*, Transaction of the ASME, 2011; 133(3): No. 031201, 1-9.
- [6]. Mukinovic, M., Brenner, G., Rahimi, A., *Aerodynamic study of vertical axis wind turbines*, Lecture Notes in Computational Science and Engineering, Springer, Berlin, 2011; 74(2): 43-49.
- [7]. Pope, K., Dincer, I., Naterer, G.F., Energy and exergy efficiency comparison of horizontal and vertical axis wind turbines, *Renewable Energy*, 2010; 35: 2102-2113.
- [8]. Chong, W.T., Pan, K.C., Poh, S.C., Fazlizan, A., Oon, C.S., Badarudin, A., Nik-Ghazali N., Performance investigation of a power augmented vertical axis wind turbine for urban high-rise application, *Renewable Energy*, 2013; 51: 388-397.
- [9]. Balduzzi, F., Bianchini, A., Carnevale, E.A., Ferrari, L., Magnani S., Feasibility analysis of a Darrieus vertical-axis wind turbine installation in the rooftop of a building, *Applied Energy*, 2012; 97: 921-9.
- [10]. Tai, F.Z., Kang, K.W., Jang, M.H., Woo, Y.J., Lee, J.H., Study on the analysis method for the vertical-axis wind turbines having Darrieus blades, *Renewable Energy*, 2013; 54: 26-31.

- [11]. Islam, M., Ting, D.S-K., Fartaj, A., Aerodynamic models for Darrieus-type straight-bladed vertical axis wind turbines (Review), *Renewable and Sustainable Energy Reviews*, 2008; 12(4): 1087-1109.
- [12]. Ottermo, F., Bernhoff, H., Resonances and aerodynamic damping of a vertical axis wind turbine, *Wind Engineering*, 2012; 36(3): 297-304.
- [13]. Paraschivoiu, I., Wind turbine design - with emphasis on Darrieus concept, Polytechnic International Press, Montreal, 2002.
- [14]. Wekesa, D.W., Wang, C., Danao, L.A., Wei, Y., Influence of operating conditions on unsteady wind performance of vertical axis wind turbines operating within a fluctuating free-stream: A numerical study, *Journal of Wind Engineering and Industrial Aerodynamics*, 2014; 135: 76-89.
- [15]. Pope, K., Naterer, G.F., Dincer, I., Tsang, E., Power correlation for vertical axis wind turbines with varying geometries, *International Journal of Energy Research*, 2011; 35: 423-435.
- [16]. Park, J., Basu, S., Manuel, L., Large-eddy simulation of stable boundary layer turbulence and estimation of associated wind turbine loads, *Wind Energy*, 2014; 17(3): 359-384.
- [17]. Riziotis, V.A., Voutsinas, S.G., Fatigue loads on wind turbines of different control strategies operating in complex terrain, *Journal of Wind Engineering and Industrial Aerodynamics*, 2000; 85(3): 211-240.
- [18]. Araújo, A.M., de Alencar Valença, D.A., Asibor, A.I., Rosas, P.A.C., An approach to simulate wind fields around an urban environment for wind energy application, *Environmental Fluid Mechanics*, 2013; 13(1): 33-50.
- [19]. Sunderland, K., Woolmington, T., Blackledge, J., Conlon, M., Small wind turbines in turbulent (urban) environments: A consideration of normal and Weibull distributions for power prediction, *Journal of Wind Engineering and Industrial Aerodynamics*, 2013; 121: 70-81.
- [20]. Lubitz, W.D., Impact of ambient turbulence on performance of a small wind turbine, *Renewable Energy*, 2014; 61: 69-73.
- [21]. Smith, J., Effects of turbulence intensity on the performance of small wind turbines, *Small Wind Conference*, 2010, Stevens Point, WI, USA.
- [22]. Mikkelsen, K., Effect of free stream turbulence on wind turbine performance, MSc thesis, Norwegian University of Science and Technology, Norway, 2013.
- [23]. Pagnini, L.C., Burlando, M., Repetto, M.P., Experimental power curve of small-size wind turbines in turbulent urban environment, *Applied Energy*, 2015; 154: 112-121.
- [24]. Kooiman, S.J., Tullis, S.W., Response of a vertical axis wind turbine to time varying wind conditions found within the urban environment, *Wind Engineering*, 2012; 34(4): 389-401.

- [25]. Danao, L.A., Eboibi, O., Howell, R., An experimental investigation into the influence of unsteady wind on the performance of a vertical axis wind turbine, *Applied Energy*, 2013; 107: 403-411.
- [26]. Gottschall, J. and Peinke, J., Stochastic modelling of a wind turbine's power output with special respect to turbulent dynamics, *Journal of Physics: Conference Series*, 2007; 75(1): No. 012045, 1-8.
- [27]. Rivas, R.A., Clausen, J., Hansen, K.S., Jensen, L.E., Solving the turbine positioning problem for large offshore wind farms by simulated annealing, *Wind Engineering*, 2009; 33(3): 287-298.
- [28]. Lignarolo, L.E.M., Ragni, D., Krishnaswami, C., Chen, Q., Simão Ferreira, C.J., van Bussel, G.J.W., Experimental analysis of the wake of a horizontal-axis wind-turbine model, *Renewable Energy*, 2014; 70: 31-46.
- [29]. Sørensen, B., *Renewable energy: Its physics, engineering, use, environmental impacts, economy, and planning aspects*, Elsevier Academic Press, New York, 2004.
- [30]. Thomas, R.N., Coupled vortex vertical axis wind turbine, US Patent No. 6,784,566, 2004.
- [31]. Dabiri, J.O., Potential order-of-magnitude enhancement of wind farm power density via counter-rotating vertical-axis wind turbine arrays, *Journal of Renewable and Sustainable Energy*, 2011; 3: No. 043104, 1-12.
- [32]. Kinzel, M., Mulligan, Q., Dabiri, J.O., Energy exchange in an array of vertical-axis wind turbines, *Journal of Turbulence*, 2012; 13(38): 1-13.
- [33]. Korobenko, A., Hsu, M.-C., Akkerman, I., Bazilevs, Y., Aerodynamic simulation of vertical-axis wind turbines, *Journal of Applied Mechanics, Transaction of the ASME*, 2014; 81: No. 021011, 1-6.
- [34]. Duraisamy, K., Lakshminarayan, V., Flow physics and performance of vertical axis wind turbine arrays, 32nd AIAA Applied Aerodynamics Conference, AIAA 2014-3139, June 2014, Atlanta, GA.
- [35]. Ganesh, R.R., Rickerl, T.L., Klimas, P.C., Aerodynamic interference of vertical axis wind turbines, *Journal of Propulsion and Power*, 1990; 6(5): 645-653.
- [36]. Li, C., Zhu, S., Xu, Y.L., Xiao, Y., 2.5D large eddy simulation of vertical axis wind turbine in high angle of attack flow, *Renewable Energy*, 2013; 51: 317-330.
- [37]. Jin, X., Zhao, G., Gao, K., Ju, W., Darrieus vertical axis wind turbine: Basic research methods, *Renewable and Sustainable Energy Reviews*, 2015: 42: 212-225.
- [38]. Gad-El-Hak, M., *Flow control: Passive, active and reactive flow management*, Cambridge University Press, London, 2000.
- [39]. Pearson, B.R., Elavarasan, R., Antonia, R.A., The response of a turbulent boundary layer to a square groove, *Journal of Fluids Engineering, Transaction of the ASME*, 1997; 119: 466-469.

Chapter 2: Straight bladed vertical axis wind turbine rotor design guide based on aerodynamic performance and loading analysis¹

2.1 Introduction

Vertical axis wind turbines (VAWTs) have received significant attention in the recent decade [1,2]. Compared to their horizontal design counterpart, VAWTs claim several advantages. The principle advantage of VAWTs is that they can harness wind energy from any direction without yawing [3]. They also operate with lower aerodynamic noise emissions and integrate more easily into architectural projects. In addition, vertical axis designs offer better accessibility for maintenance given that the generator, gearbox, and primary bearings can be located conveniently at or close to the ground [4]. On the other hand, this type of turbine has some drawbacks including self-starting requirement, large blade bending stresses, and oscillating loading of the supporting structure that may result in fatigue failure due to severe vibrations [5]. It is also commonly stated that the efficiency of vertical axis machines is lower than horizontal ones for a given rotor area, however such an argument must be taken in proper context. In fact, it has been recently shown that VAWTs can perform more efficiently than horizontal axis wind turbines (HAWTs) in certain environmental conditions; Pope et al. [6] conducted research on the influence of energy quality on wind turbines performance, and concluded that HAWTs can achieve higher efficiencies than VAWTs, only if the wind's energy quality is high. They [6] stated that the performance of a horizontal axis machine could be influenced negatively by environmental factors such as wind turbulence and wind directional variability, while VAWTs can operate smoothly with no significant deterioration under such conditions [6]. Considering the latter point, along with the fact that VAWTs can take advantage of small spaces like building rooftops makes them more appropriate for urban applications, as well as off-grid and low power production [7,8].

The VAWT concept still faces many challenges caused by the complex flow structure around and inside the rotor. The complex aerodynamics exhibited by VAWTs can be attributed to the rapid and unsteady changes in the angle of attack and the resultant wind velocity. Also, dynamic stall which occurs at low tip speed ratios further complicates the three-dimensional flowfield. Moreover, the interactions between each turbine blade with either its own wake or with

¹ This work was published as: "Ahmadi-Baloutaki, M., Carriveau, R., Ting, D.S.-K., SB-VAWT rotor design guide based on aerodynamic performance and loading analysis, Proceedings of the Institution of Mechanical Engineers, Part A: Journal of Power and Energy, 2014; 228(7): 742-759, Winner of the Best Paper Award of the Year."

the vorticity field developed downstream of the other blades, generate an impulsive aerodynamic loading on the blades [9]. A good understanding of the fundamental aspects of VAWT aerodynamics is crucial for a successful design. Numerous efforts have been made in the literature in order to better comprehend VAWTs flowfield via utilizing different analytical, numerical, and experimental approaches.

Among the various configurations of VAWTs evolved over the years, turbines with straight blades have gained much more attention in the wind industry, primarily due to their relatively simple structure and aerodynamic performance. A typical straight bladed-VAWT (SB-VAWT) with its key dimensions is depicted in Fig. 1. The three main parts of the SB-VAWT are the blades, the supporting arms, and the central shaft. The SB-VAWT is a popular design of a major category of vertical axis machines, called Darrieus turbines. A Darrieus turbine is a VAWT which is driven by aerodynamic lift, in contrast to drag driven Savonius turbines [10]. In addition to using straight blades in Darrieus machines, there are also other configurations that have utilized non-straight blades. The most common non-straight bladed VAWTs with good aerodynamic efficiency are the eggbeater type VAWTs with curved blades [1], VAWTs with canted blades [11], and VAWTs with helically twisted blades [12]. The main reason for adopting non-straight blades is to minimize the bending moments in the blades caused by centripetal acceleration as reported by several researchers [2,10,13,14]. From an aerodynamic standpoint, the non-straight bladed VAWTs have slightly more power efficiency than the similar straight bladed ones, they also offer the advantage of distributing the fluctuating aerodynamic loads which can alleviate rotor vibration and fatigue issues. This advantage is more remarkable in VAWTs with helically twisted blades; which deliver a relatively steady torque to the shaft [12,13]. The primary drawback of non-straight bladed VAWTs is the difficulty in manufacture of complex geometries and the associated higher costs that scale with the size of turbine [2]. Also, non-straight bladed VAWTs are somewhat more prone to the dynamic stall than SB-VAWTs as demonstrated by Scheurich et al. [13]. This is primarily due to the large variation of local relative velocity and local angle of attack along the blade span in turbines with non-straight blades, while straight bladed-VAWTs experience a more uniform local angle of attack in the blade spanwise direction [13].

Despite numerous works on different aspects of SB-VAWTs, a straightforward design procedure is still lacking. Because of this, several SB-VAWT designs reported in the literature are not as efficient as they could be due to poor parameter selection [10]. The current study tries to address the design criteria on the most important parameters affecting SB-VAWT performance.

The knowledge gathered from the literature and an existing analytical aerodynamic analysis are utilized to provide a comprehensive design methodology for SB-VAWTs. The double-multiple streamtube method has been employed to investigate the flow field around a SB-VAWT. Several geometric parameters concerned with the design of a SB-VAWT have been optimized with respect to the rotor aerodynamic performance. Moreover, aerodynamic forces acting on the turbine rotor have been examined at several turbine operating conditions, and the critical loading conditions have been determined. Various configurations of supporting arms have also been examined to discover the most effective scheme. In an attempt to include all significant design factors, the current paper aims to provide a tool to assist and improve the primary SB-VAWT design phase for either industrial or research purposes.

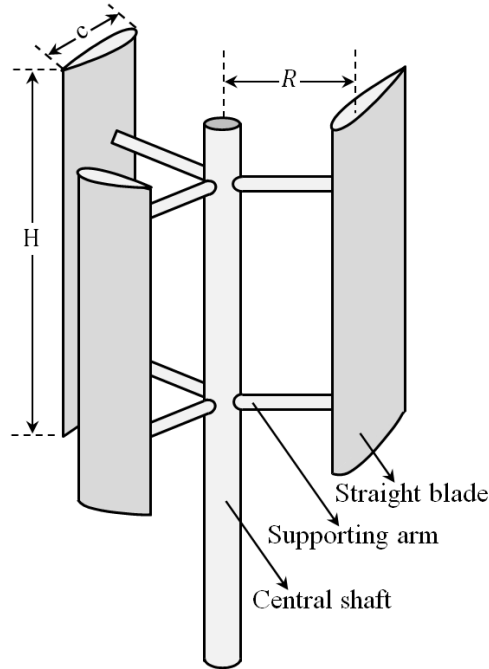


Figure 1: A typical SB-VAWT for illustration purposes

2.2 Analytical modeling

2.2.1 Local flow parameters

The local flow parameters over the blades such as wind velocity and angle of attack vary along their circular path during the turbine rotation. The flow relative velocity, W , at each azimuthal angle θ , is determined from Eq. 1 in Table 1 as the vector summation of blade tip velocity, $R\omega$, and local induced velocity, V , where λ is the tip speed ratio, $\lambda = R\omega/V_\infty$ [10].

These velocity components acting on the blade are displayed in Fig. 2a, while Table 1 summarizes the important parameters concerned with the flow around a VAWT. The local angle of attack, α , varies continuously with azimuthal angle; see Fig. 2a and Eq. 2. The tangential and normal force components can be determined from decomposition of the aerodynamic forces (lift and drag) acting on a blade, as depicted in Fig. 2b (see Eqs. 3-6). The dynamic torque in each turbine revolution is produced by the average tangential force, \bar{F}_t , as expressed by Eq. 7. Knowing the total torque (Eq. 8), and the turbine output power (Eq. 9), the turbine power coefficient, C_p , is defined as the ratio of turbine output power to the wind stream potential power as expressed by Eq. 10 [10]. The main unknown of the VAWT flow analysis is the local induced velocity which can be deduced from several methods based on different theories.

Table 1: Equations used for SB-VAWT formulation

Parameter	Equation	
Blade relative velocity	$W = V \sqrt{\left(\frac{\lambda}{V/V_\infty} + \cos\theta\right)^2 + \sin^2\theta}$	(1)
Blade angle of attack	$\alpha = \tan^{-1}\left(\frac{\sin\theta}{\frac{\lambda}{V/V_\infty} + \cos\theta}\right)$	(2)
Tangential force coefficient	$C_t = C_l \sin\alpha - C_d \cos\alpha$	(3)
Normal force coefficient	$C_n = C_l \cos\alpha + C_d \sin\alpha$	(4)
Blade tangential force	$F_t = C_t \left(\frac{1}{2} \rho A_p W^2\right)$	(5)
Blade normal force	$F_n = C_n \left(\frac{1}{2} \rho A_p W^2\right)$	(6)
Average tangential force	$\bar{F}_t = \frac{1}{2\pi} \int_0^{2\pi} F_t(\theta) d\theta$	(7)
Overall turbine torque	$Q = N \bar{F}_t R$	(8)

Total output power $P_{out} = Q\omega$ (9)

Turbine power coefficient $C_P = \frac{P_{out}}{\frac{1}{2}\rho A_r V_\infty^3}$ (10)

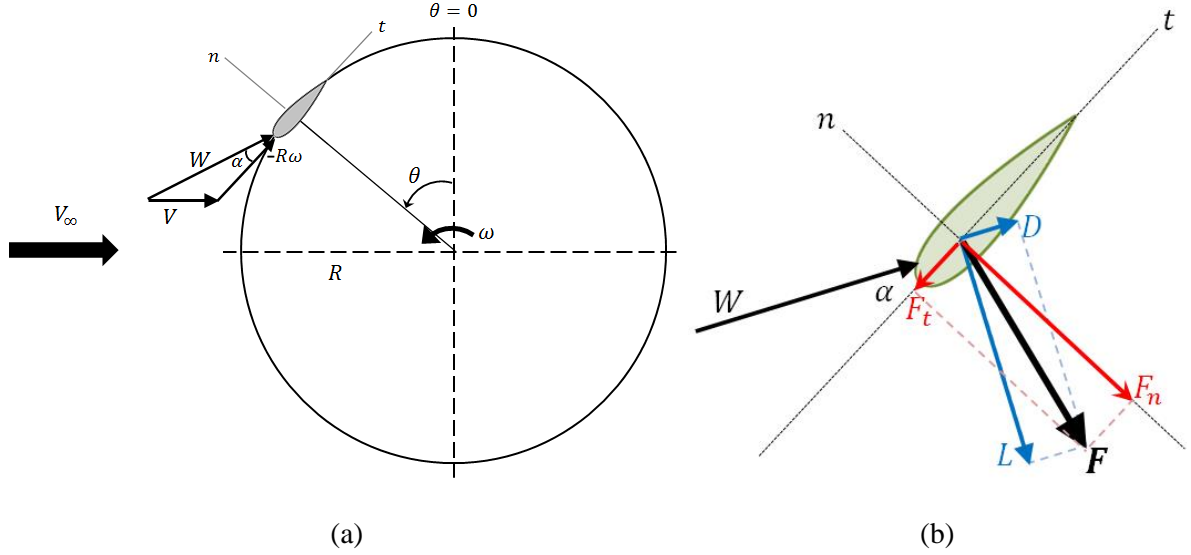


Figure 2: Schematic illustration of VAWTs operation; (a) velocity triangle to determine flow relative velocity, and (b) various force components at a particular azimuthal angle

2.2.2 Double-Multiple Streamtube model

The analytical method utilized in this study is based on an improved version of the Double-Multiple Streamtube (DMS) model [10] which considers the flow as inviscid and incompressible to determine the local induced velocity. This model divides the rotor area into a series of adjacent, aerodynamically independent parallel streamtubes and implements the momentum conservation and blade element theories for each streamtube. Since the local induced velocity differs extensively between the upstream and downstream sides of the rotor, two sets of separate calculations are performed at both sides of each streamtube called semitubes. An illustration of a typical streamtube is given in Fig. 3 where several key velocities are marked at different locations in the same figure. At each streamtube, the air flows through two actuator disks where the one-dimensional momentum conservation theory is utilized to correlate the

turbine upstream and downstream velocities, V and V' by introducing axial induction factors, u and u' for upstream and downstream regions as

$$V = uV_\infty \quad (11)$$

$$V_e = (2u - 1)V_\infty \quad (12)$$

$$V' = u'(2u - 1)V_\infty \quad (13)$$

where V_e is the equilibrium velocity in the joining region of both semitubes. A second set of equations is needed in order to determine the induction factors which is derived from the blade element theory [10]. Blade element theory uses the airfoil lift and drag data to estimate the aerodynamic forces acting on the upstream and downstream blade elements. Combining the blade element theory and momentum theory for each streamtube at the rotor upstream region ($0 \leq \theta \leq \pi$) results in the upstream induction factor as follows

$$u = \frac{\pi}{F_u + \pi} \quad (14)$$

$$F_u = \frac{\sigma}{2\pi} \int_0^\pi \left(\frac{W}{V_\infty}\right)^2 |\sec\theta| (C_n \cos\theta - C_t \sin\theta) d\theta \quad (15)$$

where σ is the rotor solidity factor. A similar set of equations is derived for the downstream region ($\pi \leq \theta \leq 2\pi$) in order to determine the downstream induction factor which can be found in [10] or [15]. An iterative algorithm has been utilized in order to calculate the flow parameters. An initial value of unity is assumed for the upstream induction factor, and the numerical process is iterated until the difference between two consecutive induction factors reaches a value less than 10^{-4} . The converged values of induction factor in upstream semitubes are used as the initial guess for the induction factors in the associated downstream semitubes. When numerical convergence is achieved, all flow quantities and the overall torque and the mechanical power are determined using expressions summarized in Table 1.

It should be noted that the DMS method was used in the current study since it is a fast and numerically inexpensive model while provides acceptable accuracy for the initial design stage. The other most widely-used models to analyze VAWT flowfield are the vortex model and the cascade model. It was found in the literature [10,14] each of these three models has their strengths and weaknesses. The vortex models are considered to be the most accurate models, but they are computationally expensive and in some cases they exhibit convergence problems. It has also been found that the DMS model suffers from low accuracy for high tip speed ratios and high

solidity VAWTs. The Cascade model gives smooth convergence even at high tip speed ratios and high solidity VAWTs with quite reasonable accuracy.

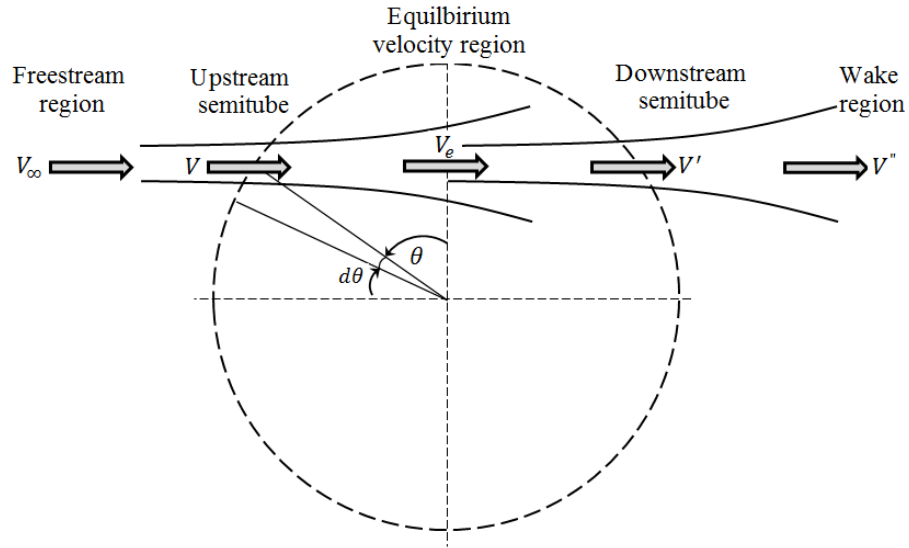


Figure 3: The double-multiple streamtube conceptual schematic with key velocities

2.2.3 Refinement of the analytical model

The analytical approach discussed in the previous section examines the flow parameters on a circular path on a two dimensional plane perpendicular to the rotor shaft. Then, the overall turbine performance is estimated by introducing the rotor height into the formulation. In order to achieve more accurate results some corrections should be applied to this method. A comprehensive discussion on these corrections has been provided in Refs. [10,14-16]. Since some of these factors have only a minor contribution in the final output, only the most significant corrections have been considered in the present study, namely blade aspect ratio, dynamic stall, and supporting arms parasitic drag.

One of the critical tasks in SB-VAWTs performance analysis is to provide the aerodynamic data of the blade used for the turbine in terms of lift and drag coefficients. The closer the blade aerodynamic coefficients are to the real values, the more accurate the analytical solution will be. In order to satisfy this, the blade force coefficients have been extracted from experimental works in the literature [17]. For instance, Fig. 4 depicts the lift and drag coefficients of a NACA0015 blade at different free-stream Reynolds numbers, selected based on the corresponding tabulated data available in Ref. [17]. At this step, the blade angle of attack, α , the blade relative velocity, W , and the corresponding local Reynolds number, $Re_\theta = Wc/\nu$, at each

azimuthal angle, θ , should be determined (see Eqs. 1 and 2 and Fig. 2b). This part of the numerical procedure is also shown in Fig. 5 for a candidate SB-VAWT having three NACA0015 blades with an aspect ratio of 20 and a rotor solidity ratio of 0.2 operating under a free-stream Reynolds number of 170,000. Figures 5a and 5b display the blade angle of attack and local Reynolds number at one complete revolution for three different tip speed ratios. Now, with blade angle of attack and local Reynolds number (α, Re_θ) at each azimuthal angle, the blade aerodynamic coefficients are extracted from relevant experimental data. This has been done for the candidate turbine in Figs. 5c and 5d. It should be noted that, for some azimuthal angles where aerodynamic coefficients are not available for the corresponding pair of α, Re_θ a linear interpolation was performed on the available data to estimate the lift and drag coefficients. It can be observed from Figs. 5c and 5d that the lift to drag ratio is high for high tip speed ratios. This point is confirmed in Fig. 5e that shows the blade lift to drag ratio over a complete revolution.

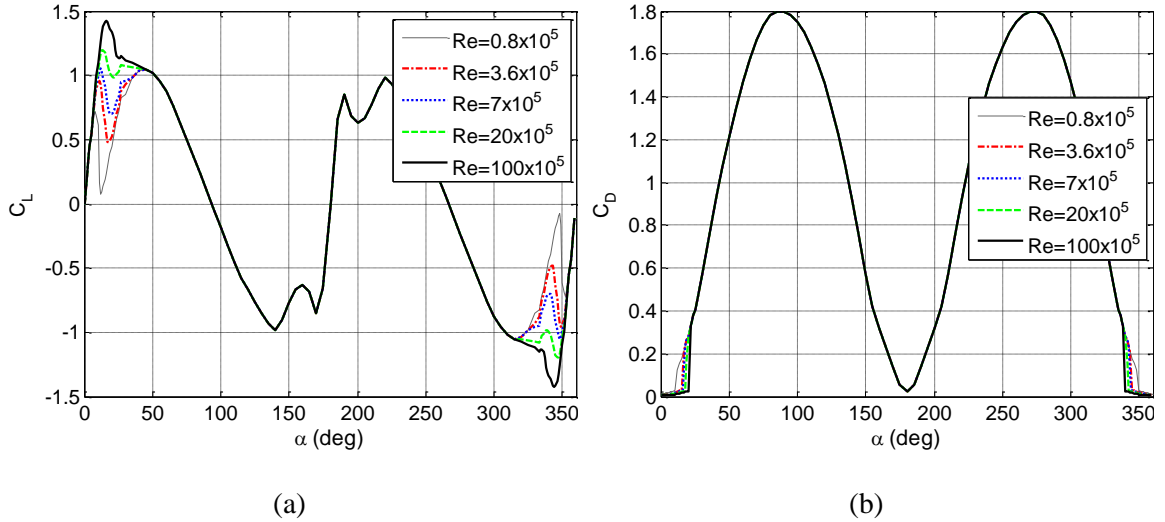
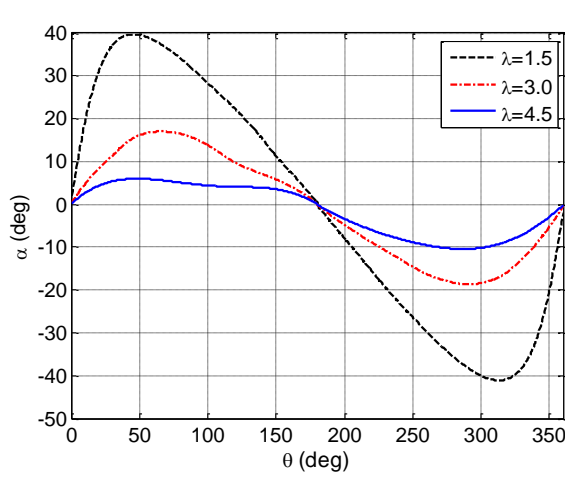
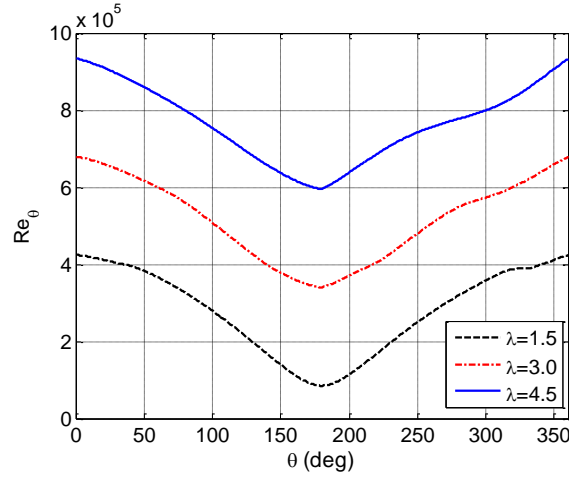


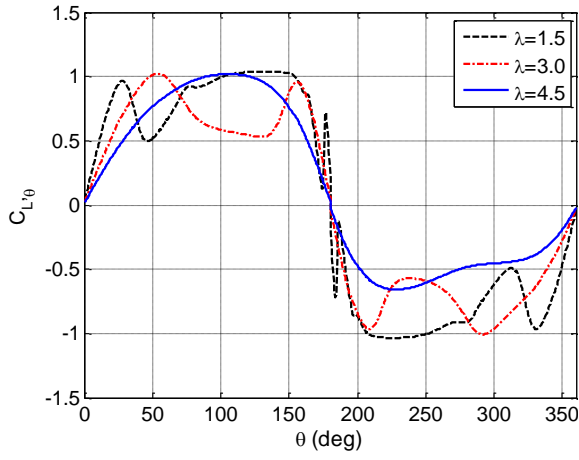
Figure 4: (a) Lift, and (b) drag coefficients of a NACA0015 blade; experimental data of Sheldahl and Klimas [17]



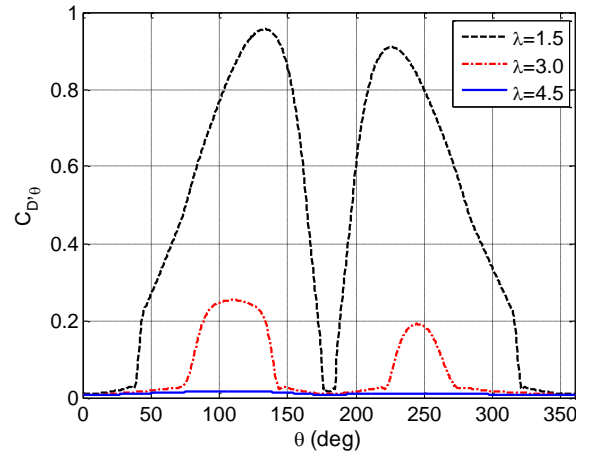
(a)



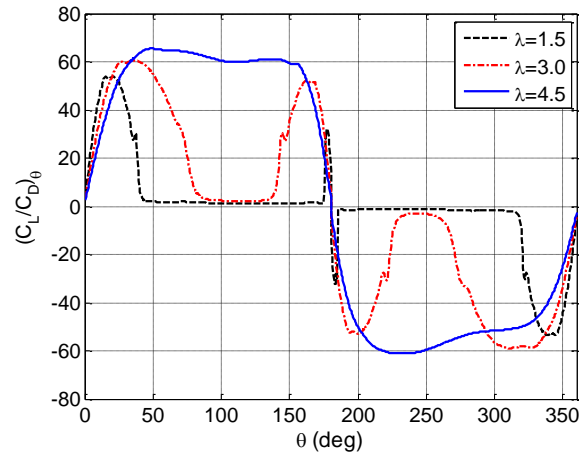
(b)



(c)



(d)



(e)

Figure 5: Variation of local blade parameters in one complete revolution of a SB-VAWT having three NACA0015 blades with $\mu = 20$, $\sigma = 0.2$, $Re_\infty = 170,000$; (a) angle of attack, (b) local Reynolds number, (c) lift coefficient, (d) drag coefficient, and (e) lift to drag ratio

The blade aerodynamic data is usually provided based on the infinite aspect ratio (two dimensional flow approximations). In order to more accurately model SB-VAWTs with finite blade length, the aerodynamic coefficients should be modified considering the effect of aspect ratio. According to the fundamental aerodynamics of wing sections, the flow over straight wings, or similarly, VAWT blades can be considered two-dimensional over their central portion [18]. However, the effects of three dimensionality increase along the spanwise direction toward the ends of the airfoil. This is accompanied with tip losses due to the vortex formation which reduces the lift-to-drag ratio. The modified lift and drag for a finite length can be estimated from the following equations [19], from which a decrease in lift and an increase in drag coefficients can be inferred. It should be noted that a more accurate method for aspect ratio modification in VAWT studies is to calculate the modified angle of attack from the induced velocity which can be determined from trailing vortices by more accurate wake modeling, such as [13] or from experimental studies.

$$\alpha' = \alpha + \frac{C_l}{\pi\mu} \quad (16)$$

$$C'_l = \frac{C_l}{1 + \frac{a_0}{\pi\mu}} \quad (17)$$

$$C'_d = C_d + \frac{C_l^2}{\pi\mu} \quad (18)$$

The blade dynamic stall is a complex and unsteady phenomenon which SB-VAWTs encounter during their operation. The dynamic stall occurs when the blade angle of attack changes rapidly with time [10]. Aerodynamic force coefficients differ quite significantly from the static ones in dynamic stall. Predicting dynamic stall response is significantly more challenging than static stall since it depends on many additional parameters such as blade profile, rate of change of angle of attack, turbulence level, type of motion, and three dimensional effects. In order to formulate the dynamic stall effect, the methodology proposed by Kirke [20] is adopted here. In this approach, the modified angle of attack is deduced based on the changing rate of the

angle of attack with time, blade resultant velocity, and blade geometric characteristics. Also, a set of empirical correlations was used to determine the aerodynamic coefficients modified for dynamic stall. Here we emphasize that the lift and drag coefficients modified at the previous stage (Eqs. 17 and 18), are further refined at this step according to the dynamic stall model. Finally, these refined aerodynamic coefficients (Eqs. 20 and 21) are used in the numerical calculation described in Sections 2.2.1 and 2.2.2. The following expressions show a summary of modified parameters and their influencing variables according to the dynamic stall model used [20].

$$\alpha'' = f(\alpha', \dot{\alpha}', W, c, t_c) \quad (19)$$

$$C_l'' = f(C_l', \alpha'', \alpha_0'') \quad (20)$$

$$C_d'' = f(C_d', C_l'') \quad (21)$$

One of the major disadvantages of SB-VAWTs is the need to use supporting arms. As will be explained later in this paper, supporting arms which connect the turbine blades to the central shaft generate additional parasitic drag which reduces the output power. Parasitic drag caused by supporting arms has been formulated in this study according to the outline described in [14]. It was shown by Islam [14] that the reduction in power coefficient due to supporting arms, $C_{P,a}$, can be estimated as

$$C_{P,a} = \frac{1}{8} N_a C_{d,a} \frac{b}{H} \lambda^3 \quad (22)$$

where N_a is the total number of turbine supporting arms, b is the supporting arm width, and $C_{d,a}$ is the drag coefficient of the supporting arm profile.

2.2.4 Code validation

In order to validate the analytical scheme used in the current study, the performance curve of a candidate SB-VAWT has been compared to field experimental results of Kjellin et al. [21], as shown in Fig. 6. The wind turbine studied by Kjellin et al. [21] had three straight NACA0021 blades and two NACA0025 inspired profile supporting arms per blade. Figure 6 shows a good agreement between the DMS predictions and the experimental data. The present method predicts slightly higher values but within the experimental uncertainty limits for the power coefficient in $2.6 < \lambda < 3.7$.

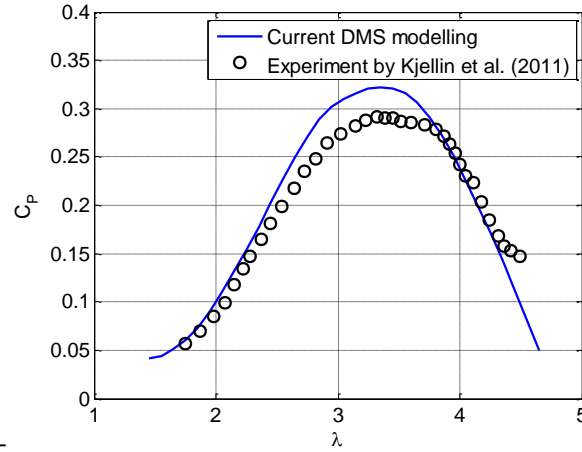


Figure 6: Power coefficient comparison of current DMS model with experimental data [21]

The numerical procedure validation using turbine power coefficient is satisfactory, but is somewhat restricted because C_p is an integral performance parameter. Comparison of flow parameters around the blades as a function of the azimuth angle is a more robust validation. One of the seminal experimental works that reported detailed flow parameters around a VAWT was performed by Akins [22] at Sandia National Laboratories. In this experimental field test, the angle of attack, normal and tangential force coefficients were reported for a wind turbine with two blades having NACA0015 profile. Figure 7 displays the results of the present analytical calculations along with the experimental data of Ref. [22] at a tip speed ratio of $\lambda = 3.7$. The agreements for the blade angle of attack and normal force coefficient between these two datasets is good at most azimuthal locations as can be observed in Fig. 7a and 7b. However, the tangential force coefficients predicted by the present DMS method deviates from the measured values, as shown in Fig. 7c. One reason behind this discrepancy is owed to limitations of the experimental measurement [22], as the skin friction force component has been ignored. Taking into account the skin friction effect in Akins' experiments would make the derived tangential force values smaller, while its effect on normal force coefficients is negligible [22]. This would move the experimental data points closer to the predicted values. Nevertheless, the fair agreement confirms that the model is principally sound. In short, the DMS analytical model appears to provide reliable results that may be used in the preliminary stages of SB-VAWT design procedures.

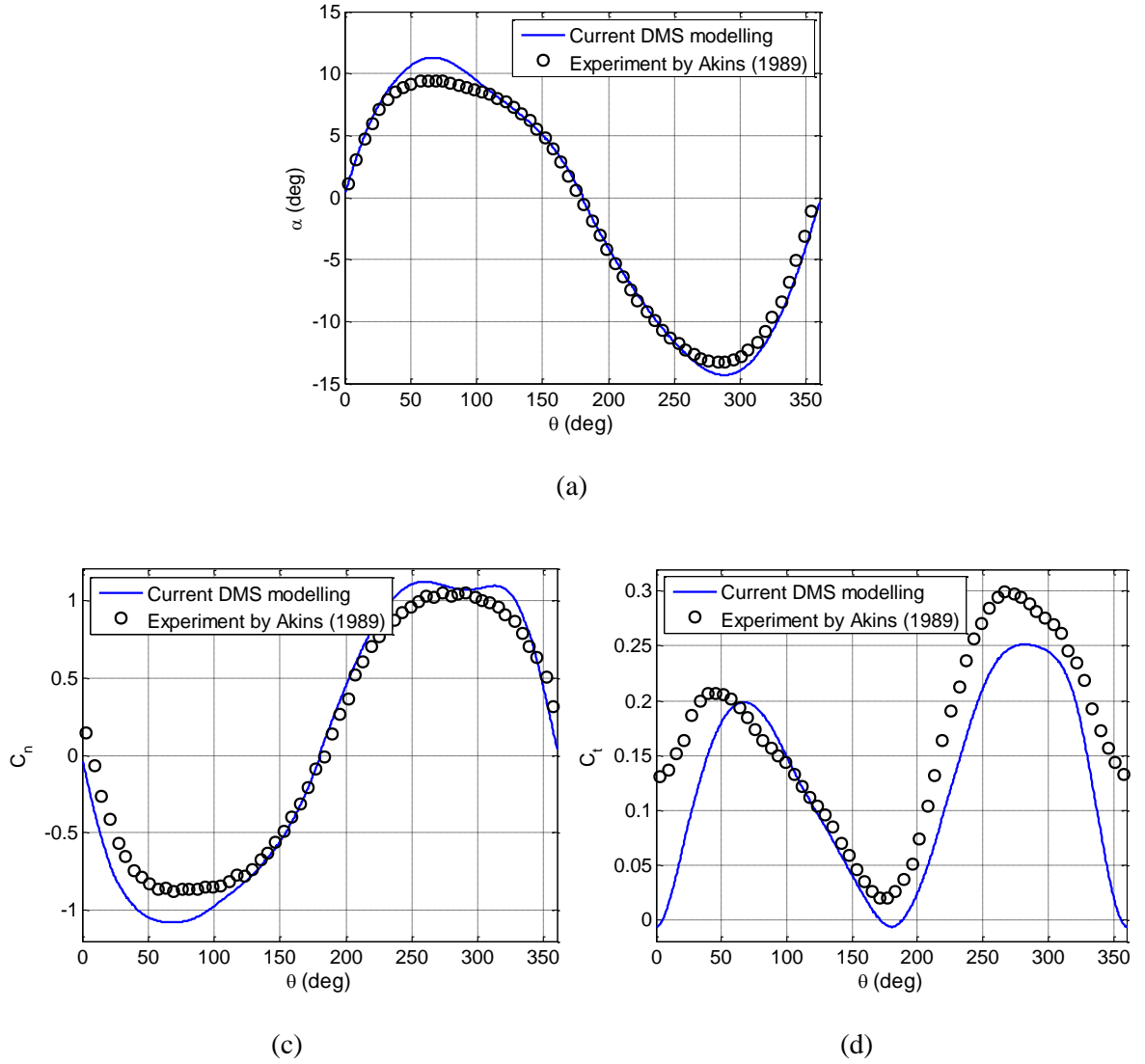


Figure 7: Comparison of current DMS method with experiment [22] at $\lambda = 3.7$; (a) blade angle of attack, (b) normal force coefficient, and (c) tangential force coefficient

Despite relatively acceptable results with current DMS modeling as observed in present work and also in [2,10,15,23,24], the accuracy of this method is still under study and further improvement has been proposed by several researchers [15,16,23]. Ferreira [16] proposed improvements to the DMS model based on insights obtained from flow simulations with a 2D free-wake panel/vortex model. He improved the correlation between upstream and downstream actuator surfaces in semitubes based on the azimuthal distribution of the shed vorticity. Another work with significant modification to the DMS model was presented by Keinan [15]. He

proposed a formulation to determine the induced velocity on the rotor surface in both direction and magnitude [15], while traditional models assume the induced velocity is parallel to the free-wind velocity. Accordingly, Keinan [15] modified the trajectory of the flow inside the rotor based on the continuity principle; as it was also assumed to be a straight line parallel to the free-wind direction in the older versions of DMS method. It should also be emphasized that the DMS method is used in wind turbine design studies primarily due to its relative simplicity and ease of implementation [10], and as mentioned earlier, this method is recommended mostly for initial design stages. More accurate methods should be utilized to better model the three dimensional flowfield around a wind turbine. Scheurich et al. [13] used the vorticity transport model and demonstrated that the interactions between a VAWT blades and their wake generated can be captured quite well if an appropriate model for the 3D wake is utilized.

2.3 Aerodynamic performance

An efficient design process for SB-VAWTs requires both aerodynamic and structural considerations. In this section, attempts to optimize several design parameters with respect to the turbine aerodynamic performance are described. The aerodynamic performance or aerodynamic efficiency of a wind turbine is usually expressed in terms of turbine power coefficient which was defined earlier by Eq. 10 as the ratio of mechanical output power to the maximum power available in the wind stream exposed to the rotor swept area [2]. Having determined turbine power coefficient at a range of tip speed ratios, a set of performance curves can be plotted for different wind speeds. Figure 8 is a typical performance curve of a SB-VAWT which depicts a few important design parameters. Usually, the turbine power coefficient increases with tip speed ratio until it reaches a maximum value before dropping, as depicted in Fig. 8. The design power coefficient, C_{P_d} , is the maximum power coefficient that the turbine can achieve during its operation. The corresponding tip speed ratio at which the turbine reaches C_{P_d} is called design tip speed ratio, λ_d . Some researchers such as Kirke [20] used a range of design tip speed ratio instead of a single operational point. Kirke [20] suggested using a design tip speed ratio range where the turbine power coefficient remains higher than seventy percent of its maximum power coefficient value over that range (see Fig. 8).

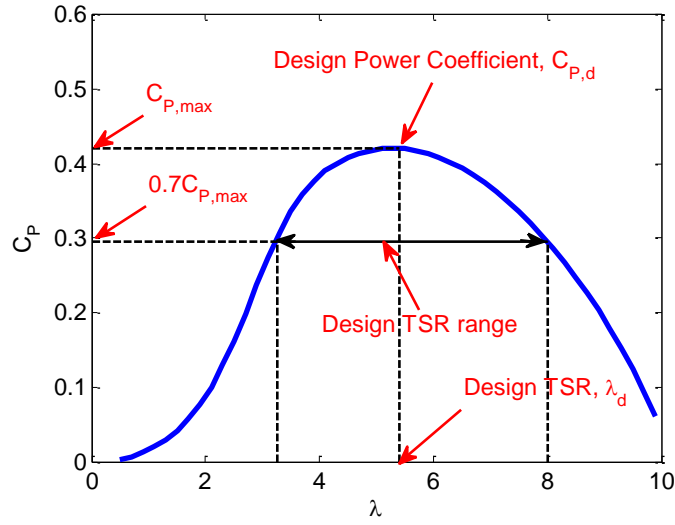


Figure 8: A typical performance curve of a SB-VAWT showing key design parameters

While designing VAWTs, it is desirable that the rotor rotates smoothly at a design speed range corresponding to the design tip speed ratio range. In fact, the design tip speed ratio will determine the rotor rotational speed, and thus puts operational constraints on the electrical equipment connected to the turbine shaft [25]. The turbine rotational speed, $\omega = \lambda U_\infty / R$, is the most important parameter influencing tip speed ratio, considering the fact that the average value of wind velocity during a certain period of time does not vary significantly [10]. Hence, the rotor geometry and structure should be designed in a proper way to allow the turbine to efficiently spin at the design rotational speed. This requires the proper selection of the material with suitable weight for different parts of the rotor such as blades, supporting arms, and shafts.

It is also desirable to select the various parameters of a wind turbine in a way to maximize the design power coefficient, C_{P_d} . In order to do this, parameters affecting the wind turbine aerodynamic performance should be evaluated and optimized with respect to power coefficient. This task is done for three important geometric parameters in the subsequent sections, namely the rotor solidity factor, the blade aspect ratio, and the rotor aspect ratio.

2.3.1 Rotor solidity factor

The solidity factor of a wind turbine, σ , is measured by the blade swept area, NcH , divided by the rotor frontal area, DH . This parameter has been used in both forms, either Nc/D or

Nc/R , by different researchers for SB-VAWTs. The latter definition is more common in the literature and therefore is adopted here. There is also another accepted convention in the wind turbine literature that considers low and high limits of $\sigma = 0.1$ and $\sigma = 1$ for the solidity factor [2,10,20,26].

The effect of turbine solidity on its aerodynamic performance has been studied using the DMS model as presented in Fig. 9. The solidity factor has been increased from 0.12 to 1 by decreasing the rotor radius while the blades swept area (blade chord length and height) was kept constant. The numerical model has been run several times for a SB-VAWT with three NACA0015 blades and a free-stream Reynolds number of 170,000. Figure 9a shows that the maximum power coefficient increases as turbine solidity increases from 0.1 to 0.4, beyond which it drops with further increase in the solidity factor. It can also be seen from Fig. 9a that the turbine performance curve becomes sharper with an increase in the solidity factor. This shrinks the design tip speed ratio range which restricts the operational range of the turbine. In short, it seems that the optimum range of the solidity factor is around 0.4, as Fig. 9a also shows that the maximum power coefficient is not substantially increased when rotor solidity goes beyond 0.4. This can be observed more clearly in Fig. 9b where the maximum power coefficient of each turbine has been drawn versus the rotor solidity factor. Altogether, it can be concluded that the optimum range of the solidity factor is $0.2 < \sigma < 0.6$ for the particular wind turbine examined. It should be noted that almost the same trend is reported by other researchers [10,14,20,27] for different VAWTs with different blade profiles and Reynolds numbers. They have also stated the same range of solidity factor between 0.2 and 0.6 as the optimum range for SB-VAWTs. This range stands for relatively low solidity or large diameter turbines, which has some disadvantages from a structural standpoint. The main drawback of such low solidity turbines is that their blades and supporting arms are exposed to high centrifugal forces as these forces are proportional to the rotor radius and rotational speed. This will be discussed in more details in Section 2.4.

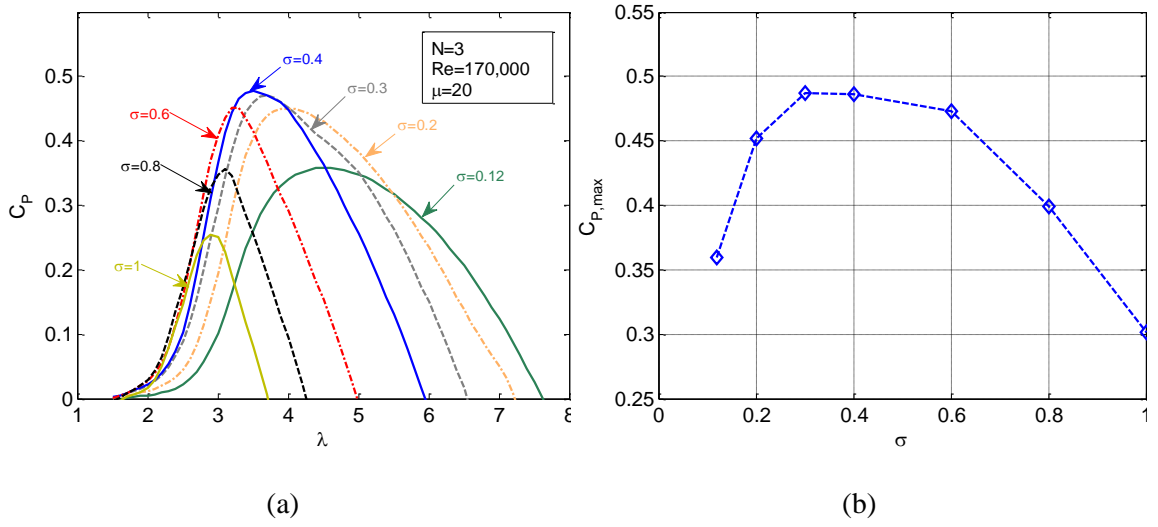


Figure 9: Effect of rotor solidity factor on the performance of a SB-VAWT; (a) performance curves at different solidity factor, (b) variation of maximum power coefficient vs. solidity factor

2.3.2 Blade aspect ratio

The blade aspect ratio is defined as the ratio of the blade length to its chord length, $\mu = H/c$. As mentioned in Section 2.2.3, the effects of three-dimensionality are more considerable in blades with smaller aspect ratio which reduces the lift-to-drag ratio. Any decrease in lift-to-drag ratio will reduce tangential forces [10]. This would decrease the turbine overall torque and consequently, turbine output power. This point has been investigated in this section for a SB-VAWT with different values of aspect ratio.

Figure 10 shows the performance curves of the same SB-VAWT studied in the previous section, except this time the solidity factor is kept constant and the aspect ratio has been varied from 5 to 60 by increasing H . Figure 10 clearly demonstrates an increase in the maximum power coefficient with the blade aspect ratio. Higher aspect ratios also broaden the turbine performance curve which increases the design tip speed ratio range. In spite of this, utilizing blades with relatively high aspect ratio has some drawbacks. Relatively long blades add a great amount of weight to the turbine; which increases the manufacturing and maintenance costs and creates a need for a more complex bearing. Moreover, such blades are exposed to larger bending moments which may need to be controlled via utilizing more than two supporting arms. Furthermore, it is shown in Fig. 10b that the rate of increase in $C_{p,max}$ diminishes when the aspect ratio exceeds a value of about 15. Therefore, it seems that the optimum value for blade aspect ratios for SB-

VAWTs could be in the range of $10 < \mu < 20$. Some other researchers [10,14,20] have also studied the effect of blade aspect ratio on the aerodynamic performance of VAWTs. Their studies suggest that blade aspect ratios lower than 7.5 should be avoided in order to attain higher power coefficients as well as broader design tip speed ratio ranges.

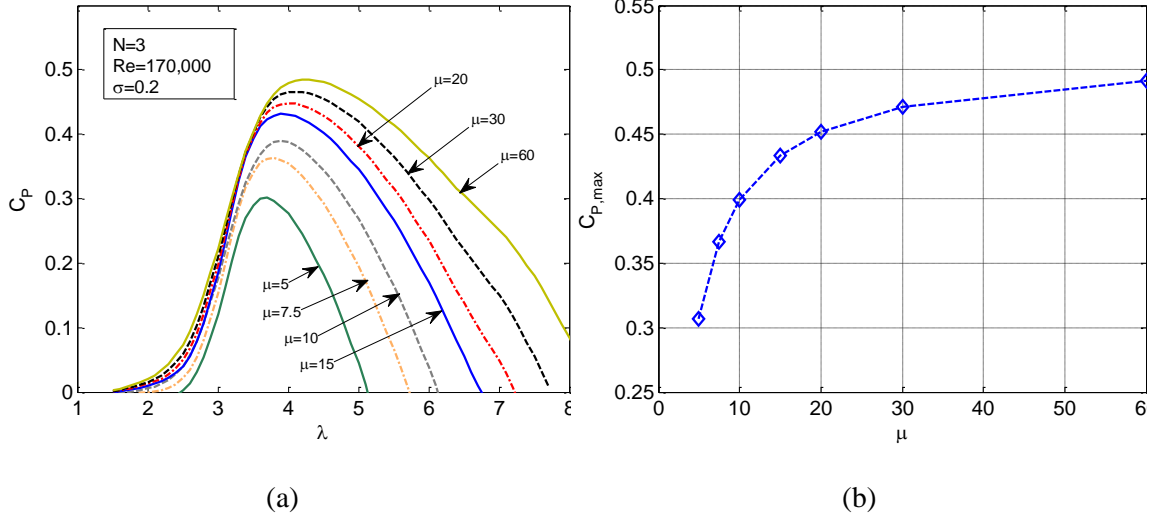


Figure 10: Effect of blade aspect ratio on the performance of a SB-VAWT; (a) performance curves at different aspect ratio, and (b) variation of maximum power coefficient vs. aspect ratio

2.3.3 Rotor swept area

The rotor swept area is the section of air enclosing the rotor during its rotation. The amount of power generated by a wind turbine depends primarily on the wind speed and the swept area, not on the blade area. For SB-VAWTs, the swept area has a rectangular shape and is defined as $A_r = DH$. Theoretically, for two SB-VAWTs with identical swept areas, the maximum amount of power available in the wind stream, $P_w = 0.5\rho A_r U_\infty^3$, is the same. Nevertheless, their aerodynamic performance might not be similar even if they have similar blade profiles. The rotor aspect ratio, H/D , which is the ratio of two sides of the rotor swept area's rectangular shape would determine the aerodynamic behavior of the SB-VAWT which is examined in this section.

The effect of rotor aspect ratio on performance curves of a SB-VAWT with three NACA0015 blades at $Re_\infty = 170,000$ is shown in Fig. 11. Figure 11a shows the turbine with $H/D = 1$ has the most favorable performance curve; having the highest power coefficient and the largest design tip speed ratio range. The performance curves of cases with $H/D = 0.5$ and 2 have the closest behavior to that of the optimum case with $H/D = 1$. These three cases also have a

very similar maximum power coefficient; see Fig. 11b. Figure 11a also shows that the performance curve becomes aerodynamically poor as the rotor aspect ratio deviates from unity. This would suggest the optimum value of rotor aspect ratio lies in the range of $0.5 < H/D < 2$. Choosing the upper and lower limits of this range depends on some design considerations. For instance, in the case of a rotor with $H/D = 0.5$, the blade manufacturing cost is reduced and bending moments are smaller since the blades are shorter. On the other hand, SB-VAWTs with $H/D = 2$ are recommended for locations with limited available land such as small wind farms inside the urban areas.

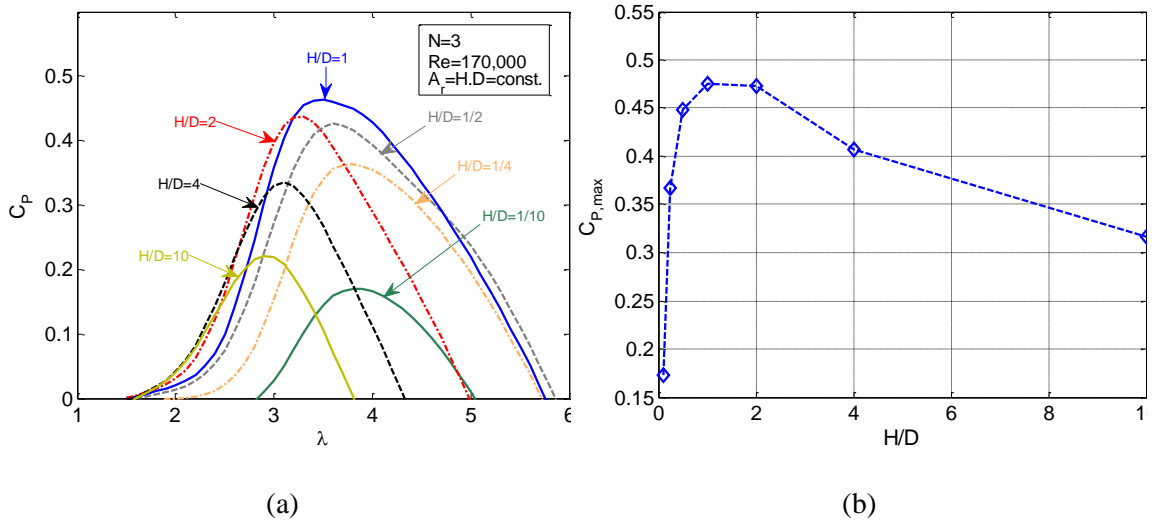


Figure 11: Effect of rotor H/D ratio on the performance of a SB-VAWT; (a) performance curves at different H/D ratio, and (b) variation of maximum power coefficient vs. H/D ratio

2.4 Aerodynamic loading

In order to propose an efficient design for a SB-VAWT, the aerodynamic criteria should be considered along with structural analyses. All parts of the turbine should be designed to withstand the corresponding loading. Two major issues concerned with structural stability of SB-VAWTs are large moment stresses and explosive radial forces [28]. SB-VAWTs with longer blades suffer more severely from moment stresses, and need to be supported by suitable supporting arms in appropriate locations. The centrifugal component of radial forces can be determined from the principle of rotating objects as

$$F_c = mR\omega^2 \quad (23)$$

This force element, F_c , should be added to the normal component of the resultant aerodynamic force, F_n (see Eq. 6), in order to estimate the total radial force as [28]

$$F_r = F_n + F_c \quad (24)$$

After finding the main force components, the corresponding stresses acting on the turbine can be determined. The different parts of the rotor should be designed in a way to minimize the stresses. This section summarizes the attempts to follow this premise, accounting for the specific aerodynamic considerations encountered by SB-VAWTs. The turbine studied in this section has the specifications detailed in Table 2 which are in the optimum range of the design factors based on the results found in Section 2.3.

Table 2: The specifications of candidate SB-VAWT studied in Section 2.4

Number of blades	$N = 3$
Solidity factor	$\sigma = 0.2$
Blade aspect ratio	$\mu = 20$
Rotor aspect ratio	$H/D = 0.66$
Free-stream Reynolds number	$Re = 170,000$
Blade profile	NACA0015

The candidate wind turbine has been analysed via the DMS method for a range of tip speed ratios. At each tip speed ratio, the tangential and normal force components within a complete revolution of the rotor are determined and their maximum values are found. For the wind turbine described in Table 2, the maximum aerodynamic forces occur at $\lambda = 4.3$. The force components over one complete revolution are plotted in Fig. 12, for this particular tip speed ratio. As can be observed from Fig. 12 the variation range of normal force is almost nine times that of the tangential force. This implies that stresses corresponding to the tangential forces are small compared to those of normal forces, as also reported by other researchers [9,10,22,26,28].

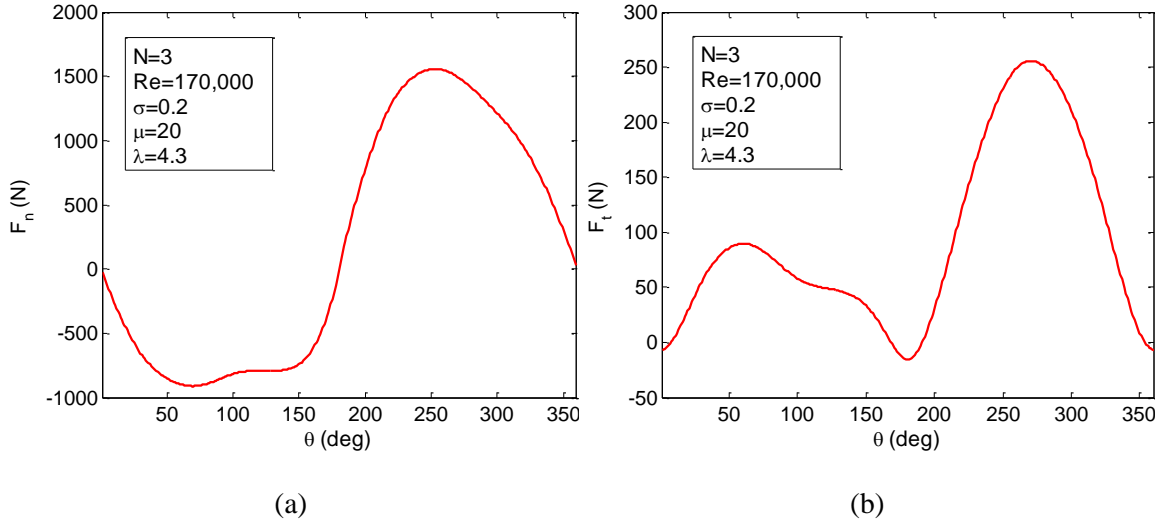


Figure 12: Aerodynamic forces as a function of azimuthal angles at $\lambda = 4.3$ for the SB-VAWT with specifications listed in Table 2; (a) normal force, and (b) tangential force

2.4.1 Number of blades

The optimum number of blades for SB-VAWTs is recommended to be three based on the relevant works in the literature [9,10,28,29]. Even though the ideal number of blades may appear to be two; and many Darrieus machines have two blades, three blades hold some advantages over two blades. SB-VAWTs with three blades tend to run more smoothly since the energy fluctuations are lower in each revolution, compared to turbines with two blades [10]. More specifically, the cyclic variations in both torque and resultant force acting on the rotor are much smaller in turbines with three blades. In fact, the aerodynamic forces on two blades at 180° apart will peak approximately in phase and will act in approximately the same direction on both blades, leading to potential problems with resonant vibrations in the tower, while those from three blades 120° apart will tend to produce an almost steady force [10]. This indicates a more favorable structural response for three blades configuration in SB-VAWTs.

2.4.2 Blade profile

One of the most crucial factors for an efficient design of a VAWT is the blade cross sectional profile. The literature on VAWTs blade profile selection and its relevant design criteria is prolific. Some researchers still recommend using the classic NACA four digit symmetric airfoils for SB-VAWTs, while several successful designs have been reported in the literature on

using asymmetric blades for SB-VAWTs [30-32]. The major advantage of asymmetric airfoils is that they exhibit superior aerodynamic characteristics at low Reynolds numbers which results in reliable self-starting. The fundamental aspects of self-starting phenomenon of Darrieus wind turbines have been discussed in detail by Hill et al. [33]. On the other hand, symmetric airfoils are still popular in VAWT design since the aerodynamic lift is produced from both sides of the airfoil during a complete turbine revolution. This indicates that there is no need to readjust the airfoil in the wind direction, and the airfoil will provide lift regardless of the wind direction [34]. More details on other features of asymmetric SB-VAWT blades in contrast to symmetric blades can be found in [32]. Islam et al. [32] examined the aerodynamic performance of a SB-VAWT with different blade profiles where they used NACA0015 blade as the representative of symmetric airfoils. Their results show that SB-VAWTs with asymmetric blades demonstrate higher power coefficients than that of NACA0015 profile at small tip speed ratios ($\lambda < 3$), while the turbine with NACA0015 blades generates more power for higher values of tip speed ratio [32].

Based on the recent discussion, it has been decided to use a symmetric blade for the candidate SB-VAWT in the current study. The more frequently used symmetric blades for Darrieus wind turbines are NACA0012, NACA0015, and NACA0018. The NACA0018 profile exhibits the poorest aerodynamic performance in terms of lift-to-drag ratio [17], while NACA0012 blade is considered too thin for wind turbine applications especially for high aspect ratio blades. Therefore, NACA0015 profile which demonstrates one of the most satisfactory performances in this field has been utilized for the turbine blades.

2.4.3 Blade-supporting-arm interaction

One of the major challenges of SB-VAWTs are the large moment stresses acting on the blades. The critical point for these stresses is the location where the connection with the supporting arms is made [28]. Hence, the quantity and location of supporting arms should be designed in a proper way to minimize the moment stresses acting on the blades. It has been stated in the literature [2,4,20,28] that using two, rather than one, supporting points for SB-VAWT blades benefits both blades and arms from a structural standpoint. In such a configuration, each supporting arm only bears half of the total radial force since the radial forces are distributed between the two arms. On the other hand, utilizing two supporting arms increase the rotor parasitic drag which results in an output power reduction for a given rotor area. Using two supports also improves the blade design with reduced overall bending moment stress along the blade length compared to a blade with a single support. This is portrayed in Fig. 13a by drawing

the bending stress, $\sigma_M = My/I_x$, along the blade length for the most commonly used configurations in SB-VAWT field. As can be inferred from Fig. 13a, the bending stress has the most hazardous distribution along the blade for the case of a single supporting arm. The bending stress distribution improves when two supporting arms are utilized at the two ends of the blade. The most desirable case happens when the rotor is supported by two arms at some intermediate locations, namely at 21% and 79% of the blade length. These optimized locations have been determined by minimizing the maximum bending stress acting on the blade while varying the position of the supporting arms along the blade length, as displayed in Fig. 13b. This figure confirms that the two-intermediate-support configuration at 21% and 79% of the blade length has the most favorable bending stress distribution with the least peak absolute values. These results are comparable to the results of Hameed and Afaq [28] who optimized the blade-arm conjunction locations by minimizing the bending stress and deflection via numerical modeling based on beam theories. They also reported the optimum location of supporting arms to be at 21% and 79% of the blade length, for a VAWT with three NACA0015 straight blades.

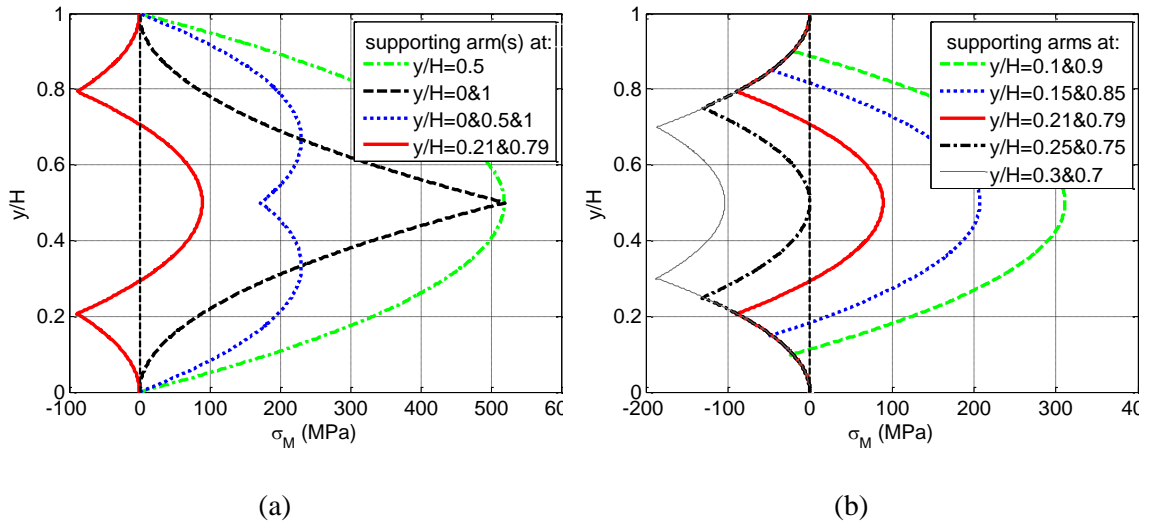


Figure 13: Bending stress distribution along the blade length of a SB-VAWT; (a) effect of supporting arm(s)' location (end, middle, intermediate), and (b) finding optimum intermediate location of supporting arms

2.4.4 Blade dimensions and material

Blade dimensions, c and H , should be selected in a way that the solidity factor and aspect ratio lie in their optimum range. Also, it should be noted that the aerodynamic forces acting on

the blade vary with the first power of the blade chord length (see Eq. 5 and 6), while bending stresses are proportional to the square of c [14]. Therefore the blade chord length should be judiciously chosen in order to avoid excessive stresses.

Blade material should have high yield strength, large stiffness, and moderate cost. The blades are also expected to last during their operating life-time (usually between 20 and 30 years), while they endure a considerable number of fatigue cycles [10]. It is also desirable that the blades are made from low density material, or hollow sections in order to reduce the overall weight of the rotor and its moment of inertia. By reducing the turbine weight, the vertical force component on the bearings is reduced. Although the literature on the candidate material for SB-VAWT blades is extremely limited, the discussion on material aspects of other wind turbines [35,36] can be utilized to select the most suitable material. The rotor moment of inertia, a measure of its resistance against a change in its state of rotational motion, can also be reduced by using lighter blades. Lighter blades enable the rotor to more smoothly adjust its rotational speed while the velocity or direction of the incoming wind changes [37].

2.4.5 Supporting arms

Supporting arms which connect the turbine blades to the tower are another important design parameter. The main characteristics of supporting arms were highlighted by Paraschivoiu [10]. They transfer torque to the central shaft, affect the natural frequencies of the rotor, and also reduce the mean and fatigue stresses on the blades. On the other hand, supporting arms increase turbine weight and manufacturing cost, and produce parasitic drag that reduces the turbine output power.

Supporting arms have to endure axial and bending stresses that result from large radial forces, $\sigma = F/A + My/I_x$. Therefore, they should be built from a material with high tensile and compressive strength. Also, their final design should exhibit adequate stiffness in order to withstand excessive bending deflections [20]. At the same time, it is desirable that the supporting arms candidate geometry offers low values of parasitic drag. Using streamlined shapes like symmetric airfoils with low drag at zero lift as supporting arms has been suggested in the literature. A comparative study has been done in this section to examine the effect of supporting arms geometry on the turbine performance, from both aerodynamic and structural standpoints. In this comparative study, the cross sectional area, A , is fixed, that is, all arm shapes have the same weight and lead to the same moment of inertia. Keeping the arms area constant would also result

in the same axial stresses, F/A . Figure 14a shows the amount of total power loss due to six supporting arms (two arms per blade) for the five candidate geometries, calculated by Eq. 22. As can be observed in Fig. 14a, using aerodynamic shapes such as a NACA0015 airfoil as supporting arms reduces the rotor parasitic drag significantly, especially at higher tip speed ratios. Cylindrical arms increase the parasitic drag more than aerodynamic shapes, but less than sharp edged geometries such as rectangles and diamonds which create a huge loss in turbine output power. The maximum stress acting on the supporting arms with different shapes has also been compared in Fig. 14b. The hollow cylinder offers the lowest stress while the NACA0015 shape arm can tolerate highest stress, mainly due to its large dimensions compared to the other geometries. In short, it can be concluded that the supporting arms for SB-VAWTs should be in aerodynamic shape and be made from high strength and high stiffness materials.

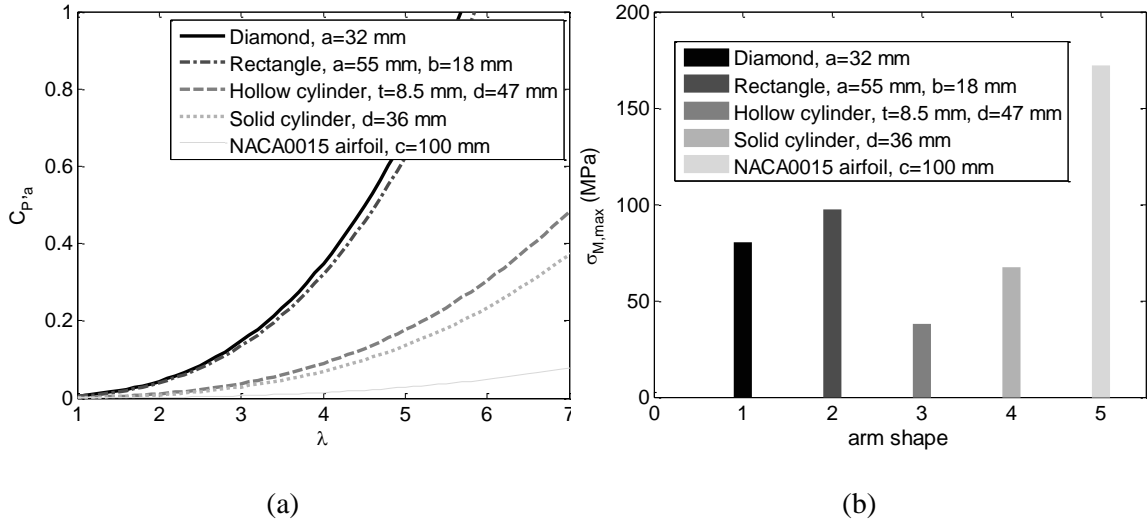


Figure 14: Effect of supporting arms geometry on the SB-VAWT performance; (a) turbine power coefficient loss due to supporting arms, and (b) maximum stress acting on supporting arms

2.4.6 Rotor interaction with electrical devices

Although the main aerodynamic challenges of SB-VAWTs have been addressed; a comprehensive design process requires some consideration of the electrical aspect of power generation. The electrical system of a wind turbine is the second most important subsystem in a wind turbine after the mechanical rotor [38], and it is responsible for about half of the total cost of the wind turbine [10]. A turbine electrical system consists of all devices used to convert rotational motion into electrical power as well as control system components. The optimal operation of an

integrated rotor-generator-control system is addressed briefly in this section since it has a close correlation to the present work, while other aspects of electrical system can be found in relevant references [10,38,39].

In the mechanical-electrical energy conversion unit of a wind turbine, the generator is the focal point for all other components [38], moreover, the type of electric generator utilized determines the nature of operation of a wind turbine as far as the rotor speed is concerned [10]. Constant speed rotors have been used when the generator is directly coupled to the grid. This is the case in the majority of smaller and older vertical and horizontal wind turbines [38]. Variable rotor speed operation is more desirable for new wind turbines since the rotational speed of rotor can be adjusted by wind speed [39]. As mentioned in Section 2.3, the design rotational speed of the rotor is determined by the design tip speed ratio which varies with both rotational speed and free-stream wind velocity; $\lambda_d = f(U_\infty, \omega)$, (also see Fig. 8). Constant speed rotors are designed to operate at an optimum point, but only for a single wind speed; which is typically designed to be the most dominant wind speed of the installation site. Variable speed turbines, on the other hand, have the ability to follow the optimal performance point of the turbine at different wind speeds [39]. This configuration requires a control unit that adjusts the rotational speed of rotor based on the feedback from an anemometer, and therefore operates the turbine at λ_d . Using multiple speed rotors can increase energy capture by 5% to 10% as shown by Paraschivoiu [10], while constant speed turbines are still preferred in some occasions due to cost considerations despite their aerodynamic disadvantages. Of the most successful documented cases, a few Darrieus VAWTs and many HAWTs are reported to have economical variable speed rotor configurations [10,38].

2.4.7 Cut-in and cut-out wind speeds

A further important design aspect is the correlation between turbine's rotor and its speed limitations. For each particular rotor, the cut-in and cut-out speeds require proper design attention. The cut-in speed is defined as the lowest wind speed at which the wind turbine delivers useful power [2]. This speed is the first point at which the total torque of the rotor within a complete revolution is positive (see Eqs. 7 and 8). At wind speeds less than the cut-in speed the rotor torque determined by Eq. 8 is negative. This region is usually referred as the turbine dead band region [10]. For a reliable design, the cut-in speed needs to be significantly lower than the site's average wind speed [10]. Moreover, the rotor should be able to generate enough starting torque at the cut-in wind speed to overcome the inertia of the entire system [37].

The cut-out speed is defined as the highest wind speed at which the turbine is allowed to deliver power [2]. The components of a turbine are not designed to withstand sustained loads above this speed. Thus, the cut-out speed needs to be sufficiently higher than the average wind speed. For instance, the cut-out speed of 25 m/s is advised by several researchers as this speed is considered to represent hazardous storm conditions [2,10,38]. The turbine control system should shut down the rotor at cut-out speed due to safety constraints. There are various methods to stop a typical HAWT such as changing the pitch of the blades or yawing the rotor out of the wind [38], which is not feasible for SB-VAWs [10]. Alternatively, utilizing mechanical or electrical brakes for shutting down a SB-VAWT is reported and recommended in the literature [10].

2.4.8 Self-starting challenge

One of the principal challenges of SB-VAWTs is their poor self-starting behaviour [33]. To achieve self-starting, a SB-VAWT should be able to accelerate from rest to a steady speed that can deliver useful torque. Therefore, self-starting ability depends on the turbine aerodynamic performance as well as the load characteristics [33]. A particular wind turbine that self-starts with a given load may not self-start when a different load is used. There are a few schemes which can result in reliable self-starting of SB-VAWTs if utilized properly. Using variable pitch configuration will solve the self-starting problem, but the manufacturing is very complex and hence, reduces the cost-effectiveness of the wind turbine for small-scale applications [2]. Also, improved self-starting can be achieved by utilizing special high-lift low-drag airfoils as investigated by Islam [32]. Self-starting challenges can also be overcome with the help of an external torque device such as a Savonius rotor, a torque tube, or an alternative electrical motor [20].

2.5 Design flowchart

A summary of the current design procedure has been presented in Fig. 15 in the form of a flowchart. Necessary references are included in this flow chart to the corresponding sections of the current paper. As can be observed in this flowchart, the main input for the design procedure is the desirable turbine rated power on which the wind turbine are usually designed [10]. Specifying the turbine rated power and introducing initial guesses for rated power coefficient and rated wind velocity results in the determination of the rotor swept area. Then, all turbine dimensions such as c , D and H are calculated in a way that design parameters such as σ , μ and H/D lie within their

optimum range, found in Sections 2.3.1 to 2.3.3. The next step would be the selection of blade and supporting arm profiles which should be done regarding the aerodynamic loading design considerations discussed in Section 2.4. The material of the different parts of the turbine should also be chosen after necessary strength analyses. The dynamic interaction of rotor with electrical devices such as the generator and control system should be considered with regard to the cut-in and cut-out speed criteria and also constant/variable rotor speed operation. All the aforementioned steps need to be done in an iterative fashion in order to reach a convergence on turbine rated parameters. The last stage is the experimental verifications which could be performed either in a wind tunnel or a wind farm [2].

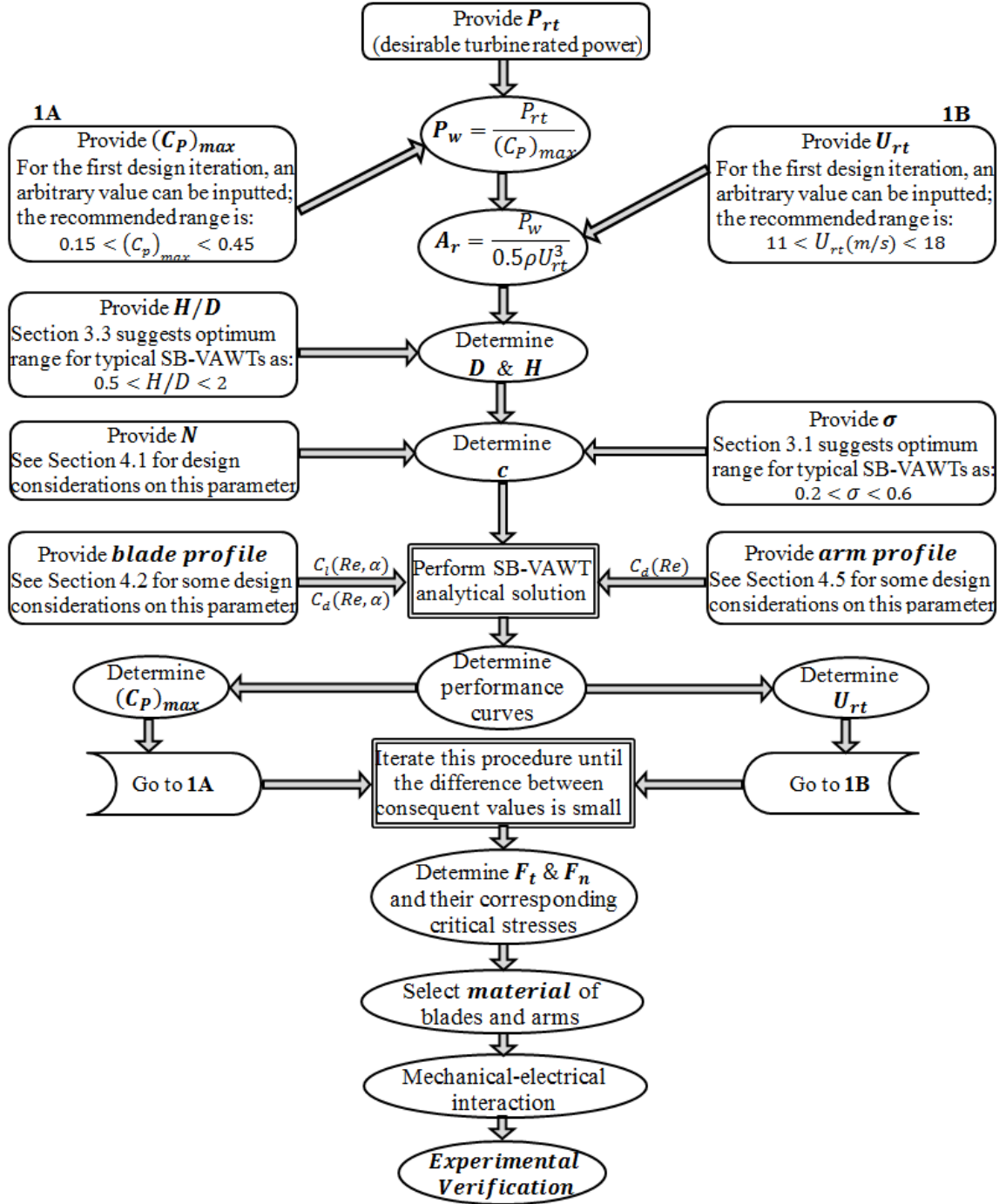


Figure 15: Flow diagram of the design methodology for SB-VAWTs

2.6 Conclusion

It has been observed that in the SB-VAWT literature there is no record on a comprehensive design that takes all major factors into consideration. Hence, researchers and

manufacturers who want to study a new aspect of the subject have to deal with plenty of data in order to identify the proper range of several parameters have been optimized before. This paper has proposed an efficient design scheme on SB-VAWTs which can save significant amount of time and resources for future investigators in their initial design stage. It can also prevent manufacturers to invest on a design whose parameters are not in the optimum range. A design flowchart has been presented in this paper which summarizes the design process discussed here.

One of the key parts of the design methodology proposed in this research is in utilizing a robust analytical method to determine the turbine aerodynamic performance and loading. The double-multiple streamtube method was formulated numerically in order to analyze the flow parameters around a SB-VAWT. This method has been validated with experimental data from the literature. The optimum range of principal design parameters, namely the rotor solidity factor, blade aspect ratio, and rotor aspect ratio have been obtained using the DMS analytical approach, and were found to be: $0.2 < \sigma_d < 0.6$, $10 < \mu_d < 20$, and $0.5 < (H/D)_d < 2$ respectively. The aerodynamic loads have also been determined for several operating conditions. The results indicate that the peak normal component of aerodynamic force is about six times larger than that of tangential component. Moreover, the centrifugal force element adds to the normal aerodynamic force to form an overall radial force which can be significant. The radial forces are the main source of axial and bending stresses on supporting arms as well as bending stresses on the blades. Hence, a smooth rotational motion of the rotor requires the proper design of the supporting arms and their connection to the blades. Different cross sectional shapes of supporting arms have been assessed in terms of aerodynamic behavior and structural strength. It was verified that using airfoil shapes for supporting arms gives better aerodynamic response than using sharp edged sections such as rectangles or diamonds. The bending stresses acting on the blades have also been minimized to find the optimum locations of the blade-supporting-arm connection by identifying bending stress minima along the blade. These locations were at 21% and 79% along the blade length. This would lead to the most conservative bending stress distribution over the blade.

2.7 References

- [1]. Tai, F.Z., Kang, K.W., Jang, M.H., Woo, Y.J., Lee, J.H., Study on the analysis method for the vertical-axis wind turbines having Darrieus blades, *Renewable Energy*, 2013; 54: 26-31.

- [2]. Aslam Bhutta, M.M., Hayat, N., Farooq, A.U., Ali, Z., Jamil, Sh.R., Hussain, Z., Vertical axis wind turbine - a review of various configurations and design techniques, *Renewable and Sustainable Energy Reviews*, 2012; 16(4): 1926-1939.
- [3]. Battisti, L., Zanne, L., Dell'Anna, S., Persico, G., Paradiso, B., Aerodynamic measurements on a vertical axis wind turbine in a large scale wind tunnel, *Journal of Energy Resources Technology*, Transaction of the ASME, 2011; 133(3): Article No. 031201, 1-9.
- [4]. MacPhee, D., Beyene, A., Recent advances in rotor design of vertical axis wind turbines, *Wind Engineering*, 2012; 36(6): 647-666.
- [5]. Ottermo, F., Bernhoff, H., Resonances and aerodynamic damping of a vertical axis wind turbine, *Wind Engineering*, 2012; 36(3): 297-304.
- [6]. Pope, K., Dincer, I., Naterer, G.F., Energy and exergy efficiency comparison of horizontal and vertical axis wind turbines, *Renewable Energy*, 2010; 35: 2102-2113.
- [7]. Chong, W.T., Pan, K.C., Poh, S.C., Fazlizan, A., Oon, C.S., Badarudin, A., Nik-Ghazali N., Performance investigation of a power augmented vertical axis wind turbine for urban high-rise application, *Renewable Energy*, 2013; 51: 388-397.
- [8]. Muller, G., Mark, F., Jentsch, M.F., Stoddart, E., Vertical axis resistance type wind turbines for use in buildings, *Renewable Energy*, 2009; 34: 1407-1412.
- [9]. Li, C., Zhu, S., Xu, Y.L., Xiao, Y., 2.5D large eddy simulation of vertical axis wind turbine in consideration of high angle of attack flow, *Renewable Energy*, 2013; 51: 317-330.
- [10]. Paraschivoiu, I., Wind turbine design - with emphasis on Darrieus concept, Polytechnic International Press, Montreal, 2002.
- [11]. Armstrong, S., Fiedler, A., Tullis, S., Flow separation on a high Reynolds number, high solidity vertical axis wind turbine with straight and canted blades and canted blades with fences, *Renewable Energy*, 2012; 41: 13-22.
- [12]. Scheurich, F., Brown, R.E., Effect of dynamic stall on the aerodynamics of vertical-axis wind turbines, *AIAA Journal*, 2011; 49(11): 2511-2521.
- [13]. Scheurich, F., Fletcher, T.M., Brown, R.E., Effect of blade geometry on the aerodynamic loads produced by vertical-axis wind turbines, *Proceedings of the Institution of Mechanical Engineers, Part A: Journal of Power and Energy*, 2011; 225: 327-341.
- [14]. Islam, M., Analysis of fixed-pitch straight-bladed VAWT with asymmetric airfoils, PhD Thesis, University of Windsor, Canada, 2008.
- [15]. Keinan, M., A modified streamtube model for vertical axis wind turbines, *Wind Engineering*, 2012, 36(2), 145-180.
- [16]. Ferreira, C.J.S., The near wake of the VAWT: 2D and 3D views of the VAWT aerodynamics, PhD Dissertation, Delft University of Technology, Netherlands, 2009.

- [17]. Sheldahl, R.E., Klimas, P.C., Aerodynamic characteristics of seven symmetrical airfoil sections through 180-degree angle of attack for use in aerodynamic analysis of vertical axis wind turbines, Sandia National Laboratories, 1981; SAND80-2114.
- [18]. Yilmaz, T.O., Rockwell, D., Flow structure on finite-span wings due to pitch-up motion, *Journal of Fluid Mechanics*, 2012; 691: 518-545.
- [19]. Kashitani, M, Miura, K., Nakao, S., Yamaguchi, Y., Effects of aspect ratio in a transonic shock tube airfoil flow, *Journal of Thermal Science*, 2012; 21(5): 435-440.
- [20]. Kirke, B.K., Evaluation of self-starting vertical axis wind turbines for stand-alone applications, PhD Thesis, Griffith University, Australia, 1998.
- [21]. Kjellin, J., Bulow, F., Eriksson, S., Deglaire, P. Leijon, M., Bernhoff, H., Power coefficient measurement on a 12 kw straight bladed vertical axis wind turbine, *Renewable Energy*, 2011; 36: 3050-3053.
- [22]. Akins, R.E., Measurements of surface pressure on an operating vertical-axis wind turbine, Sandia National Laboratories, 1989; SAND89-7051.
- [23]. Farthing, S.P., Vertical axis wind turbine induced velocity vector theory, *Proceeding of Institution of Mechanical Engineers, Part A: Journal Power and Energy*, 2009; 223: 103-114.
- [24]. Saeidi, D., Sedaghat, A., Alamdari, P., Alemrajabi, A.A., Aerodynamic design and economical evaluation of site specific small vertical axis wind turbines, *Applied Energy*, 2013; 101: 765-775.
- [25]. Kirke, B.K., Optimum matching of non-electrical loads to wind turbines, *Proceeding of Institution of Mechanical Engineers, Part A: Journal Power and Energy*, 1996; 210: 213-221.
- [26]. McLaren, K., Tullis, S., Ziada, S., Measurement of high solidity vertical axis wind turbine aerodynamic loads under high vibration response conditions, *Journal of Fluids and Structures*, 2012; 32: 12-26.
- [27]. Templin, R.J., Aerodynamic performance theory for the NRC vertical-axis wind turbine, National Aeronautical Establishment Laboratory Technical Report, Canada, LTR-LA-160, 1974.
- [28]. Hameed, S.M., Afaq, S.K., Design and analysis of a straight bladed vertical axis wind turbine blade using analytical and numerical techniques, *Ocean Engineering*, 2013; 57: 248-255.
- [29]. Castelli, M.R., De Betta, S., Benini, E., Effect of blade number on a straight-bladed vertical-axis Darreius wind turbine, *World Academy of Science, Engineering and Technology*, 2012; 61: 305-311.
- [30]. Kato, Y., Seki, K., Shimizu, Y., Vertical axis type wind power turbine, US Patent No. 4,285,636, 1981.
- [31]. Seki, K., Straight wind type wind and water turbine, US Patent No. 6,974,309, 2005.

- [32]. Islam, M., Ting, D.S-K., Fartaj, A., Desirable airfoil features for smaller-capacity straight-bladed VAWT, *Wind Engineering*, 2007; 31(3): 165-196.
- [33]. Hill, N., Dominy, R., Ingram, G., Dominy, J., Darrieus turbines: the physics of self-starting, *Proceeding of Institution of Mechanical Engineers, Part A: Journal Power and Energy*, 2009; 223: 21-29.
- [34]. Migliore, P.G., Comparison of NACA 6-series and 4-digit airfoils for Darrieus wind turbine, *Journal of Energy*, 1983; 7(4): 291-292.
- [35]. Clausen, P.D., Wood, D.H., Research and development issues for small wind turbines, *Renewable Energy*, 1999; 16: 922-927.
- [36]. Sutherland, H.J., A summary of the fatigue properties of wind turbine materials, *Wind Energy*, 2000; 3: 1-34.
- [37]. Hara, Y., Hara, K., Hayashi, T., Moment of inertia dependence of vertical axis wind turbines in pulsating winds, *International Journal of Rotating Machinery*, 2012; No. 910940, 1-12.
- [38]. Hau, E., *Wind turbines, fundamentals, technologies, application, economics*, 3rd Ed, Springer, Munich, 2013.
- [39]. Kim, Y.S., Chung, I.Y., Moon, S.I., An analysis of variable-speed wind turbine power-control methods with fluctuating wind speed, *Energies*, 2013; 6(7): 3323-3338.

Chapter 3: The role of free-stream turbulence on flow evolution in the wake of a VAWT blade¹

3.1 Introduction

Vertical axis wind turbines (VAWT) whose simplicity of design and manufacturing continue to make them a strategic choice for harnessing wind energy [1]. The study of the wake flow characteristics behind a VAWT blade is of great interest which can be useful in the improvement of the performance and design of wind turbines. Also, since wind turbines' arrangement in a farm is a crucial concern in wind engineering, turbulence evolution of the wake flow at downstream distances can provide insight into wind turbine group aerodynamic interaction [2]. Furthermore, wind turbines commonly operate in high turbulence conditions like in lower layer atmospheric turbulence or in wakes of other wind turbines [3]. Hence, the effect of free-stream turbulence (FST) on wake flow evolution of a wind turbine blade needs to be characterised appropriately. The overarching objective of the present work is to study the effect of FST on turbulence evolution of a VAWT blade wake flow.

In general, the air flow downstream of a wind turbine blade suffers from a loss in momentum because of the reduced mean velocity in the wake region. Moreover, interaction of wake generated vorticity sheets and free-stream vortices lead to the formation of a highly structured pattern in the wake region. There has been some work in the literature on the wake study of a single (wind turbine) blade [4-8]. One of the most cited studies in this area was carried out experimentally by Hah and Lakshminarayana [4]. They conducted a series of wind tunnel tests on the wake flow over a NACA 0012 airfoil using hot-wire anemometry technique and reported mean velocity profiles and several turbulence parameters. Yarusevych et al. [5] studied the development of coherent structures in the separated shear layer and wake of a NACA 0025 airfoil at low Reynolds numbers experimentally. They reported different cases of the interaction between shear layer roll-up vortices and wake structures in the near-wake region. In another experimental work using hot-wire techniques, Farsimadan and Mokhtarzadeh-Dehghan [6] implemented a particular geometrical configuration in order to replicate a practical airfoil wake and studied the effect of additional factors such as curvature and pressure gradient.

¹ This work was published as: "Ahmadi-Baloutaki, M., Ting, D.S.-K., Cariveau, R., The role of free-stream turbulence on flow evolution in the wake of a VAWT blade, *Wind Engineering*, 2013; 37(4): 401-420."

Despite the importance of FST influence on the wind turbine performance and wake flow, the literature on FST interaction with turbine blade wakes is fairly limited. Nonetheless, some studies exist in the literature on the effect of FST on the flow around an airfoil [9-17] but the majority of them either focused on the effect of external turbulence on the boundary layer domain flow [9-11], aerodynamic forces [12-14], or associate with other fields than wind turbines e.g. [15] on gas turbine blades, and [16] on a compressor cascade. There is one experimental work by Zhang et al. [17] which examined the effects of surface roughness and FST on the wake of a simulated symmetric turbine airfoil, operating in a compressible, high-speed environment. They employed FST levels of 0.9 and 5.5% but only measured flow parameters at one chord length downstream of the airfoil.

The general conclusion from the literature on FST is that an increase in FST can improve aerodynamic characteristics of an airfoil specifically in the non-linear region of the lift curve vs. angle of attack where dynamic stall occurs where this effect is also a function of the Reynolds number. This could be attributed to the energizing of the fluid particles; which have enough energy to resist the flow separation. Torres-Nieves et al. [9] studied the effect of free-stream grid turbulence on the mean flow of a S809 airfoil using 2-D PIV with turbulence intensity levels of up to 6.14%. Their results showed a decrease in aerodynamic efficiency with FST for fully attached flow, measured by the lift-to-drag ratio, however when the airfoil is mostly stalled, the effect is reversed and aerodynamic performance is slightly improved. Hoffmann [10] reported an increase in peak lift coefficient of 30% with no measurable change in the slope of the lift coefficient curve vs. angle of attack when FST increased up to 9% for the flow over the suction surface of a NACA 0015 airfoil. He also showed a significant delay in separation in his results under influence of FST with oil flow visualization; which was later confirmed by Choi et al. [11].

The lack of experimental studies on the effect of FST on the wake flow evolution of a wind turbine blade was the main motivation for the present work. In this paper, the effect of FST on lift and drag coefficients of a NACA 0015 blade is discussed first, then different flow parameters at a few wake downstream locations are presented and FST influence on wake flow evolution is characterized.

3.2 Experimental apparatus

This experimental study has been carried out in a recirculating wind tunnel whose 4m long test section has a spanwise extent of 0.762 m and a height of 0.782 m. The maximum

achievable mean velocity is approximately 20 m/s in the empty working section with a background turbulence intensity of less than 0.5%. In the presence of an orificed perforated plate (OPP) for generating turbulent flow however, the maximum achievable velocity is about 11 m/s. The experiments include aerodynamic force measurements with two load cells, and wake flow measurement using hot-wire anemometry.

A schematic of the configuration used in the present study can be seen in Fig. 1. The blade used in the experiments was a rectangular NACA 0015 blade which has an appropriate profile for VAWT application [18]. The blade cross section coordinates can be found in [18]. The mentioned symmetric blade was made from plain wood using computer numerical control (CNC) machining. After it was cut, it was painted with white acrylic paint and polished with NOVUS plastic polish to achieve a smooth surface. The blade has a chord length of 0.152 m with a span-to-chord ratio of 4.96 and a maximum thickness of 15% of the chord length. The blade was mounted horizontally in the test section at 3.3 m downstream of the wind tunnel inlet section. The blade leading edge distances from the wind tunnel floor and ceiling were 0.391 m. The blade spanned the entire width of the test section, leaving only a small gap between the blade sides and the wind tunnel walls, so that the forces acting on the blade are not transferred to the tunnel wall. Moreover, it is believed with this small gap, the possibility of air moving towards the blade upper surface causing a leakage effect was minimized, and the end effects influence on the flow development over a great portion of the blade span within the domain of interest decreased. It should be noted that all the hot-wire wake measurements were carried out in the vertical midspan plane of the wind tunnel. The angle of attack was set by a machined protractor, with an uncertainty estimated to be 0.5° .

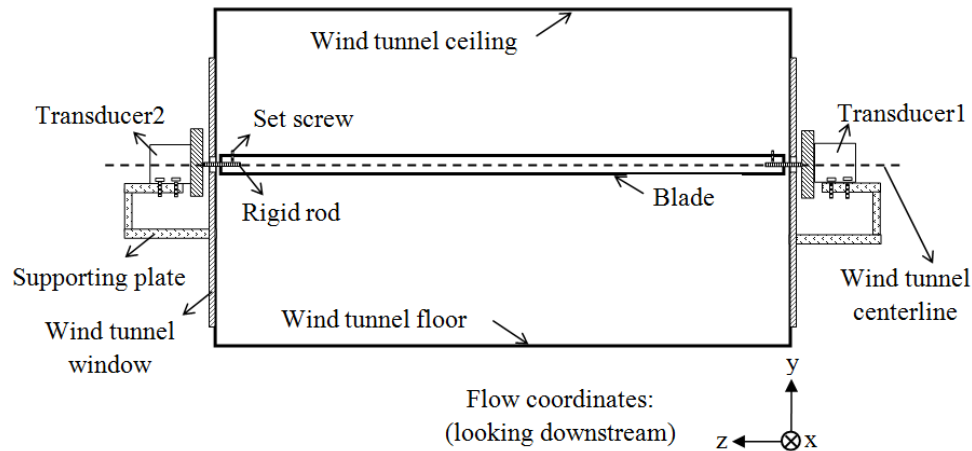


Figure 1: A schematic of the blade in wind tunnel and its connection with transducers (looking downstream)

For controlling free-stream turbulence a 6 mm thick orificed perforated plate with holes of 50.8 mm diameter and solidity ratio of 43% was placed upstream of the test model (see Fig. 2). To minimize the influence of the plate thickness on the turbulent flowfield generated, each hole was machined with a 41° chamfer angle with the sharp-edged side facing the incoming flow. It has been demonstrated that this turbulence generator is appropriate for generating quasi-isotropic turbulence [19].



Figure 2: (a) Orificed perforated plate photo (looking upstream), (b) Cross-section of the OPP

At the start of each experiment, the free-stream velocity in the wind tunnel was set using a Pitot-static tube connected to a digital manometer (DWYER series 475). The Pitot-static tube was inserted through a small hole on the side wall of the wind tunnel near the inlet section (see Fig 3). The Pitot-static tube was removed after checking the free-stream velocity and the small opening was sealed.

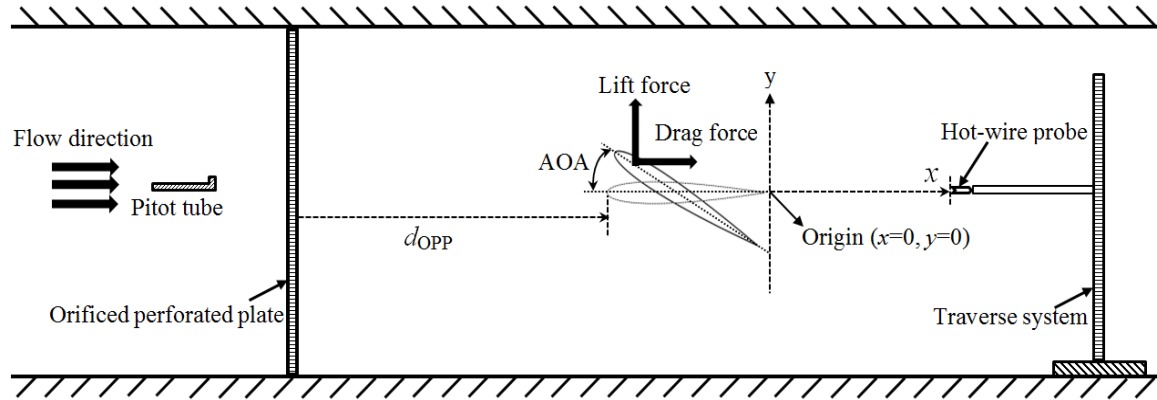


Figure 3: A schematic of experimental apparatus

For measuring lift and drag forces on the airfoil two six-axis force/torque sensor systems of ATI industrial automation (Gamma version) have been used. The maximum force measuring range and resolution of the transducers were ± 65 N, 0.0125 N and ± 32 N, 0.00625 N. The transducers were aligned horizontally and vertically and connected to aluminum angles mounted outside of the wind tunnel by bolts (see Fig. 1). To ensure a better alignment, each transducer was attached with a shaft which was inserted into a pre-drilled hole at the lateral side of the blade. The holes were drilled at one quarter of chord length distance from the leading edge of the blade which is the location of the aerodynamic center of the NACA 0015 blade [18]. The blade can be rotated about this point at desired angles of attack. At each angle of attack, the force transducers were kept stationary via supporting set screws pre-made at the upper blade surface. Extreme care was taken to check that the rods connecting the load cells to the airfoil were not touching the wind tunnel wall openings. Also, the transducers were carefully positioned before the experiment so that the x -axis was parallel to the direction of flow, and the positive y -axis was pointing up perpendicularly. The lift force was calculated by summing the force components in the y -direction from the transducers, and the drag force was the summation of the force components in the x -direction. The sampling frequency was 2 kHz, and at least 2×10^5 samples were recorded at each measurement.

Flow velocity data were obtained using a normal hot-wire probe of 55P11 type connected to a DANTEC constant temperature anemometer unit. The output signal of the hot-wire probe was sent to a National Instrument multifunction data acquisition board with a 12-bit resolution connected to a computer. The hot-wire probe, together with the temperature probe, were mounted on a 2-D traversing system with vertical and spanwise axes. The effects of the free-stream temperature drift were taken into account using the correction of Bearman [20]. For the hot-wire measurement, the analog voltage signal was first low-passed at 30 kHz using an analog filter in order to remove noise and to prevent higher frequencies from folding back (anti-aliasing). Then it was sampled at 80 kHz (which is more than twice the Nyquist frequency) over the sampling time of 25 s which resulted in 2×10^6 samples.

3.3 Results and discussion

The measurements have been performed for flow over the NACA 0015 blade in two levels of free-stream turbulence intensity (0.5% and 4.6% with the estimated uncertainty of less than 8%). The turbulence intensity, Tu , is

$$Tu(\%) = \frac{u_{rms}}{U_{mean}} \times 100 \quad (1)$$

where u_{rms} is the root-mean-square of the velocity fluctuations deduced from

$$u_{rms} = \left\{ \sum_{i=1}^N \frac{(U_i - U_{mean})^2}{N-1} \right\}^{0.5} \quad (2)$$

It should be noted that the velocity measurements have only been taken for the streamwise component of the velocity vector. Turbulence intensity for the flow without the OPP was measured to be around 0.5% at the location of the leading edge of the blade while the blade is not present in the wind tunnel. In the other case, the OPP was placed at 1.54 m upstream of the blade leading edge which resulted in a turbulence intensity of 4.6% and a 35 mm integral length scale at the leading edge of the blade, again in the absence of the blade. The upstream velocity was set at 8.12 m/s; which led to a Reynolds number of 80,000 based on the blade chord length.

The uncertainty in various reported parameters has been estimated according to the procedure of Yavuzkurt, and Benedict and Gould [21,22], and has been displayed with error bars for a few points on different graphs. Apart from the standard procedure of the uncertainty analysis, the uncertainty in the vertical location of the hot-wire probe, y , was estimated at 2 mm including uncertainty in the measured length by a smart motor used to traverse probe vertically, and uncertainty in the position of the probe's holder because of its vibrations.

3.3.1 Aerodynamic forces

Lift and drag coefficients for the smooth free-stream flow with chord Reynolds number of 80,000 displayed in Fig. 4 are calculated based on

$$C_L = \frac{F_L}{0.5\rho AU_\infty^2} \quad (3)$$

$$C_D = \frac{F_D}{0.5\rho AU_\infty^2} \quad (4)$$

Figure 4a shows that the lift coefficient increases to a peak value as angle of attack increases. This increase occurs at a region where the flow over both surfaces of the blade is attached. A similar increasing trend is also detectable in Fig. 4b for the drag coefficient. With further increase in angle of attack, flow separation occurs and the lift coefficient drops

dramatically, known as static stall. The static stall results in a sudden increase in drag coefficient which can be observed from Fig. 4b. Beyond the static stall, the changes in the force coefficients are more moderate, even though the flow is entirely stalled at the upper surface of the blade. Three datasets in Fig. 4 correspond to increasing angle of attack (from 0° to 25°), decreasing angle of attack (from 25° to 0°), and results of Ref. [18]. Figure 4 shows that during the decreasing angle of attack the stall point of the blade occurs at a lower angle of attack compared to the increasing angle of attack case, attributed to a hysteresis effect. To recover the blade from stall condition with decreasing angle of attack, the separation bubbles on the blade suction surface are being swept off which is accompanied by the potential flow reattachment. Current results agree well with those of Sheldahl and Klimas [18] for increasing angle of attack case. Both lift and drag coefficients appear marginally higher than those of Ref. [18]. This is possibly attributed to higher level of the FST in the present experiments. The effect of FST on the force coefficients will be discussed in detail in the next paragraph.

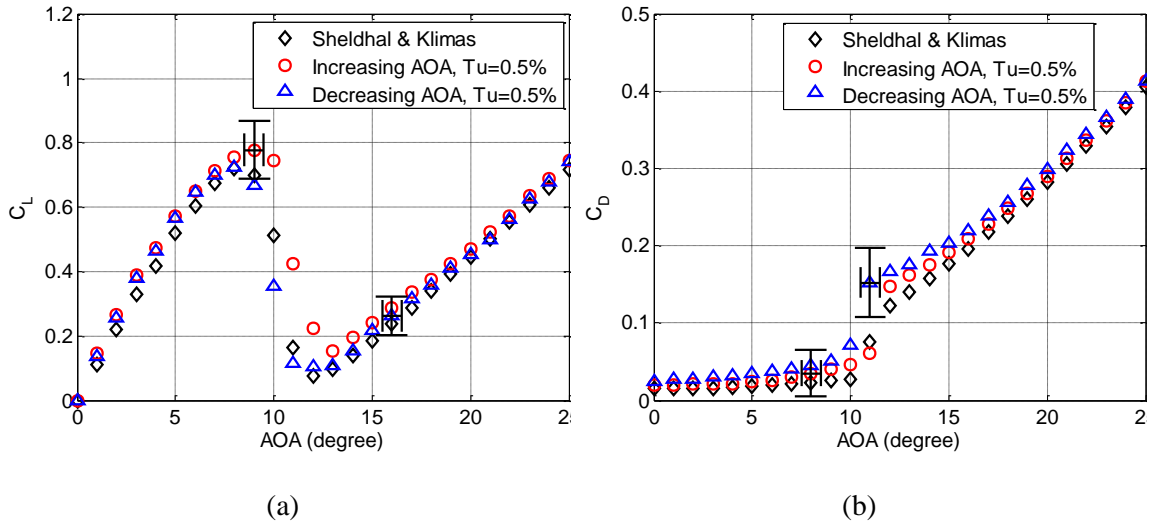


Figure 4: Coefficients of (a) lift, and (b) drag for smooth flow at $Re=80,000$, and comparison with Ref. [18]

The effects of free-stream turbulence on the force coefficients of the blade are displayed in Fig. 5. As can be seen in Fig. 5a, the maximum lift occurs at a higher angle of attack in $Tu=4.6\%$ than $Tu=0.5\%$. This means that the stall and consequently flow separation can be delayed with increasing FST. In the post-stall region, a larger increase in the lift can be observed which suggests that FST tries to remove the separated shear layer by augmenting the fluid particle momentum. On the other hand, the increase in lift with FST comes at the expense of an increase

in drag due to higher shear stress in the newly-formed turbulent boundary layer; noting that this increase in drag is within the uncertainty limits (see Fig. 5b). To have a better understanding of the FST effect on the aerodynamic forces, the lift-to-drag ratio has been calculated and plotted in Figs. 5c & 5d. Except in the stall region ($AOA \approx 10^\circ \sim 15^\circ$) where the lift-to-drag ratio increases promisingly with increasing FST, in other regions this ratio decreases under higher FST.

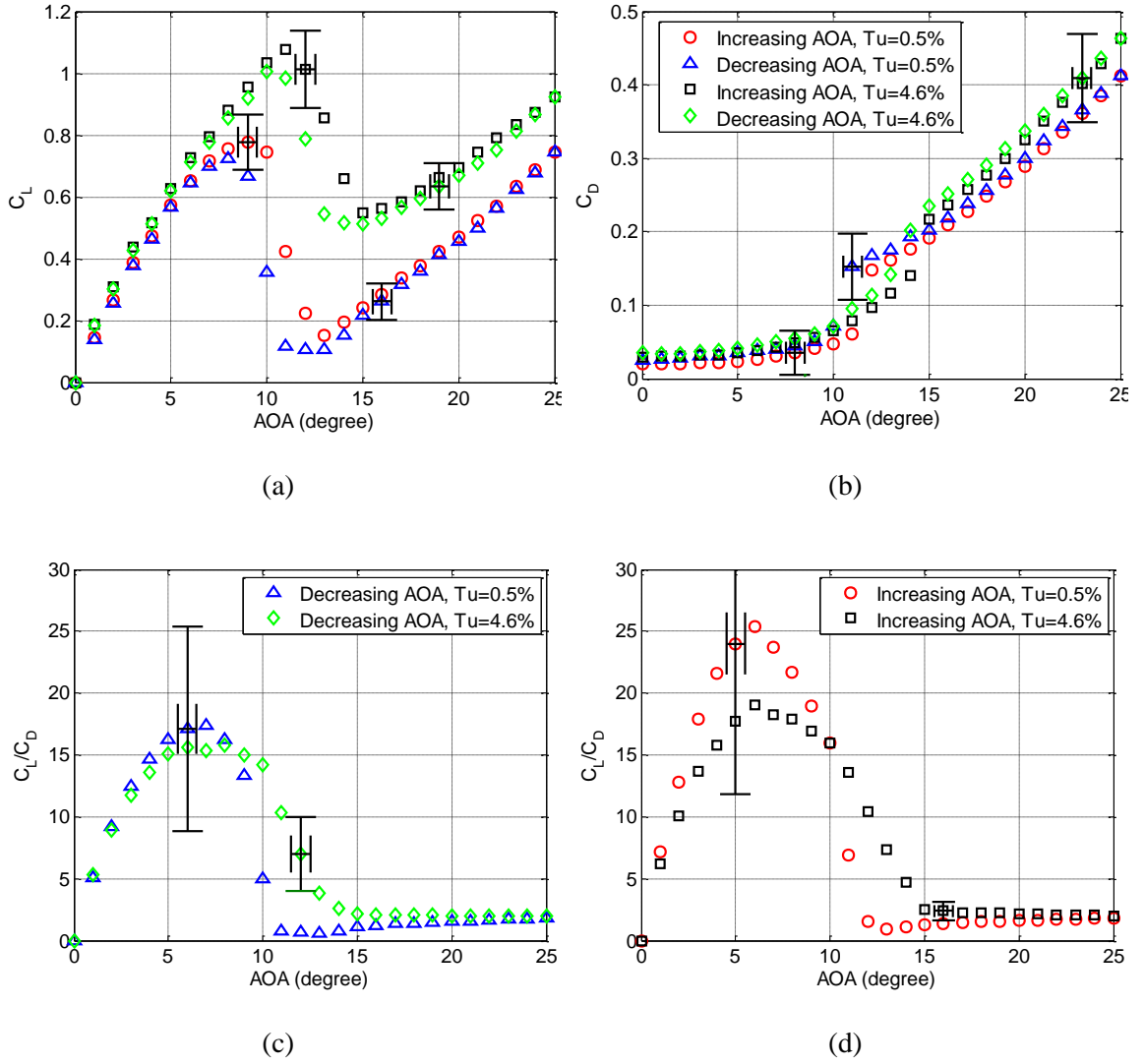


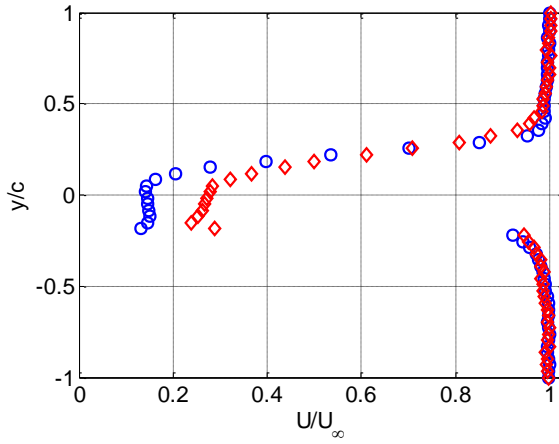
Figure 5: Effect of FST on (a) lift coefficient (graph legend is the same as b), (b) drag coefficient, (c) lift-to-drag ratio (decreasing angle of attack), (d) lift-to-drag ratio (increasing angle of attack), $Re=80,000$

3.3.2 Wake profiles

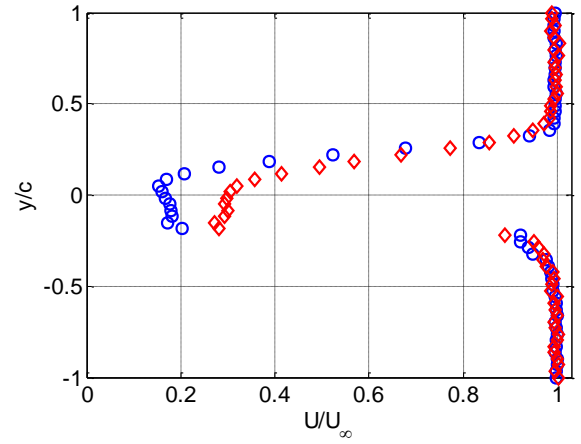
As discussed in the previous section, aerodynamic performance of the blade was improved under higher FST in the stall region. To better understand the underlying physics behind the interaction of FST with wake flow, an angle of attack in the stall region, $AOA=14^\circ$, was selected and wake flow measurements were performed at eight streamwise locations of $x/c=0.07, 0.12, 0.25, 0.50, 0.75, 1.00, 1.50$, and 2.00 downstream of the blade. The results shown below correspond to both $Tu=0.5$ and 4.6% at $AOA=14^\circ$ and $Re=80,000$. At each streamwise location, the hot-wire probe was traversed vertically across sixty measurement points from $y/c=-1$ to $+1$.

Figure 6 shows the streamwise mean velocity profiles at eight streamwise sections while sample uncertainty error bars are displayed only in Fig. 6c. The error bars do not show the uncertainty in y/c , since it has a very small value (in the range of 0.02) compared to the axis limits. It is clear from Fig. 6 that the near wake profile is highly asymmetric and it becomes progressively symmetric farther downstream. The asymmetric nature in the wake is attributed to blade aerodynamic loading (non-zero angle of attack), and the different flow patterns on the bottom and top surfaces of the blade. In fact, the literature [10, 18] confirms that the flow over a NACA 0015 blade at the same Reynolds number and angle and attack, is mostly separated on the upper surface while attached on the lower surface. At $x/c=0.07$ and 0.12 , substantial asymmetry exists in velocity profiles as can be seen in Figs. 6a & 6b. Also, abrupt changes of mean velocity magnitudes are observed between the wake center part and wake boundaries near the free-stream area. According to Hah and Lakshminarayana [4] this region can be considered as “very near wake” region where the viscous sublayer on the airfoil is not entirely mixed with the surrounding inertial area. In this region the molecular viscosity has a substantial effect on the flow evolution in the wake center region where the velocity deficit is large. They [4] called the next stage as “near wake” region where the physical characteristics of the airfoil and its aerodynamic loading have considerable effects on the development of the wake. The effect of molecular viscosity is negligible in this region for turbulent wakes. This region can be detected at streamwise locations of $x/c=0.25$ to 1.00 , where asymmetry in the mean velocity profiles is reduced in the downstream direction (see Figs. 6c to 6f). Expectedly, the velocity differences between wake center and wake boundaries becomes more moderate in the near wake region. The third region, labeled the “far wake” region sees the wake pattern as almost symmetric and the physical characteristics and aerodynamic loading have negligible effects on the evolution of the wake [4]. Present results at the two final sections, $x/c=1.50$ and 2.00 , display a nearly symmetric distribution (see Figs. 6g & 6h). This region can be assumed as far wake region where the mean velocity deficiency is the smallest among the other wake locations.

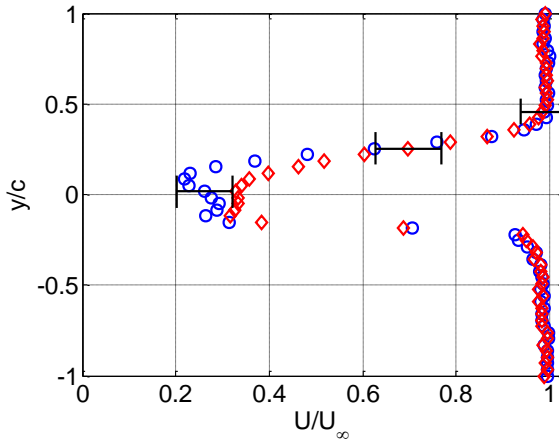
The mean velocity profiles for $Tu=4.6\%$ case on Fig. 6, also share the same trends as the $Tu=0.5\%$ case. In particular, FST seems to increase the mean velocity throughout the measurement sections. This can be attributed to the fact that higher turbulence levels tend to augment the fluid particles' momentum by energizing them. This outcome can be correlated to the literature [9-12] which showed the external FST can suppress the flow separation via energizing the boundary layer. The other point worth noting is that the FST makes the velocity profiles more symmetric as can be observed in Fig. 6.



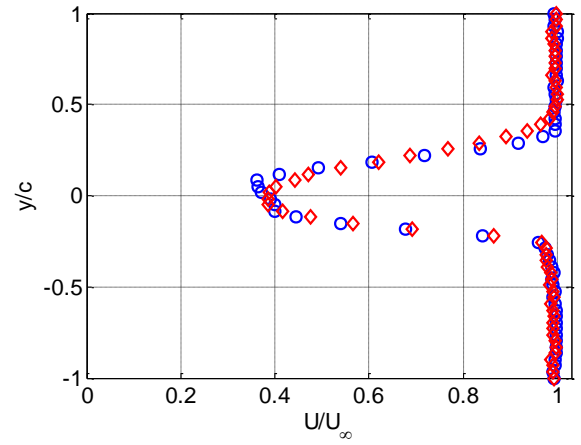
(a) $x/c=0.07$



(b) $x/c=0.12$



(c) $x/c=0.25$



(d) $x/c=0.50$

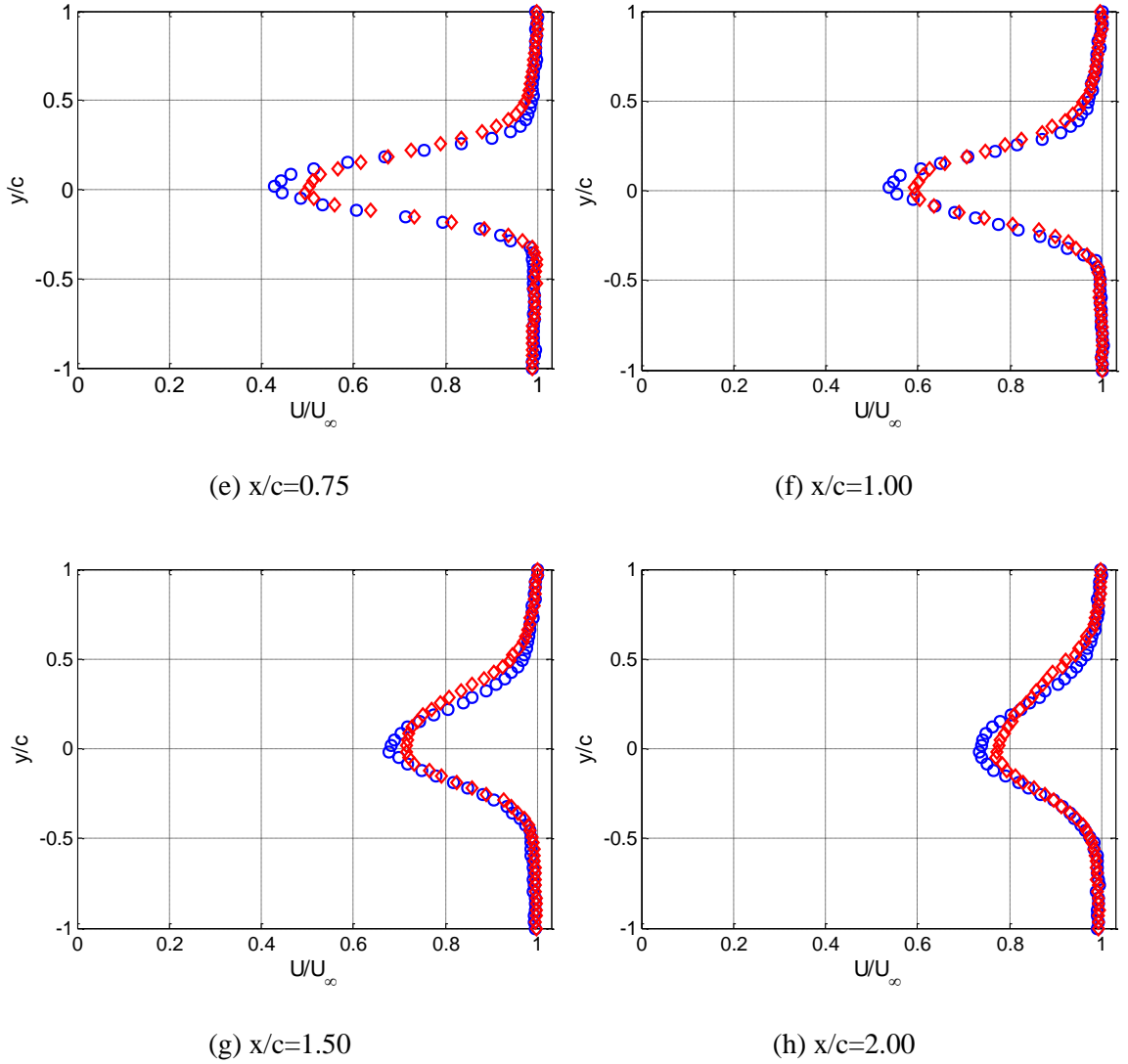


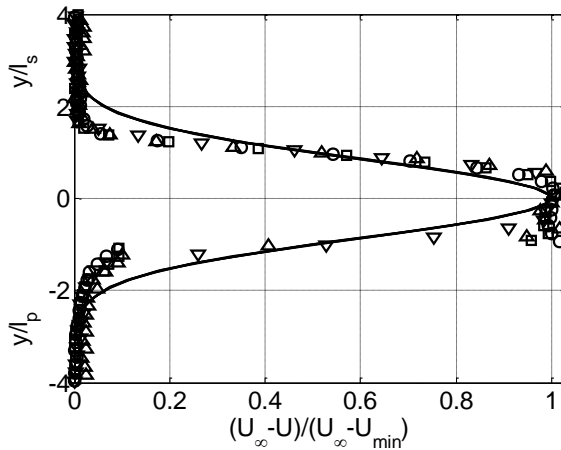
Figure 6: Effect of FST on the wake mean velocity profiles; \circ : $Tu=0.5\%$, \diamond : $Tu=4.6\%$

A subject of interest in the wake flow studies is to determine whether and where the velocity profiles become similar. It is known from the literature [4, 23, 24] that if the mean velocity profiles are described by a single velocity scale, and a single length scale, after a certain distance downstream, wake profiles are considered similar. Describing a wake flow with particular length and velocity scales enables one to predict the wake profiles at any downstream location. This is of great significance in wind turbine positioning in a wind farm. The maximum velocity deficit which is the difference between the free-stream and minimum streamwise velocities, $U_\infty - U_{min}$, can be used as the velocity scale while its corresponding vertical location can be considered as wake center. A proper length scale in wake flows, $l_{0.5}$, is the distance from

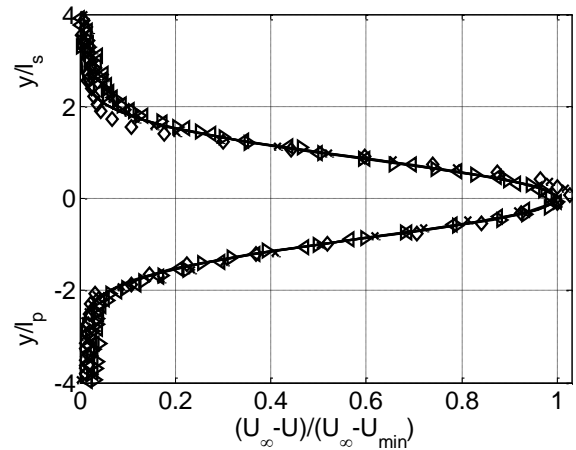
the wake center where the velocity deficit reaches half of the maximum velocity deficit. These scales are universal wake scales which can be applied in both symmetric and asymmetric wakes [4, 23, 24]; Hah and Lakshminarayana [4] suggested to use two length scales for an asymmetric wake, for lower and upper parts of the wake, that is $l_{0.5,p}$ and $l_{0.5,s}$ have been utilized for pressure and suction sides of the blade. It has been tried to check the similarity in velocity profiles in Fig. 7 by describing them in terms of aforementioned velocity and length scales. Different Gaussian functions have been suggested to describe self-similar wake profiles [4, 23, 24]. Hah and Lakshminarayana [4] used Eq. 5 for their similarity solutions of an asymmetric wake of a symmetric blade:

$$\frac{U_\infty - U}{U_\infty - U_{min}} = \exp \left[-0.6993 \left(\frac{y}{l_{0.5}} \right)^2 \right] \quad (5)$$

Figures 7a & 7c which correspond to the four first streamwise locations for $Tu=0.5$ and 4.6% show significant deviation from the Gaussian function. Figures 7b & 7d show some deviation for $x/c=0.75$ data, but negligible deviation for $x/c>1.00$. In other words, the present velocity profiles become similar around the $x/c=1.50$ streamwise location. It should be noted that the same location has been reported in Ref. [4], even though they used a different blade, different angle of attack, and different Reynolds number.



(a) $Tu=0.5\%$; \circ : $x/c=0.07$, \square : $x/c=0.12$,
 \triangle : $x/c=0.25$, ∇ : $x/c=0.50$, —: Eq. 5



(b) $Tu=0.5\%$; \diamond : $x/c=0.75$, \times : $x/c=1.00$,
 \triangleleft : $x/c=1.50$, \triangleright : $x/c=2.00$, —: Eq. 5

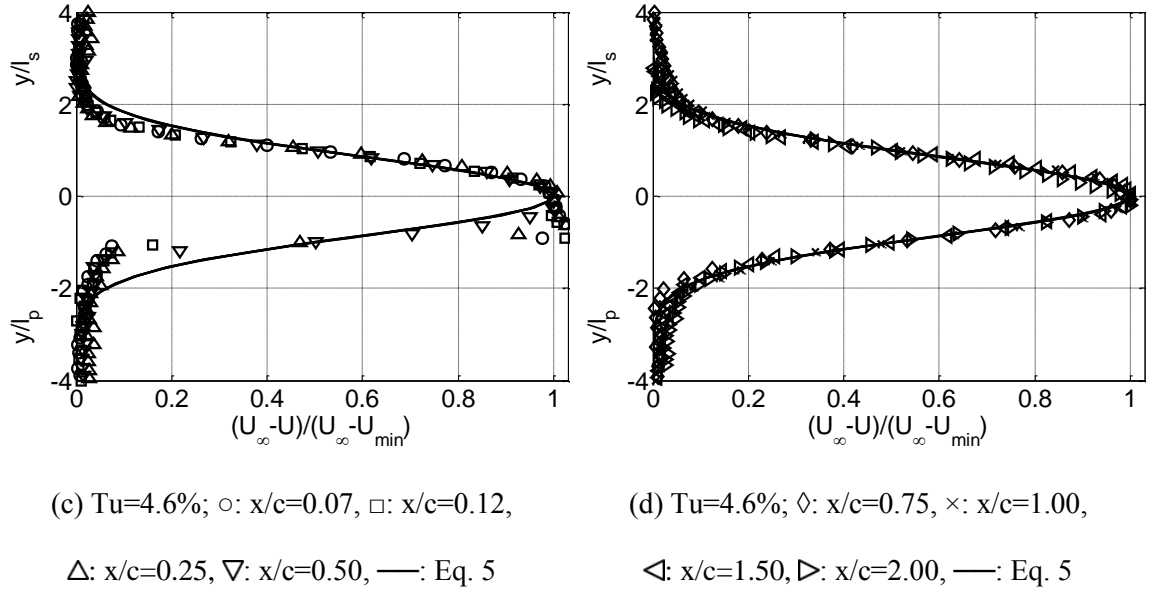


Figure 7: Similarity check for mean velocity profiles

Another interesting parameter in the wake flow studies is the wake thickness. Wake thickness, b , can be defined as the distance between the two locations on the lower and upper parts of the wake velocity profile where the velocity deficit reaches half of the maximum velocity deficit; $b = l_s + l_p$ [4, 23, 24]. Wake thickness is a measure of the flow area which is dominated and decelerated by the wake region behind an object. It is expected that the wake thickness increases as streamwise distance increases, but this increase is not visible until the $x/c=0.75$ location in the present work as shown in Fig. 8a. In fact, the wake thickness stays almost constant in the few first streamwise locations. This can probably be attributed to the aerodynamic loading on the blade which significantly affects the flow development in the near wake region. For reference, the wake thickness, b_{95} , between the two points where the mean velocity reaches 95 percent of the free-stream velocity has been plotted in Fig. 8b. Figure 8b shows the same trend observed in Fig. 8a, i.e. constant wake thickness at few first locations and then increase in the streamwise direction. As mentioned earlier, the uncertainty in displacement parameters such as y/c and also b/c and b_{95}/c is very small (in the range of 0.02), which is negligible compared to axis domain, and therefore was not displayed in Figs. 8.

Beyond the uncertainties and scatter of the first few points, both Figs. 8a & 8b shows that FST increases the wake thickness. This could be because of the higher involvement of the wake region with free-stream area under higher FST. Wake broadening by FST has been also observed

by Zhang et al. [17] who attributed this to the increased diffusion from the wake to the surrounding free-stream. Ames and Plesniak [25] also reported a similar trend, and they correlated this to the smaller peak velocity deficits.

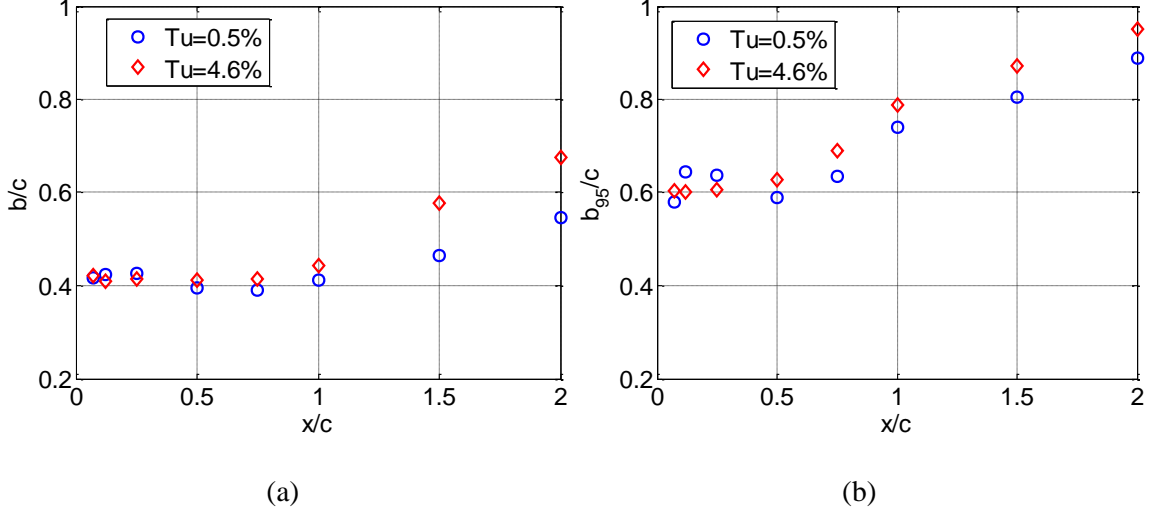
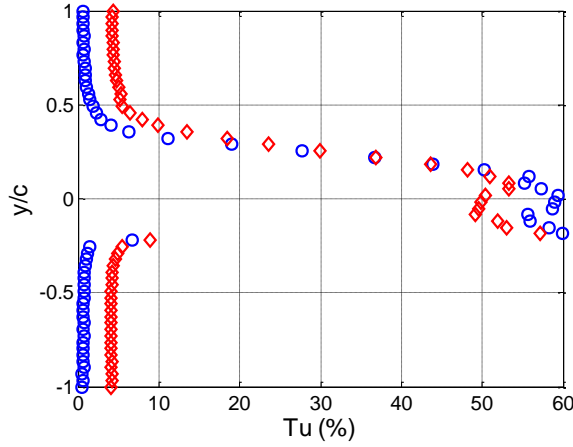


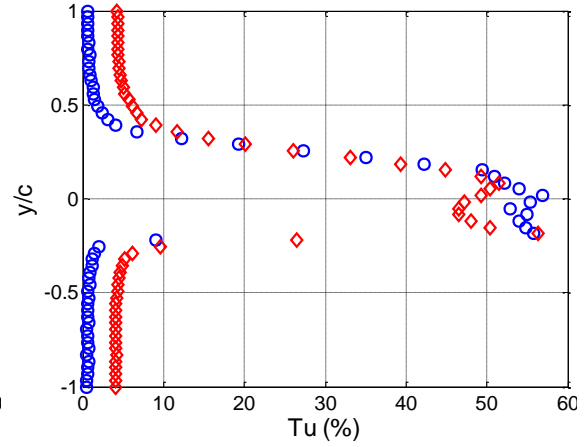
Figure 8: Effect of FST on the wake thickness, (a) wake thickness defined based on half of the maximum velocity deficit, (b) wake thickness defined based on 95% free-stream velocity

To study the flow evolution in the wake region, examining the turbulence level is of great importance since it determines the incoming flow nature to the next object downstream (another blade or wind turbine). To do so, streamwise turbulence *rms* velocity (calculated from Eq. 2) at each point has been normalized with local mean velocity at the same point to reach a relative measure of the turbulence level (see Eq. 1) in the wake flow. Turbulence intensity distributions across the wake at selected streamwise locations have been plotted in Fig. 9. At $x/c=0.07$ and 0.12 , the turbulence intensity level is higher on the upper surface of the blade than on the lower surface (see Figs. 9a & 9b). As mentioned earlier [10, 18], since this very near wake region is directly affected by the boundary layer flow over the blade, separated shear layer on the upper surface is the main source of high turbulence disturbances in the upper wake while attached flow lowers the turbulence level in the lower wake. There are great changes of turbulence intensity levels between the free-stream area and the wake center part. This trend partially persists to the $x/c=0.25$ location (see Fig. 9c) while downstream of this location ($x/c \geq 0.50$) the turbulence intensity in both upper and lower parts of the wake has very similar values (see Figs. 9d to 9h). Following the mean velocity profiles' trend, the turbulence intensity distributions is highly asymmetric in the very near wake region ($x/c=0.07$ & 0.12), fairly asymmetric in the near wake

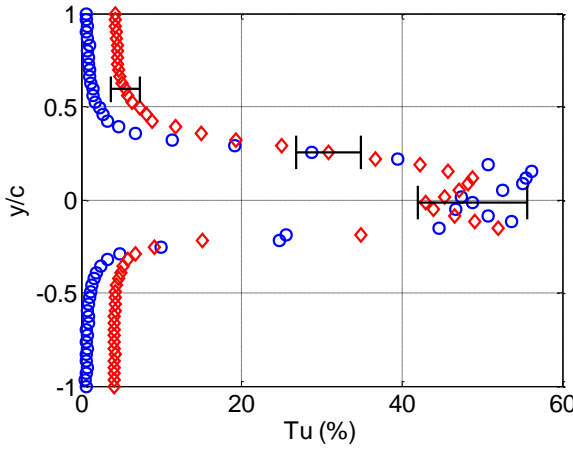
region ($0.25 \leq x/c < 1.50$), and almost symmetric at the two last locations, $x/c=1.50$ & 2.00 (see Figs. 9g & 9h). Figure 9 shows that FST tries to suppress the wake turbulence, and in doing so, it makes the turbulence intensity profiles more symmetric. The reduction in turbulence intensity level could be an indication of suppressed flow separation.



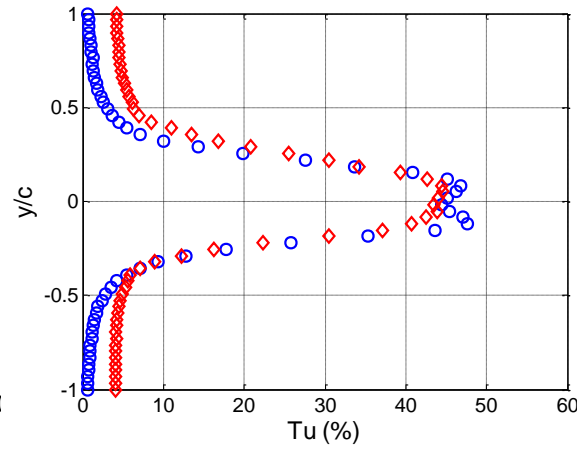
(a) $x/c=0.07$



(b) $x/c=0.12$



(c) $x/c=0.25$



(d) $x/c=0.50$

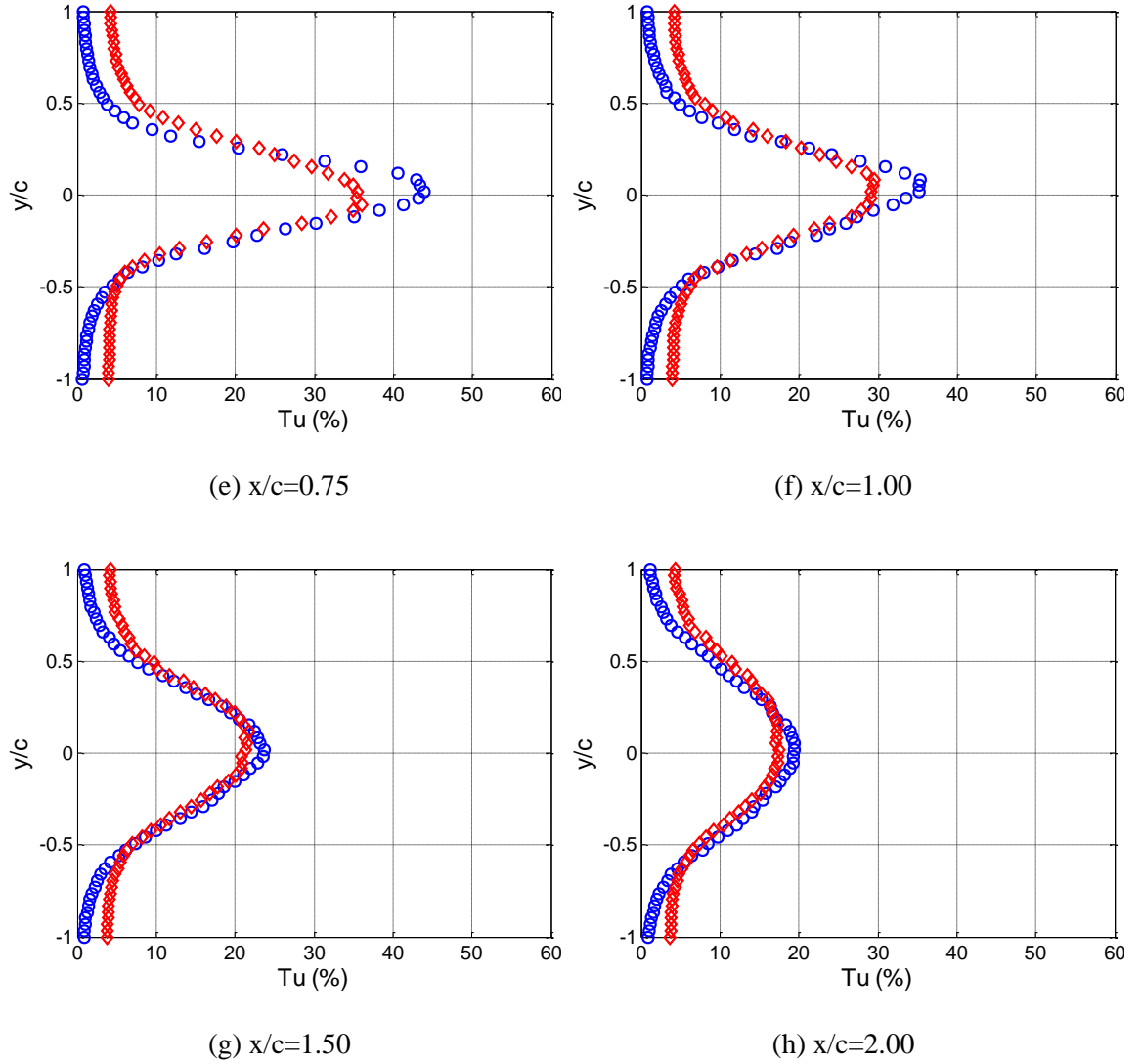
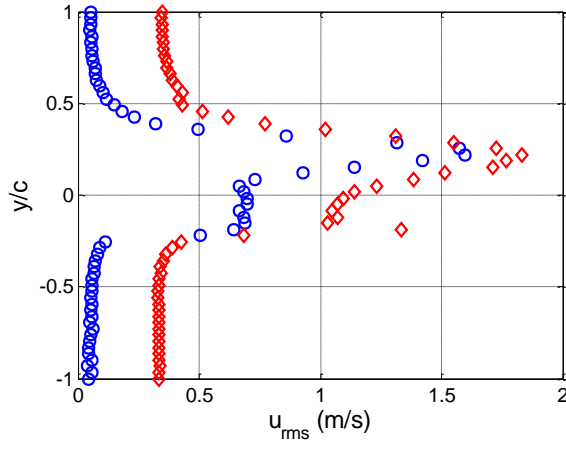


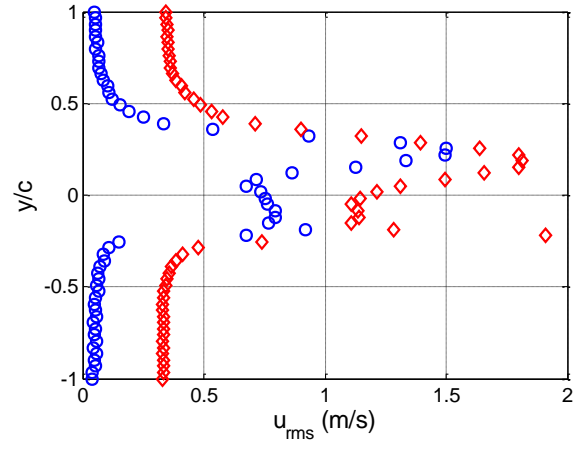
Figure 9: Effect of FST on the wake turbulence intensity profiles; \circ : $Tu=0.5\%$, \diamond : $Tu=4.6\%$

To further reveal the physics underlying wake turbulence evolution, two more turbulence quantities are examined. Streamwise turbulence *rms* velocity and streamwise turbulence strain rate are discussed here. These quantities are dimensional parameters while the quantities discussed in Figs. 6 & 9 were non-dimensional parameters. The turbulence *rms* velocity, u_{rms} , which is a statistical measure of the velocity fluctuations and representative of the strength of flow vortices has been determined from Eq. 2 and plotted in Fig. 10. For $Tu=0.5\%$ case, the turbulence *rms* velocity decrease less rapidly compared to turbulence intensity, with streamwise distance. It increases in the very near wake region, $x/c=0.07$ to 0.25 , (see Figs. 10a to 10c) and reaches its peak values at $x/c \approx 0.25$, then starts to decrease farther downstream (see Figs. 10d to

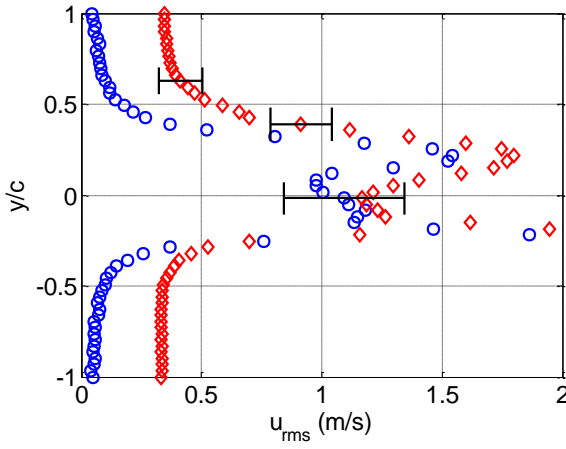
10h). Similar trends can be observed for the $Tu=4.6\%$ case, where the highest turbulence rms velocity occurs at $x/c \approx 0.25$.



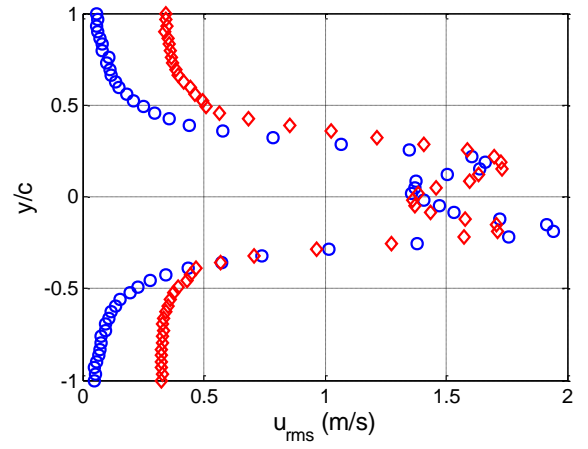
(a) $x/c=0.07$



(b) $x/c=0.12$



(c) $x/c=0.25$



(d) $x/c=0.50$

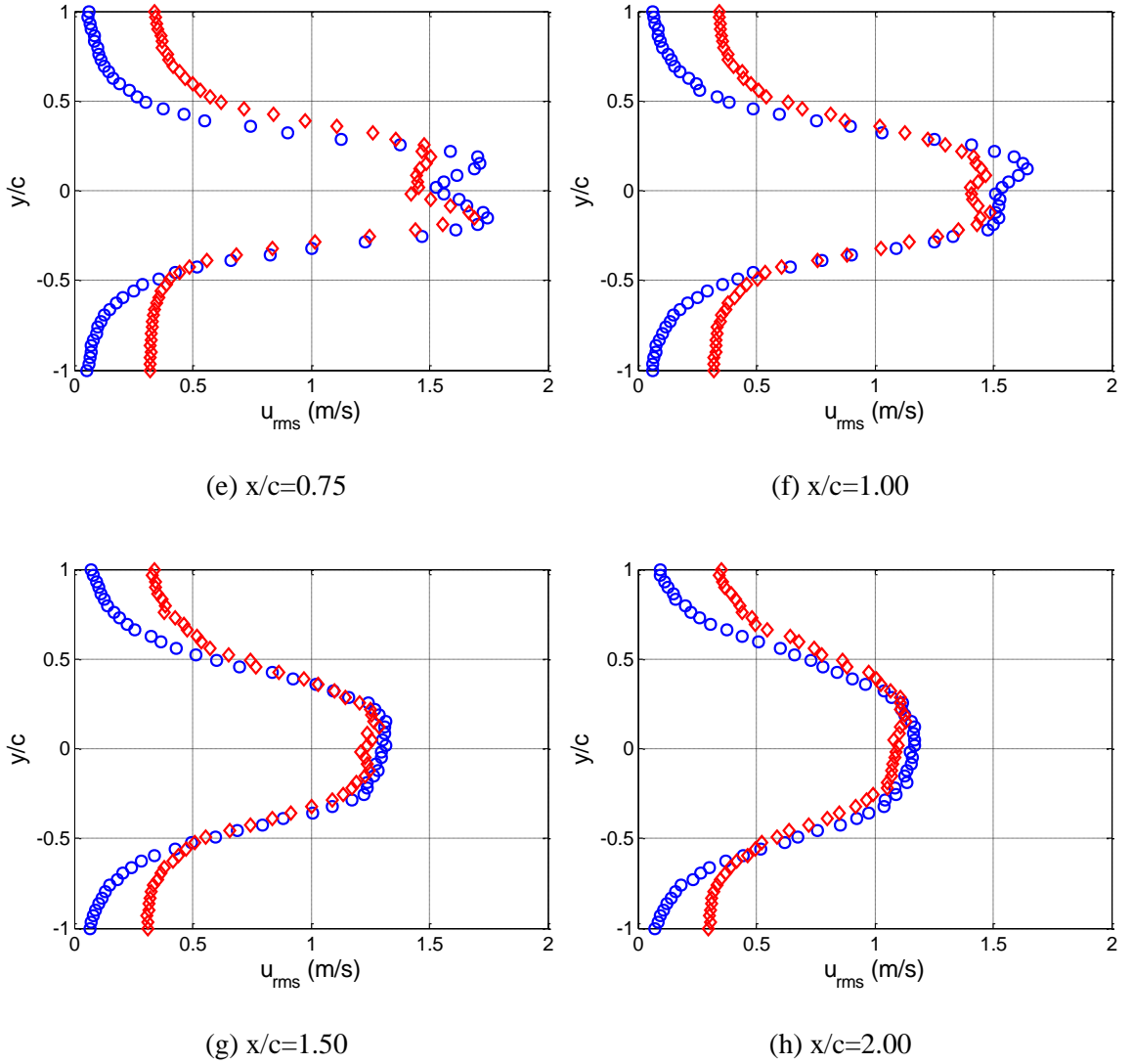


Figure 10: Effect of FST on the wake turbulence *rms* velocity profiles; \circ : $Tu=0.5\%$, \diamond : $Tu=4.6\%$

To better elucidate turbulence *rms* velocity evolution, the u_{rms} contours and colormaps are displayed in Fig. 11. Two local regions of high turbulence *rms* velocity can be observed in the vicinity of the blade trailing edge, around $y/c=-0.2$, and also in the upper part of the wake, around $y/c=+0.2$, for both free-stream conditions in Fig. 11. Also, a close examination of Fig. 10 will reveal a dip near the wake center ($0.07 < x/c < 1.00$, $-0.05 < y/c < +0.05$) for both $Tu=0.5$ & 4.6% cases; even though the clarity is limited by spatial resolution. The two peaks just above and below of the dip would indicate strong vortices, as observed also by Yarusevych et al. [5]. They [5] attributed these vortices to the separated shear layer on the blade's upper surface, and blade trailing edge generated vortices, respectively.

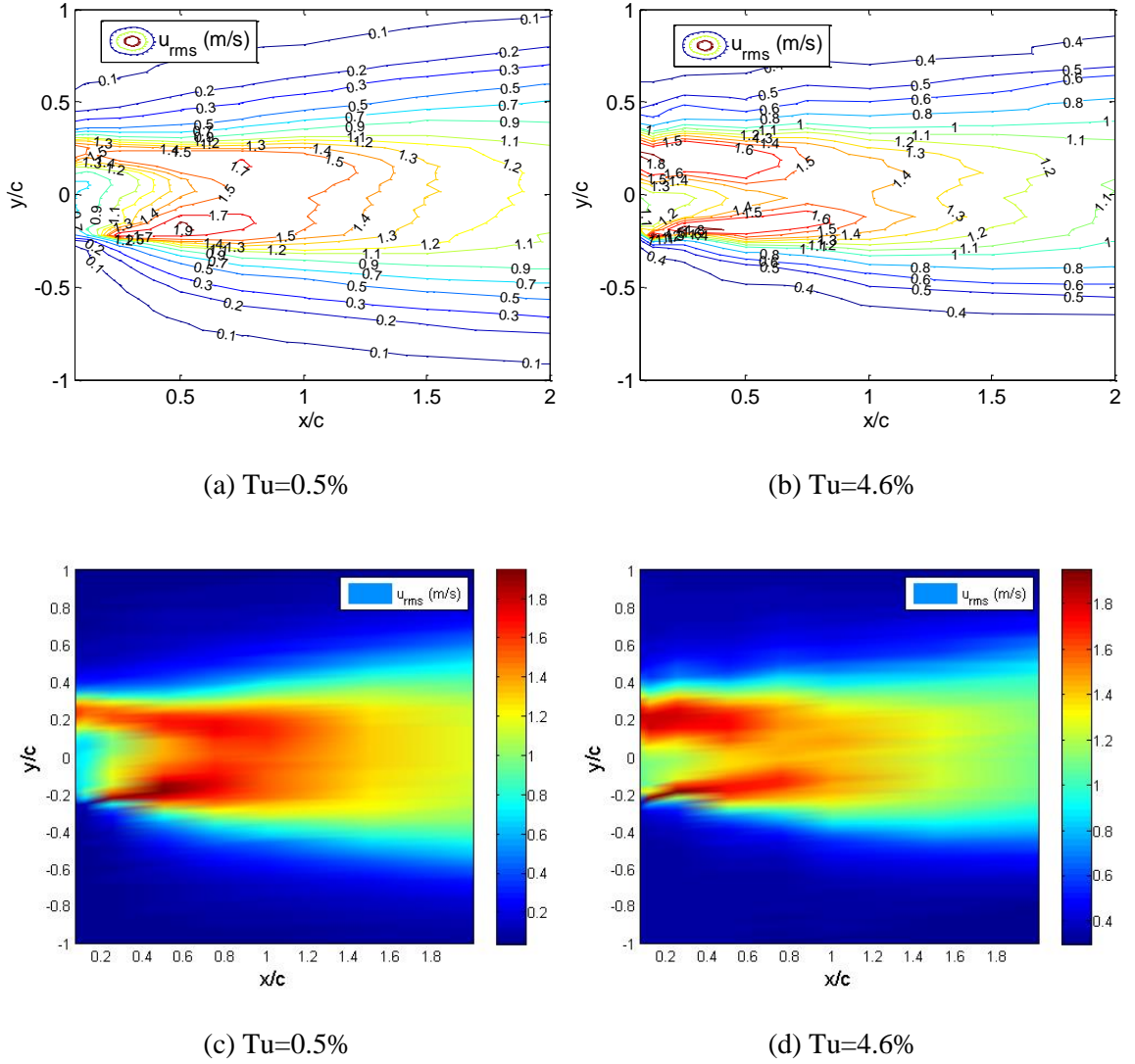


Figure 11: Turbulence rms velocity contours and colormaps, Tu=0.5 & 4.6% flow cases

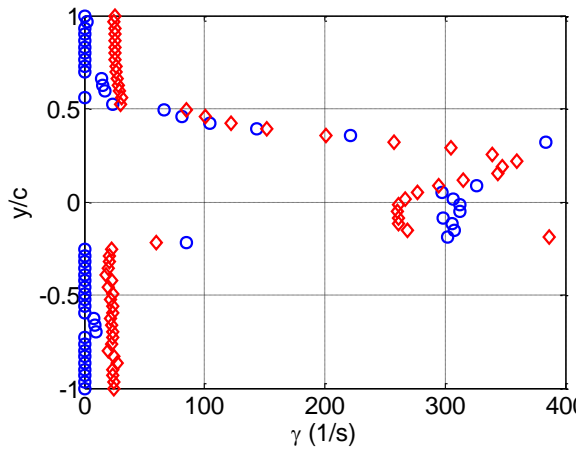
To reveal the role of eddy size on the wake flow evolution, the wake characteristics in terms of turbulence strain rate have been examined. Turbulence strain rate, γ , which is defined as [26, 27]

$$\gamma = \frac{u_{rms}}{\lambda} \quad (6)$$

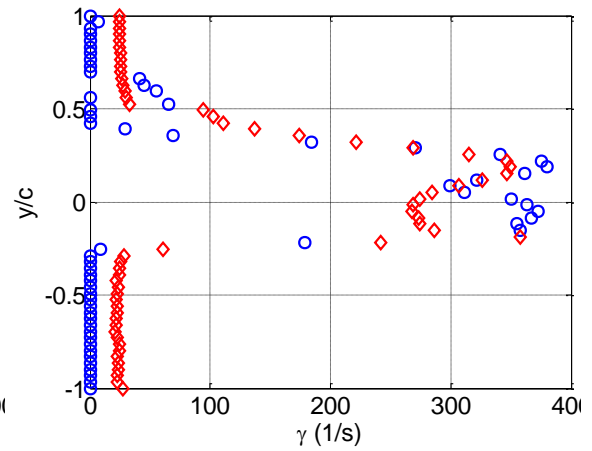
is a turbulence quantity which contains the effects of both turbulence fluctuations and turbulence length scales. λ is the Taylor microscale and the procedure given in Refs. [28, 29] has been utilized to estimate it. Figure 12 illustrates that the turbulence strain rate variation is similar to that of turbulence rms velocity. For Tu=0.5%, the strain rate increases in the very near wake

region from $x/c=0.07$ to $x/c=0.25$ (see Figs. 12a to 12c), and reaches a peak value at $x/c=0.25$. Then it decreases farther downstream as can be observed in Figs. 12d to 12h. A roughly similar trend is observed for the $Tu=4.6\%$ case where the highest values of the turbulence strain rate occur at $x/c=0.12$. Since the turbulence strain rate is a measure of the ratio of turbulence fluctuations to turbulence length scales, it can be said that the role of turbulence fluctuations is more significant than turbulence length scales in the very near wake region; while turbulence length scales become more influential farther downstream.

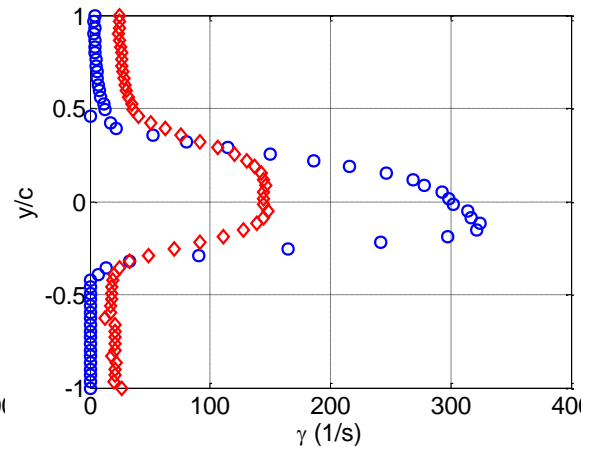
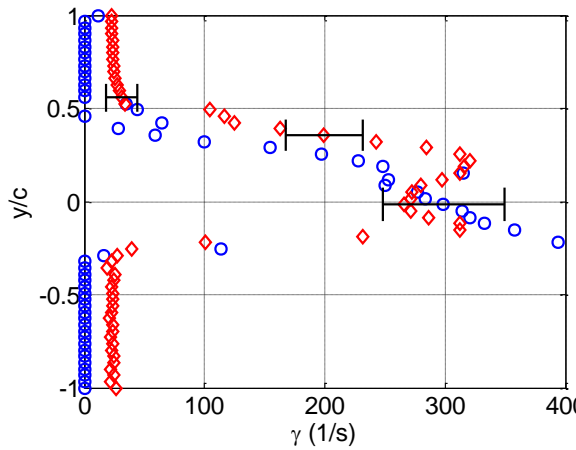
To characterize the effect of FST on the turbulence strain rate from Fig. 12, it can be stated that the FST decreases the turbulence strain rate in the wake center part almost at all streamwise locations, compatible with the trends observed in Figs. 6 & 9. As well, this decrease in turbulence strain rate under higher FST may be correlated to the role of external FST on the flow separation delay as demonstrated by literature [9-12].



(a) $x/c=0.07$



(b) $x/c=0.12$



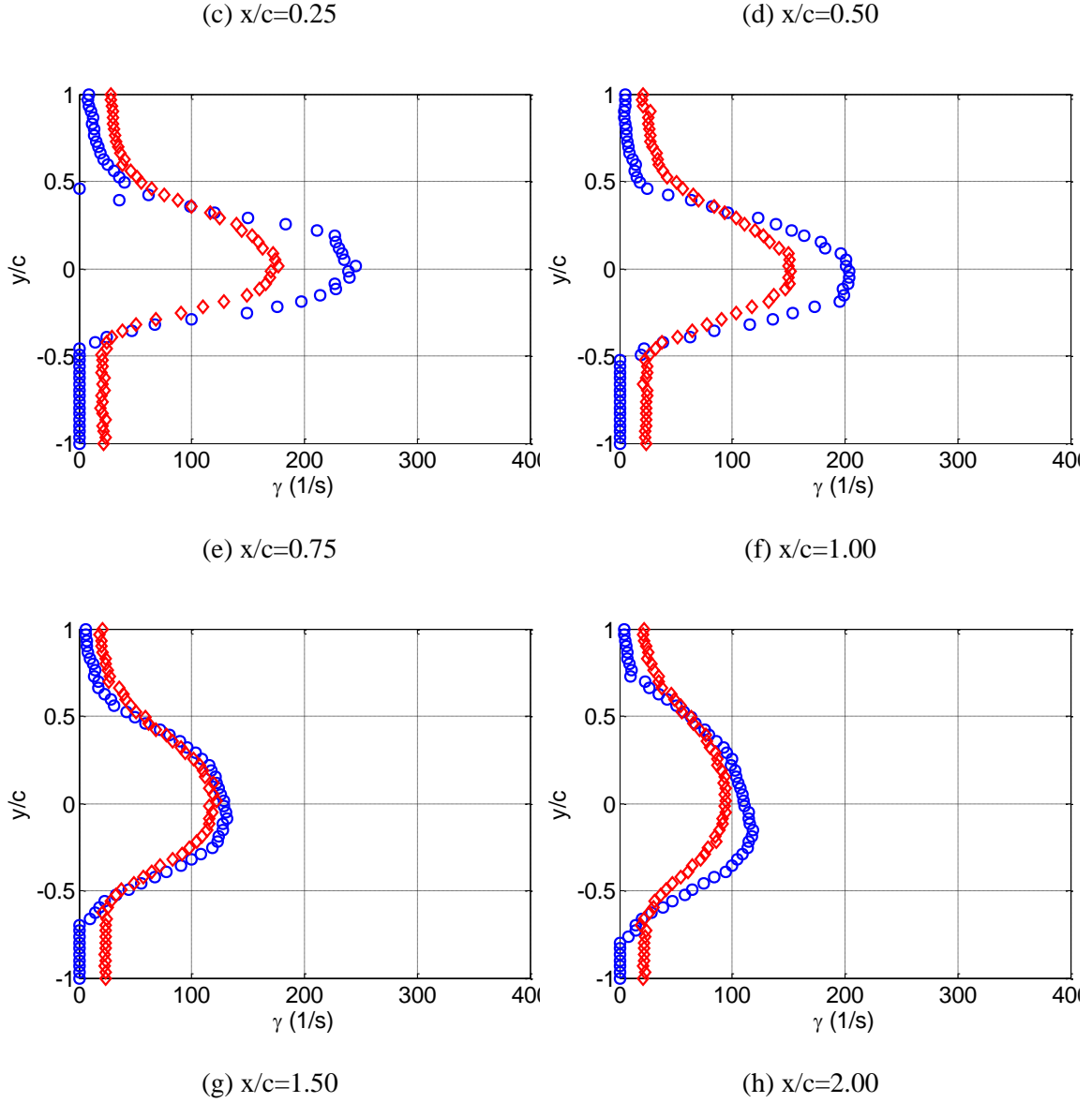


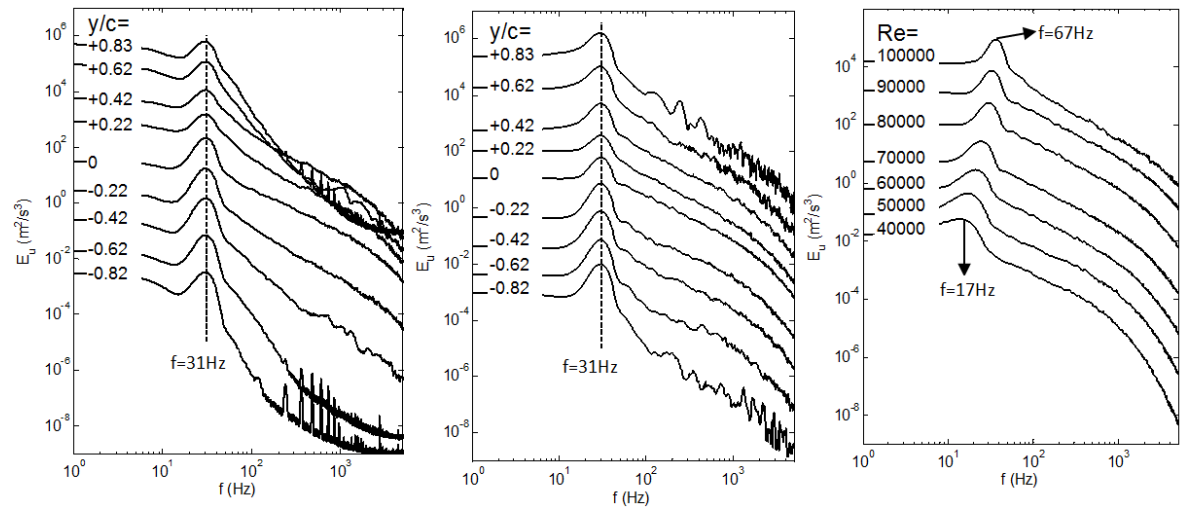
Figure 12: Effect of FST on the wake turbulence strain rate profiles; \circ : $Tu=0.5\%$, \diamond : $Tu=4.6\%$

3.3.3 Frequency analysis

From a practical viewpoint, the vortex structures behind an object can result in undesirable structural vibrations and noise generation [5]. Therefore, a good understanding of the vortex shedding phenomenon is of practical importance. Huang and Lin [7] showed that vortex structure in the wake of a NACA 0012 blade can behave similar to that of a bluff body at post-stall angles of attack, and flow separation occurs without subsequent reattachment. In such

conditions, the wake characteristics of a blade can be approximated with the wake of a cylinder, while wake structure of a cylinder has been investigated extensively in the literature [30].

Vortex shedding frequency of the VAWT blade in the present study has been deduced from turbulence energy spectrum of the streamwise velocity fluctuation component, as shown in Fig. 13. Figure 13a & 13b show the energy spectrum graphs at $x/c=0.50$ and 1.50 for nine vertical locations across the wake, for the $Tu=0.5\%$ case. The amplitude of each spectrum is stepped by two orders of magnitude with respect to the spectrum at the previous vertical location for clarity. In all vertical points of both streamwise locations, strong meaningful peaks centered at $f=31\text{ Hz}$ is clearly observable (see Figs. 13a & 13b). It should be noted that the frequency resolution of the FFT function in MatLab used in this research was 0.0381 Hz . For both Figs. 13a & 13b the peak amplitudes are larger in the wake lower part than the wake upper part. The smaller amplitudes in the upper wake may be attributed to the fact that the vortices created from the upper surface interacted with separated shear layer vortices [5], which tends to destroy the vortex shedding pattern. No energy spectrum graph corresponding to the $Tu=4.6\%$ flow case is shown here since no distinguishable peak is observed in those graphs. This implies that random interaction of FST with wake flow which tends to destroy the original vortical structure. Figure 13c shows the energy spectrum for several Reynolds numbers, for $Tu=0.5\%$, $AOA=14^\circ$ at $x/c=0.75$. The graphs correspond to the vertical locations where the turbulence *rms* velocity is maximum. At each Reynolds number a dominant peak attributed to vortex shedding occurs while that peak shifts to higher frequencies as Re increases. This trend agrees with that of Refs. [5] and [7], even though different blades have been used in [5] and [7]. More studies on other blades with different turbulence inflow conditions can be found in [31–35].



(a)

(b)

(c)

Figure 13: Energy spectrum of the streamwise velocity fluctuation component; $Tu=0.5\%$, $AOA=14^\circ$; (a) $x/c=0.50$ & $Re=80,000$, (b) $x/c=1.50$ & $Re=80,000$, (c) $x/c=0.75$ at several Reynolds numbers

3.4 Conclusion

An experimental investigation has been performed to study the effect of free-stream turbulence on the turbulence evolution of the wake of a NACA 0015 blade. Force measurements have been carried out over the range of 0 to 25 degrees angle of attack, and at a constant Reynolds number of 80,000. It has been shown that higher free-stream turbulence of $Tu=4.6\%$ improves the blade aerodynamic performance in the stall region; it delays the stall and increases the lift-to-drag ratio. A post-stall angle of attack, $AOA=14^\circ$, has been chosen for wake flow evolution study, performed by hot-wire measurements. Various flow quantities such as mean velocity, turbulence intensity, turbulence *rms* velocity and turbulence strain rate were evaluated at several wake streamwise locations.

Highly asymmetric profiles have been observed in the very near wake region accompanied by notable changes in several quantities such as mean velocity, turbulence intensity and turbulence strain rate between wake center part and free-stream area. Moving farther downstream, changes became more moderate in the wake region compared to the free-stream area, along with a gradual change to the symmetric profiles. A similarity check has been done for wake mean velocity profiles which showed the profiles follow similarity solutions if proper velocity and length scales were selected. Similarity exists in the wake profiles after the $x/c=1.00$ streamwise location quite well for both $Tu=0.5\%$ and 4.6% flow cases.

Introducing free-stream turbulence of 4.6% to the flow decreased the mean velocity deficit and turbulence intensity at all streamwise locations. While turbulence *rms* velocity and turbulence strain rate were decreased by external free-stream turbulence at locations downstream of the very near wake region. Free-stream turbulence also increases the wake thickness at locations downstream of $x/c=0.5$, contributing to the higher involvement of the wake region with free-stream area.

3.5 References

- [1]. Aslam Bhutta, M.M., Hayat, N., Farooq, A.U., Ali, Z., Jamil, Sh.R., Hussain, Z., Vertical axis wind turbine - a review of various configurations and design techniques, *Renewable and Sustainable Energy Reviews*, 2012; 16(4): 1926-1939.
- [2]. Lackner, M.A., Elkinton, C.N., An analytical framework for offshore wind farm layout optimization, *Wind Engineering*, 2007; 31(1): 17-31.
- [3]. Ivanell, S., Sørensen, J., Henningson, D, *Wind energy*, Springer, Berlin, 2007.
- [4]. Hah, C., Lakshminarayana, B., Measurement and prediction of mean velocity and turbulence structure in the near wake of an airfoil, *Journal of Fluid Mechanics*, 1982; 115: 251-282.
- [5]. Yarusevych, S., Sullivan, P.E., Kawall, J.G., On vortex shedding from an airfoil in low-reynolds-number flows, *Journal of Fluid Mechanics*, 2009; 632: 245-271.
- [6]. Farsimadan, E., Mokhtarzadeh-Dehghan, M.R., An experimental study of the turbulence quantities in the boundary layer and near-wake of an airfoil placed at upstream of a 90° bend, *Experimental Thermal and Fluid Science*, 2010; 34(8): 979-991.
- [7]. Huang, R.F., Lin, C.L., Vortex shedding and shear-layer instability of wing at low-Reynolds numbers, *AIAA Journal*, 1995; 33: 1398-1403.
- [8]. Junga, Y.W., Park, S.O., Vortex-shedding characteristics in the wake of an oscillating airfoil at low Reynolds number, *Journal of Fluids and Structures*, 2005; 20: 451-464.
- [9]. Torres-Nieves, S., Maldonado, V., Castillo, L., Meneveau, C., Kang, H.S., The role of large scales of turbulence in wind turbine blades at various angles of attack, *AIAA Theoretical Fluid Mechanics Conference*, Honolulu, Hawaii, 2011, AIAA paper, No. 2011-3613.
- [10]. Hoffmann, J.A., Effects of free-stream turbulence on the performance characteristics of an airfoil, *AIAA Journal*, 1991; 29(9): 1353-1354.
- [11]. Choi, J., Teng, S., Han, J., Ladeinde, F., Effect of free-stream turbulence on turbine blade heat transfer and pressure coefficients in low Reynolds number flows, *International Journal of Heat and Mass Transfer*, 2004; 47: 3441-3452.
- [12]. Devinant, P., Laverne, T., Hureau, J., Experimental study of wind-turbine airfoil aerodynamics in high turbulence, *Journal of Wind Engineering and Industrial Aerodynamics*, 2002; 90: 689-707.
- [13]. Amandolese, X., Szechenyi, E., Experimental study of the effect of turbulence on a section model blade oscillating in stall, *Wind Energy*, 2004; 7: 267–282.
- [14]. Cao, N., Ting, D.S-K., Cariveau, R., The performance of a high-lift airfoil in turbulent wind, *Wind Engineering*, 2011; 35(2): 179-196.
- [15]. Steelant, J., Dick, E., Modeling of laminar-turbulent transition for high freestream turbulence, *Journal of Fluids Engineering*, *Transactions of the ASME*, 2001; 123: 22-30.

- [16]. Zaki, T.A., Wissink, J.G., Rodi, W., Durbin, P.A., Direct numerical simulations of transition in a compressor cascade: the influence of free-stream turbulence, *Journal of Fluid Mechanics*, 2010; 665: 57–98.
- [17]. Zhang, Q., Lee, S.W., Ligrani, P.M., Effects of surface roughness and freestream turbulence on the wake turbulence structure of a symmetric airfoil, *Physics of Fluids*, 2004; 16(6): 2044-2053.
- [18]. Sheldahl, R.E., Klimas, P.C., Aerodynamic characteristics of seven symmetrical airfoil sections through 180-degree angle of attack for use in aerodynamic analysis of vertical axis wind turbines, Sandia National Laboratories, 1981; SAND80-2114.
- [19]. Liu, R., Ting, D.S-K., Turbulent flow downstream of a perforated plate: Sharp-edged orifice versus finite-thickness hole, *Journal of Fluids Engineering*, 2007; 129: 1164-1171.
- [20]. Streamline streamware installation and users guide, Dantec Dynamics, Denmark, 2000.
- [21]. Yavuzkurt, S., A guide to uncertainty analysis of hot-wire data, *Journal of Fluids Engineering*, Transaction of the ASME, 1984; 106: 181–186.
- [22]. Benedict, L.H., Gould, R.D., Towards better uncertainty estimates for turbulence statistics, *Experiments in Fluids*, 1996; 22: 129-136.
- [23]. Sreenivasan, K.R., Narasimha, R., Equilibrium parameters for two-dimensional turbulent wakes, *Journal of Fluids Engineering*, Transactions of the ASME, 1982; 104(2): 167-170.
- [24]. Wygnanski, I., Champagne, F., Marasli, B., On the large-scale structures in two-dimensional, small-deficit, turbulent wakes, *Journal of Fluid Mechanics*, 1986; 168: 31-71.
- [25]. Ames, F.E., Plesniak, M.W., The influence of large-scale, high intensity turbulence on vane aerodynamics losses, wake growth, and the exit turbulence parameters, *ASME Journal of Turbomachinery*, 1997; 119: 182-192.
- [26]. Honkan, A., Andreopoulos, Y., Vorticity, strain-rate and dissipation characteristics in the near-wall region of turbulent boundary layers, *Journal of Fluid Mechanics*, 1997; 350: 29-96.
- [27]. Ting, D.S-K., Checkel, M.D., The effect of mean turbulent strain rate on the flame speed of premixed, growing flames, *Journal of Engineering for Gas Turbines and Power*, 2001; 123: 175-181.
- [28]. Belmabrouk, H., Michard, M., Taylor length scale measurement by laser Doppler velocimetry, *Experiments in Fluids*, 1998; 25: 69-76.
- [29]. Segalini, A., Orlu, R., Schlatter, P., Alfredsson, P.H., Ruedi, J.D., Talamelli, A., A method to estimate turbulence intensity and transverse Taylor microscale in turbulent flows from spatially averaged hot-wire data, *Experiments in Fluids*, 2011; 51: 693-700.

- [30]. Williamson, C.H.K., Vortex dynamics in the cylinder wake, *Annual Review of Fluid Mechanics*, 1996; 28: 477-539.
- [31]. Sengupta, T.K., De, S., Gupta, K., Effect of free-stream turbulence on flow over aerofoil section at high incidence, *Journal of Fluids and Structures*, 2001; 15(5): 671-690.
- [32]. Ravi, S., Watkins, S., Watmuff, J., Massey, K., Petersen, P., Marino, M., Ravi, A., The flow over a thin airfoil subjected to elevated levels of freestream turbulence at low Reynolds numbers, *Experiments in Fluids*, 2012; 53(3): 637-653.
- [33]. Michálek, J., Monaldi, M., Arts, T., Aerodynamic Performance of a Very High Lift Low Pressure Turbine Airfoil (T106C) at Low Reynolds and High Mach Number With Effect of Free Stream Turbulence Intensity, *Journal of Turbomachinery*, 2012; 134(6): Article No. 061009.
- [34]. Ravi, S., Watkins, S., Watmuff, J., Fisher, A., Transient loads over a thin airfoil subjected to large-scale freestream turbulence, *AIAA Journal*, 2013; 51(6): 1473-1485.
- [35]. Samson, A., Sarkar, S., Effects of free-stream turbulence on transition of a separated boundary layer over the leading-edge of a constant thickness airfoil, *Journal of Fluids Engineering, Transactions of the ASME*, 2016; 138(2): Article No. 21202.

Chapter 4: An experimental study on the interaction between free-stream turbulence and a wing-tip vortex in the near-field¹

4.1 Introduction

Streamwise vortices are encountered in a wide range of practical applications of aerodynamics and hydrodynamics. A primary variant of these streamwise vortices are the trailing vortices or wing-tip vortices that roll up around the tips of finite-length lifting surfaces, such as wings and propellers [1]. These vortices, which are known to be persistent and intense, can cause many adverse effects on the near-field aerodynamics in both fixed and rotary wing applications. These include high noise, vibrations, mechanical fatigue, and erosion in aerodynamic objects such as aircraft wings, helicopter blades, propeller vanes, and wind turbine blades [2]. Whereas the formation, structure, and evolution of wingtip vortices have been extensively investigated, their interaction with external disturbances has not received much attention. Free-stream turbulence in particular, either atmospheric or introduced by other nearby objects, can highly influence these vortices. This is the topic of current study.

The process of wing tip vortex formation depends on flow conditions as well as wing geometry [3]. These include Reynolds number, angle of attack, wing boundary layer turbulence, planform shape, aspect ratio, and wing tip shape. The large number of factors affecting vortex formation makes it extremely difficult to generalize the characterization of this process. Nevertheless, the origin of a tip vortex in the flow around a lifting surface is well understood. The commonly adopted theory for the occurrence of such vortices is concerned with the spanwise pressure gradient over the wing pressure and suction surfaces that accelerates the fluid around the tip [4]. Besides, the pressure difference between the wing surfaces creates a roll up movement from the pressure surface towards the suction surface. As the vortex moves downstream of the wing, the streamwise vorticity from the wing shear layer is entrained into the vortex and a spiral shape forms around the vortex farther downstream [5].

In addition to the fundamental interest for better understanding the interaction of free-stream turbulence with trailing vortices, a stronger motivation for such a study was prompted when Sarpkaya and Daly [6] found that external turbulence can enhance the vortex decay rate [6].

¹ This work was published as: “Ahmadi-Baloutaki, M., Carriveau, R., Ting, D.S.-K., An experimental study on the interaction between free-stream turbulence and a wing-tip vortex in the near-field, *Aerospace Science and Technology*, 2015; 43: 395-405.”

This finding is of practical importance in that the trailing vortices exhibit strong stability and slow decay rates and, therefore, introducing external turbulence may have a controlling effect on such vortices [1]. Sarpkaya and Daly [6] observed an increase in the decay rate of trailing vortices generated by two NACA 0012 wings surrounded by grid turbulence in a towing tank in the range of 0.45%–3.16% turbulence intensity, and $0.12\text{--}1.16 \times 10^5$ Reynolds number. In a wind tunnel study of a vortex immersed in external turbulence, Bandyopadhyay et al. [7] studied the vortex development under two fine and coarse screens ($Tu=1.13\%$ and 1.26%), and two small and large perforated plates ($Tu=1.48\%$ and 4.85%). Using cross-wire measurement and flow visualization, they [7] characterized the interaction of external turbulence with trailing vortices as the intermittent exchange of fluids between the vortex core and free-stream region. Bandyopadhyay et al. [7] demonstrated that this exchange of fluid and momentum is controlled by organized vortical motions that wrap around the vortex just outside the core. Another wind-tunnel study of vortex interaction with external turbulence carried out by Beninati and Marshall [8] showed the turbulence is advected into the vortex core from the free-stream, which becomes entrained into the vortex core within several core lengths downstream of the vortex. This entrainment persisted up to about $x/c = 14$ axial distance, while the turbulence kinetic energy in the core seems to reach an asymptotic state which remained unchanged for streamwise locations beyond $x/c = 14$. The vortex in this study was generated using a four-blade vortex generator having NACA 0012 profile at a Reynolds number of 0.97×10^5 [8]. Heyes et al. [9] also investigated the effect of external turbulence on a trailing vortex of a NACA 0012 wing using particle image velocimetry and hot-wire anemometry. In their wind-tunnel study they investigated the flow at two Reynolds numbers of 1×10^5 and 2.2×10^5 , where the turbulence intensity in the flow with and without grid was 5% and 1%, respectively. They [9] observed that the external turbulence would noticeably affect the vortex formation and roll-up process, with negligible effect on the fully formed vortex. These findings are somewhat different from the results of Bailey et al. [10] which show slight variations in the trailing vortex formation stage under free-stream turbulence. Using hot-wire anemometry and flow visualization in their wind tunnel study on a half-span NACA 0012 wing section, Bailey et al. [10] reported higher turbulence in the vortex core in the wake far-field in the presence of grid turbulence. The flow condition of the Bailey et al.'s [10] study included a Reynolds number of 2.4×10^5 , two turbulence grid generators with turbulence intensity of 2.5% and 5%, while a boundary layer trip was used on the wing's suction surface at 10% chord location.

There are also a few numerical studies on the vortex interaction with external turbulence including the high-resolution numerical simulations carried out by Holzapfel et al. [11] who reported an enhancement of vortex decay rate with increasing external turbulence intensity. The

turbulence examined in their study ranged from 0.7% to 24%, normalized by the maximum tangential velocity of the vortex. Holzapfel et al. [11] also indicated that stretching, tilting and merging of free-stream vortices caused by the primary vortex are the prominent mechanisms in vortex evolution and decay. Another numerical study by Melander and Hussain [12] showed an increased rate of dissipation of turbulent kinetic energy in the vicinity of the secondary structures around the primary vortex. Marshall and Beninati [13] in their direct numerical simulation study found that the free-stream turbulent eddies could penetrate the vortex core and initiate the large-scale vortex instability and breakup by bending and distorting the vortex. They observed that the external turbulence wraps around the large-scale vortex and advects radially inward toward the vortex core [13].

Although there is no concrete agreement in the literature regarding the effect of free-stream turbulence on a wing tip vortex flowfield, some conclusions can be made from the common trends reported. It seems that the overall effect of the external turbulence is to increase the decay rate of the tip vortex and this effect weakens as the vortex progresses downstream. The agreement is relatively strong regarding this trend in the wake far-field. In the near-field, however, contradicting results have been reported, mainly due to the complexity of this region that includes the vortex formation process which strongly depends on numerous flow parameters as mentioned earlier. Nonetheless, the literature in this area is fairly limited. Subsequently, additional detailed experimental works may offer value. The main objective of the current study is to contribute to the understanding of external turbulence interaction with a tip vortex in this particular region. This interaction is investigated by characterizing several flowfield quantities using hot-wire anemometry in a wind tunnel experimental study. The experiments were designed in a way to provide insightful information regarding the vortex behavior in the formation and development stages under external free-stream turbulence.

4.2 Experimental setup and data measurement

4.2.1 Apparatus

The current experimental study has been carried out in a closed-circuit wind tunnel with a 0.76×0.76 m cross-section. The maximum achievable mean velocity is approximately 34 m/s in an empty working section with a background turbulence intensity of about 0.5%. It should be noted that this level of turbulence measured in the no-grid case mainly reflects the unsteadiness in the inlet conditions and should not be interpreted as real turbulence. In the presence of a grid

turbulence generator, the maximum achievable velocity is about 21 m/s. The mean velocity and turbulence intensity were nearly uniform in the core of the test section in the absence of the wing. Most of the flowfield parameters reported in this work are normalized by the corresponding free-stream velocity value for both low and high free-stream turbulence intensity levels.

A rectangular-planform NACA 0015 wing with a 0.152 m chord and 0.41 m span was used to generate the trailing vortex. This model which has a sharp tip at its free end was mounted vertically as a half-wing at the center of the lower wall of the test section as depicted in Fig. 1a. The wing was connected to a load cell outside of the wind tunnel while a custom fabricated protractor was attached to the load cell to quantify the wing angle of attack.

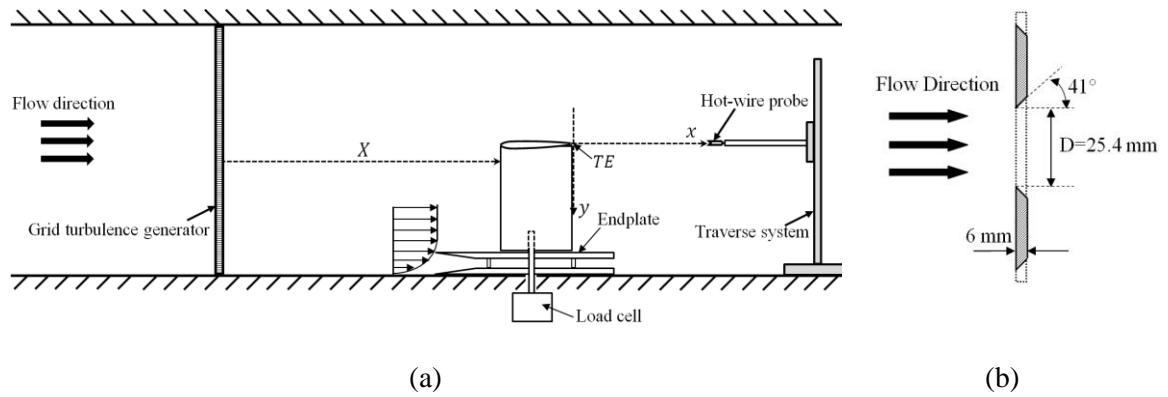


Figure 1: (a) A schematic side view of experimental fixture, (b) cross-section of the orificed perforated plate

A $0.006 \times 0.46 \times 0.46$ m Plexiglas endplate with sharp leading edges was fixed to the wind tunnel bottom wall at 35 mm height to overcome the wind tunnel boundary layer as displayed schematically in Fig. 1a. To ensure this, the thickness of boundary layer developed from the wind tunnel entrance at the leading edge of the endplate should be smaller than the endplate height [14]. The endplate height was selected to be 35 mm which is larger than the boundary layer thickness of free-stream flows with and without grid measured at the endplate's leading edge in the absence of the endplate. A small gap about 1 mm was left between the wing section and the endplate to prevent transferring of forces acting on the wing to the endplate, as well as minimizing the leakage of flow through the gap [15].

In order to generate a free-stream flow with high turbulence intensity, an orificed perforated plate was located upstream of the wing section as shown in Fig. 1a. Figure 1b displays a schematic cross-section of this perforated plate which was made of 6 mm thick Aluminum with

holes of 25 mm diameter and solidity ratio of 43%. All holes were machined with a 41° chamfer angle with the sharp-edged side facing the incoming flow to minimize the influence of the plate thickness on the generated turbulent flowfield (see Fig. 1b). The perforated plate which was spanning the entire wind tunnel section was located 0.77 m upstream of the wing section, resulted in turbulence intensity of 4.6% and integral length scale of 23 mm at the wing's leading edge section in the absence of the wing. The free-stream turbulence intensity decayed to 3.1% downstream of the wing at $x/c=1.03$. The procedures for determining the turbulence intensity and integral length scale from hot-wire measurements can be found in [16]. It has been shown that the turbulence generated downstream of the perforated plate used in this work is a quasi-isotropic turbulence as shown by Liu et al. [17] for the same wind tunnel flow parameters.

4.2.2 Instrumentation and measurement details

Aerodynamic forces acting on the wing were measured by using a six-axis force/torque sensor system of ATI industrial automation (Gamma version). The maximum and resolution of the force measuring range of this load cell were 32 N, 6.25×10^{-3} N, respectively. The load cell was aligned horizontally and vertically, and was connected to aluminum angles mounted outside the wind tunnel as depicted in Fig. 1a. The connection between the load cell and wing section was made possible via a shaft; which was inserted into a pre-drilled hole at the lateral side of the wing. This hole was drilled at 0.25 chord length from the wing leading edge; which is the location of the aerodynamic center of the NACA 0015 airfoil [18]. The supporting shaft was secured via set screws within the wing, so the blade could rotate freely and be fixed at any desired angle of attack while the load cell remained stationary. Significant care was taken to ensure that the shaft connecting the load cell to the wing was not touching the wind tunnel wall. Moreover, the exposed portion of the shaft between the endplate and wind tunnel wall was covered from airflow by a small cylinder, to mitigate aerodynamic influences on the shaft per se. The force measurements were carried out at a sampling rate of 2 kHz while 2×10^5 samples were collected at each case. The lift and drag forces were calculated by averaging the force data in the z- and x- directions, respectively. The coordinate system used in this study is presented in Fig. 2. This figure is a schematic of the wind tunnel test section after a 90° rotation to better illustrate the experimental details. As can be observed in Fig. 2, at angle of attack of 10°, the wing's trailing edge is located below the origin of the coordinate system at about $z/c=-0.13$.

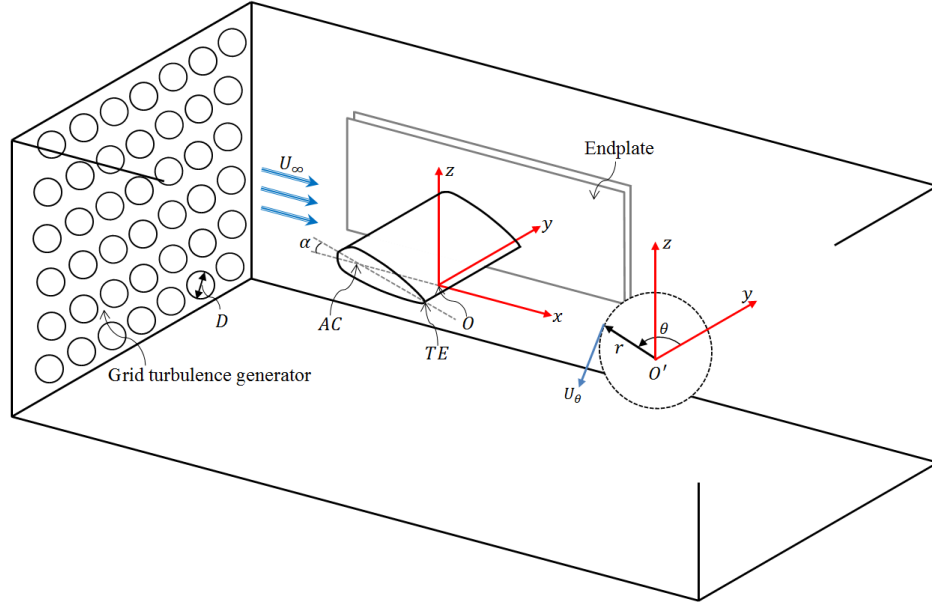


Figure 2: Sketch of the experimental arrangement in the wind tunnel test section showing the coordinate system

A DANTEC hot-wire unit operating at constant temperature mode with a X-probe hot-wire was utilized to measure the velocity field in the vortex flowfield. The probe used in this study was a Dantec 55P51 X-probe with platinum-plated tungsten wire sensor, diameter of $5\text{ }\mu\text{m}$, length of 1.25 mm , wire separation of 1 mm , and prong length of 8.4 mm . The probe was calibrated separately for velocity and angle response using the manufacturer calibration unit equipped with laboratory pressurized air. The calibration drift may occur because of several factors as described in [19], where changes in flow temperature and particle contamination on the wire are believed to have the most contribution. The effects of the ambient temperature drift were taken into account using the correction of Bearman [19]. Regarding the other error sources, two calibration sets were carried out at the beginning and the end of each experiment with the same known velocities. The change in the calibration results was less than 0.1% which was an indication of low error in the calibration process. The hot-wire signals were sampled at 80 kHz and were recorded on a PC through a 12-bit resolution A/D converter board, while 10^6 samples were taken at each point. In other words, the results are time-averaged values over 12.5 seconds sampling period. The analog voltage signal was first low-passed at 30 kHz using an analog filter to remove noise and to prevent higher frequencies from folding back (anti-aliasing).

The two-stage calibration procedure for velocity and angle is described in Ref. [20], while more detailed information can be found in Refs. [21,22]. The velocity calibration was done by exposing the probe to a set of known velocities created by the pressurized air exiting from the calibration unit's nozzle. The calibration curve fit used to convert the voltage to velocity values was a 4th degree polynomial. The yaw angle calibration was carried out by positioning the probe at a set of yaw angles using the rotating holder. The yaw factor for each wire is then determined over a range of yaw angles. Using calibration velocity and yaw factor obtained for both wires, the effective cooling velocities can then be determined for each wire.

The hot-wire measurement in this study were conducted at a constant Reynolds number of 1.6×10^5 based on the wing chord length and an angle of attack of 10° . This particular angle of attack was selected in the current study since the NACA 0015 wing has very high (near maximum) aerodynamic efficiency in terms of lift-to-drag ratio at this angle of attack. The measurement planes which were perpendicular to the free-stream velocity vector were located downstream of the wing trailing edge at four streamwise locations of $x/c=0.1, 0.42, 0.77$ and 1.03 . Each measurement plane consists of 21×21 grid points covering a range of $-0.1 < y/c < 0.23$ and $-0.26 < y/c < 0.07$ where grid increments in both y and z directions were 2.5 mm. Probe traversing was achieved through an automated traverse system, SmartMotor of Animatics corporation, with a position resolution of $2.5 \mu\text{m}$. In order to measure three components of velocity field, the "rotating X-probe" method proposed by Le Huu Nho and Beguier [23] was used. This method includes conducting two separate sets of hot-wire measurements at each point by placing the probe at horizontal and vertical planes crossing that measurement point. At each set of measurement, the effective cooling velocity for each wire was determined using the wire calibration velocity and yaw factor as described earlier. This results in four correlated effective cooling velocities measured by two wires at two measurement sets. These effective cooling velocities, then, formed a system of equations to determine the three components of the velocity vector. This system of equations along with a guide to its solution procedure can be found in Ref. [23].

4.2.3 Uncertainty

The procedure described by Refs. [24,25] together were used with the instrumentation manuals to determine the uncertainty in several parameters reported in this study. The uncertainty in lift and drag coefficients has been estimated to be less than 13% and 16%, respectively, while the uncertainty in angle of attack was around 0.5° . The maximum uncertainty in time-averaged

velocity components measured by the hot-wire anemometer was determined to be about 3% for U , 9.2% for V , and 9.5% W . Moreover, the uncertainty in circumferential velocity, U_θ , was estimated to be less than 13% for all flow cases studied. The uncertainty in the location of the hot-wire probe was estimated to be about 2 mm including the uncertainty in the position of the probe's holder and uncertainty in the measured distance by the automated motor used to traverse the probe [16].

In addition to the uncertainty discussed, there is another source of error in measuring the tip vortices, known by vortex wandering. This phenomenon is the lateral movement of the vortex core which may be self-induced or a consequence of free-stream unsteadiness [26,27]. There are a few methods to quantify the vortex wandering amplitude including an experimental method proposed by Chow et al. [28], and an analytical approach proposed by Devenport et al. [27]. In this research, however, no correction has been applied for wandering effects as the present measurements were performed in the wake near-field, $x/c < 1$. According to many researchers [26-28], the effect of vortex wandering is negligible in this region.

4.3 Results and discussion

4.3.1 Aerodynamic loads

Lift and drag coefficients which have been determined from the following equations [18] are plotted in Figs. 3 and 4 for the low and high free-stream turbulence cases, respectively.

$$C_L = \frac{F_L}{0.5\rho AU_\infty^2} \quad (1)$$

$$C_D = \frac{F_D}{0.5\rho AU_\infty^2} \quad (2)$$

In Eqs. 1 and 2, F_L and F_D are the time-averaged values of lift and drag forces measured by the load cell, ρ is the fluid density, and A is the wing planform area. The blockage ratio for the configuration used in the current work is determined to be 1.7% and 4.7%, for the two low and high limits of angle of attack range studied, 0° and 25° , respectively. The literature suggests that for blockage ratios less than 7.5%, no correction is needed [18]. Therefore, the tunnel blockage has not been discussed further in this paper. Figure 3 shows the lift and drag coefficients of the wing section for the no-grid case at a Reynolds number of 1.6×10^5 . The results of two dimensional testing (infinite aspect ratio) by Sheldahl and Klimas [29] for a wing having the same NACA 0015 airfoil profile at the same Reynolds number have also been plotted in Fig. 3 for

comparison purposes. In this regard, the Lanchester-Prandtl wing theory relates the angles of attack and drag coefficients as functions of aspect ratio at constant lift coefficients for wings with an elliptic lift distribution via the following expressions [30]

$$\alpha = \alpha_{\infty} + \frac{C_L}{\pi AR} \quad (3)$$

$$C_D = C_{D_{\infty}} + \frac{C_L^2}{\pi AR} \quad (4)$$

$$C_L = \frac{C_{L_{\infty}}}{1 + \frac{a_0}{\pi AR}} \quad (5)$$

where subscript ∞ denotes a wing with infinite aspect ratio. In order to compare the current results with theoretical results, the aerodynamic coefficients of a finite wing having $AR = 5.4$ were determined using Eqn. 3 to 5 from 2D data of Ref. [29]. The theoretical results obtained by these equations have also been plotted in Fig. 3 within the validity range of the Lanchester-Prandtl wing theory; which is the linear region of the lift curve [30]. Figure 3 shows that the agreement between current and theoretical results is quite fair, even though these theoretical correlations are for wings with an elliptic lift distribution.

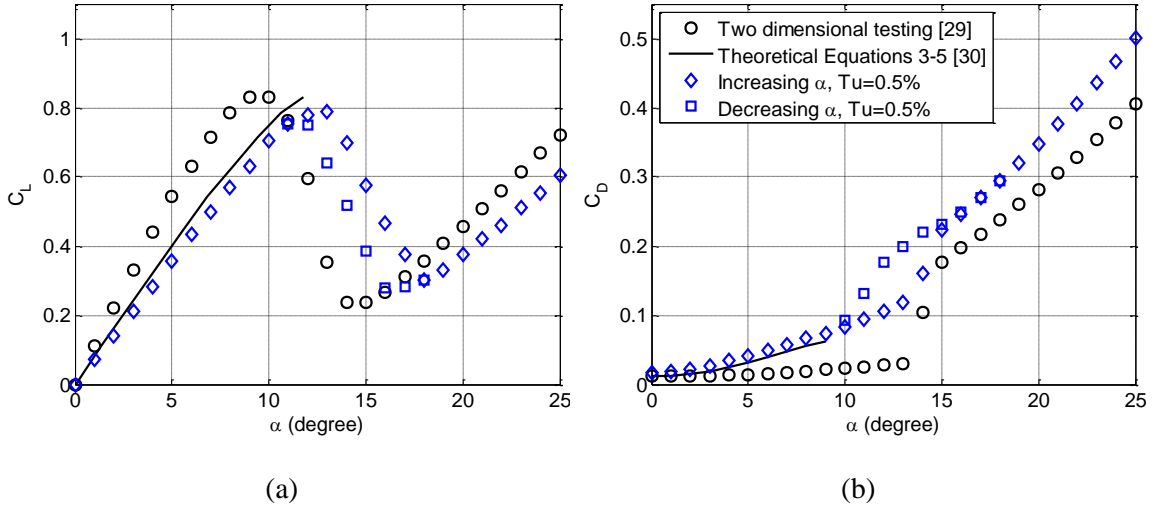


Figure 3: Aerodynamic coefficients of the NACA 0015 wing with $AR=5.4$ at $Re=1.6 \times 10^5$, (a) lift, (b) drag

As can be observed from Fig. 3, the wing section has higher lift and lower drag at 2D flow scenario for most angles of attack, mainly due to the losses in the wing tip regions for a finite span wing section. Moreover, the slope of the lift curve is slightly smaller for the finite

wing section than that of a 2D airfoil. Figure 3a also shows that for the flow around the finite wing section, the static stall occurs at a higher angle of attack while the stall region becomes wider. The drag coefficients for a finite wing section have higher values due to the 3D losses in the tip regions as can also be observed in Fig. 3b. Moreover, the dramatic increase in drag due to the static stall takes place at a higher angle of attack for flow around the finite wing section compared to a 2D airfoil. Beyond the static stall, the changes in force coefficients are more moderate, even though the flow is entirely stalled on the wing suction surface [31].

Figure 4 shows the aerodynamic coefficients of the wing section studied under two levels of free-stream turbulence. It should be noted that in all of the experiments in the current research no boundary layer trip was used on the wing surface. As can be observed in Fig. 4a, higher free-stream turbulence increases the lift coefficient for attached, stall, and post-stall regions of the lift curve. Moreover, the linear region of lift curve becomes broader under higher free-stream turbulence as the slope of this curve remains almost unchanged as also reported in Refs. [31-33]. This external turbulence would delay the static stall and consequently postpone the flow separation [33]. This can be attributed to the postulation that the bypass transition of the wing boundary layer occurred due to the effect of external free-stream turbulence. The bypass transition is a process at which a laminar boundary layer rapidly breakdowns to turbulence due to the exposure to moderate levels of free-stream turbulence. The newly turbulent boundary layer formed on the wing surfaces has higher resistance against flow separation due to the larger momentum of the fluid particles near the wall. Figure 4a also shows that the free-stream turbulence widens the stall region while the slope of decreasing lift becomes milder. The latter is a finding that we have not uncovered in the literature thus far.

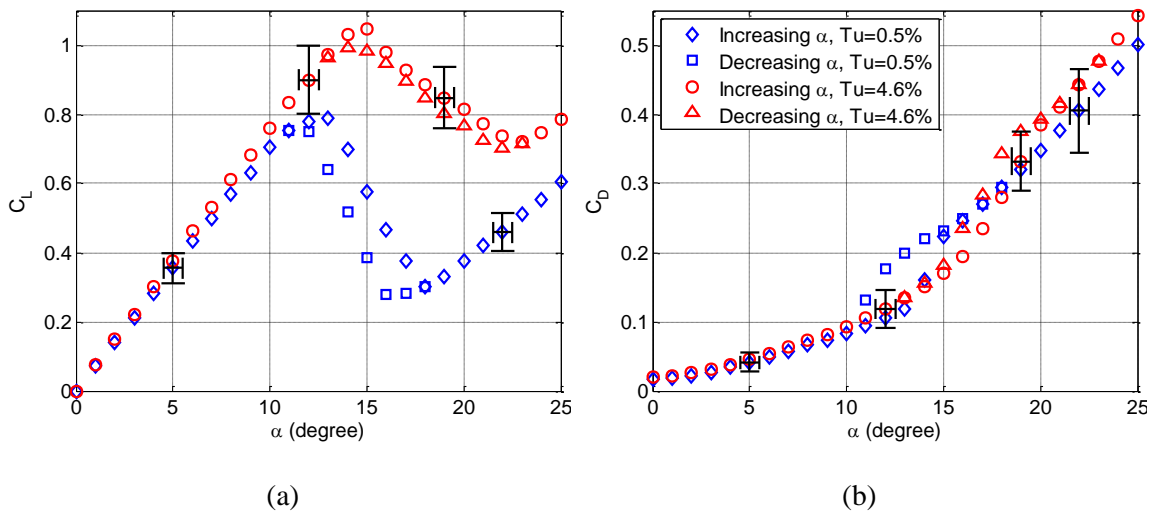
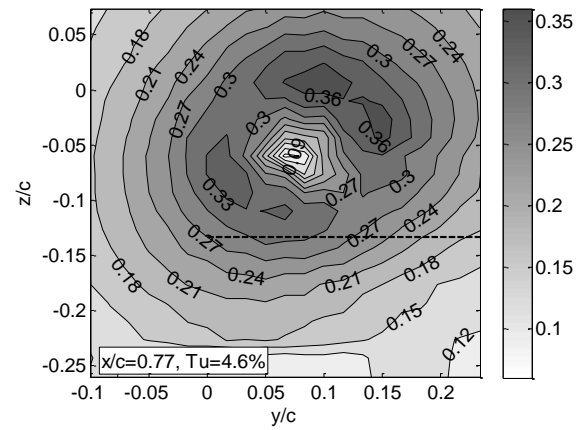
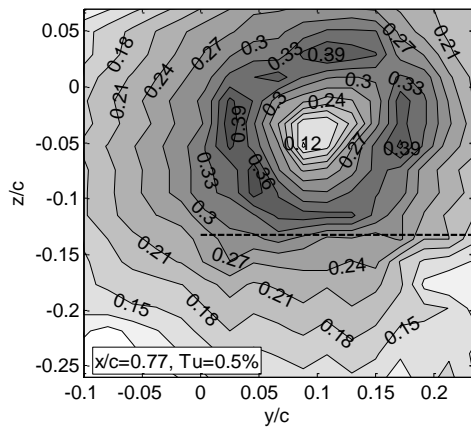
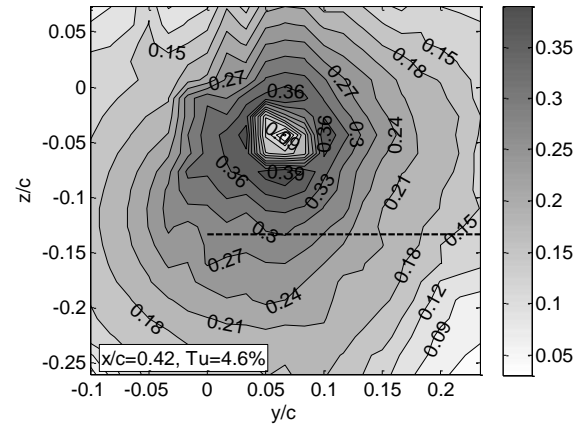
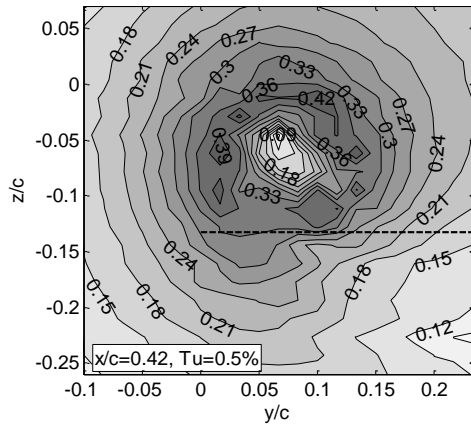
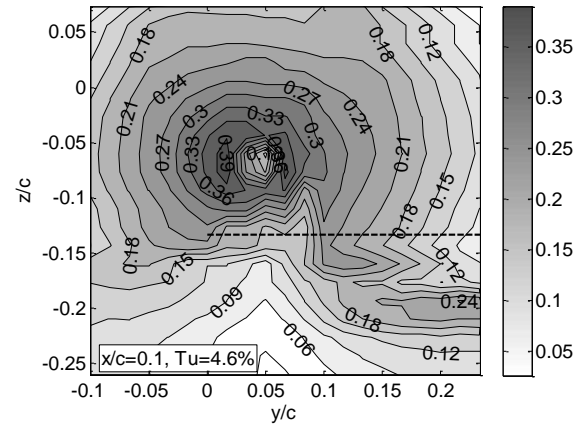
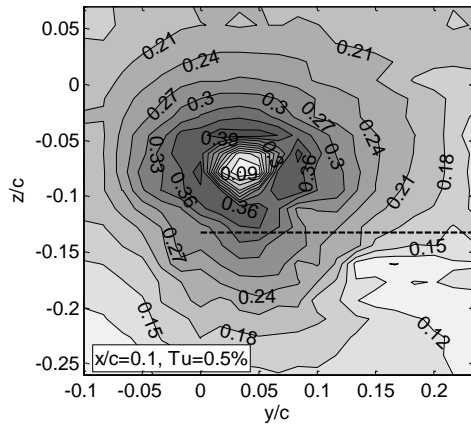


Figure 4: Effect of free-stream turbulence on the wing aerodynamic coefficients at $Re=1.6 \times 10^5$,
(a) lift, (b) drag

The effect of free-stream turbulence on the wing drag is an overall increase throughout the whole range of angles of attack except a small portion of the stall region as can be seen in Fig. 4b. The increase in drag coefficient under free-stream turbulence is very small in the linear region of the lift curve, while it is more notable in the post-stall region. This increase in drag is presumably due to the higher shear stress which exist in the turbulent boundary layer formed over the wing surfaces in $Tu=4.6\%$ case [31]. Another interesting point observed in both Fig. 4a and 4b is the significant moderation of the hysteresis phenomenon under external free-stream turbulence which is in agreement with results of Hoffmann [33].

4.3.2 Mean velocity data

Out of several mean flow parameters measured in this work, the crossflow velocity and circumferential velocity are analysed in this section in more detail as it is believed to be the best tool to study the axial development of the tip vortex. The normalized crossflow velocity contours, defined as the resultant of the V and W components of the time-averaged velocity vector, $U_{cf} = \sqrt{V^2 + W^2}$, are presented in Fig. 5, where the straight dashed line at $z/c=-0.13$ in these graphs represent the location of the wing's trailing edge, looking upstream. The vortex structure is well captured at $x/c=0.77$ and 1.03 while there is some deviation from a typical vortex pattern in the locations near the wing's trailing edge especially at $x/c=0.1$. For both free-stream turbulence cases shown in Fig. 5, the vortex area increases as the measurement planes progress downstream. This increasing diffusion of the vortex was explained by Chow et al. [28], who attributed this to the fact that the tip vortex gains strength from the feeding sheet of boundary layer vorticity. Moreover, the crossflow velocity appears to be nearly axi-symmetric near the vortex center especially at $x/c=0.77$ and 1.03 while the asymmetry becomes more pronounced with increasing radial distance from the vortex center. Figure 5 also shows that the free-stream turbulence tends to increase the vortex diffusion which is more evident at $x/c=0.77$ and 1.03 while less recognizable at $x/c=0.1$ and 0.42 .



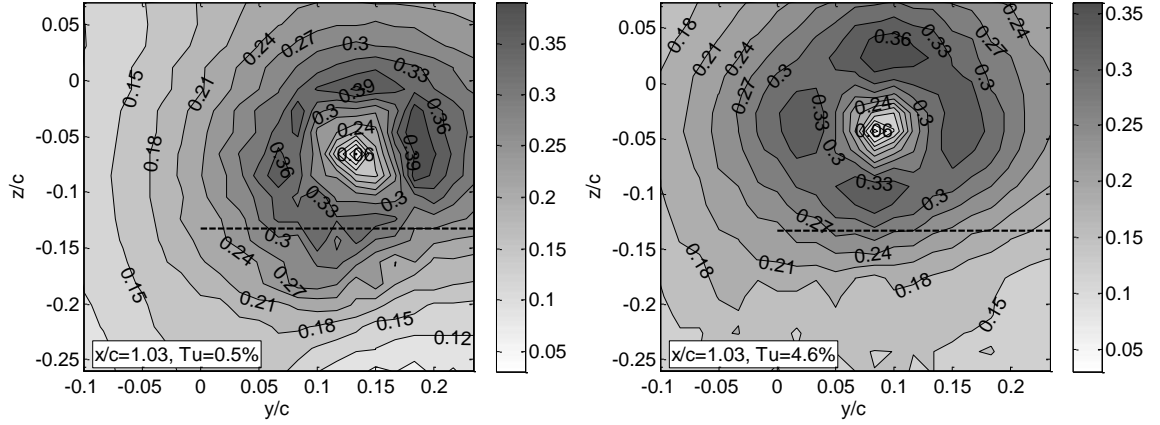


Figure 5: Contours of crossflow velocity normalized by the free-stream velocity for $Tu=0.5\%$ and 4.6% at four streamwise measurement planes

Another important mean flow parameter in the vortex flowfields is circumferential velocity, which is determined from relation below in the cylindrical coordinates depicted in Fig. 2.

$$U_{\theta} = V \sin \theta - W \cos \theta \quad (6)$$

Figure 6 shows the radial profiles of circumferential velocity for $Tu=0.5\%$ and 4.6% cases. The circumferential radial profiles in Fig. 6 were estimated by fitting concentric circles to the iso-contours of the magnitude of the circumferential velocity using a MatLab function. This function uses a series of points having coordinates of z and y and same U_{θ} , and returns a fitted circle into these points. The output of this function is the center and radius of this circle for each U_{θ} iso-contour. The circles having the lowest errors in this fitting process were used in this research. All profiles have a distinct peak located at some radial distance from the vortex center. This distance is known as the vortex core radius in the literature. The approach proposed by Iversen et al. [34] was used to find the location at which $U_{\theta} = 0$. This so-called linear method is based on the assumption of the circumferential velocity has a linear profile in the vortex core. The locus of $U_{\theta} = 0$ is where a change in the sign of U_{θ} occurs. In fact, this should be done in two steps for V and W to find their sign-changing locations, resulting in the y and z locations of $V=0$ and $W=0$. After determining the vortex center, the r and θ at each measurement point can be easily estimated according to their definitions depicted in Fig. 2.

As can be observed in Fig. 6a, the circumferential velocity curves for the no-grid case are very close to each other and no clear trend can be deduced with respect to the streamwise

distance, except at $x/c=0.1$ with slightly higher peak at somewhat shorter radial distance. This is in agreement with results of Chow et al. [28] and Birch and Lee [26] who reported the variation in the peak circumferential velocity and core radius of the vortex were negligible with increasing streamwise location downstream of the wing for a no-grid flow case. On the other hand, the circumferential velocity profiles for the $Tu=4.6\%$ case demonstrate an increasing trend with respect to the streamwise distance at radial locations far from the vortex center, while the peak velocity decreased slightly and moved to larger radial positions (see Fig. 6b). These trends were also reported by Bailey et al. [10] under several external free-stream turbulence levels they studied, even though their measurement planes were in the range of $x/c > 1$.

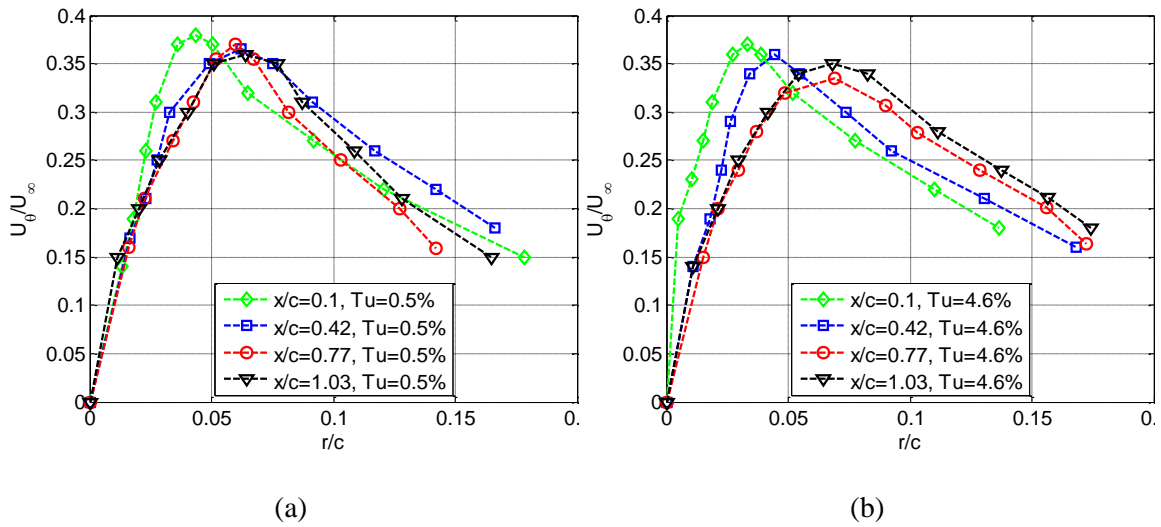


Figure 6: The effect of free-stream turbulence on circumferential velocity variations (a) $Tu=0.5\%$, (b) $Tu=4.6\%$

For comparative purposes, the circumferential velocity profiles have been examined according to the analytical solution proposed by Phillips [35] in Fig. 7. Phillips [35] suggested that the circumferential velocity profiles in the cores of wing-tip vortices tend to be self-similar if normalized by the peak velocity, $U_{\theta,max}$, and the peak radius, $r_{\theta,max}$, as the following

$$\frac{U_{\theta}}{U_{\theta,max}} = \frac{1}{0.716\left(\frac{r}{r_{\theta,max}}\right)} \left(1 - \exp\left(-1.2526\left(\frac{r}{r_{\theta,max}}\right)^2\right) \right) \quad (7)$$

The circumferential velocity profiles are expected to follow this curve fit for non-turbulent free-stream flow in the range of $r/r_{\theta,max} < 1.2$ as explained by Phillips [35]. Figure 7 shows that the circumferential velocity profiles in the current trailing vortex study are self-similar

not only for the no-grid case, but also for the turbulent free-stream flow. The collapse of data is fairly consistent within the validity range of Eq. 7, but the scatter increases when moving outside of this range.

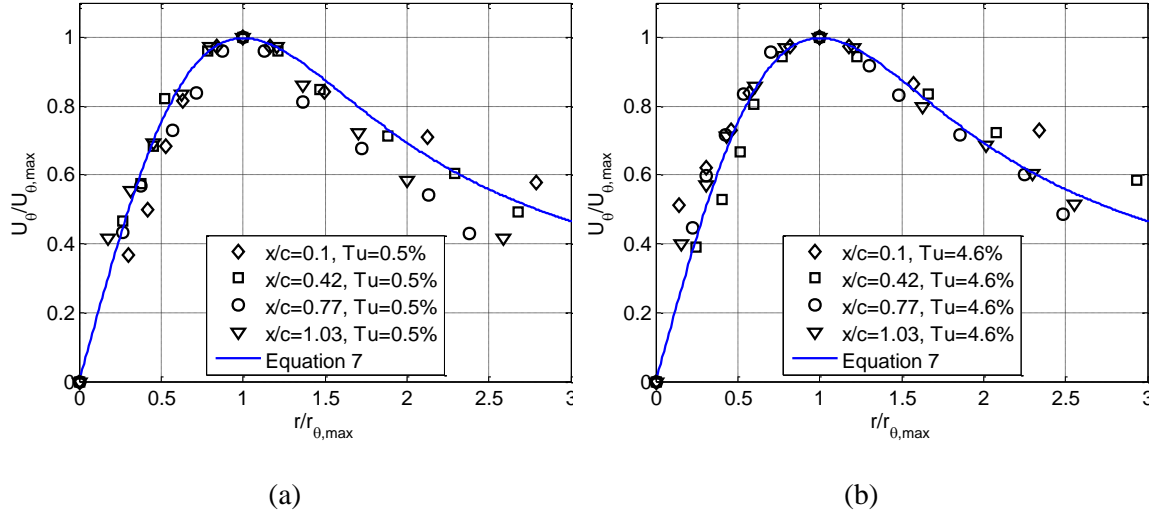


Figure 7: Comparison of circumferential velocity with analytical solution (a) $Tu=0.5\%$, (b) $Tu=4.6\%$

4.3.3 Vortex trajectory

In the current study the center location of a tip vortex was identified as the location of minimum circumferential velocity at each measurement plane. This approximation procedure has been adopted from other works in the literature on trailing vortices [10,28,36,37]. The uncertainty in the location of vortex center depends on a few factors including the accuracy of traverse system to move the hot-wire probe, numerical procedure used to estimate the vortex center, and the effect of vortex wandering. The uncertainty in the location of vortex center was estimated to be less than 3 mm considering the accuracy of traverse system and error in the numerical procedure used to estimate the vortex center. As mentioned earlier, no correction was used to quantify the effects of vortex wandering as the current measurements were performed in the wake near-field region.

Figure 8 shows the movement of vortex center with increasing streamwise location downstream of the wing. Also plotted in Fig. 8 are the results of two other experimental works [26,37] on the same NACA 0015 wing at $\alpha=10^\circ$ but somewhat higher Reynolds numbers. The spanwise movement of the vortex has a monotonic trend towards the wing center as demonstrated

in Fig. 8a. On the other hand, Fig. 8b shows the movement of the vortex in the direction of lift which does not show a definite pattern, even though the vortex moves generally in an upward direction. It should also be noted that the vortex center stays at a higher position from the tip of the wing at all streamwise locations, considering that the wing tip is located at $z/c = -0.13$ when $\alpha = 10^\circ$. This inboard and upward motion of the tip vortex can be attributed to the continuing roll-up of the shear layer arriving from the inboard regions [37]. This roll-up process causes spanwise vorticity to be rotated into the axial direction and added to the outer layer of the tip vortex. Figure 8 also shows that the vortex trajectory was not significantly affected by the introduction of free-stream turbulence; which is in agreement with results of Bailey et al. [10].

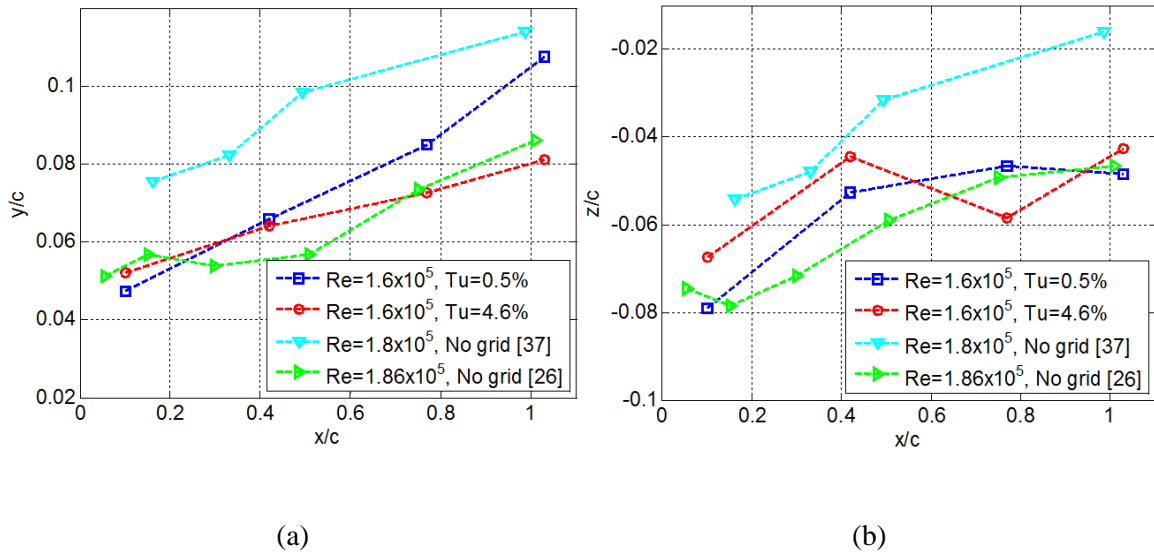
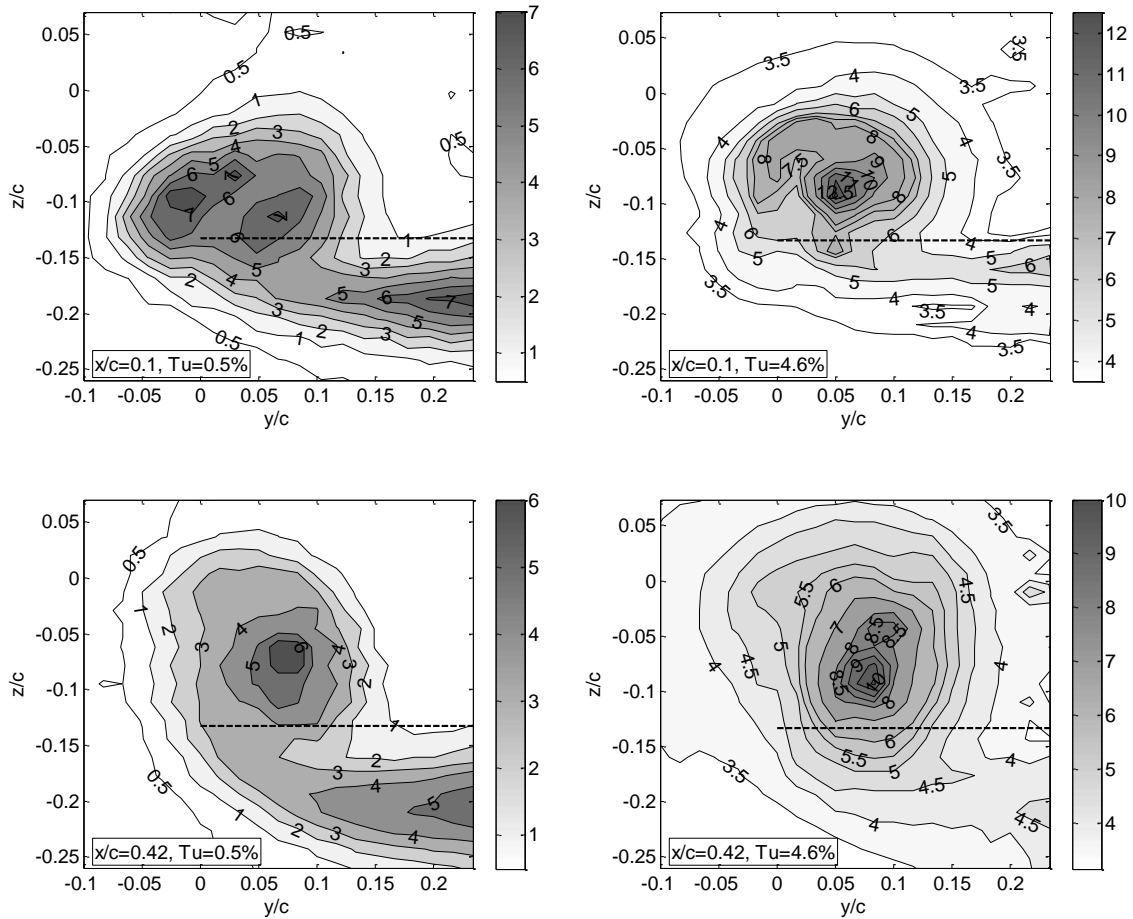


Figure 8: Location of vortex center vs. streamwise distance in (a) the spanwise direction, (b) the lift direction

4.3.4 Turbulence intensity

Figure 9 shows the contours of streamwise turbulence intensity, defined as the percentage ratio of rms velocity fluctuation to the free-stream velocity. The so-called spiral pattern existing in tip vortex flowfields is evident in all graphs of Fig. 9. This spiral consists of a circular-like shape around the vortex core containing the maximum turbulence intensity region and a tail along the wing's trailing edge with concentrated turbulence intensity. Devenport et al. [27] attributed the high variation in turbulence intensity at the tail of the spiral to the merging of shear layers on lower and upper surfaces of the wing. In the very near wake, namely at $x/c=0.1$ section, it seems the vortex is still in the formation process where small secondary vortices are observed in the

vortex core. These secondary vortices that may have origins from either the tip roll-up movement or the boundary layer vorticity tube, tend to merge together and form the so-called trailing vortex [26]. For both free-stream turbulence levels, the turbulence intensity contours surrounding the vortex core display an asymmetric pattern while the asymmetry decreased with increasing downstream distance (see Fig. 9). Another observation from Fig. 9 is that the external free-stream turbulence increases the turbulence intensity peak inside the vortex core. As can also be observed in Fig. 9, the spiral shape of the vortex is almost fully-formed in all streamwise locations for $Tu=0.5\%$ case, while this shape is being gradually distorted for $Tu=4.6\%$ case as the streamwise distance increases. This can be deduced from the observation that the so-called tail of the vortex disappears into the relatively higher free-stream turbulence, even though the vortex core remains clearly visible. This may be attributed to the tendency of free-stream turbulence eddies to breakdown the tip vortex structure as explained by Marshall and Beninati [13]. However, this is not certain as this phenomenon can be also correlated to the vortex wandering.



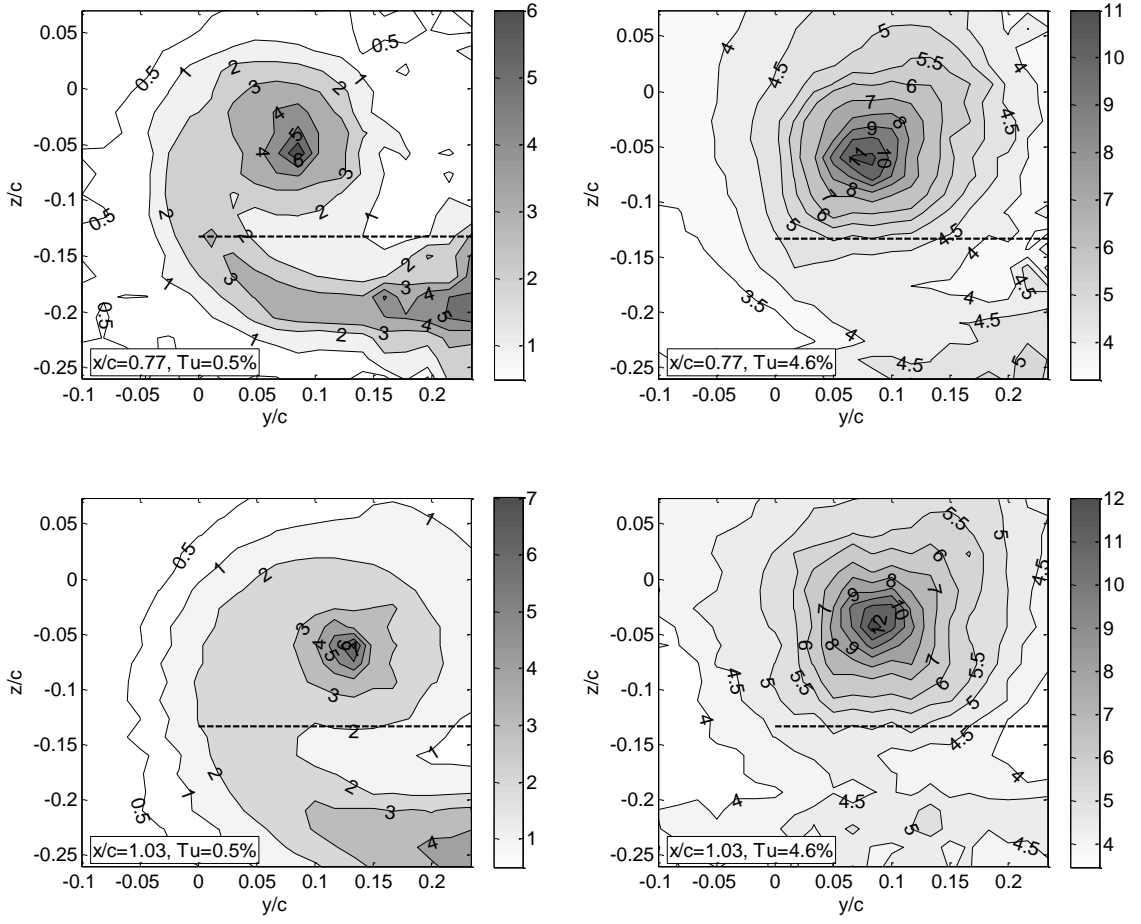


Figure 9: Contours of streamwise turbulence intensity for $Tu=0.5\%$ and 4.6% at four measurement planes

4.3.5 Circulation

The mean circulation as a function of radial distance was determined using the line integral expressed by Eq. 8 while the integration has been calculated numerically using trapezoidal rule. Furthermore, the circulation values have been normalized by the wing base circulation, Γ_0 , which is determined from Eq. 9.

$$\bar{\Gamma}(r) = \oint \bar{U}_\theta(r) \cdot r d\theta \quad (8)$$

$$\Gamma_0 = \frac{1}{2} C_L U_\infty c \quad (9)$$

Normalized circulation profiles for both free-stream turbulence levels have been plotted in Fig. 10. Figure 10 shows that the radial circulation remains essentially unchanged within the

vortex core as the vortex evolves downstream for both free-stream turbulence cases. As the radial distance increases, however, the mean circulation changes in a non-consistent way for $Tu=0.5\%$ case, while notably increases with increasing streamwise distance for $Tu=4.6\%$ case.

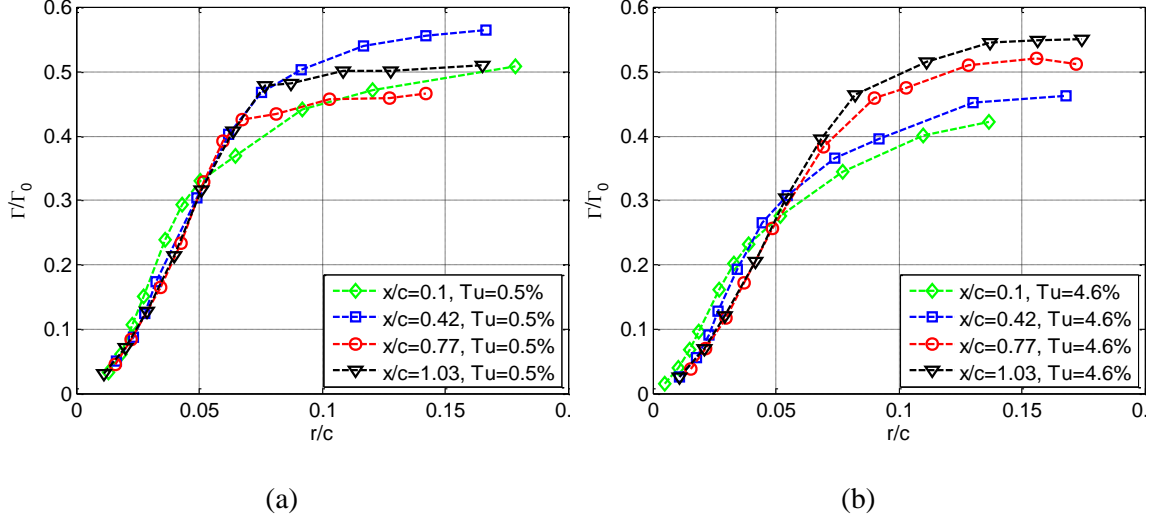


Figure 10: The effect of free-stream turbulence on the circulation within the vortex (a) $Tu=0.5\%$,
(b) $Tu=4.6\%$

To examine the asymptotic behavior of the trailing vortex studied in this work the method first proposed by Hofmann and Joubert [38] and then by Philips [35] is utilized here. This method describes a turbulent vortex, based on the analogy with the turbulent boundary layers theory [35,38]. According to this method, the vortex becomes approximately self-similar with three distinct regions as the radial distance increases from the vortex center: the vortex core, the logarithmic region and a defect region. The circulation data is first normalized by the circulation value at $r_{\theta,max}$, and then fitted separately into the three regions with the following expressions in a semi-logarithmic plot.

$$\frac{\Gamma}{\Gamma_{\theta,max}} = A \left(\frac{r}{r_{\theta,max}} \right)^2 \quad (10)$$

$$\frac{\Gamma}{\Gamma_{\theta,max}} = B \ln \left(\frac{r}{r_{\theta,max}} \right) + C \quad (11)$$

$$\left(1 - \frac{\Gamma}{\Gamma_{\theta,max}} \right) = D \left(\frac{r}{r_{\theta,max}} \right) + E \quad (12)$$

The fitting coefficients A to E depend on several parameters including the wing configuration, Reynolds number, downstream measurement location and turbulence characteristics of the vortex flowfield. The fitting was started from the logarithmic region. This was done by finding the best line fitted to the data points in the validity range of Eq. 11, which is $0.5 < r/r_{\theta, max} < 1.4$. Consequently, the end of the core region and the beginning of the defect region are determined once the limits of the logarithmic region are fixed. The next steps would be the fitting of Eqs. 10 and 12 to the corresponding data points in the core and defect regions, separately. The fitted coefficients of the current data are presented in Table 1, while the fitted curves are presented in Fig. 11 only for two measurement planes due to space limitations. The coefficients of the current work are comparable with the coefficients of Birch and Lee [26] who reported $A = 1.65$, $B = 2.14$, $C = 1$, and also coefficients of Ramaprian and Zheng [37] who reported $A = 1.74$, $B = 2.14$, $C = 1$. It should be noted that no fitting coefficients were reported for the defect region in these two studies, possibly due to deviation of the experimental data from analytical solutions. This deviation is observed in the current study too, as experimental data do not collapse well onto the fitted curves in the defect region. In fact, it was found by Phillips [35] that the experimental results are nearly self-similar in the core and logarithmic regions, while the self-similarity of experimental data in the defect region highly depends upon the conditions occurring during vortex formation.

Table 1: Fitted coefficients of the current data using analytical expressions, Eqs. 10-12

Tu (%)	x/c	A	B	C	D	E
0.5	0.1	1.84	2.42	0.94	-0.18	0.13
	0.42	1.92	2.13	0.92	-0.14	0.14
	0.77	1.49	2.23	0.93	-0.07	0.06
	1.03	1.57	2.12	0.89	-0.04	0.04
4.6	0.1	1.62	2.24	0.94	-0.28	0.26
	0.42	1.78	2.27	0.91	-0.19	0.16
	0.77	1.70	2.04	0.89	-0.11	0.12
	1.03	1.55	2.26	0.92	-0.14	0.14

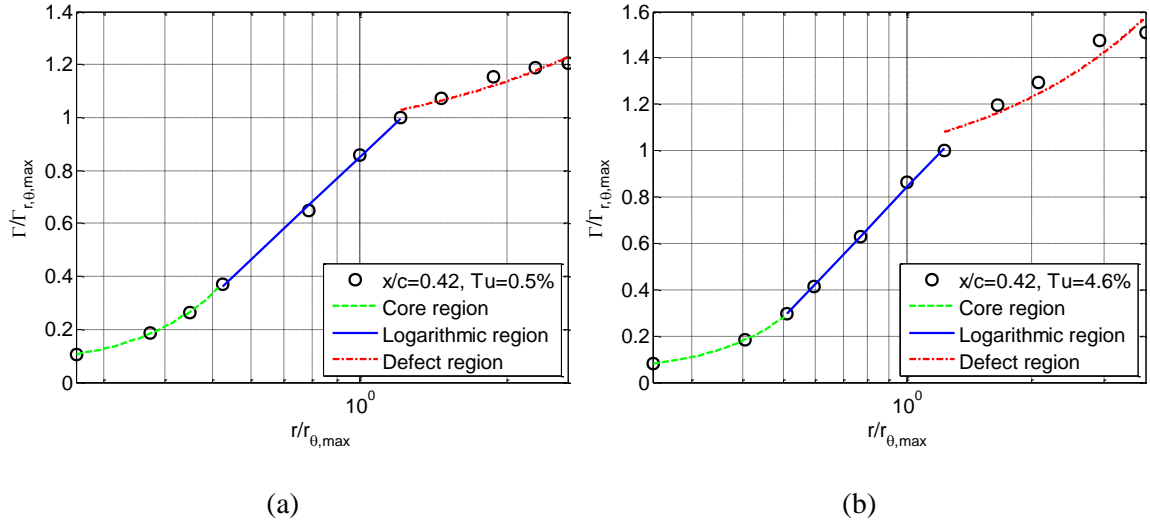


Figure 11: Comparison of the circulation data with analytical solution of Eqs. 10-11 at $x/c=0.42$
(a) $Tu=0.5\%$, (b) $Tu=4.6\%$

4.4 Conclusion

The interaction of external free-stream turbulence with a wing-tip vortex has been studied experimentally. Load cell and hot-wire measurements were conducted for a flow over a NACA 0015 wing section at a Reynolds number of 1.6×10^5 and an angle of attack of 10° at two levels of free-stream turbulence of 0.5% and 4.6%, without and with a grid turbulence generator, respectively. The free-stream turbulence significantly altered the wing aerodynamic coefficients by delaying static stall, enhancing lift, and increasing drag. The tip vortex downstream of the wing has been captured with good accuracy through measurement of the velocity field using hot-wire anemometry. The crossflow velocity contours show that the free-stream turbulence tends to increase the vortex diffusion especially at $x/c=0.77$ and 1.03 . The free-stream turbulence does not notably affect the vortex trajectory along the streamwise axis, while increases the turbulence intensity peak. The circumferential velocity and vortex circulation were also increased under external turbulence with increasing streamwise distance at radial locations away from the vortex center.

4.5 References

- [1]. Bailey, S.C.C., Tavoularis, S., Measurements of the velocity field of a wing-tip vortex, wandering in grid turbulence, *Journal of Fluid Mechanics*, 2008; 601: 281–315.
- [2]. Heyes, A.L., Smith, D.A.R., Modification of a wing tip vortex by vortex generators, *Aerospace Science and Technology*, 2005; 9: 469–475.
- [3]. Giuni, M., Green, R.B., Vortex formation on squared and rounded tip, *Aerospace Science and Technology*, 2013; 29(1): 191–199.
- [4]. Sohn, M.H., Chang, J.W., Visualization and PIV study of wing-tip vortices for three different tip configurations, *Aerospace Science and Technology*, 2012; 16: 40–46.
- [5]. Das, A., Wichmann, G., On the physics and kinematics of vortex motion in the downstream of a high aspect ratio wing with high-lift devices, *Aerospace Science and Technology*, 2004; 8: 489–498.
- [6]. Sarpkaya, T., Daly, J.J., Effect of ambient turbulence on trailing vortices. *Journal of Aircraft*, 1987; 24: 399–404.
- [7]. Bandyopadhyay, P.R., Stead, D.J., Ash, R.L., Organized nature of a turbulent trailing vortex, *AIAA Journal*, 1991; 29: 1627–1633.
- [8]. Beninati, M.L., Marshall, J.S., An experimental study of the effect of free-stream turbulence on a trailing vortex, *Experiment in Fluids*, 2005; 38: 244–257.
- [9]. Heyes, A.L., Jones, R.F., Smith, D.A.R., Wandering of wing-tip vortices, *Proceedings of 12th International Symposium on the Applications of Laser Techniques to Fluid Mechanics*, Lisbon, Portugal, 2004.
- [10]. Bailey, S.C.C., Tavoularis, S., Lee, B.H.K., Effects of freestream turbulence on wing-tip vortex formation and near-field, *Journal of Aircraft*, 2006; 43: 1282–1291.
- [11]. Holzäpfel, F., Hofbauer, T., Darracq, D., Moet, H., Garnier, F., Gago, C.F., Analysis of wake vortex decay mechanisms in the atmosphere, *Aerospace Science and Technology*, 2003; 7: 263–275.
- [12]. Melander, M.V., Hussain, F., Coupling between a coherent structure and fine-scale turbulence, *Physical Review E*, 1993; 48: 2669–2689.
- [13]. Marshall, J.S., Beninati, M.L., External turbulence interaction with a columnar vortex, *Journal of Fluid Mechanics*, 2005; 540: 221–245.
- [14]. Pelletier, A., Mueller, T.J., Effect of endplates on two-dimensional airfoil testing at low Reynolds number, *Journal of Aircraft*, 2001; 38(6): 1056–1059.
- [15]. Kупpa, S., Marchman, J.F., End plate gap effect on a half wing model at low Reynolds numbers, *AIAA paper No. 1987-2350*.
- [16]. Ahmadi-Baloutaki, M., Carriveau, R., Ting, D.S-K., Effect of free-stream turbulence on flow characteristics over a transversely-grooved surface, *Experimental Thermal and Fluid Science*, 2013; 51: 56–70.

- [17]. Liu, R., Ting, D.S.-K., Checkel, M.D., Constant Reynolds number turbulence downstream of an orificed perforated plate, *Experimental Thermal Fluid Science*, 2007; 31: 897–908.
- [18]. Pope, A., Harper, J.J., *Low speed wind tunnel testing*, John Wiley and Sons, New York, 1966.
- [19]. Bradshaw, P., *An introduction to turbulence and its measurement*, Thermodynamics and Fluid Mechanics Series, Elsevier, 2013.
- [20]. Jørgensen, F.E., *How to measure turbulence with hot-wire anemometers - a practical guide*, Dantec Dynamics, Denmark, 2002.
- [21]. Browne, L.W.B., Antonia, R.A., Chua, L.P., Calibration of X-probes for turbulent flow measurements, *Experiments in Fluids*, 1989; 7: 201-208.
- [22]. Bruun, H.H., Nabhani, N., Al-Kayiem, H.H., Fardad, A.A., Khan, M.A., Hogarth, E., Calibration and analysis of X hot-wire probe signals, *Measurement Science and Technology*, 1990; 1: 782-785.
- [23]. Le Huu Nho, E., Beguier, C., Velocity measurements in 3D turbulent flows by means of a rotating X-wire probe, *Measurement Science and Technology*, 1995; 6: 843–850.
- [24]. Benedict, L.H., Gould, R.D., Towards better uncertainty estimates for turbulence statistics, *Experiments in Fluids*, 1996; 22: 129–136.
- [25]. Yavuzkurt, S., A guide to uncertainty analysis of hot-wire data, *Journal of Fluids Engineering, Transaction of the ASME*, 1984; 106: 181–186.
- [26]. Birch, D., Lee, T., Investigation of the near-field tip vortex behind an oscillating wing, *Journal of Fluid Mechanics*, 2005; 544: 201–241.
- [27]. Devenport, W.J., Rife, M.C., Liapis, S.I., Follin, G.J., The structure and development of a wing-tip vortex, *Journal of Fluid Mechanics*, 1996; 312: 67–106.
- [28]. Chow, J.S., Zilliac, G.G., Bradshaws, P., Mean and turbulence measurements in the near-field of a wingtip vortex, *AIAA Journal*, 1997; 35: 1561–1567.
- [29]. Sheldahl, R.E., Klimas, P.C., Aerodynamic characteristics of seven symmetrical airfoil sections through 180-degree angle of attack for use in aerodynamic analysis of vertical axis wind turbines, Sandia National Laboratories, 1981; SAND80-2114.
- [30]. Abbott, I.H., Von Doenhoff, A.E., *Theory of wing sections*, Dover publications, New York, 1966.
- [31]. Devinant, P., Laverne, T., Hureau, J., Experimental study of wind-turbine airfoil aerodynamics in high turbulence, *Journal of Wind Engineering and Industrial Aerodynamics*, 2002; 90: 689-707.
- [32]. Ahmadi-Baloutaki, M., Ting, D.S.-K., Carriveau, R., The role of free-stream turbulence on flow evolution in the wake of a VAWT blade, *Wind Engineering*, 2013; 37(4): 401–420.

- [33]. Hoffmann, J.A., Effects of free-stream turbulence on the performance characteristics of an airfoil, *AIAA Journal*, 1991; 29(9): 1353–1354.
- [34]. Iversen, J.D., Corsiglia, V.R., Park, S., Backhus, D.R., Brickman, R.A., Hot-wire, laser-anemometer, and force measurements of interacting trailing vortices, *Journal of Aircraft*, 1979; 16(7): 448–454.
- [35]. Phillips, W.R.C., Turbulent trailing vortex during roll-up, *Journal of Fluid Mechanics*, 1981; 105: 451–467.
- [36]. Shekariz, A., Fu, T.C., Katz, J., Huang, T.T., Near-field behavior of a tip vortex. *AIAA Journal*, 1993; 31: 112–118.
- [37]. Ramaprian, B.R., Zheng, Y., Measurements in rollup region of the tip vortex from a rectangular wing, *AIAA Journal*, 1997; 35: 1837–1843.
- [38]. Hoffman, E., Joubert, P., Turbulent line vortices, *Journal of Fluid Mechanics*, 1963; 16: 395–411.

Chapter 5: Performance of a vertical axis wind turbine in grid generated turbulence¹

5.1 Introduction

Aerodynamic performance of a wind turbine can be significantly affected by wind turbulence [1]. In addition, turbulence intensity can increase mechanical stresses on turbine components [2] and reduce the fatigue life of the turbine structure [3]. The impact of wind turbulence is especially crucial for small wind turbines since they are typically installed near to ground where obstacles such as buildings, trees, etc. can result in high levels of free-stream turbulence [4]. Moreover, wind turbulence approaching small wind turbines in urban areas can be many times greater than that of a rural wind farm [5].

Vertical axis wind turbines (VAWT); which play an important role in the small wind turbine market are the topic of current study. These machines offer several benefits over their horizontal design counterparts including insensitivity to yaw, lower noise emission, and better integration in architectural projects [6]. Despite the importance of the wind turbulence in VAWTs' power generation, the available literature on the topic is relatively scarce.

A commonly used approach for reporting the turbine power curves is to determine the output power as statistical averages of power measurements binned by wind speed, whereby the variance of the data is lost [1,7]. Such an approach is heavily dependent on the sample size of the output data and thus the effect of free-stream turbulence is not captured by this method. In other words, the time duration of wind speed data over which the wind turbulence is calculated is crucial and can affect the interpretation of output results. The International Electrotechnical Commission (IEC) standard recommends 10 minute interval for calculating the turbulence intensity [7]. There are, nonetheless, a few studies that attempted to characterize the effect of wind turbulence on the turbine's performance by using more appropriate time durations related to the time scales present in the atmospheric wind. These works by Kooiman and Tullis [8], Lubitz [9], and Smith [10] were all performed in atmospheric environment with no control on the level of free-stream turbulence. The difference between these studies [8-10] by other works on

¹ This work was published as: "Ahmadi-Baloutaki, M., Carriveau, R., Ting, D.S.-K., Performance of a vertical axis wind turbine in grid generated turbulence, Sustainable Energy Technologies and Assessments, 2015; 11: 178-185."

atmospheric performance testing is that they [8-10] used different time intervals, related to the time scales in the atmospheric wind, to determine the wind turbulence.

Kooiman and Tullis [8] studied the effects of wind velocity and direction fluctuations on the energy production of a VAWT by urban environment testing on a rooftop. The turbine's output power was found to vary with wind velocity fluctuations, but roughly independent of direction fluctuations [8]. Kooiman and Tullis [8] compared their urban performance testing with an earlier work on the same wind turbine in a low turbulence wind tunnel ($Tu < 2\%$) as their "smooth" flow performance benchmark. They [8] reported a marginal reduction in the turbine's performance from the smooth flow values for $Tu < 15\%$, and almost a linear reduction with increasing turbulence intensity for $Tu > 15\%$. Using the similar methodology of Kooiman and Tullis [8], Lubitz [9] conducted a series of performance testing of a HAWT in an open farm to investigate the effect of ambient turbulence on the turbine output power. According to Lubitz [9], the turbine energy production was altered by ambient turbulent level, but the impact was different at various wind speeds. Wind turbulence levels lower than 14% resulted in increased output power, while no consistent trend was reported for higher turbulence levels. Smith [10] reported performance curves and annual energy productions (AEP) for seven small wind turbines at varying levels of wind turbulence. There was 9% to 32% variation in turbines AEP over the studied turbulence intensity range [10]. Most of the turbines had lower AEP in both the extreme low and high turbulence levels; except one, whose AEP was increased with increasing turbulence intensity [10].

As mentioned earlier, all of the works cited above used the same methodology to quantify the effect of wind turbulence; which is highly dependent on the sample size. It can be argued that using a different sample size may lead to different conclusions. Besides, there is no consensus on the effect of free-stream turbulence on the wind turbine's operation as different trends have been reported in the literature. This may be partially due to the different turbulent flow types studied by different researchers, complicated by varying amounts of wind shear and unsteady wind.

This highlights the need for systematic performance testing under controlled turbulent flows with uniform and steady wind conditions. To achieve better experimental control, it would be advantageous to start with the simplest form of inflow turbulence, isotropic turbulence. To this end a grid in wind tunnel testing has been employed to generate isotropic turbulence. The current study attempts to investigate the influence of free-stream turbulence intensity on the aerodynamic performance of a Darrieus-type VAWT by creating steady quasi-isotropic turbulent winds using a grid in a wind tunnel.

5.2 Experimental setup

5.2.1 Model description

Experiments were conducted in a closed-loop wind tunnel whose 1.8 m long test section has a 0.76 m by 0.76 m cross section. The maximum achievable velocity is about 34 m/s in the empty working section with a background turbulence intensity of less than 0.5%. In the presence of a grid turbulence generator however, the maximum achievable velocity is approximately 21 m/s. The mean velocity and turbulence intensity were nearly uniform in the core of the wind tunnel in absence of the VAWT. A schematic of the wind tunnel test section including the wind turbine and the grid turbulence generator is shown in Fig. 1.

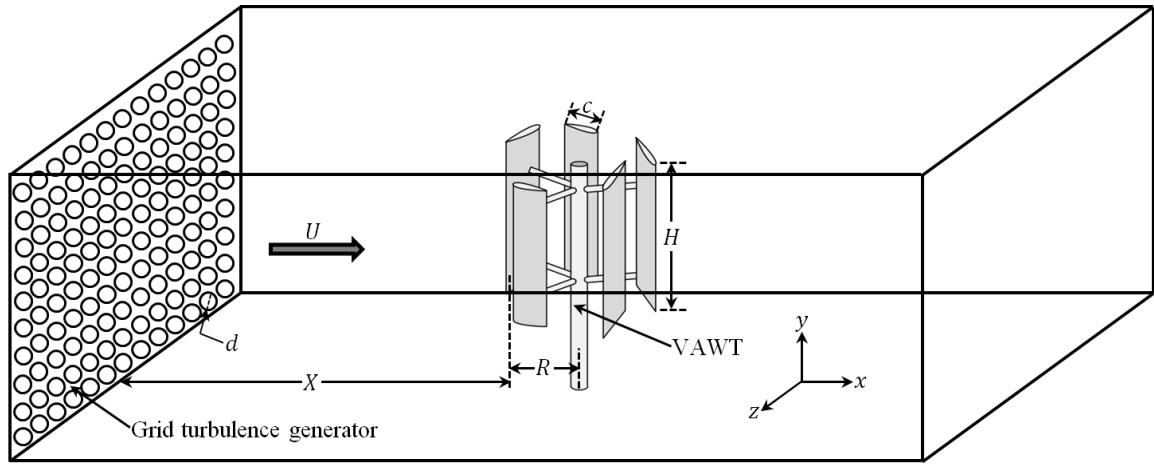


Figure 1: A schematic illustration of the experimental fixture including the grid turbulence generator and VAWT

The VAWT used in the current study is a commercial mini wind turbine, P-10 model, manufactured by Shanghai Aeolus Windpower Technology Co., Ltd [11]. This wind turbine has five straight blades made from Aluminum with hollow section as depicted in Fig. 1. The blades of this wind turbine have a custom-made asymmetric airfoil profile. The coordinates of this airfoil profile have been digitized and plotted in Fig. 2. Blade chord length and height were 45 mm and 0.3 m, respectively. This results in a blade aspect ratio of 6.6 which is close to the optimum range of this parameter for straight bladed-VAWTs (SB-VAWT); $10 < AR_{opt} < 20$, as determined in Ref. [12]. The rotor diameter of the turbine was 0.3 m which corresponds to a rotor aspect ratio of unity, which is in the desirable range for SB-VAWTs; $0.5 < (H/D)_{opt} < 2$ [12]. The solidity

ratio of this wind turbine, however, is far from the optimum values. The current SB-VAWT is categorized under high-solidity turbines ($s > 1$) with a solidity ratio of 1.5, while many works have reported the optimum range of this variable to be $0.2 < s_{opt} < 0.6$ as explained in Ref. [12]. Each blade was connected to the central shaft via two supporting arms at intermediate locations of 0.33 and 0.66 of the blade height. The supporting arms were Aluminum bars with rectangle cross-section of 2 mm by 25 mm.

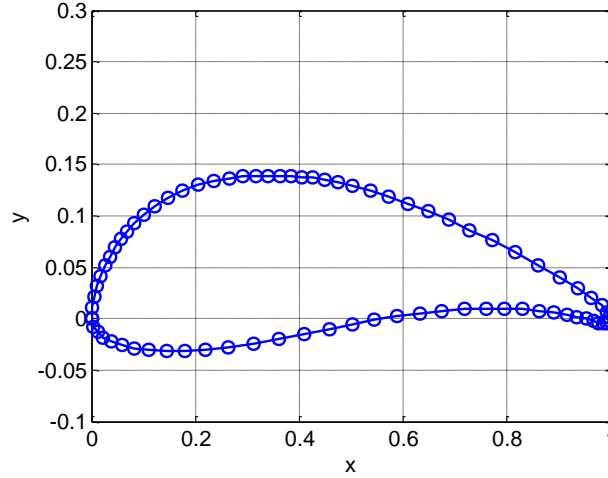


Figure 2: Airfoil profile of the VAWT blades used in this study

Although wind tunnel testing provides the benefit of controlled flow conditions, it introduces further sources of error due to the effect of blockage. VAWTs blockage effects have not been thoroughly studied since these machines present a unique aerodynamic obstruction in wind tunnels. The flowfield surrounding VAWTs is asymmetric, periodic, unsteady, separated and highly turbulent. Garrett and Cummins [13] investigated the blockage effects on the aerodynamic operation of a wind turbine in a confined channel. They [13] concluded that the effect of channel blockage on the turbine output power depends on the turbine solidity and tip speed ratio as well as the rotor swept area to the channel size ratio. Ross and Altman [14] reviewed the existing works on VAWT blockage and evaluated different methodologies on this parameter. According to Ross and Altman [14] the VAWT blockage ratio can be determined as

$$B = \frac{1}{4} \frac{\text{rotor frontal area}}{\text{test section area}} \quad (1)$$

The setup used in the present study has a blockage ratio of 3.8% according to Eq. 1. The literature suggests that for blockage ratios less than 5%, no correction is needed for output results [13-15]. Therefore, the tunnel blockage will not be discussed further in this paper.

For controlling the free-stream turbulence an orificed perforated plate (OPP) with circular holes was located upstream of the wind turbine as depicted in Fig. 1. Also shown in Fig. 3, this plate spanned the entire wind tunnel test section. The OPP was made from 6 mm thickness Aluminum with 25.4 mm diameter holes resulting in a solidity ratio of 43%. In order to minimize the effect of the plate thickness on the generated turbulent flow, all holes were machined with a 41° chamfer angle with the sharp-edged side facing the incoming flow as portrayed in Fig. 3b.

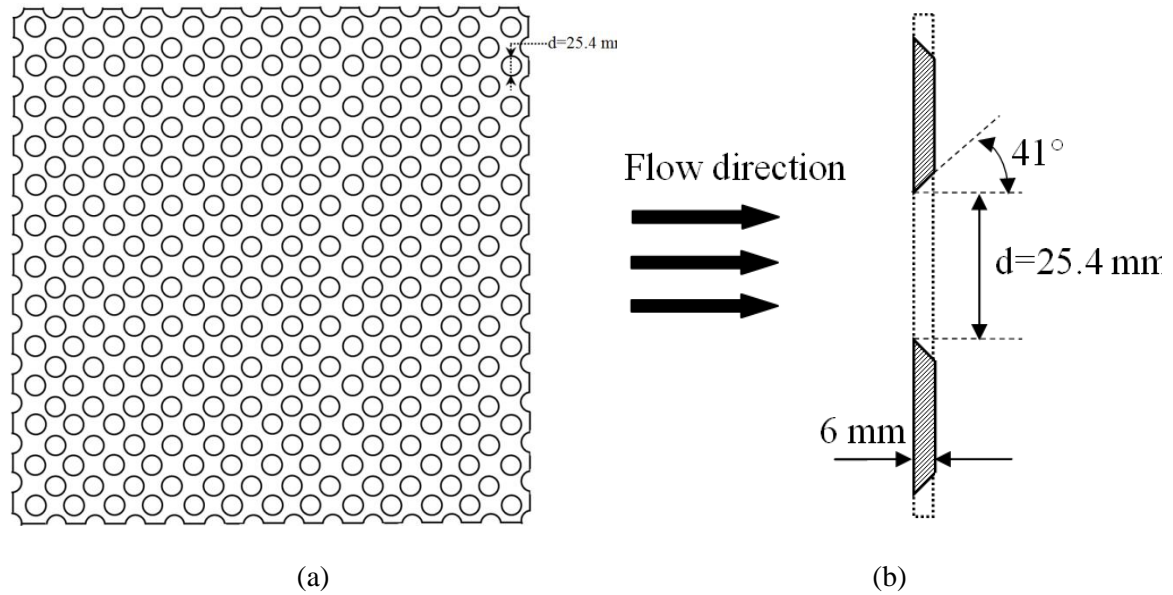


Figure 3: Schematic illustrations of the orificed perforated plate, (a) front view, and (b) side view

5.2.2 Instrumentation

The free-stream velocity in the wind tunnel was set using a Pitot-static tube connected to a digital manometer (DWYER series 475) at the beginning of each experiment. The Pitot tube was inserted through a small hole on the test section ceiling near the inlet section. The Pitot tube was removed after checking the free-stream velocity and the small opening was sealed with duct tape.

The turbulence characteristics of free-stream flowfields in the absence of the wind turbine were measured using hot-wire anemometry. A DANTEC hot-wire unit operating in constant temperature mode with an X-probe of 55P61 type was utilized for this purpose. The probe was

calibrated using the manufacturer calibration manual equipped with laboratory pressurized air. The curve was used to calibrate the X-probe hot-wire is a 4th degree polynomial provided by the hot-wire unit supplier with small calibration error in the range of 2.5%. Manshadi [16] showed there are advantages in calibration of X-probe hot-wires by Genetic Algorithm over other calibration curves such as polynomials and curves based on the King's law. In this work, the mean and turbulence velocities downstream the grid were also measured by a normal 1-D probe with results very close to those of the X-probe.

The output signal of the hot-wire probe was sent to a National Instrument multifunction data acquisition board with a 12-bit resolution connected to a computer. The hot-wire analog voltage signal was first low-passed at 30 kHz using an analog filter to remove noise and to prevent higher frequencies from folding back (anti-aliasing). Then it was sampled at 80 kHz over the sampling time of 12.5 seconds; which resulted in one million samples. The hot-wire probe was traversed using an automated traversing system with a position resolution of 2.5 μm .

The output power of the wind turbine was measured by tracking the voltage across an external load having an electrical resistance of $R_l = 153 \Omega$. This type of resistor was selected to mimic the turbine's intended operation as part of a battery charging system. The external resistor was connected to the wind turbine generator; an AC PMG 3 phase unit. This generator was connected to a 1N5399 MIC rectifier that was used to convert the generator AC current to a DC one. The output DC voltage across the resistor was measured by a National Instrument 9215 data acquisition card at a sampling frequency of 1 kHz. The uncertainty in voltage measure by this instrument was deduced to be less than 0.1 volts. The rms current of the circuit, I , was then calculated and used to determine the amount of power dissipated in the resistor as

$$P_l = R_l I^2 \quad (2)$$

The rotational speed of the rotor was measured using a digital Stroboscope HHT31R series operating outside of the test section. The uncertainty in rotor speed measurement was about 0.2 RPM for rotational speeds greater than 300 RPM. For rotor speeds less than 300 RPM this stroboscope was not capable to operate due to some limitations confirmed by the manufacturer. Video recording was used instead, to measure the rotor speed for $\omega < 300$ RPM. A high-performance NIKON D5200 camera with capturing rate of 60 frames per second has been used to record videos having 60 second length. The uncertainty in rotor speed measurement was less than 1.6 RPM for rotational speeds less than 300 RPM.

5.3 Results and discussion

5.3.1 Free-stream turbulence characteristics

The grid turbulence generator described in Section 2.1 was located at three locations upstream of the wind turbine at $X/d=12, 17$, and 27 (see Fig. 1). The turbulence intensity at these locations in the absence of the turbine was determined by

$$Tu(\%) = \frac{u_{rms}}{\bar{U}} \times 100 \quad (3)$$

where \bar{U} is time-averaged value of the streamwise velocity signal and u_{rms} is the root-mean-square of the velocity fluctuations in streamwise direction calculated from

$$u_{rms} = \sqrt{\sum_{i=1}^n \frac{(U_i - \bar{U})^2}{n-1}} \quad (4)$$

Figure 4a shows the variation of turbulence intensity with respect to the streamwise distance from the OPP at several free-stream velocities. As can be seen in this graph, the average value of turbulence intensity at $X/d=12, 17$, and 27 locations is 10, 7.5, and 5%, respectively. This range of turbulence intensity was generated in this research to mimic the low portion of turbulence intensity range in atmospheric flows. According to the literature, the turbulence intensity in atmospheric boundary layers depends on the height from the ground and the roughness distribution of the ground or terrain where the wind is blowing [5]. The turbulence intensity takes small values as low as 5% in open calm seas and large values as high as 20% in urban areas [5]. It should be noted that, however, the turbulent flows generated in this study are nearly-isotropic turbulence and free of any shear effects. This was done since the main objective of this research was to study the effect of free-stream turbulence intensity, even though results should be interpreted with care since the wind shear effects are present in real atmospheric flows.

Figure 4a shows that there is a slight variation in turbulence intensity with free-stream velocity at each location. Moreover, the turbulence intensity is reduced with increasing the streamwise location implying the turbulence decay as can be observed in Fig. 4a [17]. The corresponding values of integral length scale at the same locations have been plotted in Fig. 4b. The integral length scale was determined by the numerical procedure described in Ref. [17]. As evident in Fig. 4b, the variation in the integral length scale is very small with respect to free-stream velocity at each streamwise location downstream of the grid.

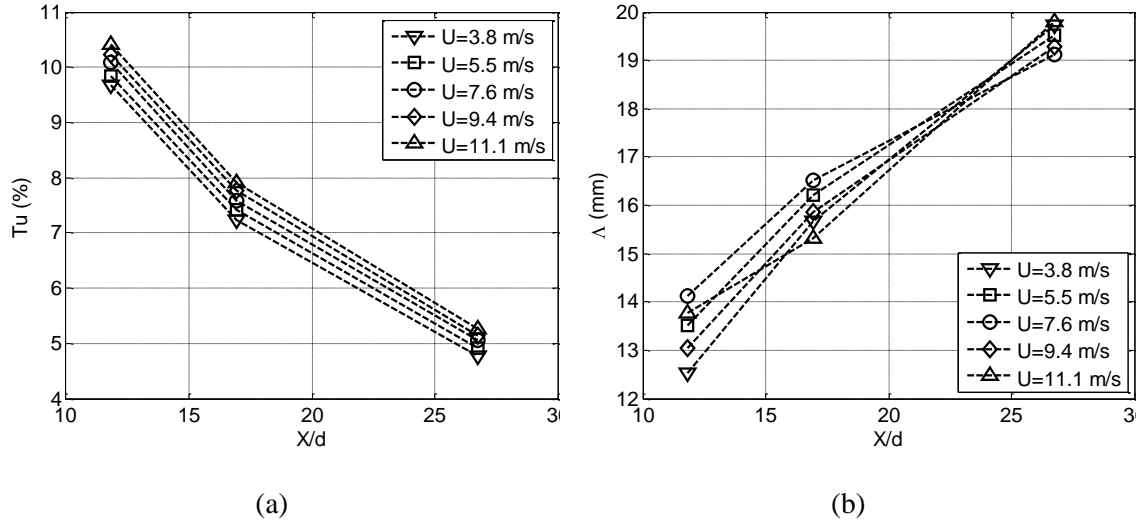


Figure 4: The variation of (a) turbulence intensity, and (b) integral length scale with streamwise distance from grid generator

Further turbulence characteristics of the flow downstream of the OPP are presented in Fig. 5 for $X/d=12, 17$, and 27 locations at a free-stream velocity of 7.6 m/s. Figures 5a-c show the streamwise velocity fluctuation, u , at the three aforementioned locations. The amount of turbulence fluctuations is reduced with increasing streamwise location as expected. Figures 5d-f depict the probability density function (PDF) of the turbulence distribution at the three measured locations. A Gaussian distribution described by the following equation has also been plotted in Figs. 5d-f for reference [17].

$$f(u, \mu, \sigma) = \frac{1}{\sigma\sqrt{2\pi}} e^{-\frac{(u-\mu)^2}{2\sigma^2}} \quad (5)$$

where μ and σ indicate the mean and the standard deviation of the velocity fluctuation vector u , respectively. As can be observed in Figs. 5d-f, all PDF graphs have symmetrical Gaussian-like distributions. In addition, the skewness and flatness factors of the PDF distributions presented in Fig. 5 are very close to the values of a Gaussian distribution ($S \approx 0$, $F \approx 3$) [17]. This would suggest the turbulence generated downstream the OPP can be nearly-isotropic. PDF graphs for all other free-stream velocities have the same trend and therefore are not shown here. This condition, however, is not sufficient for a turbulent flow to be isotropic. Extensive three-dimensional measurements of the flowfield downstream of the grid are needed to judge whether the turbulence pattern is isotropic. These measurements were performed by Liu and Ting [18] for the same grid turbulence generator and wind tunnel flow conditions.

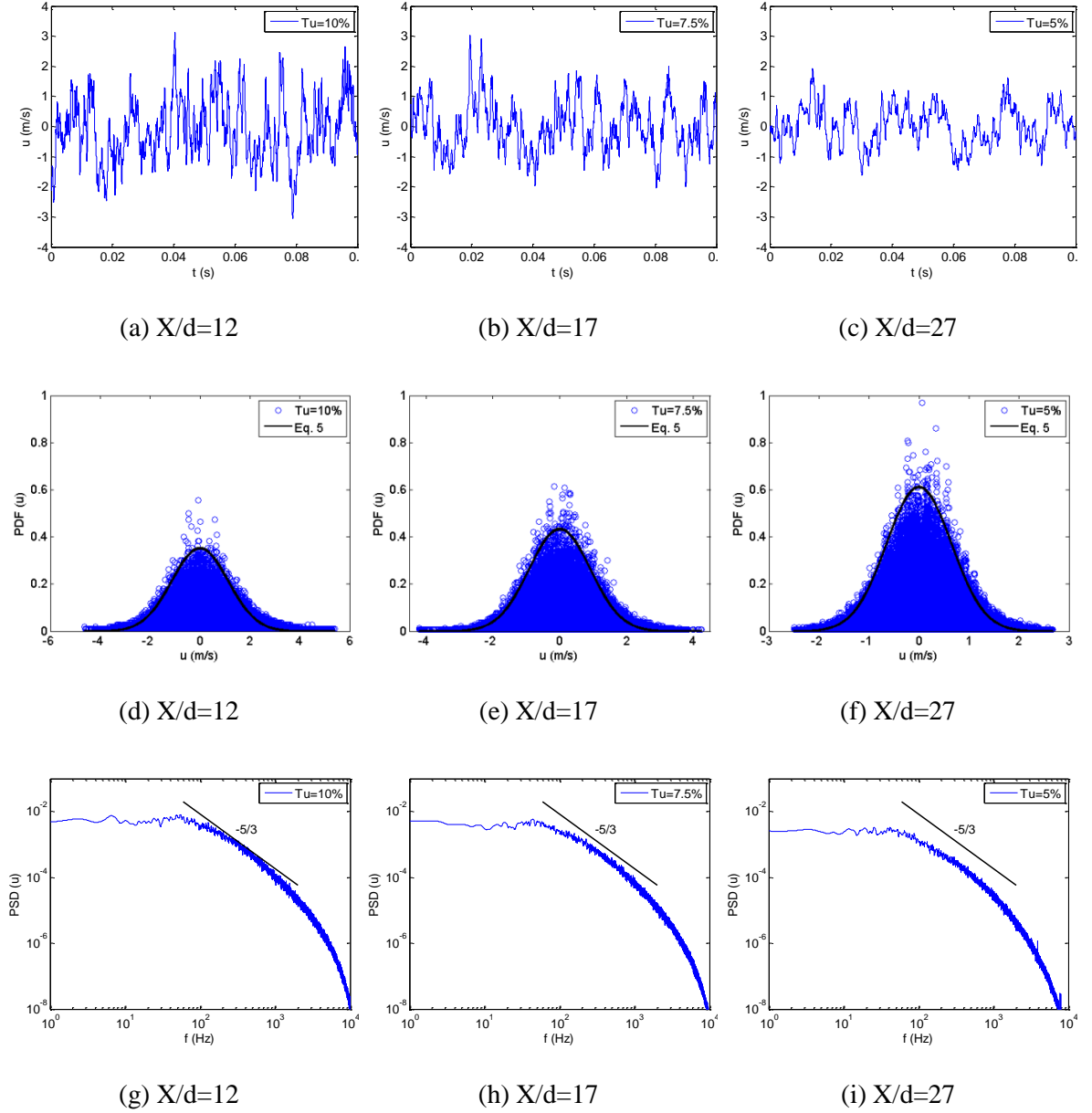


Figure 5: Turbulence characteristics of the flow downstream of the grid; (a-c) streamwise velocity fluctuation, (d-f) probability density function, and (g-i) frequency spectra

The frequency spectra of the turbulent signals have been determined by plotting the power spectral density (PSD) of the streamwise component of velocity fluctuations using MATLAB. Figure 5g-i show the frequency spectra for three streamwise locations of $X/d=12$, 17, and 27 downstream of the grid at a free-stream velocity of 7.6 m/s in an empty working wind tunnel section. According to the Kolmogorov's turbulence hypothesis, the spectra of velocity

fluctuation should collapse at high frequencies for an isotropic turbulence at large Reynolds numbers [17]. It was also reported that in isotropic turbulence the spectra demonstrated three distinct frequency regions [17]. The first region is the energy containing range that includes large-scale energetic eddies at relatively low frequencies characterized by flat spectra. The second one is the inertial region at intermediate frequencies which contains eddies associated with energy transfer from larger to smaller motions with negligible loss of turbulence kinetic energy characterized by a slope of $-5/3$ in logarithmic coordinates. The third region is the viscous subrange that is associated with the dissipation of the kinetic energy at small scales due to viscosity at high frequencies [17]. The turbulence generated downstream the OPP grid in the present work appears to comply with Kolmogorov's turbulence hypothesis since the three aforementioned frequency regions are recognizable in their PSD graphs in Figs. 5g-i. In order to identify the inertial region an auxiliary line with $-5/3$ slope have been plotted in these graphs. The turbulence decay is also evident in Figs. 5g-i as the energy content of the signals decreases with streamwise distance. In short, the free-stream turbulence generated upstream of the wind turbine in the current study has characteristics of a quasi-isotropic turbulence.

5.3.2 Wind turbine performance testing

Figure 6 shows selected parameters measured during the wind tunnel performance testing of the turbine under several levels of free-stream turbulence. The flow with $Tu=0.5\%$ corresponds to the non-obstructed or smooth flow case. Figure 6a shows the output voltage measured across the external resistance with respect to the free-stream velocity. There is a dramatic increase in the output voltage in the presence of grid turbulence that is, from $Tu=0.5\%$ to 5% . The increase in the output voltage with further increase in turbulence intensity is very small, but greater than the uncertainty limits. The power output jump from “no turbulence” $Tu=0.5\%$ case to free-stream turbulent flow with $Tu=5\%$ is possibly due to a fundamental change in the underlying flow regime around the blades, from laminar to turbulent.

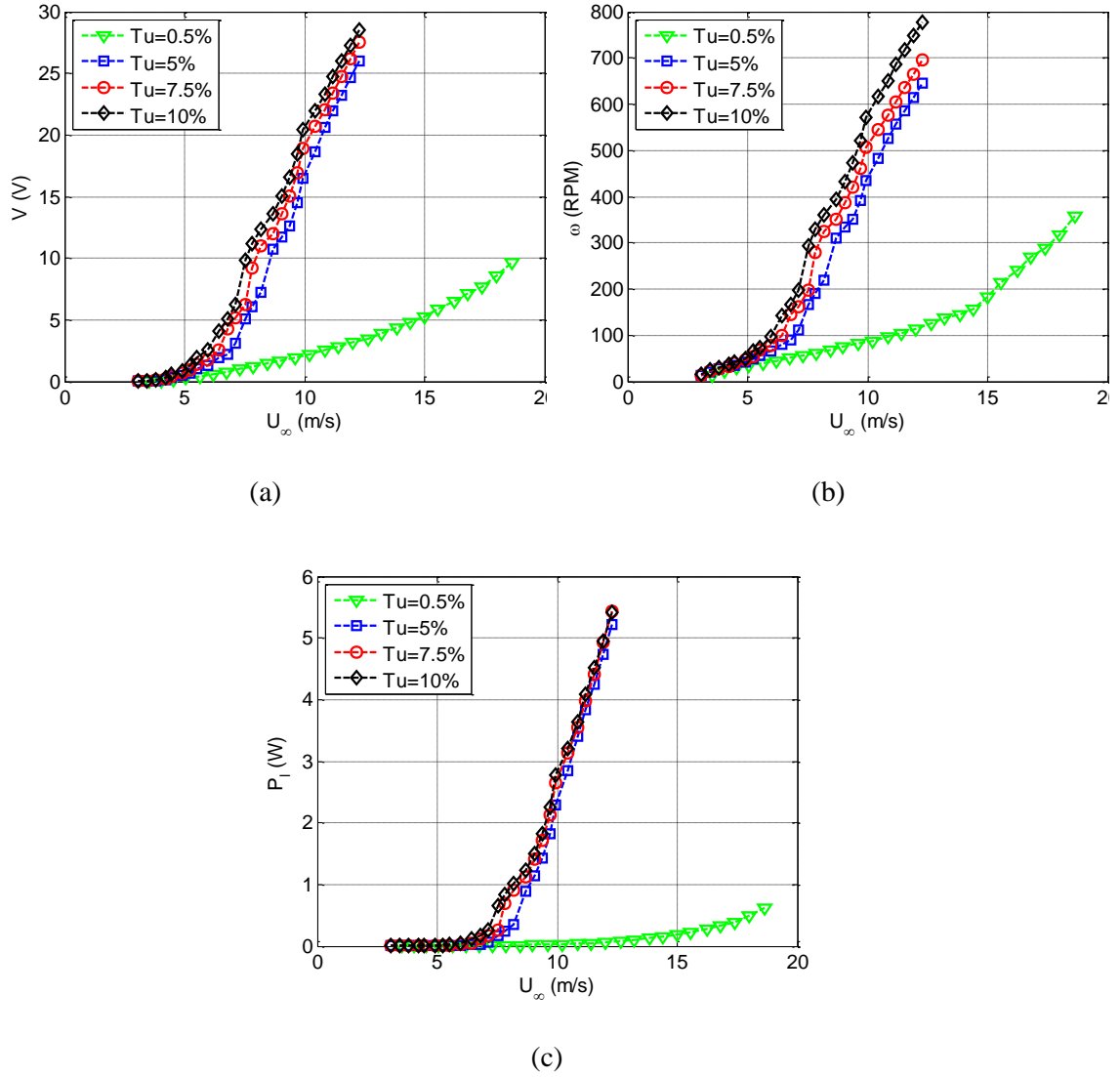


Figure 6: Effect of free-stream turbulence on the wind turbine output parameters; (a) voltage output, (b) rotational speed, and (c) power output

The rotor's rotational speed at various free-stream velocities is plotted in Fig. 6b. Almost the same trend observed in Fig. 6a can be seen in this graph. Another improvement in the turbine aerodynamic operation is the reduction in the self-starting speed in the presence of grid turbulence. As evident in Fig. 6b, the turbine self-started at 3.5 m/s in $Tu=0.5\%$ flow case, while the self-starting occurred at 3 m/s in flows under grid turbulence effect. Figure 5c shows the turbine's electrical output power dissipated across the external resistance determined by Eq. 2. The significant improvement in turbine's aerodynamic performance observed in Figs. 6a and 6b

can also be detected in Fig. 6c by noticing the substantial increase in output power in the grid turbulent flows compared to the smooth free-stream case.

The wind turbine total power output consists of the electrical power dissipated by an external load, and the power consumed to overcome the losses in the internal components of the rotor's electrical circuit including the windings and the rectifier. Therefore, the total power output, P , can be deduced as

$$P = P_l + P_w + P_r \quad (6)$$

The electrical losses which depend on the rotational speed of the rotor have been estimated at several speeds as documented in Appendix D. Then, the turbine's total power output is plotted against free-stream wind speed in Fig. 7a. This graph shows almost the same trend as the power output in Fig. 6c. The performance curve of the VAWT used in the current study is also plotted in Fig. 7b. A typical performance curve of a wind turbine shows the turbine power coefficient, C_p , versus the blade tip speed ratio, λ . These parameters are defined as [12]

$$C_p = \frac{P}{\frac{1}{2}\rho A_r U_\infty^3} \quad (7)$$

$$\lambda = \frac{R\omega}{U_\infty} \quad (8)$$

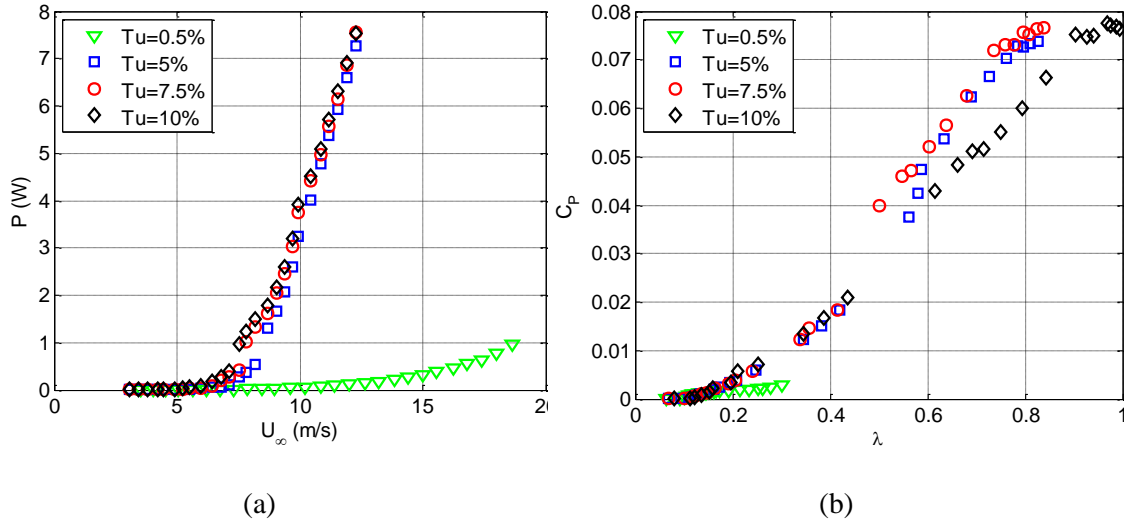


Figure 7: (a) Wind turbine total power output, and (b) wind turbine performance curves at several free-stream turbulence levels

According to Fig. 7b, the power coefficient takes on very small values and the tip speed ratio reaches only as high as 0.3 for $Tu=0.5\%$ flow case. A wind turbine may not be considered useful for power generation since these ranges of parameters are very small. On the other hand, introducing grid turbulence to the flow increases both turbine power coefficient and tip speed ratio. To determine the effect of free-stream turbulence on the turbine performance curve, different curves in Figs. 7b should be compared at the same tip speed ratios. As can be seen in Figs. 7b, the increase in turbine power coefficient due to the effect grid turbulence is small. The turbine performance curves may be extended to the tip speed ratios greater than one; however, this was not performed in the present experiments owing to safety considerations. It should be noted that when the results of the current study are going to be interpreted the limited tip speed ratio range studied here should be considered.

To conclude the effect of external free-stream turbulence on the wind turbine performance, consideration of the effect of free-stream turbulence on a single blade may provide insight. This is discussed in this section and possible reasons are stated for this effect. First, as demonstrated in the literature, external free-stream turbulence improves the blade aerodynamic efficiency by increasing the lift-to-drag ratio, delaying the dynamic stall, and postponing the flow separation over the blade surfaces [19,20]. These positive effects were also observed and discussed in Fig. 5 of Chapter 3 and Fig. 4 of Chapter 4. These benefits are also expected to occur when blades operate as part of the wind turbine for Darrieus rotors [6,12,21]. Also known from the literature, stall effects are more severe at low tip speed ratios where turbine blades experience a wide range of angle of attack which is mostly located in the stall region of the blade [6,21,22]. This can be observed in Fig. 5a of Chapter 2 where the blade's angle of attack was plotted versus azimuthal position for three values of tip speed ratio. Considering the operational tip speed ratio for the wind turbines tested in this chapter was less than one (see Fig. 7b), it is expected the turbine blades operate at high angles of attack (see Fig. 5a of Chapter 2), and therefore, experience stall. Thus, it seems that the positive effects of the external free-stream turbulence generated by the grid can be more effective at low tip speed ratios which are the range under study in the current work. It should be noted the effect of free-stream turbulence on the blade's aerodynamic operation is marginal in the pre-stall region at low angles of attack (see Fig. 5 of Chapter 3 and Fig. 4 of Chapter 4), and consequently, should not influence the wind turbine operation at high tip speed ratios (see Fig. 5a of Chapter 2) by much.

Free-stream turbulence would also affect the critical Reynolds number and consequently influences the turbine blades aerodynamic performance. This has been shown in many works in

the literature that high free-stream turbulence reduces the critical Reynolds number and promotes early transition on the blade surfaces [23,24]. This would result in improvements in the blades aerodynamic performance such as higher lift-to-drag ratio, dynamic stall delay, and flow separation deferment, as mentioned earlier.

Another turbulence characteristic worth considering in this analysis is the turbulence integral length scale. As known from turbulence theory two of the main important parameters of each turbulent flow are turbulence intensity and turbulence integral length scale. The turbulence intensity which is a dimensionless parameter was varied in a range close to the operational range of wind turbines. However, the integral length scale which was in the range of 12 to 20 mm in the current study (see Fig. 4b) was of the same order of magnitude of the blade chord length (45 mm), while one order of magnitude smaller than the turbine diameter (300 mm). This may suggest that the effect of the turbulence generated in this work was limited to the blade aerodynamic performance. In other words, larger length scales (of the same order of magnitude of the turbine diameter) should exist in a turbulent flow to influence the turbine performance as a whole as discussed in Refs. [25,26].

5.4 Conclusion

Aerodynamic performance testing of a vertical axis wind turbine has been performed under different levels of free-stream turbulence in a closed-loop wind tunnel. The free-stream turbulence was controlled by changing the location of a grid turbulence generator upstream of the wind turbine. This resulted in steady turbulent free-stream flows that provided controlled testing conditions unlike the atmospheric performance testing. The turbulence generated in the current study was nearly-isotropic in nature. The grid generated turbulent flows with turbulence intensities of 5, 7.5, and 10% caused a substantial increase in the turbine output power compared to the smooth flow case with 0.5% turbulence intensity. The increase in turbine power coefficient due to the effect of grid turbulence, however, was small at the tip speed ratio range studied. This may be correlated to the positive effects of the free-stream turbulence on the aerodynamic performance of the single blades, in that the integral length scale was only an order of magnitude smaller than the turbine blade chord length, and hence, the effect is probably limited to the boundary layer. The turbine output power was slightly increased by increasing the turbulence intensity beyond 5% in the grid generated turbulent flows. Introducing the external free-stream turbulence also improved the self-starting behavior of the vertical axis wind turbine.

5.5 References

- [1]. EL-Shimy, M., Probable power production in optimally matched wind turbine generators, *Sustainable Energy Technologies and Assessments*, 2013; 2(1): 55–66.
- [2]. Park, J., Basu, S., Manuel, L., Large-eddy simulation of stable boundary layer turbulence and estimation of associated wind turbine loads, *Wind Energy*, 2014; 17(3): 359–384.
- [3]. Riziotis, V.A., Voutsinas, S.G., Fatigue loads on wind turbines of different control strategies operating in complex terrain, *Journal of Wind Engineering and Industrial Aerodynamics*, 2000; 85(3): 211–240.
- [4]. Araújo, A.M., de Alencar Valença, D.A., Asibor, A.I., Rosas, P.A.C., An approach to simulate wind fields around an urban environment for wind energy application, *Environmental Fluid Mechanics*, 2013; 13(1): 33–50.
- [5]. Sunderland, K., Woolmington, T., Blackledge, J., Conlon, M., Small wind turbines in turbulent (urban) environments: A consideration of normal and Weibull distributions for power prediction, *Journal of Wind Engineering and Industrial Aerodynamics*, 2013; 121: 70–81.
- [6]. Aslam Bhutta, M.M., Hayat, N., Farooq, A.U., Ali, Z., Jamil, Sh.R., Hussain, Z., Vertical axis wind turbine - a review of various configurations and design techniques, *Renewable and Sustainable Energy Reviews*, 2012; 16(4): 1926–1939.
- [7]. Gottschall, J., Peinke, J., Stochastic modelling of a wind turbine's power output with special respect to turbulent dynamics, *Journal of Physics: Conference Series*, 2007; 75(1): No. 012045, 1–8.
- [8]. Kooiman, S.J., Tullis, S.W., Response of a vertical axis wind turbine to time varying wind conditions found within the urban environment, *Wind Engineering*, 2012; 34(4): 389–401.
- [9]. Lubitz, W.D., Impact of ambient turbulence on performance of a small wind turbine, *Renewable Energy*, 2014; 61: 69–73.
- [10]. Smith, J., Effects of turbulence intensity on the performance of small wind turbines, *Small Wind Conference*, 2010, Stevens Point, WI, USA.
- [11]. Shanghai Aeolus Windpower Technology Co., Ltd, <http://www.sawt.com.cn/>.
- [12]. Ahmadi-Baloutaki, M., Carriveau, R., Ting, D.S–K., Straight-bladed vertical axis wind turbine rotor design guide based on aerodynamic performance and loading analysis, *Proceedings of the Institution of Mechanical Engineers, Part A: Journal of Power and Energy*, 2014; 228: 718–741.
- [13]. Garrett, C., Cummins, P., The efficiency of a turbine in a tidal channel, *Journal of Fluid Mechanics*, 2007; 588: 243–251.

- [14]. Ross, A., Altman, A., Wind tunnel blockage corrections: Review and application to Savonius vertical-axis wind turbines, *Journal of Wind Engineering and Industrial Aerodynamics*, 2011; 99: 523–538.
- [15]. Medici, D., Ivanell, S., Dahlberg, J.Å., Alfredsson, P.H., The upstream flow of a wind turbine: Blockage effect, *Wind Energy*, 2011; 14(15): 691–697.
- [16]. Manshadi, M.D., The Importance of Turbulence in Assessment of Wind Tunnel Flow Quality, in: Lerner, J.C., (Ed.), *Wind Tunnels and Experimental Fluid Dynamics Research*, InTech, 2011; 261–278.
- [17]. Hinze, J.O., *Turbulence*, 2nd Ed, McGraw-Hill, New York, 1975.
- [18]. Liu, R., Ting, D.S-K., Turbulent flow downstream of a perforated plate: Sharp-edged orifice versus finite-thickness hole, *Journal of Fluids Engineering*, 2007; 129: 1164–1171.
- [19]. Hoffmann, J.A., Effects of free-stream turbulence on the performance characteristics of an airfoil, *AIAA Journal*, 1991; 29(9): 1353–1354.
- [20]. Devinant, P., Laverne, T., Hureau, J., Experimental study of wind-turbine airfoil aerodynamics in high turbulence, *Journal of Wind Engineering and Industrial Aerodynamics*, 2002; 90: 689–707.
- [21]. Paraschivoiu, I., *Wind turbine design – with emphasis on Darrieus concept*, Polytechnic International Press, Montreal, 2002.
- [22]. Mikkelsen, K., Effect of free stream turbulence on wind turbine performance, MSc thesis, Norwegian University of Science and Technology, Norway, 2013.
- [23]. Mandal, A.C., Venkatakrishnan, L., Dey, J., A study on boundary-layer transition induced by free-stream turbulence, *Journal of Fluid Mechanics*, 2010; 660: 114–146.
- [24]. Ahmadi-Baloutaki, M., Sedaghat, A., Saghafian, M., Badri, M.A., Control of Transition over Aerofoil Surfaces using Active Suction, *International Journal of Flow Control*, 2013; 5(3-4): 187–200.
- [25]. Bertenyi, T., Wickens, C., McIntosh, S., Enhanced energy capture through gust tracking in the urban wind environment, 29th ASME Wind Energy Symposium, Orlando, FL, USA. 2010.
- [26]. Chamorro, L.P., Guala, M., Arndt, R.E.A., Sotiropoulos, F., On the evolution of turbulent scales in the wake of a wind turbine model, *Journal of Turbulence*, 2012; 13(27): 1–13.

Chapter 6: A wind tunnel study on the aerodynamic interaction of vertical axis wind turbines in array configurations¹

6.1 Introduction

Optimal positioning of wind turbines in a wind farm is crucial in today's wind market [1,2]. Wind turbines in a wind farm modify the structure of the wind flow by creating turbulence structures and reducing the wind velocity [3,4]. Therefore, the wind stream in a wind farm is partly undisturbed and partly varied by the wake of the upstream turbines. This modified wind flow will typically result in lower power output for the wind turbines located downstream, as compared to an isolated turbine [5,6]. To avoid these wind and power fluctuations and to reduce structural vibrations and fatigue loads, wind turbines are typically spaced far apart, occupying large areas of land [7-9].

The turbine spacing constraint for horizontal axis wind turbines (HAWTs) dictates that these turbines must be spaced 3-5 turbine diameters apart in the crossflow direction and 6-10 diameters apart in the streamwise direction to maintain 90% of the performance of an isolated turbine [10]. While HAWTs shed wakes and wind trails that negatively affect the neighboring turbines in both crossflow and downstream directions, the wake of vertical axis wind turbines (VAWTs) can potentially provide constructive aerodynamic interactions for a group of turbines. The literature suggests that when two counter-rotating VAWTs are placed close together, the flow induced by each turbine is oriented in the same direction, resulting in reduced turbulence and vortex shedding [6,11]. The mutual coupling effect existing between rotors can result in positive interactions, improving the power performance of VAWTs while reducing the footprint of turbines. Considering the fact that VAWTs can harness wind energy from any direction [12], this lack of directional sensitivity can enable turbines to extract energy from adjacent wakes; something seemingly less attainable for HAWTs. This potential benefit of VAWTs in group installations, combined with relatively lower manufacturing and maintenance costs, and less aerodynamic noise makes them a promising alternative to HAWTs [13]. While there are many studies on the optimal positioning of HAWTs in a wind farm, the aerodynamic interaction of

¹ This work is submitted for publication as: "Ahmadi-Baloutaki, M., Carriveau, R., Ting, D.S.-K., A wind tunnel study on the aerodynamic interaction of vertical axis wind turbines in array configurations, Renewable Energy, Under review."

VAWTs, particularly counter-rotating machines, has been investigated only in a handful of studies [6,11,14-16].

The idea of employing counter-rotating VAWTs was first patented by Thomas in 2004 [11]. He claimed that putting a pair of VAWTs in a counter-rotating configuration can result in aerodynamic efficiency enhancement of the pair through vortex interaction between the two adjacent rotors [11]. According to him, the high solidity rotors are a good choice for this scenario as they can be more efficient in the coupled vortex interaction phenomenon. He further explained that the separation distance between two turbines should be as small as safely possible for maximum effectiveness [11]. The other important outcome from this patent is that the counter-rotating configuration has the most efficiency when the pair of turbines is perpendicular to the prevailing wind direction [11]. Two series of full-scale field measurement of counter-rotating VAWTs in a wind farm was reported in two separate studies by Dabiri [6] and Kinzel et al. [14]. Dabiri [6] measured the aerodynamic performance of counter-rotating VAWTs in two-, three- and six-turbine configurations under natural wind conditions. In the two-VAWT configuration testing, Dabiri [6] found an increase, though small, in the counter-rotating turbines' performance compared to that of isolated installation. In the array testing, he reported the performance of the turbine located downstream of a counter-rotating pair recovered to within 5% of the isolated turbine performance when the streamwise distance increased to four turbine diameters [6]. This outcome was significantly emphasized by Dabiri [6] in comparison to the recovery distance of HAWTs which is up to 15-20D for a similar level of wake recovery. Dabiri's [6] results are comparable to those of Kinzel et al. [14] who found the flow velocities return to 95% of the undisturbed wind within 6D downstream of a counter-rotating pair. Kinzel et al. [14] studied the flowfield of an array of nine counter-rotating pairs of the same VAWTs and in the same wind farm as in Dabiri's study [6].

There have also been a few numerical simulations on counter-rotating VAWTs due to a recent interest in distributed small wind applications. Korobenko et al. [15] conducted a series of full-scale, three dimensional, time-dependent numerical simulations on a pair of counter-rotating VAWTs. They reported a slight drop in the predicted aerodynamic torque of the pair compared to the single turbine. Korobenko et al. [15] attributed this reduction to the small separation distance between the turbines (0.32D) that caused the turbines' blades to encounter the wake of the blade from other neighboring turbine. This resulted in higher drag on a particular blade, and consequently less aerodynamic torque [15]. The aerodynamic performance of pairs of counter-rotating and co-rotating VAWTs was also analyzed numerically by Duraisamy and

Lakshminarayan [16] in their two dimensional flow modeling. They found that pairs of counter-rotating or co-rotating VAWTs can generate more power than an isolated turbine by taking advantage of the beneficial induced velocity field [16].

As briefly reviewed, all recent works on counter-rotating VAWTs are either field measurements, analytical, or numerical simulations. Although these studies provide valuable information regarding the aerodynamic interaction of a group of wind turbines, they have some limitations. Field measurements are subject to various terrain effects, the stochastic nature of wind and meteorological conditions; making the repetition of the observation improbable if not impossible [4,10]. Numerical simulations still suffer from the lack of accuracy in turbulence modelling especially in separated flow regions [17], and analytical solutions use many simplifications which make them suitable mostly for engineering applications [18]. Wind tunnel testing, on the other hand, provides controlled conditions to systematically study this subject. Therefore, the objective of this study was to analyze the aerodynamic interaction of counter-rotating VAWT arrays using a series of wind tunnel measurements under controlled flows with uniform and steady wind conditions. The broader goal of the current research is to determine the optimal conditions for positioning turbines in a wind farm to achieve improved performance based on the constructive aerodynamic interaction among the turbines.

6.2 Experimental apparatus

6.2.1 Wind tunnel and VAWT model

Experiments were conducted in the atmospheric boundary layer wind tunnel at Western University whose specifications are detailed in Ref. [19]. The wind turbines were located 6 m downstream of the tunnel inlet section where the tunnel has a 3.3 m width and 2 m height cross section. The maximum achievable velocity is approximately 27.7 m/s in the empty working section.

Three identical VAWTs manufactured by Shanghai Aeolus Windpower Technology Co., Ltd [20] were used in the current study. These wind turbines are a commercial mini wind turbine, P-10 model, and each has five straight blades made of aluminum with a hollow section as depicted in Fig. 1. The blades of these wind turbines have a custom-made asymmetric airfoil profile which can be found in Ref. [21]. The dimensions of the turbines used in this work are listed in Table 1. Also included in this table is the optimum range of geometrical parameters of straight bladed VAWTs (SB-VAWT) according to Refs. [22-24]. As can be observed in Table 1,

the current wind turbines have the blade aspect ratio and the rotor aspect ratio very close to the optimum range, while their solidity factor is outside of this range. The connection between the blades and the central shaft was made possible via two supporting arms at intermediate locations of 0.33 and 0.66 of the blade height. The supporting arms were aluminum bars with rectangle cross-section of 2 mm by 25 mm. It should be noted that the blades of one turbine were inverted to make the rotational direction of the rotor opposite to its counterpart. This was done in order to create a pair of counter-rotating turbines.

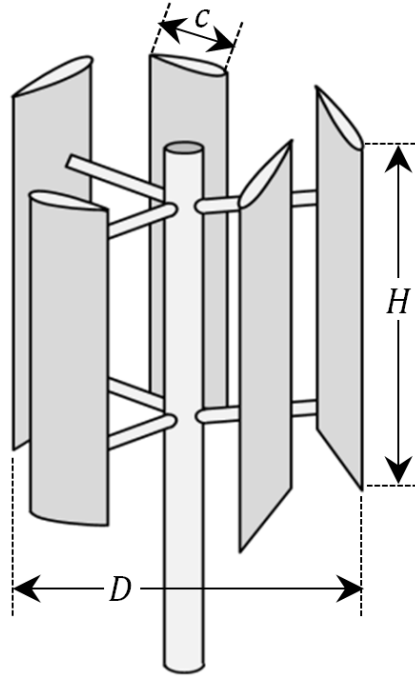


Figure 1: A schematic of a SB-VAWT

Table 1: Geometrical parameters of the current SB-VAWT and the optimum range of these parameters

Parameter	Current SB-VAWT	Optimum range for SB-VAWTs
N	5	
c (m)	0.045	
H (m)	0.3	
D (m)	0.3	

H/D	1	[0.5 , 2]
AR	6.6	[10 , 20]
σ	1.5	[0.2 , 0.6]

Four different configurations of wind turbine arrays studied in the current research are described in Table 2. Due to space limitation, only the schematic of the three-VAWT configurations (Arrays 3 and 4) is presented here, in Fig. 2. The details of the other arrays can be extracted from this schematic and Table 2. In all turbine arrays listed in Table 2 the x-axis is a symmetry line and parallel to the tunnel side walls. The origin of the coordinate system, O , is located 20D downstream from the wind tunnel inlet section and 5.5D from tunnel side walls as indicated in Fig. 2. The shaft centerline of all turbines in Arrays 1 and 2 was positioned along the y-axis, while the spacing of these arrays can be found in Table 2. In Arrays 3 and 4, two turbines were located along the y-axis, and the third turbine is installed downstream of the two upstream ones along the x-axis, as can be observed in Fig. 2. It should also be noted that the aerodynamic performance of each wind turbine was measured individually while installed at the origin of the coordinate system.

Table 2: Description of different configurations of wind turbine arrays studied

Array #	Array description	Spacing	Distance from wall	Figure
1	Two-VAWT, counter-rotating	$s/D = 1$	$w/D = 4$	4
2	Two-VAWT, co-rotating	$s/D = 1$	$w/D = 4$	5
3	Three-VAWT, triangular configuration, several downstream distances	$s/D = 0.5,$ $b/D = 1.5, 3, 4.5$	$w/D = 4.25$	7
4	Three-VAWT, triangular configuration, several separation distances	$b/D = 4.5$ $s/D = 0.5, 1, 1.5$	$w/D < 3.75$	8

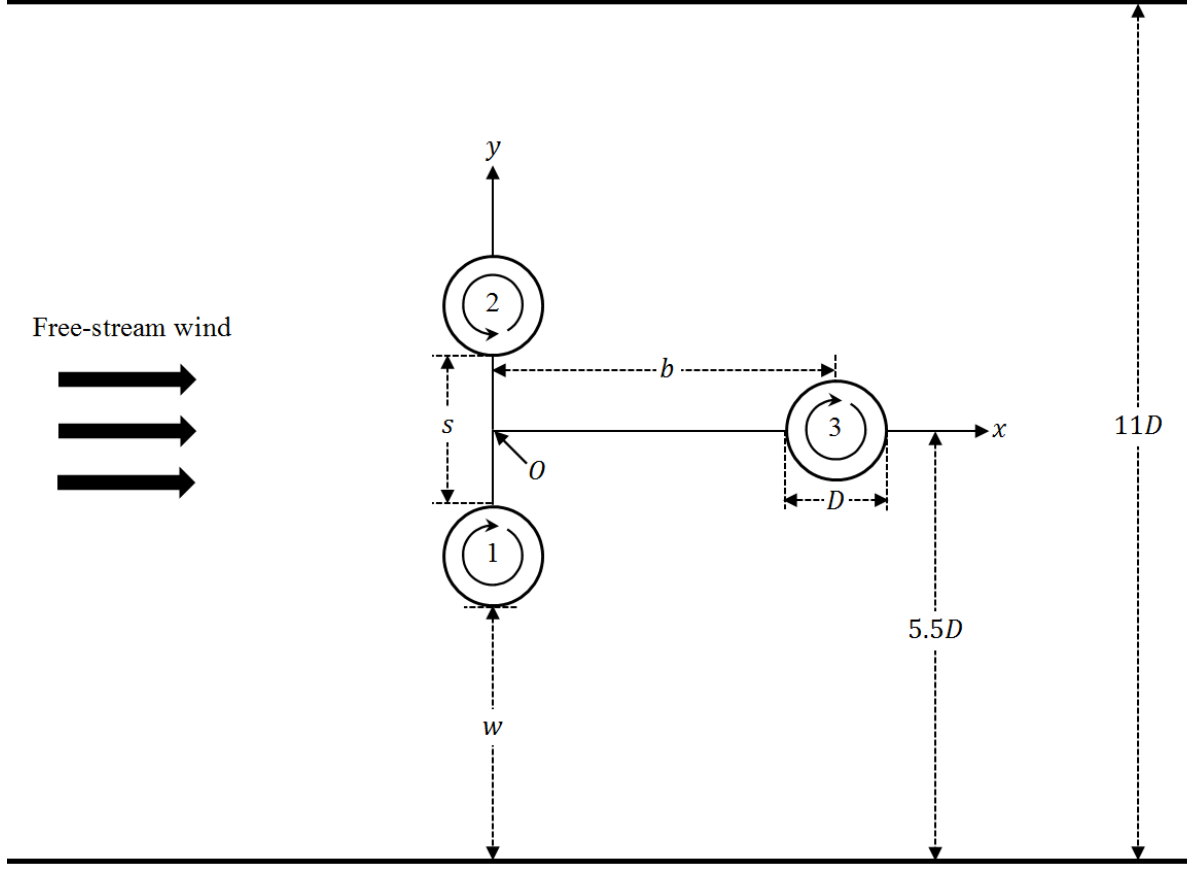


Figure 2: Top-view schematic of the wind tunnel test section showing a three-VAWT array in a triangular configuration

Even though wind tunnel testing benefits from controlled flow conditions, it suffers from some sources of error, most notably, the blockage effects. VAWTs form a unique aerodynamic obstruction in wind tunnels since the flowfield around them is asymmetric, unsteady, separated and highly turbulent. The tunnel blockage influences the turbine output power, and this effect depends upon parameters such as the turbine solidity, the operating tip speed ratio, and the rotor swept area to the tunnel size ratio [25]. A review on different methodologies used to characterize the VAWT blockage was published by Ross and Altman [26]. They proposed a blockage ratio for VAWTs in wind tunnel testing as the following [26].

$$B = \frac{1}{4} \frac{\text{rotor frontal area}}{\text{test section area}} \quad (1)$$

The literature suggests no correction for output results of blockage ratios less than 5% [25-27]. Among the several turbine arrays studied in the current work, the three-VAWT

configuration had the highest blockage ratio, approximately 1.2%, and hence, no blockage correction was required in the current study.

6.2.2 Data acquisition and processing

A Pitot-static tube connected to a digital manometer (DWYER series 475) was used to measure the free-stream velocity in the wind tunnel at the beginning of each test. The Pitot tube was inserted through a small hole on the tunnel ceiling. The turbulence intensity of the free-stream flow was measured by a TSI hot-wire unit operating at constant temperature mode with a normal 1-D probe and determined by

$$Tu(\%) = \frac{u_{rms}}{\bar{U}} \times 100 \quad (2)$$

where \bar{U} is time-averaged value of the streamwise velocity signal and u_{rms} is the root-mean-square of the velocity fluctuations in the streamwise direction calculated from

$$u_{rms} = \sqrt{\sum_{i=1}^n \frac{(U_i - \bar{U})^2}{n-1}} \quad (3)$$

More information regarding the procedure for determining the turbulence intensity from hot-wire measurements can be found in Ref. [28]. The maximum uncertainty in free-stream velocity and turbulence intensity was determined to be about 4.5% and 8%, respectively.

In order to measure the output power of the wind turbines, three identical external loads were connected to each turbine outlet. These external loads were HS series power resistors manufactured by TE Connectivity Co. having 150 ohms electrical resistance. This type of resistor was used to mimic the turbines' intended operation as part of a battery charging system. Each power resistor was connected to the wind turbine generator which was a three-phase permanent magnet generator. The AC current created by the turbine generators was converted into a DC current using a 1N5399 MIC rectifier. The output DC voltage across each resistor was measured by a National Instrument 9215 data acquisition card at a sampling rate of 1 kHz over 120 seconds in each experiment. The uncertainty in voltage measurement by this method was deduced to be less than 0.1 volts. The rms current of the circuit, I , was then calculated and used to determine the amount of power dissipated within the resistor as

$$P_l = R_l I^2 \quad (4)$$

The wind turbine total power output was then calculated by adding up the electrical power dissipated by the external load and the power consumed to overcome the losses in the

internal components of the turbine's electrical circuit including the windings and the rectifier as detailed in Ref. [21].

The rotational speed of the rotor was measured using an optical tachometer PLT200 manufactured by Monarch Instruments. This tachometer which has up to 8 m of measurement distance range was located outside of the wind tunnel test section, mounted on a tripod. In testing cases where more than one turbine was involved, the tachometer was used in sequence to measure the rotational speed of the turbines individually. The uncertainty in rotor speed measurement and other performance parameters was estimated according to the procedure described in Ref. [28] and plotted as typical error bars at selected data points in the next section.

6.3 Results and discussion

6.3.1 Two-VAWT arrays

The results of performance testing of Arrays 1 and 2 which are two-turbine arrays are presented in this section. The turbines in Arrays 1 and 2 were operated in a free-stream flow having a low turbulence level along the turbine's blade span. The streamwise mean velocity and turbulence intensity profiles of the free-stream flow against the vertical distance from the wind tunnel floor, z , are plotted in Fig. 3 in the empty working tunnel while free-stream velocity was constant at 9.5 m/s. It should be noted that the vertical distance of the lower edge of the wind turbine blades from the tunnel floor is 0.15 m. This indicates that the $0.5 < z/H < 1.5$ portion of the profiles shown in Fig. 3 correspond to the turbine blades' span. The same low-turbulence free-stream flow was used when testing the individual turbines of Arrays 1 and 2 in an isolated installation. The free-stream wind speed was varied from 6 to 14 m/s for all arrays tested in 2 m/s increments.

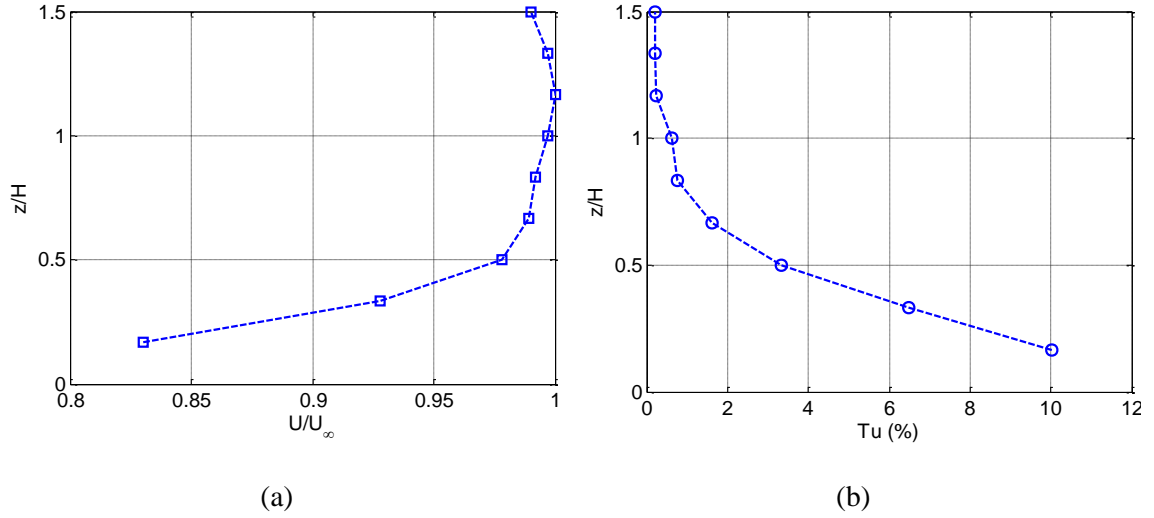


Figure 3: (a) Mean velocity and (b) turbulence intensity profiles of the free-stream flow versus vertical distance from the wind tunnel floor in the empty working tunnel for $U_\infty=9.5$ m/s.

Figure 4 displays the results of performance testing of Array 1 which is a pair of counter-rotating VAWTs having a separation distance of one rotor diameter. Also, several output parameters reported in Fig. 4 for the VAWTs tested in this configuration were compared to the measurements performed on the same wind turbines tested in a single installation. The turbines' power output and rotational speed are plotted in Figs. 4a and 4b, while Fig. 4c shows the turbine performance curve in terms of power coefficient, C_p , versus tip speed ratio, λ . These parameters are defined as [22]

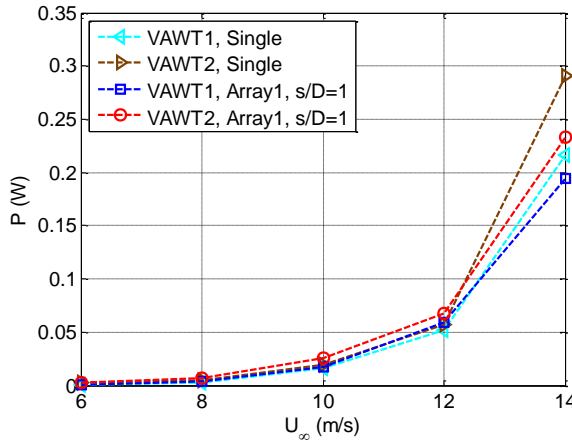
$$\lambda = \frac{R\omega}{U_\infty} \quad (5)$$

$$C_p = \frac{P}{0.5\rho A_r U_\infty^3} \quad (6)$$

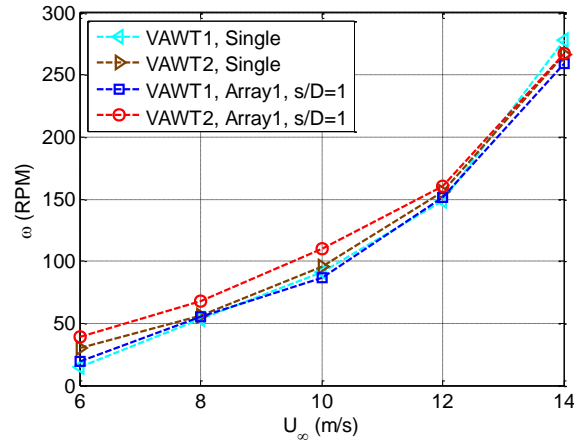
Figures 4a and 4b show an increasing trend for power output and rotational speed versus wind speed, as expected. A dramatic increase can be observed for these parameters especially for the power output when wind speed increases from 12 to 14 m/s. A possible reason for this jump is the improved operational range of the turbine at this wind speed. This is observable in Fig. 4c where the turbine reaches higher power coefficient and tip speed ratio at wind speed of 14 m/s. According to Fig. 4c, the power coefficient takes on very small values and the tip speed ratio reaches just above 0.3. This range of operational tip speed ratio indicates that the turbine blades are partially under stall conditions. A wind turbine may not be considered useful for power

generation since these ranges of parameters are very small. A reason for such small ranges of parameters for the turbines used in this work is that the solidity factor of these turbines is not in the optimum range for SB-VAWTs as discussed in Table 1.

Comparing the results of group installation to those of single installation in Figs. 4a-c shows that the turbine output parameters are very close to each other in both cases. This indicates that the turbines performance is not affected negatively by the neighbouring turbine, which is the case in HAWT farms for the same spacing. Moreover, the ratio of turbine power coefficient in the group installation to the single installation remains just above unity for all wind speed tested except for 14 m/s (see Fig. 4d). A quantitative comparison may not be valid for this graph (Fig. 4d) since all variations of the power coefficient are in the uncertainty limits (see Fig. 4c). Despite, it can be concluded that installing two VAWTs in a counter-rotating configuration perpendicular to the free-stream flow direction results in a slight improvement of each turbine performance, possibly due to the positive interaction of the induced flows around them as suggested by the literature.



(a)



(b)

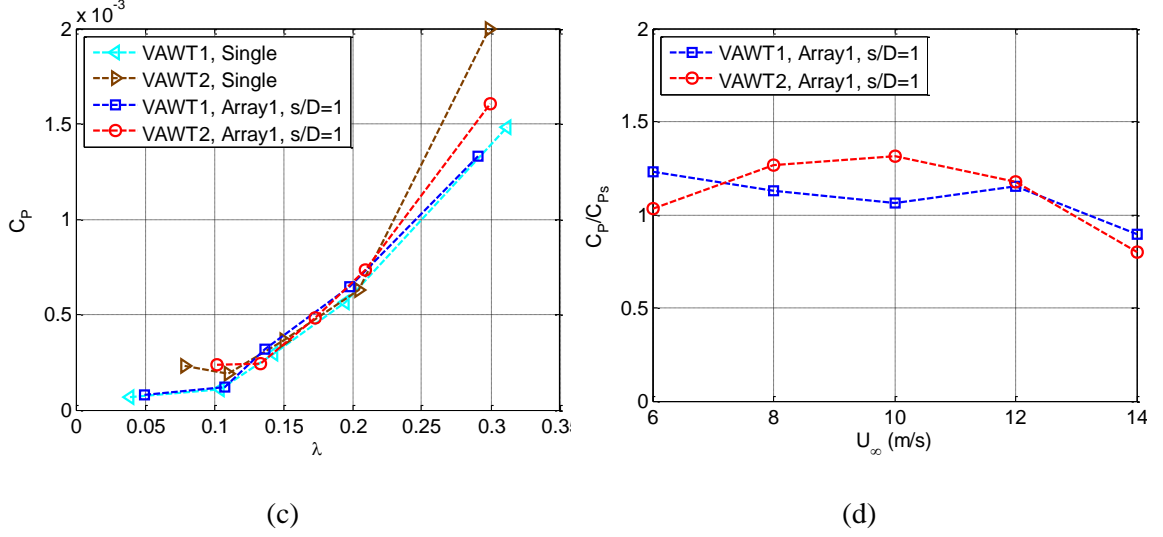


Figure 4: Performance parameters for Array 1 (counter-rotating pair) compared to the single installation

A co-rotating pair which is a commonly installed configuration in VAWT farms was also tested in the current wind tunnel study, denoted as Array 2. Figure 5 shows the output results of this co-rotating pair where the turbine spacing was one rotor diameter. Almost the same trends observed for the power output and rotational speed in Array 1 can be seen in Array 2 too (see Figs. 5a and 5b). These trends include the dramatic increase in power output and rotational speed at 14 m/s which may be attributed to the improved operational range of the turbine at this wind speed as evident in Fig. 5c.

By comparing the output parameters of turbines in single and group installations in Figs. 5a-c, it can be observed that the aerodynamic performance of turbines in co-rotating configuration exhibits a decreasing trend with respect to the wind speed, even though the changes are small. This trend can be more clearly seen in Fig. 5d where the ratio of turbine power coefficient in the group installation to the single installation drops from values over unity to values below unity as the free-stream velocity increases. The positive aerodynamic interaction at lower wind speeds may be due to an overall circulating bulk of fluid forming around the pair, while this structure seems to be destructed at higher velocities. This postulation needs to be verified via detailed flow measurements.

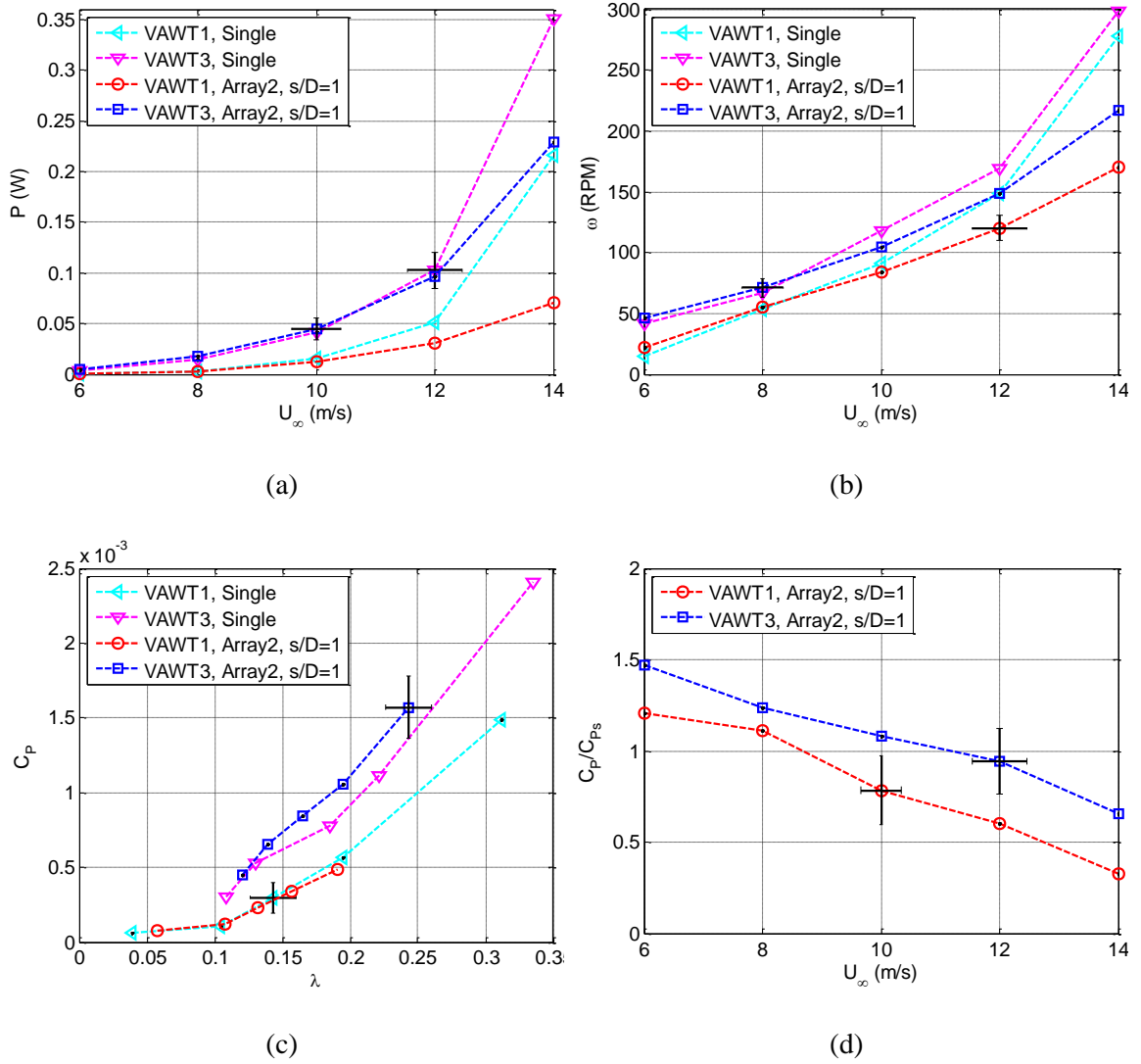


Figure 5: Performance parameters for Array 2 (co-rotating pair) compared to the single installation

6.3.2 Three-VAWT arrays

The effect of a counter-rotating pair on the aerodynamic performance of a downstream turbine is studied in Arrays 3 and 4. Only the output parameters of VAWT 3 are discussed in this section since the performance variations of this turbine is the main goal of the current discussion. The aerodynamic performance of VAWT 3 in several group installations were compared the performance of this VAWT in the isolated installation at two different flow conditions. One of these flows had a low turbulence level of 0.2% which is the same turbulence level used for testing

the groups of turbines. In addition, a turbulent free-stream flow having turbulence intensity in the range of 4% to 6% varying along the turbine blade span was used in testing VAWT 3 in the isolated installation. This free-stream turbulence was created by a turbulence generator located upstream of the turbine at the tunnel inlet section spanning the whole tunnel's width. This turbulence generator consisted of a series of equilateral triangles having sides of 0.13 m. This turbulent flow testing was performed to create a turbulent reference base for comparison purposes with the group installation of Arrays 3 and 4 in which VAWT 3 was operating in the turbulent wake of a counter-rotating pair. Due to the complexity of the wake region of the counter-rotating pair, it was extremely difficult to generate a turbulent flow that mimics the flow structure of this region. Therefore, the turbulent flow results should be interpreted with some care when comparing to the results of the group configurations. Figure 6 shows the mean velocity and turbulence intensity profiles of the free-stream flow in the empty working tunnel section while free-stream velocity was constant at 9.5 m/s. Again, it is noteworthy to mention that the $0.5 < z/H < 1.5$ portion of the profiles presented in Fig. 6 correspond to the turbine blades' span.

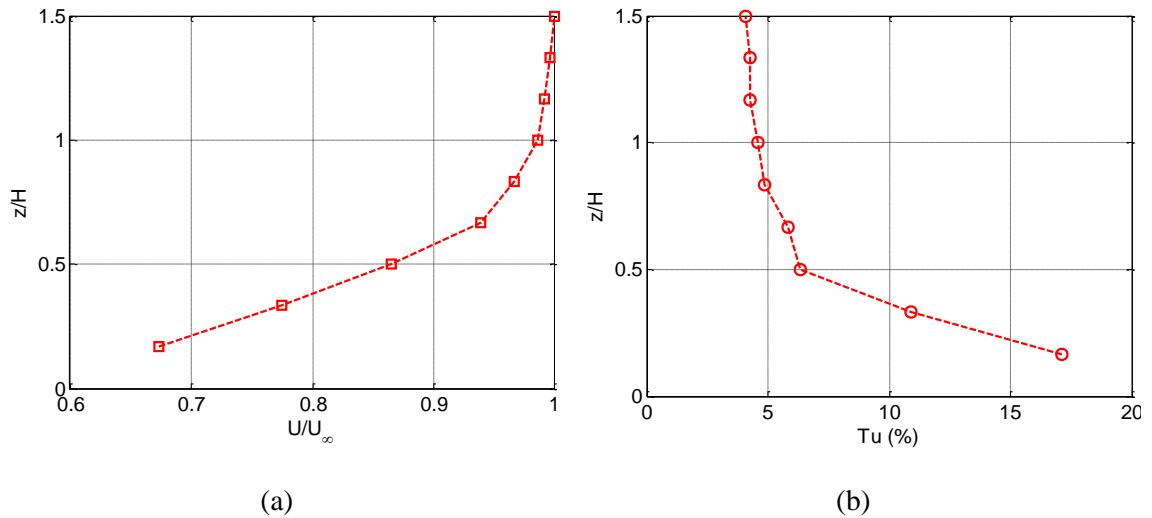


Figure 6: (a) Mean velocity and (b) turbulence intensity profiles of the free-stream flow against the vertical distance from the wind tunnel floor in the empty working tunnel using a turbulence generator at the tunnel inlet, $U_\infty=9.5$ m/s.

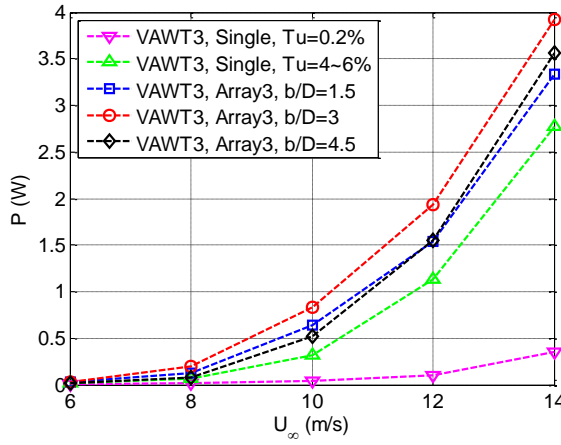
The power output, rotational speed and performance curves of the downstream turbine at different conditions of Array 3 are plotted in Figs. 7a, 7b and 7c, respectively. An expected increasing trend for power output and rotational speed versus wind speed is observed in Figs. 7a and 7b, for all cases. Comparing the turbine output in the single installation under low and high

turbulence flow conditions indicates that the power output and rotational speed of the turbine were significantly increased with increasing the free-stream turbulence (see Figs. 7a and 7b). Following the same comparison in Fig. 7c, it can be observed that the high turbulence flow also increases the turbine power coefficient and tip speed ratio over the same range of wind speed. This increase can be attributed to the effect of free-stream turbulence on a single blade as well as a SB-VAWT. As known from the literature, the free-stream turbulence improves the blade aerodynamic efficiency by increasing the lift-to-drag ratio, delaying the dynamic stall, and postponing the flow separation over the blade surfaces [29-31]. As can be deduced from the tip speed ratio range in Fig. 5c, the turbine blades are operating in the stall region at the low turbulence flow case [22,24,32]. Therefore, it seems that the free-stream turbulence improves the turbine performance by enhancing the aerodynamic efficiency of its blades.

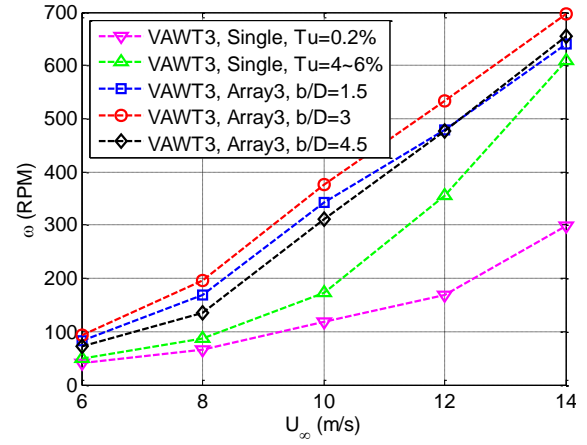
Comparing the downstream turbine's output in single and group installations in Figs. 7a-c shows that the aerodynamic performance of this turbine is enhanced when operating downstream of a counter-rotating pair. According to Figs. 7a and 7b, the output power and rotational speed of the downstream turbine is increased in all cases compared to the isolated installation in both flows with different turbulence levels. Figure 7c also shows that the performance curves of the downstream turbine are extended to the higher tip speed ratio range compared to the single turbine case. Also evident in Fig. 7c, the slope of increasing power coefficient versus tip speed ratio is larger in group installations than the single installation. The ratio of turbine power coefficient in the group installation to that of the single installation at constant wind speeds is plotted in Fig. 7d for single VAWT testing in low turbulence flow, and in Fig. 7e for single VAWT testing in high turbulence flow. As can be observed in these figures, the ratios presented are larger than unity at all turbine configurations tested. This is promising in that the groups of VAWTs in a wind farm can be installed in such a configuration to achieve higher efficiencies. Another interesting outcome from these results is the power coefficient ratio reaches significantly higher values when compared to the low turbulence flow over a single turbine. This ratio takes values as high as 20 when compared to the single VAWT testing in low turbulence flow (see Fig. 7d), while the highest ratio in comparison with the high turbulence flow over a single turbine is just below 3 (see Fig. 7e). This may be an indication of the notion that the flowfield downstream a counter-rotating pair has characteristics closer to those of a turbulent flow.

Figure 7 also shows the effect of streamwise distance of the downstream VAWT from the counter-rotating pair on the aerodynamic performance of the downstream turbine. The downstream turbine was tested at three streamwise distances of 1.5, 3, and 4.5 rotor diameters

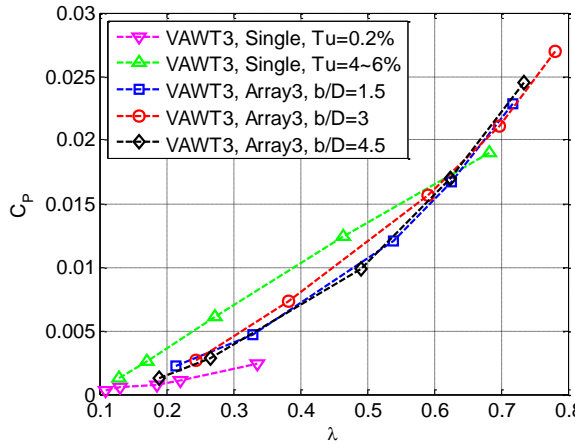
from the pair while the spacing between the pair was kept constant at half a rotor diameter. No monotonic trend can be concluded from Fig. 7 regarding the particular effect of the downstream distance. This figure shows an enhancement in the aerodynamic performance of the downstream turbine when the downstream distance increases from 1.5D to 3D, while a drop is observed with further increase in the downstream distance to 4.5D. This trend is more recognizable in Fig. 7d and 7e as many data points collapse onto each other in other graphs of Fig. 7. For the turbine spacing studied in Fig. 7, it may be concluded that the optimum downstream distance is somewhere between 1.5D and 4.5D, close to 3D downstream of the counter-rotating pair.



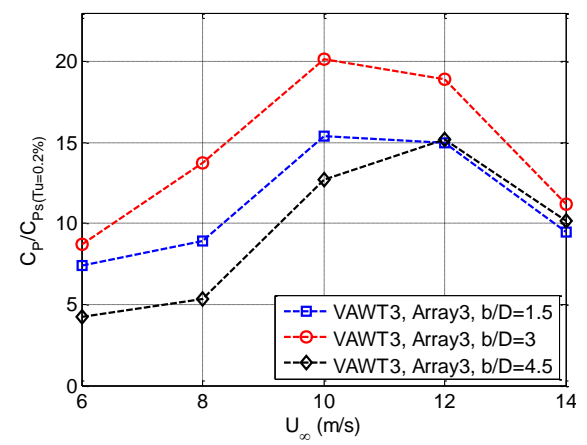
(a)



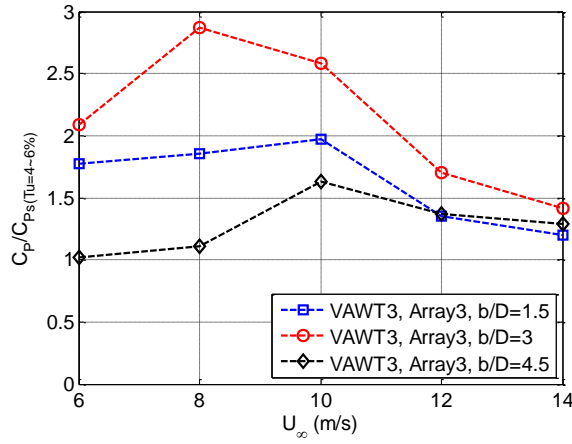
(b)



(c)



(d)



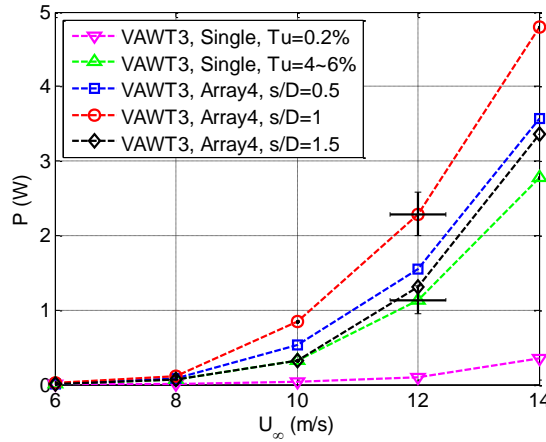
(e)

Figure 7: Performance parameters for Array 3 (three-VAWT configuration) and the effect of streamwise distance of the downstream turbine from the counter-rotating pair on the downstream turbine performance

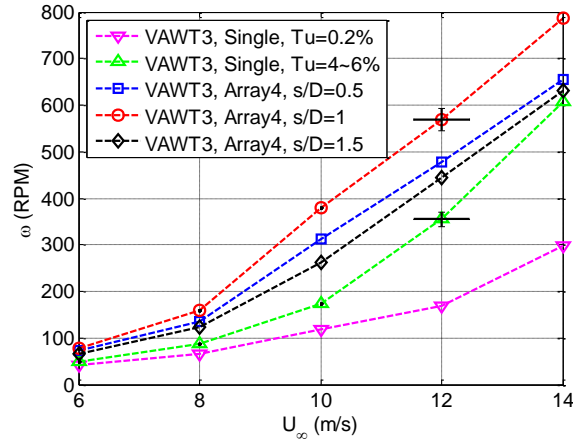
The aerodynamic performance of VAWT 3 operating downstream of a counter-rotating pair is also analyzed in Fig. 8 while the turbine spacing in the pair was varied. Figures 8a and 8b show the power output and rotational speed of the downstream turbine at different conditions, while the performance curves of this turbine are displayed in Fig. 8c. Comparing the downstream turbine output in single and group installations in Figs. 8a-c indicates that the aerodynamic performance of this turbine is improved when operating downstream of a counter-rotating pair, almost in all cases and at a majority of wind speeds. It can be observed in Figs. 8a and 8b that the output power and rotational speed of the downstream turbine is increased in all cases compared to the isolated installation having different turbulence levels. The downstream turbine in such a group installation also operates at higher tip speed ratio range and takes larger power coefficients, as evident in Fig. 8c. Figures 8d and 8e show the ratio of turbine power coefficient in the group installation to that of the single installation in low and high turbulence flows, respectively. The power coefficient ratio is larger than unity at almost all turbine arrays studied which is an indication of the positive effect of the counter-rotating pair on the downstream turbine. This ratio reaches values as high as 22 when compared to the isolated turbine testing in low turbulence flow as evident in Fig. 8d, while the highest power coefficient ratio of this array to the single turbine testing under high turbulence flow is just above 2.5 as can be seen in Fig. 8e. As mentioned

earlier when discussing Fig. 5, this is presumably because the flowfield downstream a counter-rotating pair has characteristics closer to those of a flow having high free-stream turbulence.

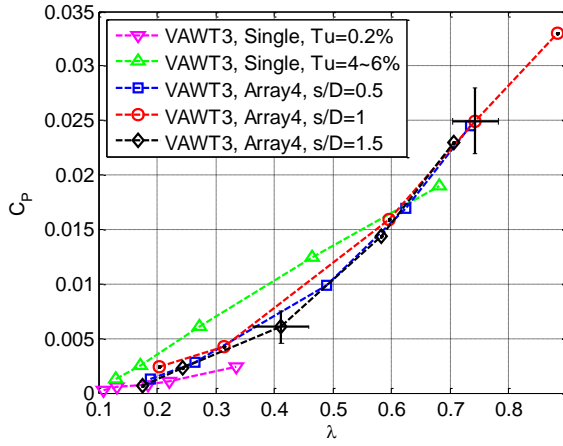
The effect of turbine spacing in the counter-rotating pair on the aerodynamic performance of the downstream turbine is also depicted in Fig. 8. Three separation distances of 0.5, 1, and 1.5 rotor diameters were tested while the streamwise distance of the downstream turbine from the counter-rotating pair was kept constant at 4.5 rotor diameter. For this VAWT configuration, it can be observed that the downstream turbine reaches higher efficiencies when the spacing between the two turbines of the counter-rotating pair increased from 0.5D to 1D, while a decrease in its aerodynamic performance is evident with increasing the spacing from 1D to 1.5D (see Figs. 8d and 8e). The variation in the downstream turbine performance with respect to the pair spacing may be attributed to the characteristics of the jet-type flowfield between the upstream pair. Detailed flow measurements can be an asset in this regard to shed some lights on the flow structure among the turbines. Nevertheless, for the flow conditions described in the current study, it may be concluded that a VAWT operating 4.5D downstream of a counter-rotating pair reaches its maximum efficiency when the spacing between two turbines of the pair is around a rotor diameter.



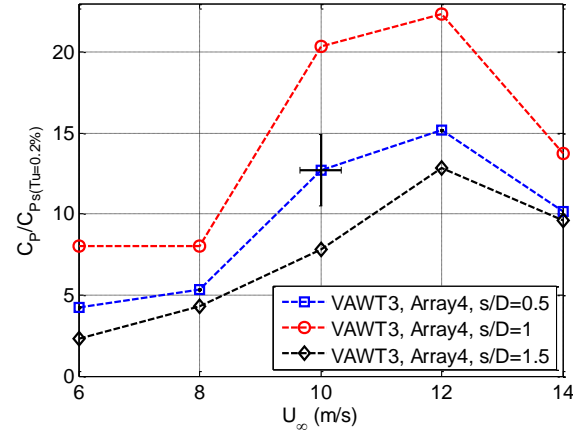
(a)



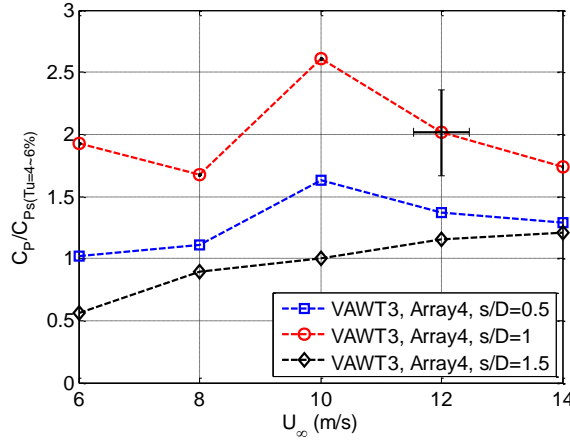
(b)



(c)



(d)



(e)

Figure 8: Performance parameters for Array 4 (three-VAWT configuration) and the effect of turbine spacing in the counter-rotating pair on the downstream turbine performance

The optimum range of spacing between two counter-rotating turbines as well as the downstream distance of the third turbine depends on several parameters such as the turbines physical parameters and the tip speed ratio [6,33]. For the range of flow parameters studied in the current research, the optimum range of the streamwise distance of the downstream turbine from the counter-rotating pair and the spacing between the two turbines of the pair was determined to be around three and one rotor diameter, respectively. Nonetheless, for all spacing parameters the improvement in the downstream turbine performance was in the range of 1 to 3, except for a few data points where below unity, when compared to the isolated turbine testing in high turbulence

flow. The same order of magnitude enhancement was also reported in the field-testing works [6,14]. This indicates that this range of performance enhancement is fairly achievable with counter-rotating SB-VAWT arrays, provided optimum range of spacing is selected.

The promising performance improvement achieved in the current research can be further examined by studying a wider range of spacing parameters as well as considering offset configuration of the downstream turbine from the upstream pair's centerline. Additionally, similar studies on the aerodynamic interaction of circular cylinders may provide insights to help us further analyze the VAWTs interaction. The crossflow past two stationary side-by-side circular cylinders where the free-stream is perpendicular to the line connecting the centers of cylinders is widely studied in the literature [34-36]. Sumner et al. [34] conducted extensive experiments on crossflow past two cylinders where the Reynolds numbers was in the range of 500 to 3000 and the gap (rim-to-rim distance) between two cylinders varied from 0 to 5D. They categorized the flow pattern into three groups based on the gap between cylinders. For small spacing of $0 < s/D < 0.25$, the single bluff-body flow was observed where the higher-momentum fluid started entering through the gap reducing the drag of both cylinders and increasing the streamwise extent of the vortex region. For intermediate spacing of $0.25 < s/D < 1.25$, the biased flow behaviour was reported. In this flow pattern, the cylinder towards which the flow is biased has a narrow near-wake and higher frequency vortex shedding, while the other cylinder has a wider near-wake and lower frequency vortex shedding. The symmetric flow pattern was observed for large spacing of $1.25 < s/D < 5$ where the biased flow disappeared and cylinders behave as independent, isolated bluff bodies.

The effect of side-by-side cylinders on a downstream cylinder is also studied in the literature. Gu and Sun [37] and Bao et al. [38] categorized the crossflow past equilateral-triangular cylinders into three groups based on the cylinders spacing. For small spacing of $0.7 < s/D < 1$, the proximity interference dominates the flow pattern which is exhibited as the single bluff body flow behaviour. For intermediate spacing of $1.5 < s/D < 2$, the vortex shedding occurs always behind the downstream cylinder and this cylinder considerably suppresses the vortex shedding from the upstream ones. This flow pattern reflects the complicated effect from the combination of proximity and shear layer interferences. For large spacing of $s/D > 3$, the flow feature is mainly dominated by shear layer interference and a fully developed vortex shedding occurs behind all the cylinders.

In addition to the flow past stationary cylinders, the aerodynamic interaction of counter-rotating circular cylinders was investigated in the literature. Two major flow problems were

studied for the crossflow past two side-by-side counter-rotating circular cylinders, namely doublet-like and reverse doublet-like configurations. The reverse doublet-like configuration in which the induced flow between two cylinders is in the same direction of free-stream is more interesting to us since its rotational direction is the same as that of in counter-rotating VAWTs in the current research. The doublet-like configuration, however, attracted more researchers as it represents a classical fluid flow problem, namely the doublet flow. There are two works in the literature by Kumar et al. [39] and Chan et al. [40] that studied both doublet-like and reverse doublet-like cases and compared them together. The focus of these studies was on the wake structure and vortex shedding suppression.

Kumar et al. [39] studied the flow past two rotating cylinders with the same rotation rates in a side-by-side configuration in the Reynolds number range of 100 to 500, spacing range of $0.8D < s/D < 6.5D$, and tip speed ratio range of 0 to 5. In the doublet-like configuration, increasing the rotation rate made the vortices downstream the cylinders become more compact. There is a critical rotation rate where a complete suppression of vortex shedding can be achieved. This critical value of tip speed ratio was reported to be around 2 almost for all flow conditions studied in the doublet-like configuration. The results of Kumar et al. [39] are in agreement with those of Chan et al. [40] and Yoon et al. [41]. For reverse doublet-like configuration, however, the vortex shedding suppression was only observed for $Re < 200$. At larger Reynolds numbers, increasing the rotation rate made the wake wider and more turbulent. Chan et al. [40] attributed this to the chaotic mixing of the wake due to the relative rotation directions.

The studies on the flow structure of counter-rotating cylinders suggest that the flow around a pair of counter-rotating VAWTs depends on the turbine spacing and the tip speed ratio. It can also be inferred that the suppression of vortex shedding downstream of the turbines may be a key element in forming an accelerated wind zone between the two turbines in the pair to influence the downstream turbine positively. This calls for detailed flow measurements in the turbine wakes to characterize the wake flow and vortices shed from turbines based on the turbine rotational speed, wind velocity and turbine spacing.

6.4 Conclusion

A series of wind tunnel measurements was conducted to study the aerodynamic interaction of vertical axis wind turbines in group installations. This was done to systematically investigate the scenarios where constructive aerodynamic interaction occurs among the vertical

axis wind turbines. Installing two side-by-side turbines in a counter-rotating configuration resulted in a slight improvement in the aerodynamic performance over the sum of the isolated installation. The pair of counter-rotating vertical axis wind turbines also improved the power generation of a turbine located downstream of the pair substantially, possibly due to the beneficial channeled flowfield through the gap of the upstream pair. A series of tests were also performed to find the optimum range for the spacing parameters in the three-turbine arrays. Over the range of studied conditions, the output power of a vertical axis wind turbine operating downstream of a counter-rotating pair reached a local maximum when the streamwise distance from pair was three rotor diameters, and the spacing between two turbines of the pair was one rotor diameter.

6.5 References

- [1]. Son, E., Lee, S., Hwang, B., Lee, S., Characteristics of turbine spacing in a wind farm using an optimal design process, *Renewable Energy*, 2014; 65: 245-249.
- [2]. Meyers, J., Meneveau, C., Optimal turbine spacing in fully developed wind farm boundary layers, *Wind Energy*, 2012; 15(2): 305-317.
- [3]. Tescione, G., Ragni, D., He, C., Simão Ferreira, C.J., van Bussel, G.J.W., Near wake flow analysis of a vertical axis wind turbine by stereoscopic particle image velocimetry, *Renewable Energy*, 2014; 70: 47-61.
- [4]. Ganesh, R.R., Rickerl, T.L., Klimas, P.C., Aerodynamic interference of vertical axis wind turbines, *Journal of Propulsion and Power*, 1990; 6(5): 645-653.
- [5]. McKay, P., Carriveau, R., Ting, D.S.-K., Wake impacts on downstream wind turbine performance and yaw alignment, *Wind Energy*, 2013; 16(2): 221-234.
- [6]. Dabiri, J.O., Potential order-of-magnitude enhancement of wind farm power density via counter-rotating vertical-axis wind turbine arrays, *Journal of Renewable and Sustainable Energy*, 2011; 3, 043104.
- [7]. Sai, P.C., Yadav, R.S., Raj, R.N., Gupta, G.R.K., Design and simulation of high efficiency counter-rotating vertical axis wind turbine arrays, *International Conference and Utility Exhibition 2014 on Green Energy for Sustainable Development (ICUE 2014)*, March 2014, Pattaya City, Thailand.
- [8]. Lignarolo, L.E.M., Ragni, D., Krishnaswami, C., Chen, Q., Simão Ferreira, C.J., van Bussel, G.J.W., Experimental analysis of the wake of a horizontal-axis wind-turbine model, *Renewable Energy*, 2014; 70: 31-46.
- [9]. McKay, P., Carriveau, R., Ting, D.S.-K., Farm wide dynamics: the next critical wind energy frontier, *Wind Engineering*, 2011; 35(4): 397-418.
- [10]. Sørensen, B., *Renewable energy: Its physics, engineering, use, environmental impacts, economy, and planning aspects*, Elsevier Academic Press, New York, 2004.

- [11]. Thomas, R.N., Coupled vortex vertical axis wind turbine, US Patent No. 6,784,566, 2004.
- [12]. Tjiu, W., Marnoto, T., Mat, S., Ruslan, M.H., Sopian, K., Darrieus vertical axis wind turbine for power generation I: Assessment of Darrieus VAWT configurations (Review), *Renewable Energy*, 2015; 75: 50-67.
- [13]. Pope, K., Dincer, I., Naterer, G.F., Energy and exergy efficiency comparison of horizontal and vertical axis wind turbines, *Renewable Energy*, 2010; 35: 2102-2113.
- [14]. Kinzel, M., Mulligan, Q., Dabiri, J.O., Energy exchange in an array of vertical-axis wind turbines, *Journal of Turbulence*, 2012; 13(38): 1-13.
- [15]. Korobenko, A., Hsu, M.-C., Akkerman, I., Bazilevs, Y., Aerodynamic simulation of vertical-axis wind turbines, *Journal of Applied Mechanics, Transaction ASME*, 2014; 81, 021011.
- [16]. Duraisamy, K., Lakshminarayan, V., Flow physics and performance of vertical axis wind turbine arrays, 32nd AIAA Applied Aerodynamics Conference, AIAA 2014-3139, June 2014, Atlanta, GA.
- [17]. Li, C., Zhu, S., Xu, Y.L., Xiao, Y., 2.5D large eddy simulation of vertical axis wind turbine in consideration of high angle of attack flow, *Renewable Energy*, 2013; 51: 317-330.
- [18]. Bedon, G., Castelli, M.R., Benini, E., Optimization of a Darrieus vertical-axis wind turbine using blade element - momentum theory and evolutionary algorithm, *Renewable Energy*, 2013; 59: 184-192.
- [19]. Wind Tunnel Testing: A General Outline, The Boundary Layer Wind Tunnel Laboratory, The University of Western Ontario, London, Canada, May 2007.
- [20]. Shanghai Aeolus Windpower Technology Co., Ltd., <<http://www.sawt.com.cn/>>.
- [21]. Ahmadi-Baloutaki, M., Carriveau, R., Ting, D.S.-K., Performance of a vertical axis wind turbine in grid generated turbulence, *Sustainable Energy Technologies and Assessments*, In press, Available online January 2015.
- [22]. Paraschivoiu I., Wind turbine design - with emphasis on Darrieus concept, Montreal, Polytechnic International Press, 2002.
- [23]. Islam, M. Analysis of fixed-pitch straight-bladed VAWT with asymmetric airfoils, PhD Thesis, University of Windsor, Windsor, Canada, 2008.
- [24]. Ahmadi-Baloutaki, M., Carriveau, R., Ting, D.S.-K., Straight-bladed vertical axis wind turbine rotor design guide based on aerodynamic performance and loading analysis, *Proceeding of Institution of Mechanical Engineers, Part A: Journal Power & Energy*, 2014; 228(7): 742-759.
- [25]. Garrett, C., Cummins, P., The efficiency of a turbine in a tidal channel, *Journal of Fluid Mechanics*, 2007; 588: 243-51.

- [26]. Ross, A., Altman, A., Wind tunnel blockage corrections: Review and application to Savonius vertical-axis wind turbines, *Journal of Wind Engineering and Industrial Aerodynamics*, 2011; 99: 523-538.
- [27]. Dossena, V. , Persico, G., Paradiso, B., Battisti, L., Dell'Anna, S., Brighenti, A., Benini, E., An experimental study of the aerodynamics and performance of a vertical axis wind turbine in a confined and unconfined environment, *Journal of Energy Resources Technology*, Transactions of the ASME, 2015; 137(5), 051207.
- [28]. Ahmadi-Baloutaki, M., Carriveau, R., Ting, D.S.-K., Effect of free-stream turbulence on flow characteristics over a transversely-grooved surface, *Experimental Thermal and Fluid Science*, 2013; 51: 56-70.
- [29]. Hoffmann, J.A., Effects of free-stream turbulence on the performance characteristics of an airfoil, *AIAA Journal*, 1991; 29(9): 1353-1354.
- [30]. Devinant, P., Laverne, T., Hureau, J., Experimental study of wind-turbine airfoil aerodynamics in high turbulence, *Journal of Wind Engineering and Industrial Aerodynamics*, 2002; 90: 689-707.
- [31]. Amandolese, X., Szechenyi, E., Experimental study of the effect of turbulence on a section model blade oscillating in stall, *Wind Energy*, 2004; 7(4): 267-282.
- [32]. Armstrong, S., Fiedler, A., Tullis, S., Flow separation on a high Reynolds number, high solidity vertical axis wind turbine with straight and canted blades and canted blades with fences, *Renewable Energy*, 2012; 41: 13-22.
- [33]. Chen, X., Agarwal, R., Optimal placement of horizontal - and vertical-axis wind turbines in a wind farm for maximum power generation using a genetic algorithm, *ASME 2011 5th International Conference on Energy Sustainability*, ES 2011; August 2011, Washington, DC.
- [34]. Sumner, D., Wong, S.S.T., Price, S.J., Paidoussis, M.P., Fluid behaviour of side-by-side circular cylinders in steady cross-flow, *Journal of Fluids and Structures*, 1999; 13: 309-338.
- [35]. Carini, M., Giannetti, F., Auteri, F., On the origin of the flip-flop instability of two side-by-side cylinder wakes, *Journal of Fluid Mechanics*, 2014; 742: 552-576.
- [36]. Kim, S., Alam, M.M., Characteristics and suppression of flow-induced vibrations of two side-by-side circular cylinders, *Journal of Fluids and Structures*, 2015; 54(1): 629-642.
- [37]. Gu, Z., Sun, T., Classifications of flow pattern on three circular cylinders in equilateral-triangular arrangements, *Journal of Wind Engineering and Industrial Aerodynamics*, 2001; 89: 553-568.
- [38]. Bao, Y., Zhou, D., Huang, C., Numerical simulation of flow over three circular cylinders in equilateral arrangements at low Reynolds number by a second-order characteristic-based split finite element method, *Computers and Fluids*, 2010; 39: 882-899.

- [39]. Kumar, S., Gonzalez, B., Probst, O., Flow past two rotating cylinders, *Physics of Fluids*, 2011; 23: Article No. 014102.
- [40]. Chan, A.S., Dewey, P.A., Jameson, A., Liang, C., Smits, A.J., Vortex suppression and drag reduction in the wake of counter-rotating cylinders, *Journal of Fluid Mechanics*, 2011; 679: 343-382.
- [41]. Yoon, H.S., Kim, J.H., Chun, H.H., Choi, H.J., Laminar flow past two rotating circular cylinders in a side-by-side arrangement, *Physics of Fluids*, 2007; 19: Article No. 128103.

Chapter 7: Conclusions and recommendations

7.1 Research outcomes

Even though vertical axis wind turbines (VAWTs) play an important role in the small wind turbine market, their design and commercialization still encounter many challenges. A series of studies was presented in this thesis to improve the VAWTs design and enhance their aerodynamic performance.

In Chapter 2, a design guide for straight bladed-VAWTs (SB-VAWTs) based on the turbine aerodynamic performance and loading was presented. Formulation and aerodynamic analysis of SB-VAWT flowfield were also discussed to better comprehend the turbine operation. This design methodology can save significant amount of time and resources for future investigators in their initial design stage. This chapter also includes a design flowchart which summarizes the design process discussed in the current research. The optimum range of several design parameters including the rotor solidity factor, blade aspect ratio, and rotor aspect ratio has been determined and were found to be: $0.2 < \sigma_d < 0.6$, $10 < \mu_d < 20$, and $0.5 < (H/D)_d < 2$ respectively. The optimum range of these loads was determined with the goals of smooth rotational motion and maximum efficiency. The results indicate that the peak normal component of aerodynamic force is about six times larger than that of tangential component. Different cross sectional shapes of supporting arms have been assessed in terms of aerodynamic behavior and structural strength. It was verified that using airfoil shapes for supporting arms gives better aerodynamic response than using sharp edged sections such as rectangles or diamonds. The bending stresses acting on the blades have also been minimized to find the optimum locations of the blade-supporting-arm connection by identifying bending stress minima along the blade. These locations were at 21% and 79% along the blade length. This would lead to the most conservative bending stress distribution over the blade.

The effect of free-stream turbulence on VAWTs performance was studied experimentally in three stages in this thesis, discussed in Chapters 3, 4, and 5. Turbulent flows were generated in the wind tunnel using a grid in a shape of an orificed perforated plate with circular holes. These turbulent flows generated were quasi-isotropic having uniform mean flow profiles, free of any wind shear effects. Chapter 3 presented the results of two-dimensional wind tunnel testing of a VAWT blade under two levels of low and high free-stream turbulence. Aerodynamic force measurements demonstrated that high level of free-stream turbulence improves the blade

aerodynamic performance in stall and post-stall regions by delaying the stall and increasing the lift-to-drag ratio, while does not affect the blade in the pre-stall region significantly. Introducing free-stream turbulence to the flow over a VAWT blade decreased the mean velocity deficit and turbulence intensity. Free-stream turbulence also increased the wake thickness downstream of the blade, contributing to the higher involvement of the wake region with free-stream area.

In Chapter 4, the aerodynamic performance of a VAWT blade under two levels of low and high free-stream turbulence was studied experimentally by three-dimensional wind tunnel testing. The free-stream turbulence significantly altered the wing aerodynamic coefficients by delaying static stall, enhancing lift, and increasing drag. The tip vortex downstream of the wing has been captured with good accuracy through measurement of the velocity field using hot-wire anemometry. The results showed the free-stream turbulence does not notably affect the vortex trajectory along the streamwise axis, while increases the turbulence intensity peak. The circumferential velocity and vortex circulation were also increased under external turbulence with increasing streamwise distance at radial locations away from the vortex center.

After studying the effect of free-stream turbulence on the aerodynamic performance of a VAWT blade under two- and three-dimensional flow conditions in Chapters 3 and 4, the free-stream turbulence effect on a VAWT operation was studied in Chapter 5. The turbine power output was substantially increased in the presence of the grid turbulence at the same wind speeds, while the increase in turbine power coefficient due to the effect of grid turbulence was small at the same tip speed ratios. Among grid generated turbulent flows, the increase in power output with increasing turbulence intensity was marginal. Moreover, the self-starting behavior of the vertical axis wind turbine is improved under the influence of external free-stream turbulence.

Chapter 6 presented the experimental study on the aerodynamic interaction of VAWTs in array configurations. This was performed by conducting a series of wind tunnel measurements on several configurations of two- and three-turbine arrays. The counter-rotating configuration resulted in a slight improvement in the aerodynamic performance of each turbine compared to the single case, while the co-rotating installation caused the performance reduction of turbines at some free-stream velocities. Several measurements were also carried out for three-turbine arrays with different spacing where a turbine was operating downstream of a counter-rotating pair. An enhancement in the aerodynamic performance of the downstream turbine was observed almost in all arrays and at most of wind speeds. For the spacing parameters studied the optimum range of the streamwise distance of the downstream turbine from the counter-rotating pair and the spacing

between the two turbines of the pair was determined to be about three and one rotor diameters, respectively.

7.2 Recommendations for future works

The findings of the studies performed in this research mainly serve as recommendations to the improvement of VAWT aerodynamics. As VAWTs still encounter many challenges towards commercialization in a utility scale, the information presented in this thesis provides valuable insights to help understanding the aerodynamic behavior of this kind of turbines. While the analyses performed captured the general operating characteristics and performance of VAWTs under different flow conditions, recommendations can be made to further enhance the current analyses.

The approach modelled to analyze the VAWTs aerodynamics can be extended to include greater detail. Simplifications were made for a few parameters as the analyses were conducted for the initial design stage. Only the most important VAWT flow parameters including blade aspect ratio, dynamic stall, and supporting arms parasitic drag were considered in the present modelling. Further refinements can be added to such analytical approaches for more accurate results. Beyond the initial design phase, more precise and reliable numerical methods such as Large Eddy Simulation (LES) or vorticity transport modeling can be utilized to detail the three-dimensional flowfield around a wind turbine. Another interesting suggestion is to consider variable conditions for the incoming flow, instead of uniform free-stream velocity distribution, to include the effect of free-stream turbulence into the model.

The analytical approach used in this thesis was based on SB-VAWTs. This approach, however, can be modified to model the VAWTs with non-straight blades. This is of great importance as there has been a great interest on these VAWTs in the recent few years. The most common non-straight bladed VAWTs with good aerodynamic efficiency are the egg-beater type VAWTs with curved blades, VAWTs with canted blades, and VAWTs with helically twisted blades. Since the computational cost of modeling such turbines is very high, simple, yet robust analytical approaches can be extremely valuable to researchers, especially in the initial design stage.

The role of free-stream turbulence on the VAWTs operation was also studied in this thesis, even though up to limited details. All turbulent flows generated were quasi-isotropic having different levels of free-stream turbulence intensity, while free of any turbulence shear

effects. Therefore, a future research to complement the current study can be investigating the free-stream turbulence shear effects on the aerodynamic performance of VAWTs. Moreover, the range of free-stream turbulence intensity studied in this thesis was restricted due to the limitations of the grid turbulence generator utilized. Hence, studying the effect of free-stream turbulence intensity on the VAWTs operation in a larger range can be another idea for future research.

The aerodynamic interaction of a group of VAWTs was studied via wind tunnel testing in the present thesis, however the number of various arrays tested was limited. More turbine arrays can be examined in future studies to reach further comprehensive results on the VAWTs aerodynamic interaction. Moreover, the turbine output parameters measured in the current research were limited to the turbine power output and rotor speed as well as the free-stream velocity and turbulence details. Measurement of flowfield parameters in the wake of turbines and in the region between them can shed more lights on the underlying physics of their interaction. Hot-wire anemometry and Particle Image Velocimetry (PIV) can be employed for such measurements.

Another interesting recommendation for future research is to implement the boundary layer control techniques on the VAWT blades to enhance the VAWTs aerodynamic performance. This can be done by improving the aerodynamic performance of the VAWT blades in terms of the lift-to-drag ratio for Darrieus turbines. Applying passive boundary layer control such as machining grooves on the blades is a potential suggestion in this regard.

Appendix A: Effect of free-stream turbulence on flow characteristics over a transversely-grooved surface¹

Nomenclature

a	length of aluminum plate in streamwise and spanwise direction, 609 mm	u_{rms}	root-mean-square of the velocity fluctuations
b	spacing between every two consecutive grooves, 3.57 mm	U	streamwise velocity component
D	diameter of perforated plate hole, 50.8 mm	U_i	instantaneous velocity
e	width of a groove at the valley, 1.15 mm	U_{mean}	time-averaged velocity
F	flatness factor of streamwise velocity fluctuation	$U_{\infty up}$	upstream free-stream velocity, 8.12 m/s
h	depth of a groove, 1.62 mm	U_{∞}	local free-stream velocity at each streamwise section
L	total length of the plate in streamwise direction, 656.6 mm	w	width of a groove at the peak, 3.57 mm
N	number of sample points in hot-wire measurement, 2×10^6	x	streamwise distance from the leading edge of the plate
OPP	orificed perforated plate	y	vertical position from the surface
PDF	probability density function	Greek letters	
R_u	auto-correlation function	δ	boundary layer thickness
Re_L	Reynolds number based on plate's total length, $Re_L = U_{\infty up} L / \nu$, 3.4×10^5		energy dissipation rate per unit mass
Re_x	Reynolds number based on streamwise distance, $Re_x = U_{\infty up} x / \nu$	ε	
Re_{δ}	Reynolds number based on boundary layer thickness, $Re_{\delta} = U_{\infty up} \delta / \nu$	η	Kolmogorov microscale
S	skewness factor of streamwise velocity fluctuation	Λ	integral length scale
t	time	τ_{Λ}	integral time scale
Tu	turbulence intensity	ϑ	kinematic viscosity of air, $1.548 \times 10^{-5} \text{ m}^2/\text{s}$
u	streamwise velocity fluctuation, $u = U_i - U_{mean}$		

¹ This work was published as: "Ahmadi-Baloutaki, M., Cariveau, R., Ting, D.S.-K., Effect of free-stream turbulence on flow characteristics over a transversely-grooved surface, Experimental Thermal and Fluid Science, 2013; 51: 56-70."

A.1 Introduction

Boundary layer control is an important field of fluid mechanics. Of the two main categories of boundary layer control, active and passive, passive control has attracted greater consideration as it requires no auxiliary power and hence appears more economical and simpler to implement compared to its counterpart [1]. Surface modification by using grooves is a well-known passive flow control approach. Changing the surface geometry with transversely cut grooves can be used to control flow separation [2]. Transverse grooves can serve as vortex generators introducing vortices and increasing momentum of the boundary layer region [3]. In typical boundary layer flows, the momentum of near-wall fluid particles can be reduced by both the wall shear and the adverse pressure gradient. At some point, the retarded fluid particles cannot remain attached to the wall and depart or break away from the bounding surface. The surface streamline nearest to the wall leaves the body and the boundary layer is said to separate. The added energy from vortex generation geometries enables near-wall fluid particles to resist and delay separation. Due to the large energy losses associated with boundary layer separation, separation control is of immense importance to the performance of air, land, and sea vehicles, turbomachines, diffusers, and many other engineering systems involving fluid flow. Generally it is desirable to postpone separation so that form drag is reduced, stall is delayed, lift is enhanced, and pressure recovery is improved [1].

The influence of grooves on flow characteristics is not yet fully understood. Since various types of grooves with different sizes have been studied, a wide variety of results have been reported. Depending on the combination of the groove's depth, width, and spacing, different trends are evident. Of the efforts focused on optimizing the features of these grooves, Walsh's [4,5] work, conducted at NASA Langley research center is among the most notable efforts focused on aerodynamic application of grooves. Although the majority of his efforts are focused on longitudinal grooves, he has also studied transverse grooves. He reported separation control, loss reduction, and turbulence intensity growth in the boundary layer region using grooved surfaces. Sutardi and Ching [6] reported an increase in mean velocity, streamwise and wall-normal turbulence intensities in the near-wall region immediately downstream of a transverse square groove in a turbulent boundary layer. They also confirmed that the mentioned increase propagated outwards from the wall with increasing streamwise distance downstream of the groove. Later, in two separate publications [7,8] they disseminated the influence of three different sized transverse square grooves and three different shaped transverse grooves (square, semicircular and triangular) on a turbulent boundary layer. They confirmed many of the

qualitative results of their previous work. An increase in the mean velocity and turbulence intensity downstream of a groove was also reported in the work of Choi and Fujisawa [9]. They demonstrated the existence of quasi-stable vortex flows within the groove and speculated that a vortex is responsible for changes in the grooved flow. Elavarasan et al. [10] and Pearson et al. [11] found an increase in turbulence intensity caused by the grooves and also a significant increase in skin friction just downstream of the groove followed by a decrease below the smooth-wall value and an oscillatory relaxation to the smooth wall value. Robarge et al. [12] summarized several rules of thumb for achieving the most effective separation control by use of indented surface treatments. They also reported a study on a recessed groove placed spanwise across a NACA0015 airfoil. Laminar separation control and loss reduction were important effects of the groove on the flow. They attributed this outcome to a two-dimensional vortex structure inside the groove energizing the boundary layer. Tantirige et al. [13] used a photochromic tracer to investigate the effect of two V-shaped grooves on the turbulent boundary layer. The mean velocity profiles above the grooves were similar to those over smooth surfaces, but displaced downstream, and turbulence intensity increased immediately after the grooves. They found enhancement of heat and mass transfer rates by spanwise grooves and attributed this to energetic bursts inside the groove.

In addition to the aforementioned experimental works, there have been a number of numerical efforts studying the mechanism involved with flow over grooves. In spite of the fact that most of the turbulence models used in the numerical procedures have some deficiencies especially at flow-separated regions, Dubief et al. [14] showed the ability of numerical methods in reproducing realistic turbulent structures using a large eddy simulation technique. They investigated a rectangular groove engraved in a flat plate; which had dimensions of the order of the boundary layer thickness. Their results demonstrate an increase in the level of turbulence downstream of the groove and also a reduction in the spatial extent of coherent structures above and after the groove. In another large eddy simulation, Luo et al. [15] studied the mechanisms of a relatively wide spanwise groove for the passive control of a laminar separation bubble on the suction surface of a low-speed highly loaded low-pressure turbine blade. They stated that using a grooved surface led to shortening of the flow separation bubble, which contributed to the flow loss reduction. This was attributed to the fact that the groove made the boundary layer behind it thinner and promoted earlier transition in the separation bubble.

All of the aforementioned studies were conducted in “smooth” flow. In practice, most flows are turbulent and hence, the effect of free-stream turbulence needs to be recognized. Such is

the objective of this study, where “smooth” and “turbulent” free-streams are forced over both smooth and grooved surfaces. To investigate the effect of free-stream turbulence on the flow over such surfaces, flow parameters including velocity profiles, boundary layer thickness values, and turbulence intensity profiles are presented. Moreover, to reveal further details of the flow, turbulence statistical parameters like skewness and flatness factors and also turbulence length scales have been investigated. The experimental study was performed for a flow over two flat plates with smooth and transversely grooved surfaces using hot-wire anemometry.

A.2 Experimental details

The experiments were performed in a closed-loop wind tunnel with a 4 m long test section. The cross section of this wind tunnel at the entrance is 0.762 m by 0.762 m. The cross-sectional area increases gradually downstream to overcome the boundary layer build-up on the wind tunnel ceiling and the floor. Consequently, the dimensions of the end of the working section are 0.762 m wide and 0.782 m high. The maximum achievable mean velocity is approximately 20 m/s in the empty working section with a background turbulence intensity of less than 0.5%. In the presence of a perforated plate for generating turbulent flow however, the maximum achievable velocity is about 11 m/s.

A 0.609 m by 0.609 m plate made from 9.5 mm thick aluminum with an average surface roughness of 292.6 nm was mounted on Plexiglas; which was attached via screws to two mounting steel angles (see Fig. 1). The entire assembly was placed at the center plane of the wind tunnel and fastened with four screws. The upstream edge of the Plexiglas was machined to have a 30 degree angle bevel for directing the flow smoothly at the bottom surface of the plate to avoid flow disturbances at the leading edge of the plate (see Fig. 1b). The Plexiglas was cut in a way that the aluminum plate could be slid onto it. With this scheme, smooth and grooved plates could be interchanged for testing.

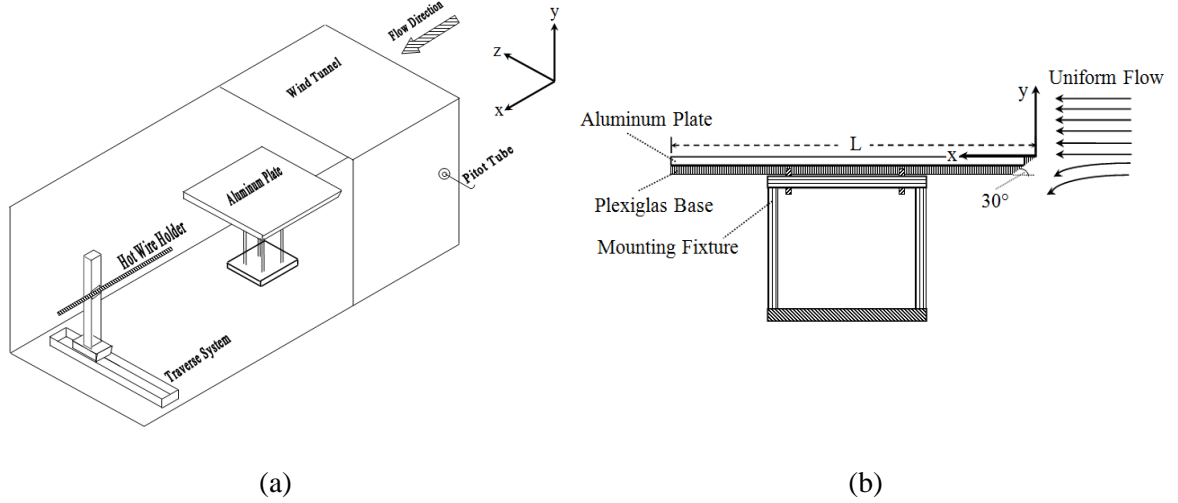


Figure 1: (a) Schematic of experiment layout, (b) Schematic of the designed fixture

In order to study the influence of the grooves on the flow, some grooves were cut around the center on one side of the aluminum plate while the other side remained smooth. The geometry of the plate and grooves are detailed in Fig 2. All grooves have a trapezoidal geometry with 1.62 mm depth, 3.57 mm width at the peak and 1.15 mm width at the valley. Also, there was 3.57 mm distance between every two consecutive grooves, and a total of 29 grooves were cut on the plate with a computer numerical control (CNC) machine.

For the present study, a section in the center of the wind tunnel was selected for measurements and the plate leading edge distances from the wind tunnel inlet section and wind tunnel floor at centerline were 3.53 m and 0.305 m respectively. Nine streamwise sections were selected for the measurement as shown by cross marks in Fig. 2a. Non-dimensionalized distances of these sections from the leading edge in the streamwise direction are reported in Table 1, where L is total length of the plate including the small Plexiglas leading edge in the streamwise direction that is 656.6 mm (see Fig. 1b). In Table 1 the values of various parameters at the last vertical measurement point have also been presented as the free-stream value. The second and eighth streamwise locations were at the beginning and the end of the grooved area respectively. The spacing between each two-measurement section was 36.57 mm and the distance of the first point from the leading edge was 205.9 mm. At each section, measurements have been carried out at forty points in the wall-normal direction with 1.77 mm spacing while the height of the first point from the surface was 2.54 mm. Due to space limitation, only results at the first, fifth, seventh and ninth streamwise locations are discussed; subsequently, the results at the second, third, fourth,

sixth and eighth sections are omitted. Also measurements were performed at two sections in the spanwise direction from the middle streamwise location ($x/L=0.53$) in the measurement line with 25.4 mm distance for checking the two-dimensionality of the flow. Since the measured variables at these two sections were very close to each other and to the 5th section, the assumption of two-dimensional flow over the flat plate in the present study was considered valid. It should be noted that the smooth part of the plate has been considered as the origin of the vertical axis ($y=0$) for both smooth and grooved surfaces. This assumption introduced some errors in grooved surface flow since it is known that the effective wall in a rough surface is somewhere between groove's peak and valley. This error can be considered as a part of uncertainty in the measurement whereas dimensional mean profiles (U vs. y) have been reported in this paper instead of wall-variable profiles (u^+ vs. y^+).

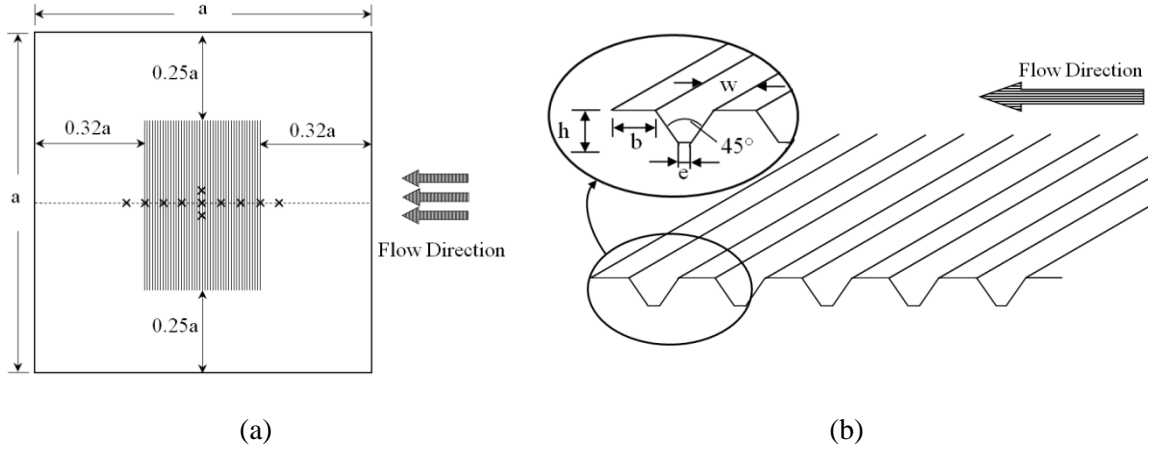


Figure 2: (a) Grooved area on the aluminum plate, (b) Groove trapezoidal geometry

Table 1: Free-stream values of different parameters at nine streamwise sections.

Streamwise location No.		1	2	3	4	5	6	7	8	9
x/L	Free-stream	0.31	0.37	0.42	0.48	0.53	0.59	0.64	0.70	0.76
$U_{\infty}(\text{m/s})$	smooth	8.29	8.21	8.33	8.18	8.21	8.20	8.28	8.36	8.31
	turbulent	8.17	8.29	8.21	8.25	8.34	8.30	8.27	8.32	8.27
$Tu(\%)$	smooth*	0.61	0.49	0.56	0.61	0.59	0.66	0.57	0.58	0.66
	turbulent	3.96	3.85	3.81	3.64	3.66	3.60	3.68	3.58	3.54
$\delta(\text{mm})$	smooth	30.98	32.76	32.76	36.32	36.32	43.43	46.99	48.76	48.76
	turbulent	32.76	34.54	36.32	38.10	41.65	46.99	50.54	52.32	54.10
s	smooth	0.064	0.011	0.016	0.000	0.210	0.234	0.150	0.358	0.213

	turbulent	0.062	0.045	0.029	0.023	0.036	0.039	0.030	0.034	0.037
F	smooth	3.060	3.079	2.975	3.112	3.008	3.112	3.129	3.172	3.152
	turbulent	2.942	2.953	2.949	2.939	2.950	2.967	2.971	2.953	2.983
ε (m ² /s ³)	turbulent	1.218	1.253	1.253	1.253	1.279	1.290	1.362	1.416	1.429
η (mm)	turbulent	0.234	0.233	0.233	0.233	0.232	0.231	0.228	0.226	0.225
Λ (mm)	turbulent	37.58	36.87	38.40	39.35	37.38	39.11	39.79	39.78	41.69
Λ/η	turbulent	159.9	158.0	164.6	168.7	161.1	168.9	174.2	175.7	184.6

* Note that Tu can be slightly higher than 0.5% in the presence of the test plate.

For controlling free-stream turbulence an orificed perforated plate (OPP) with holes of 50.8 mm diameter and 6 mm thick and solidity ratio of 43% was placed upstream of the test plate (see Fig. 3). To minimize the influence of the plate thickness on the turbulent flowfield generated each hole was machined with a 41° chamfer angle with the sharp-edged side facing the incoming flow. It has been demonstrated by Liu et al. [16] that this turbulence generator is appropriate for generating quasi-isotropic turbulence. Quasi-isotropic turbulence is a form of turbulence; which has very similar characteristics to those of isotropic turbulence. For referencing, it should be noted that isotropic turbulence has no directional preference and flow velocity fluctuation components have values that do not vary in magnitude more than +/- 20% [16].

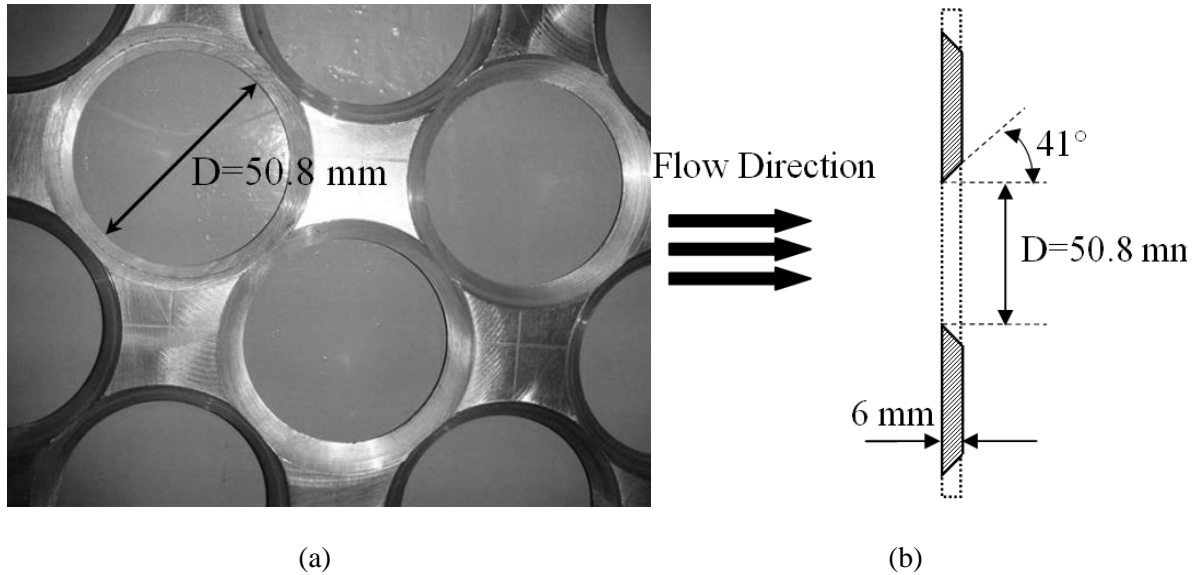


Figure 3: (a) Orificed perforated plate for controlling turbulence, (b) Cross-section of the plate

A DANTEC Streamline automated anemometry system operated in constant temperature mode was utilized for flow velocity measurements. A boundary layer hot-wire probe of type 55P15 was used. The sensor diameter and its total length were 5 μm and 1.25 mm respectively. The output signal of the hot-wire probe was sent to a 12-bit National Instruments multifunction data acquisition board connected to a computer. The hot-wire probe, together with the temperature probe, were mounted on a 2-D traversing system with vertical and spanwise axes. The effects of the free-stream temperature drift were taken into account using the correction of Bearman [17]. For the hot-wire measurement, the analog voltage signal was first low-passed at 30 kHz using an analog filter in order to remove noise and to prevent higher frequencies from folding back (anti-aliasing). Then it was sampled at 80 kHz (which is more than twice the Nyquist frequency) over the sampling time of 25 s, which resulted in 2×10^6 samples. At the start of an experiment, the free-stream velocity in the wind tunnel was set with the help of a Pitot-static tube, which was connected to a digital manometer (DWYER series 475). The Pitot-static tube was inserted through a small hole on the side wall of the wind tunnel near the inlet section such that the tube hole was facing the incoming flow (see Fig 1a). This Pitot-static tube was removed after checking the free-stream velocity and the small opening was sealed.

A.3 Results and discussion

The measurements were made for two cases of flow over the smooth and grooved plates, in two levels of free-stream turbulence intensity (0.5% and 4.4%). The turbulence intensity was calculated via:

$$Tu(\%) = \frac{u_{rms}}{U_{mean}} \times 100 \quad (1)$$

where u_{rms} is the root-mean-square of the velocity fluctuations defined as

$$u_{rms} = \left\{ \sum_{i=1}^N \frac{(U_i - U_{mean})^2}{N-1} \right\}^{0.5} \quad (2)$$

Turbulence intensity for the flow without the OPP was measured to be around 0.5% at the location of the leading edge of test plate while the test plate was not present in the wind tunnel. In the other reported case, the OPP was placed at 1.56 m upstream of the test plate which resulted in a turbulence intensity of 4.4% and a 36 mm integral length scale at the leading edge of the test plate, again in the absence of the test plate. The upstream velocity was set at 8.12 m/s; which led to a Reynolds number of 3.4×10^5 based on plate's total length in the flow direction.

A.3.1 Uncertainty analysis

The uncertainty in reported parameters has been estimated according to the procedure of Refs. [18-20]. The total uncertainty of a measured parameter is a combination of bias and precision uncertainties. At first, the bias uncertainty in the instantaneous flow velocity measured by hot-wire was deduced and afterwards the bias uncertainty in the other turbulence parameters was expressed in terms of uncertainty in the instantaneous velocity. The complete procedure can be found in [18]. In addition to bias uncertainty, the precision uncertainty of independent repeated measurements has been determined from the student's t distribution with 95% confidence interval. The total uncertainty of each parameter has been calculated for the range of measurements and has been displayed by error bars on the graphs for a few points at a streamwise section of $x/L=0.53$. Moreover, the uncertainty in the vertical location of the hot-wire probe, y , was estimated as 2.11 mm including uncertainty in the measured length by a smart motor used to traverse probe vertically, and uncertainty in the position of the probe's holder because of its vibrations.

A.3.2 Velocity profiles

Figure 4 shows the velocity profiles at five streamwise sections for all four flow cases; $Tu=0.5\%$ and 4.4% flows over smooth and grooved plates. In the present study the smooth flow ($Tu=0.5\%$) over the smooth plate was considered as the base case. For all sections, velocity values have been normalised with the local free-stream value.

Figures 4a to 4d show the boundary layer thickness increases with x/L which is in agreement with boundary layer theory. This increase can be easily observed for all flow cases along the flow direction. The influence of the free-stream turbulence on the flow over a flat plate can be noticed from the change in the velocity profiles. The OPP introduces nearly-isotropic turbulence to the flow, creating fuller velocity profiles and thickening the boundary layer. Such a trend is observable in all measurement sections for both smooth and grooved surfaces.

The grooves affect the flow such that the velocity profiles become fuller. These profiles have large curvature and hence are more resistant to the flow separation [1]. The change between smooth-plate and grooved-plate flow is very small until $x/L=0.42$ but becomes larger with advancement in the grooved region. It should be noted that the mentioned change cannot be seen for the first section since this section is located upstream of the grooved region. That change is

largest at $x/L=0.7$ (not shown here) which is the end of the grooved region. After that, at $x/L=0.76$ (Fig. 4d) the effect decreases due to absence of the continuous groove effect. The explained effect of the grooves on the velocity profile is more remarkable in the presence of enhanced free-stream turbulence for all sections. This could be caused by the coupled augmentation of free-stream turbulence with groove-generated turbulence. Sample error bars at streamwise section of $x/L=0.53$ have been included in Fig. 4b to show the typical measured uncertainties.

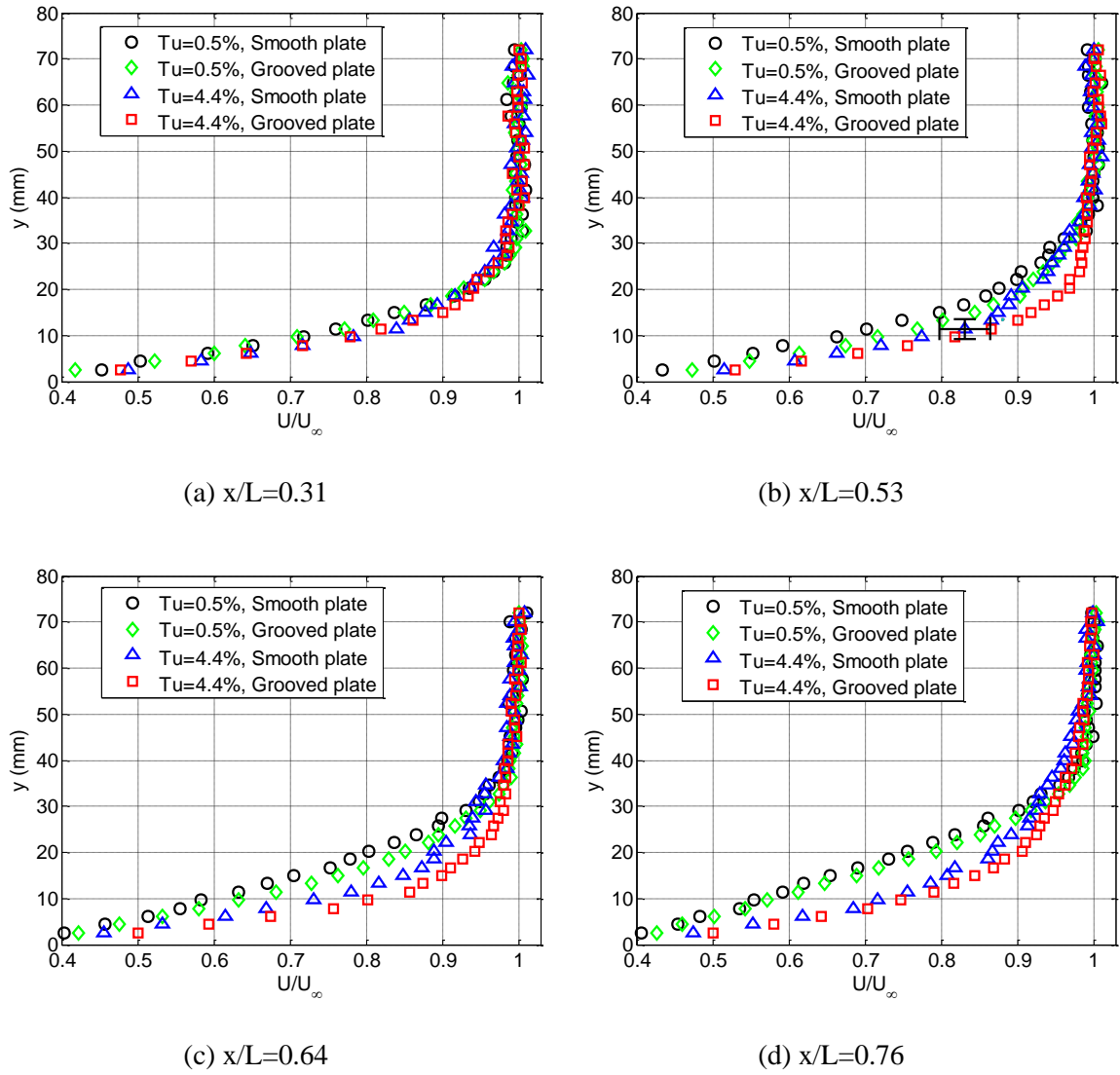
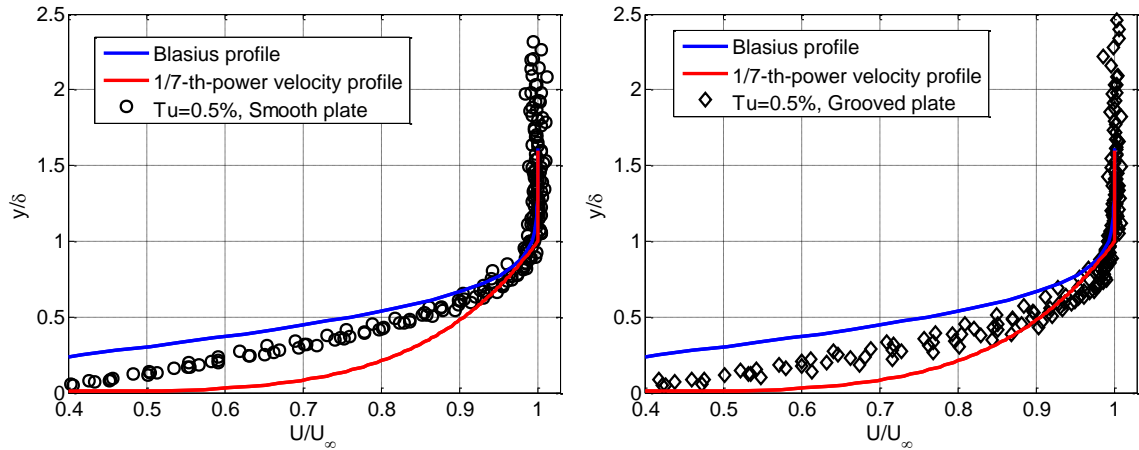


Figure 4: Effect of free-stream turbulence and transverse grooves on velocity profiles, typical error bars are shown in (b)

For interest, boundary layer velocity profiles over the smooth plate for flows with turbulence intensities of 0.5% and 4.4% have been compared with typical laminar and turbulent velocity profiles. The Blasius velocity profile for a flow over a flat plate is obtained from the similarity solutions for a laminar boundary layer [1]. For turbulent boundary layer on a flat plate there are some useful approximations from similarity solutions. The following velocity distribution, the one-seventh-power distribution has been suggested based on the similarity concept [1].

$$\frac{U}{U_\infty} = \left(\frac{y}{\delta}\right)^{\frac{1}{7}} \quad (3)$$

Figure 5 compares the velocity profiles obtained in this study with those predicted by similarity solutions. $Tu=0.5\%$ data points place somewhere between Blasius and one-seventh-power profiles which confirms that $Tu=0.5\%$ flow is not a laminar flow (see Figs. 5a & 5b). In fact, Van Ingen [21] stated that for wind tunnel flows, only flows with $Tu<0.1\%$ can be assumed to be laminar. Also, the small gap between Plexiglas base and aluminum plate which can be seen in Fig. 1b might have also contributed to some additional disturbances, up to 0.66% turbulence intensity in the free-stream region as per Table 1. Hence, recognizing that the incoming uniform flow with 0.5% turbulence intensity has a fair amount of turbulence fluctuations, along with the additional turbulence due to the gap, could lead to a classification of the $Tu=0.5\%$ flow as a non-Laminar. Moreover, the $Tu=0.5\%$ flow over the grooved plate has velocity profiles closer to one-seventh-power profile, due to effect of surface roughness (see Figs. 5b). On the other hand, comparison of the flow with turbulence intensity of 4.4% with one-seventh-power velocity distribution is reasonable. This agreement can be observed as fairly acceptable in Figs. 5c & 5d for $Tu=4.4\%$ case over smooth and grooved surfaces.



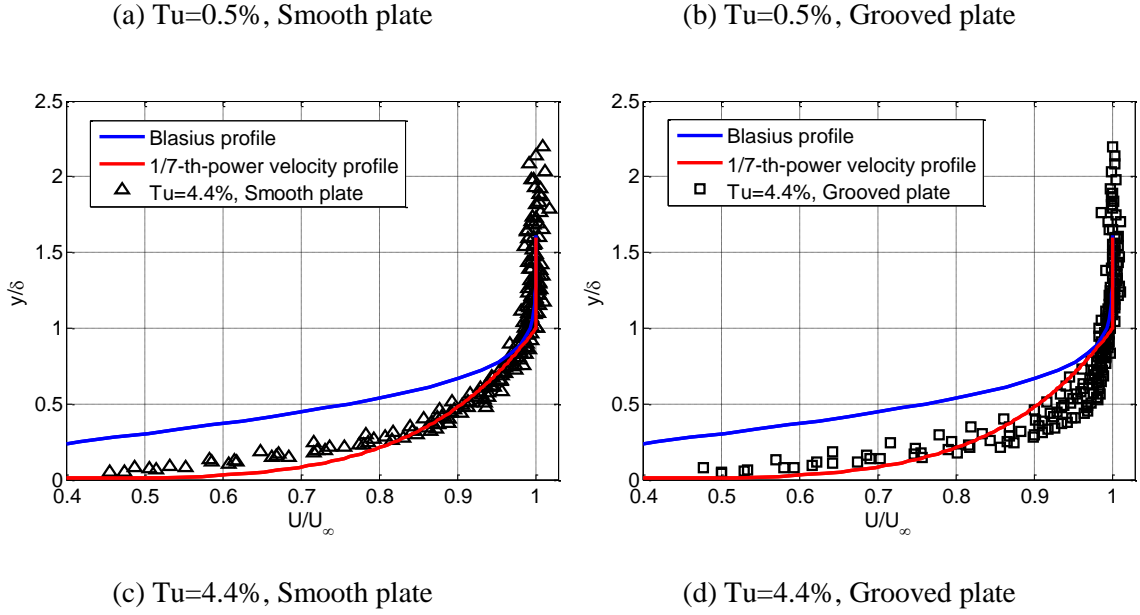


Figure 5: Comparison of velocity profiles for flow over the smooth and grooved surface;
 $Tu=0.5\%$ and 4.4%

Non-dimensional values of boundary layer thickness have been plotted against Reynolds number based of streamwise distance from leading edge of the plate in Fig. 6. The boundary layer thickness, δ , is considered to be the height from the wall to the location where the local velocity is 99% of the local free-stream value. Figure 6 confirms the enlargement of the boundary layer region under the effect of free-stream turbulence. Roughening the surface via grooves also thickens the boundary layer. The combined effects of both free-stream turbulence and spanwise grooves increase the boundary layer thickness the most, compared to the cases where only one of those elements was present in the flow.

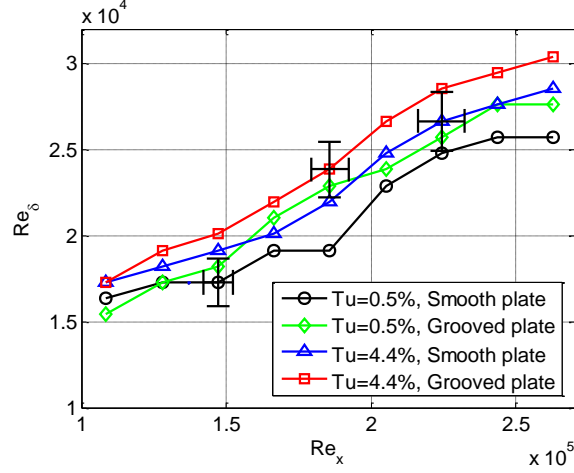


Figure 6: Boundary layer thickness in the terms of Re_δ versus Re_x at nine streamwise sections for flow over smooth and grooved surfaces; $Tu=0.5\%$ and 4.4%

A.3.3 Turbulence moments

To further reveal the underlying physics behind the interaction of the free-stream turbulence with a grooved boundary layer, various moments of streamwise velocity fluctuations are deduced. Turbulence intensity, which is a measure of the strength of vortices in the flow, has been illustrated in Fig. 7 for all four flow cases versus vertical distance from the wall. Literature [6-8,10,13] suggests that the boundary layer is energized in the presence of transversely oriented grooves and this introduces turbulent vortices to the near-wall region. If this is so, then we expect to see an increase in turbulence intensity when grooves are present.

As shown in Fig. 7, the overall trend of the turbulence intensity is decreasing with vertical distance from the surface. Next to the wall, turbulence intensity is high due to wall turbulence and it decreases as we move away from the surface. Outside the boundary layer region the value of turbulence intensity remains roughly constant at each streamwise section. For the base flow case, turbulence intensity at the outer boundary layer region is around 0.5% and remains almost unchanged at all sections. As well, the increase in the boundary layer thickness with increasing streamwise distance as observed in Figs. 4 and 6 can also be deduced from Fig. 7.

Introducing free-stream turbulence causes significant increase in the turbulence intensity throughout the boundary layer, with a larger increase for the outer half of the layer. Again, the decreasing turbulence intensity trend in wall-normal direction exists for the $Tu=4.4\%$ case in the boundary layer. Outside the boundary layer, the turbulence intensity remains approximately

constant with respect to vertical distance from the wall while it decreases in the streamwise direction due to the dissipative nature of turbulence; moving from Fig. 7a to 7d. Accordingly, the turbulence intensity values in the outer boundary layer region at streamwise sections of $x/L=0.31$, 0.53, 0.64, 0.76 are 3.96, 3.66, 3.68, and 3.54 percent.

As expected, using grooves on the surface increases turbulence intensity which can be observed from comparison of $Tu=0.5\%$ flow cases of smooth and grooved plates in Fig. 7. This increase exists for all sections which are located in the grooved region and also for the last section located downstream of the grooved region. The mentioned increase is more remarkable at the sections closer to the end of the grooved area i.e. at $x/L=0.70$ and 0.76. Another interesting point regarding the effects of the grooves is that the increase in turbulence intensity propagates toward the edge of the boundary layer as we move streamwise into the grooved region. In fact, at the locations closer to the beginning of the grooved area, grooves affect the flow domain mostly at the near-wall region while at the farther streamwise locations this effect spreads through the whole boundary layer area, see Fig. 7c. It should be noted that there is not any meaningful change for the first streamwise section, $x/L=0.31$ (Fig. 7a), since it is located upstream of the grooved area. On the other hand, at the last section, $x/L=0.76$ (Fig. 7d), where is located downstream, outside the grooved region, the amount of increase in turbulence intensity is reduced, perhaps due to the diminishing effect of the grooves at that section in the absence of continual turbulent kinetic energy input.

As expected, the boundary layer is most altered under the combined effect of the free-stream turbulence and groove-generated turbulence. Using grooves under free-stream turbulence intensifies the augmentation in turbulence intensity not only in the near-wall region but also in the outer half of the boundary layer. Similarly, this increase is more notably at the streamwise sections closer to the end of the grooved area.

Altogether, the observed increase in turbulence intensity due to free-stream turbulence and spanwise grooves causes momentum augmentation of the fluid particles which otherwise have been weakened under the influence of the boundary layer shear stress. This indicates the possibility of using grooves for flow separation control; which is more effective under free-stream turbulence.

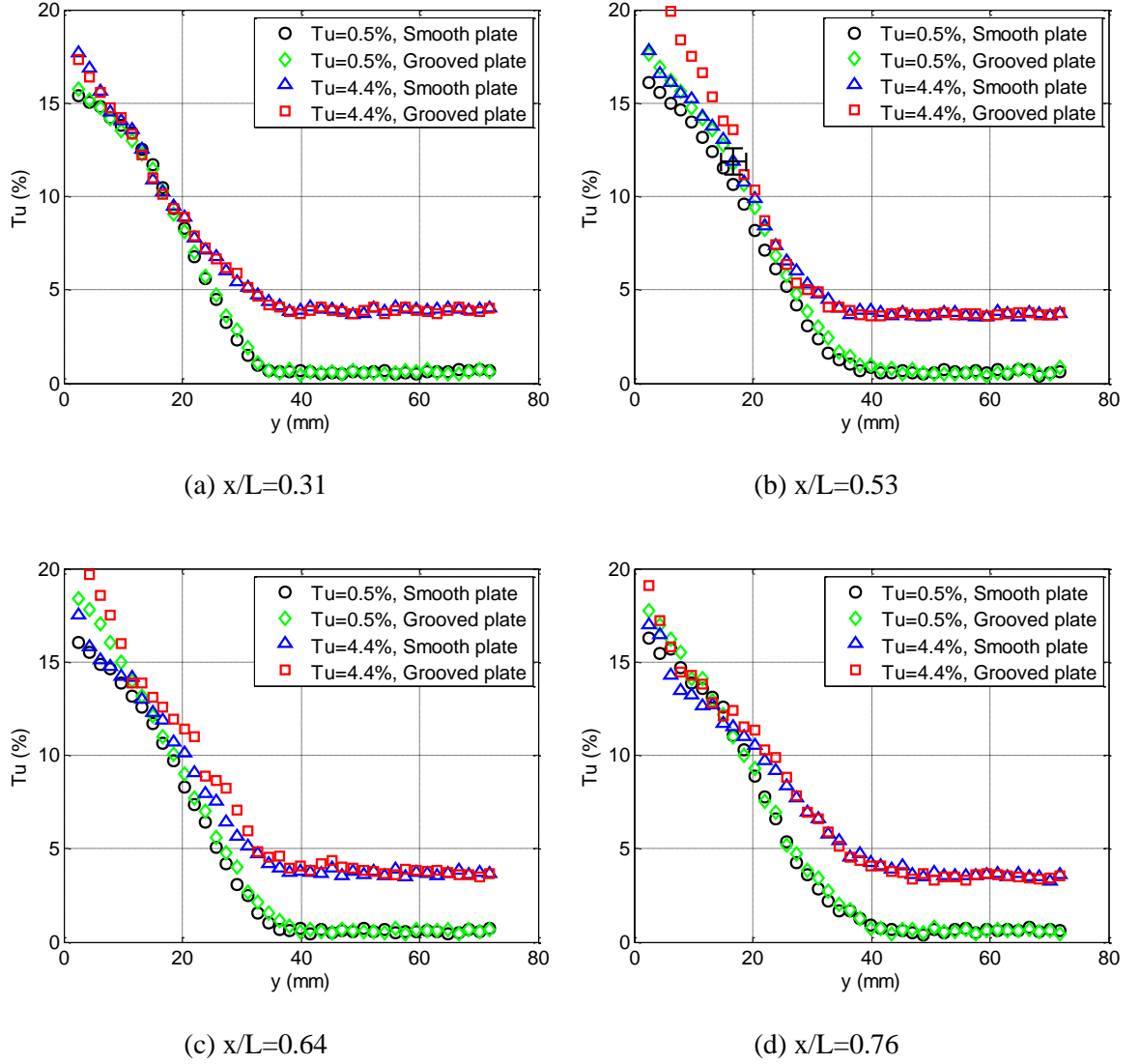


Figure 7: Effect of free-stream turbulence and transverse grooves on turbulence intensity profiles, typical error bars are shown in (b)

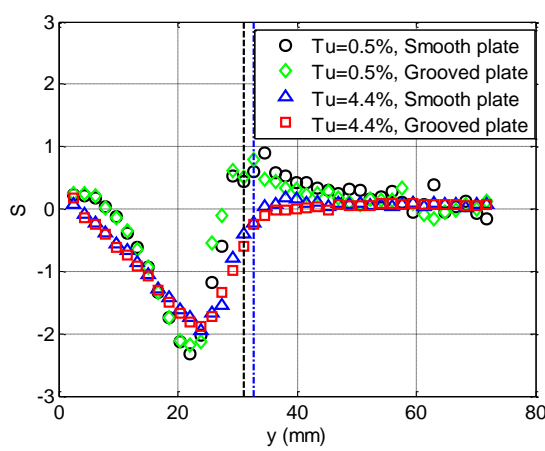
As confirmed in the previous section, grooves introduce additional turbulence to the boundary layer; which may skew the velocity fluctuation distribution. To examine this, skewness and flatness factor profiles are analysed here. Skewness, the third moment of velocity, is a measure of the lack of statistical symmetry in the flow fluctuation, while flatness, the fourth moment of velocity, is a measure of the fluctuation amplitude distribution [22]. They, as displayed in Figs. 8 and 9, have been calculated via the following relations:

$$S = \sum_{i=1}^N \frac{(U_i - U_{mean})^3}{N-1} / u_{rms}^3 \quad (4)$$

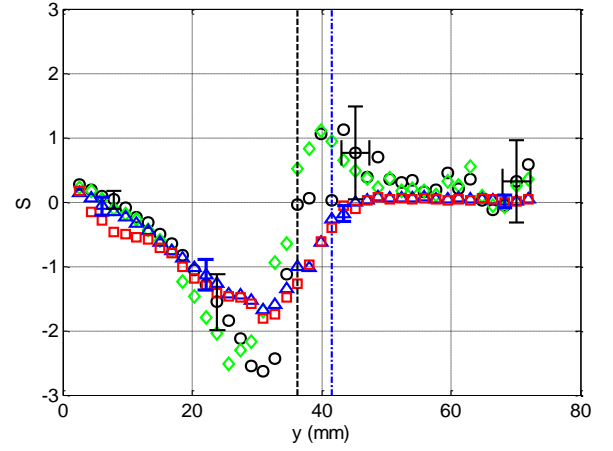
$$F = \sum_{i=1}^N \frac{(U_i - U_{mean})^4}{N-1} / u_{rms}^4 \quad (5)$$

For the base flow case, Fig. 8 shows that the skewness factor has a near zero value next to the wall. Then it becomes progressively more negative with increasing distance from the wall until it reaches a minimum value inside the boundary layer, beyond which it recovers to zero, the free-stream value. A significant scatter in the $Tu=0.5\%$ data especially outside the boundary layer can be seen in Fig. 8 since there is very little turbulence and thus, small variation in the turbulence value leads to large variation in the skewness factor which results in high uncertainty values as shown by error bars in Fig. 8c.

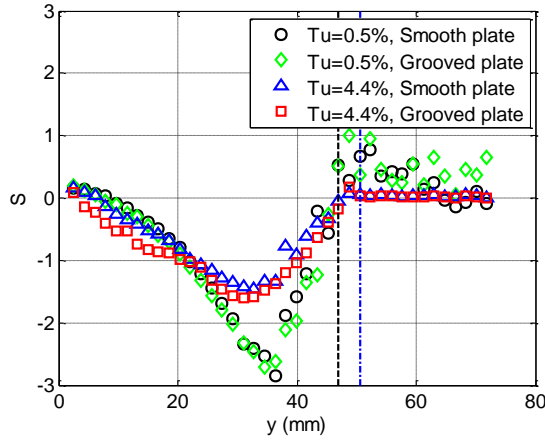
Free-stream turbulence ($Tu=4.4\%$) tends to smoothen the skewness profiles; it lessens the minimum value in the boundary layer and eliminates the overshoot in the vicinity of the boundary layer edge; which existed in the base flow case. The skewness factor in the free-stream region, which in this case is totally dominated by free-stream turbulence, remains almost unchanged at around zero, which is the skewness factor of a Gaussian distribution. The effect of the grooves on skewness factor is very subtle and since that change is of the same order as the uncertainty no obvious conclusions can be drawn.



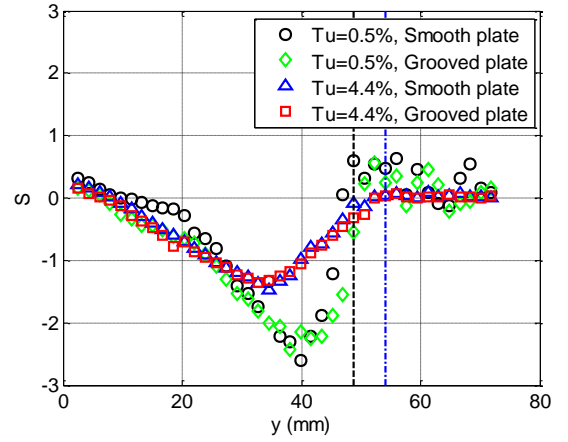
(a) $x/L=0.31$



(b) $x/L=0.53$



(c) $x/L=0.64$

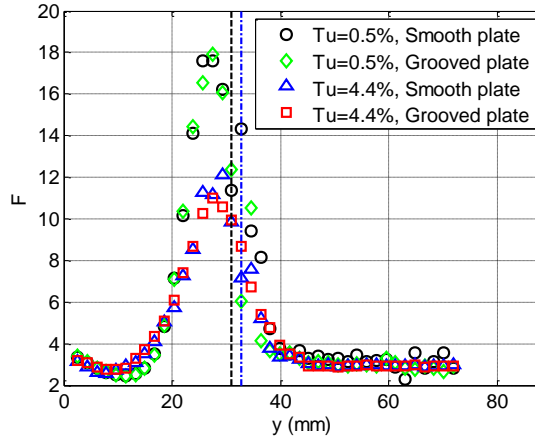


(d) $x/L=0.76$

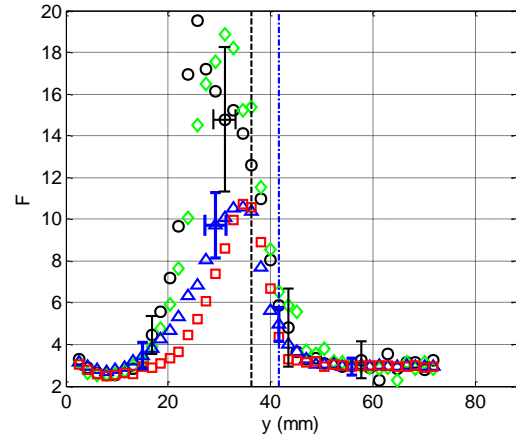
Figure 8: Effect of free-stream turbulence and transverse grooves on skewness factor, dashed and dash-dotted vertical lines represent the boundary layer edge for $Tu=5.5\%$ & 4.4% flows over the smooth plate, typical error bars are shown in (b)

Figure 9 shows that in general the flatness factor is around 3 next to the wall, then with moving farther in the vertical-wall direction, it decreases to approximately around 2.5 before it increases to a maximum peak value which is much higher than 3 in the vicinity of the boundary layer edge. After the peak, flatness factor decreases to a value around 3 in the free-stream region. Similar to skewness factor response, there is considerable scatter in flatness factor for the $Tu=0.5\%$ flow because of the low free-stream turbulence. This has been confirmed by high estimated uncertainty values displayed in Fig. 9c.

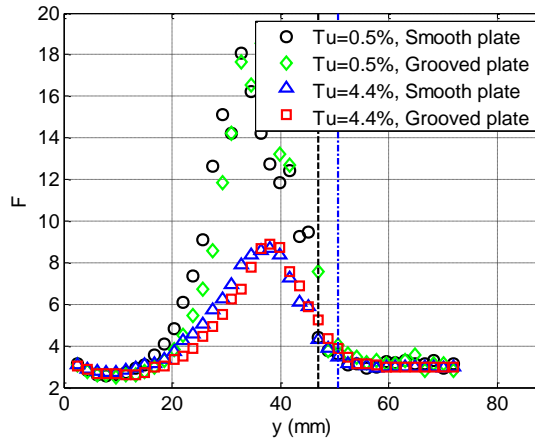
Introducing free-stream turbulence smoothens the flatness factor profiles and makes the data scatter smaller. Also, it lessens the maximum peak near the boundary layer edge. Outside the boundary layer the flatness factor for the generated quasi-isotropic turbulence has a very small deviation from its Gaussian value, 3, as expected. This point has been confirmed by the small uncertainty at this region compared to $Tu=0.5\%$ case. Similar to the skewness factor data, since the change in flatness factor caused by grooves is of the same order as the uncertainty, no meaningful conclusions can be made.



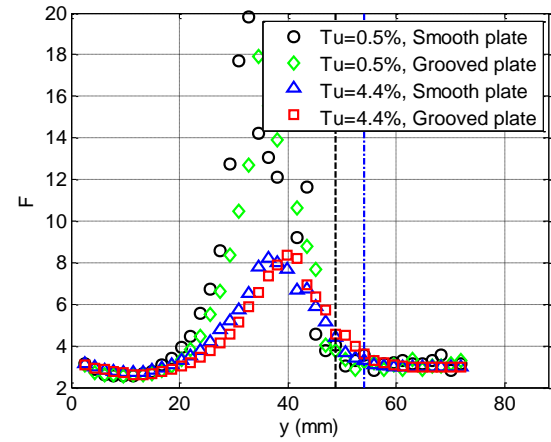
(a) $x/L=0.31$



(b) $x/L=0.53$



(c) $x/L=0.64$

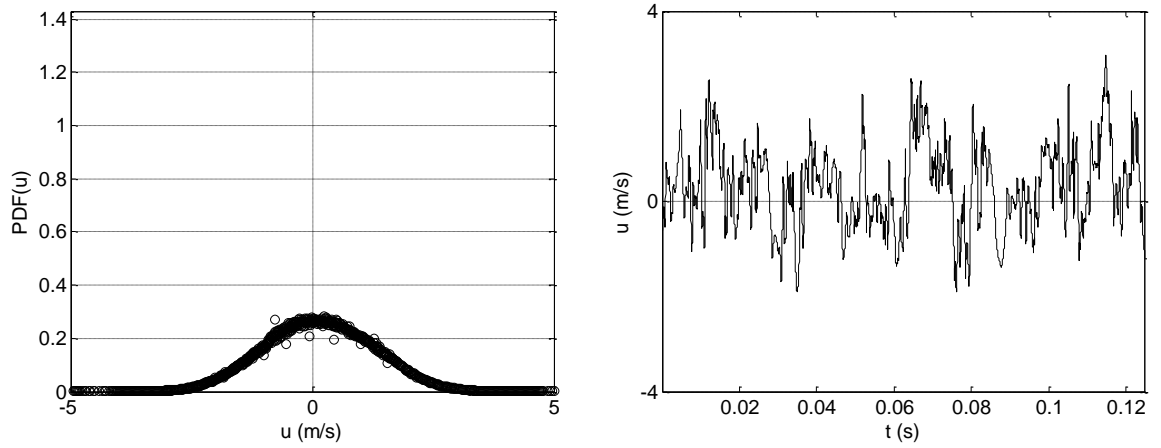


(d) $x/L=0.76$

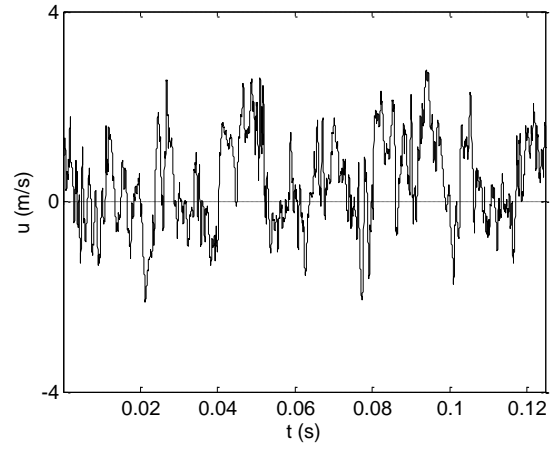
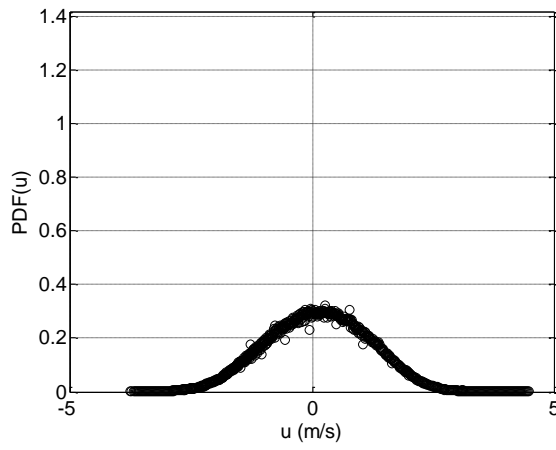
Figure 9: Effect of free-stream turbulence and transverse grooves on skewness factor, dashed and dash-dotted vertical lines represent the boundary layer edge for $Tu=5.5\%$ & 4.4% flows over the smooth plate, typical error bars are shown in (b)

Considering together skewness and flatness profiles (Figs. 8 & 9), it seems that at some vertical distance inside the boundary layer near to its edge, negative and positive peaks can be observed for skewness and flatness profiles respectively. These have also been reported by Alving and Fernholz [23]. They stated that these peaks are associated with the entrainment of free-stream fluid into the boundary layer increasing the boundary layer resistance to flow separation.

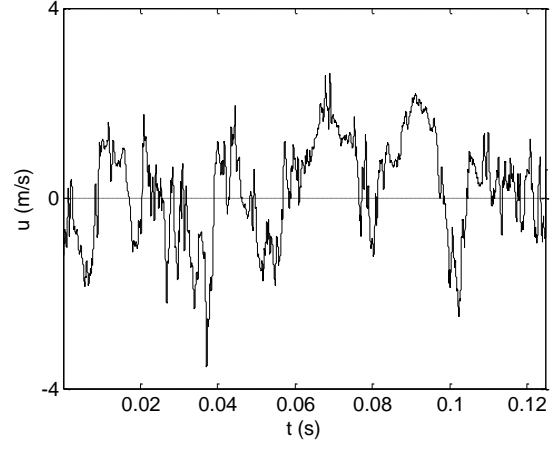
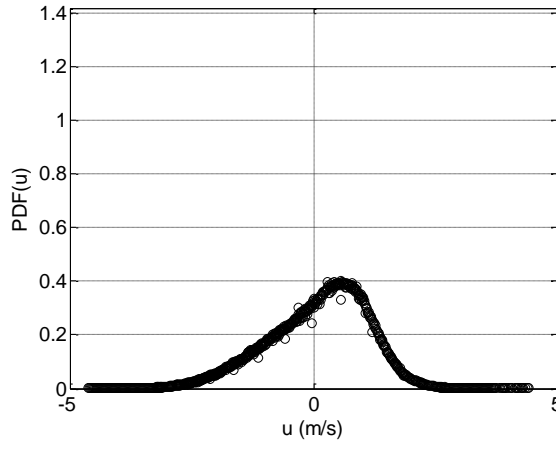
For a more comprehensive analysis on the features of the turbulence signal, skewness and flatness factors should be reviewed in conjunction with the probability density function (PDF) of the turbulence distribution. PDF graphs of streamwise velocity fluctuation, u , at the streamwise section of $x/L=0.53$, for the flow over a smooth plate under influence of OPP are shown in Fig. 10 at selected vertical distances from the wall. PDF graphs for all other streamwise sections have the same trend and hence are not shown here. In this figure, corresponding velocity fluctuation time traces are also plotted to elucidate the discussion. Figs. 10a & 10b ($y/\delta=0.06$ & 0.14) show Gaussian-like distribution, confirming skewness and flatness factors for those locations from Figs. 8 & 9 ($S \approx 0$, $F \approx 3$). At $y/\delta=0.31$, 0.70 (Figs. 10c & 10d) the PDFs deviate from the symmetrical Gaussian shape with zero mean, clearly portraying an anisotropic turbulence at these regions. The time traces especially at $y/\delta=0.70$ clearly depicts that the velocity experiences high negative peaks while it spends most of the time in the positive values. Outside the boundary layer at $y/\delta=1.38$ (Fig. 10e) the PDF and the time trace confirm the free-stream turbulence is isotropic.



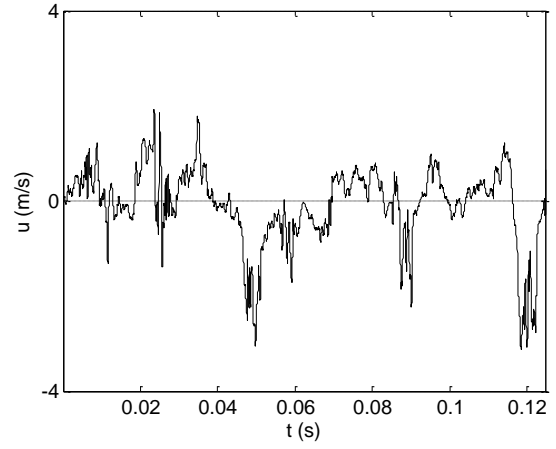
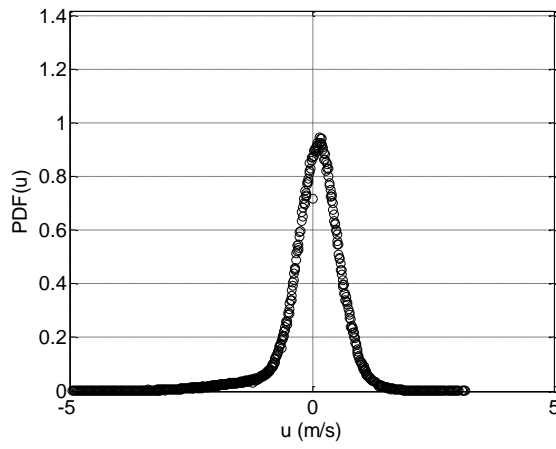
(a) $y/\delta=0.06$; $S=0.079$, $F=3.173$



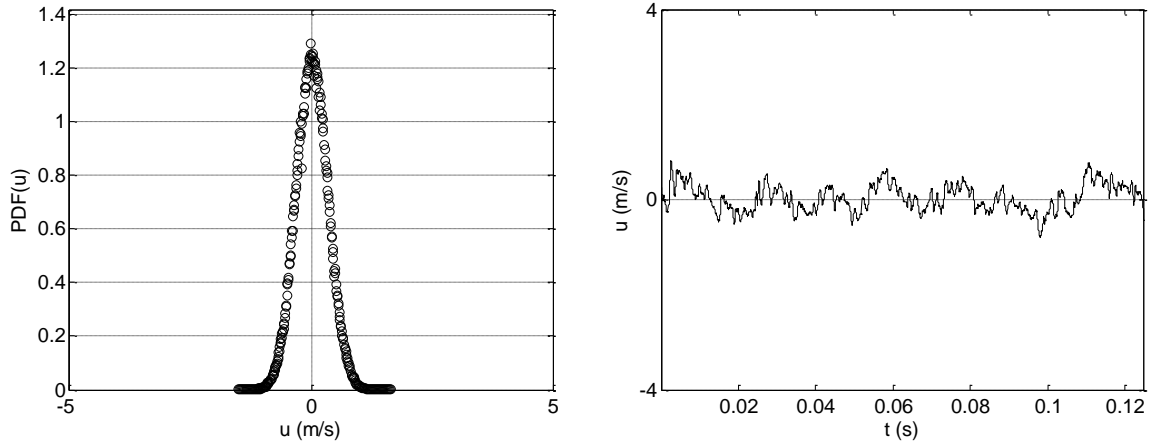
(b) $y/\delta=0.14$; $S=-0.052$, $F=2.764$



(c) $y/\delta=0.31$; $S=-0.455$, $F=3.286$



(d) $y/\delta=0.70$; $S=-1.606$, $F=9.85$



(e) $y/\delta=1.38$; $S=0.012$, $F=3.018$

Figure 10: Probability density function (PDF) of streamwise velocity fluctuation and velocity fluctuation variation vs. time at streamwise section $x/L=0.53$ for smooth surface flow with $Tu=4.4\%$

A.3.4 Turbulence length scales

The Kolmogorov scale describes the dissipation range eddies while integral length scales are associated with the energy-containing eddies [24]. The Kolmogorov length scale is defined as [22]:

$$\eta \equiv \left(\frac{\nu^3}{\epsilon} \right)^{\frac{1}{4}} \quad (6)$$

where ν is the kinematic viscosity and ϵ is the energy dissipation rate, which in an isotropic turbulent flow can be expressed as [22]:

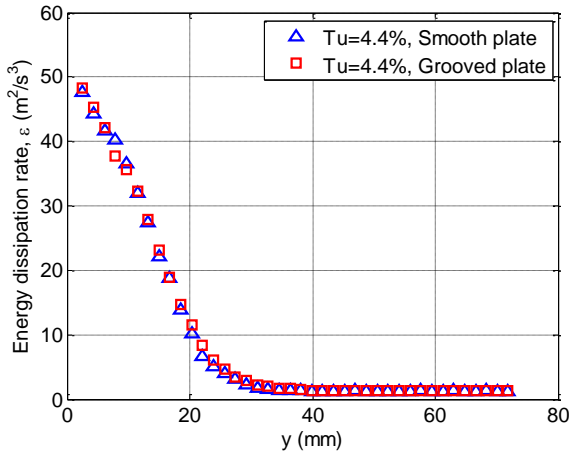
$$\epsilon = 15\nu \left(\frac{\partial u}{\partial x} \right)^2 \quad (7)$$

Taylor's frozen eddy hypothesis has been utilized for approximation of spatial rates from the measured temporal rates, i.e., $\partial/\partial x = (\partial/\partial t)/U_{mean}$. The use of Taylor's hypothesis is questionable in flows with high turbulence intensity like boundary layer regions. To improve its applicability, the instantaneous velocity, rather than mean velocity, was used according to Mallinson et al. [25]. Although their work includes a synthetic jet flow study, it could give more acceptable results in post-processing turbulent signals regardless of flow type. Using aforementioned assumption results in:

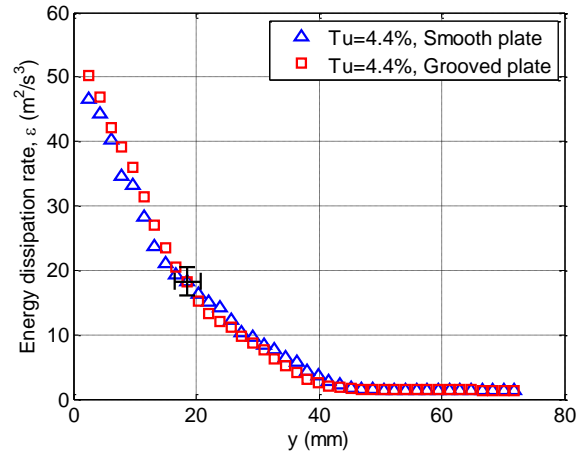
$$\bar{\epsilon} = \frac{15\nu}{N} \sum_{i=1}^{N-1} \frac{1}{U_i^2} \left(\frac{u_{i+1} - u_i}{\Delta t} \right)^2 \quad (8)$$

Figure 11 shows the values of energy dissipation rate at sample streamwise sections for the $Tu=4.4\%$ flow over both smooth and grooved surfaces. As mentioned earlier, majority of turbulence parameters like energy dissipation rate and turbulence length scales do not have context in the smooth free-stream ($Tu=0.5\%$) flow and therefore have not been presented. Figure 11 shows that the energy dissipation rate has a higher value in the vicinity of the wall due to larger turbulence generation in that area. Then it decreases within the boundary layer with distance from the wall until it levels off to approximately zero in the free-stream region.

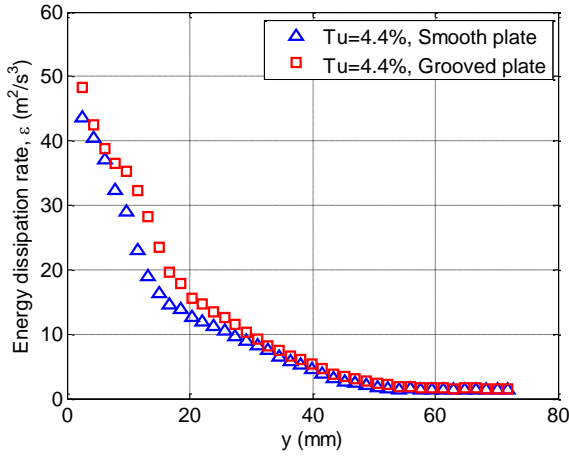
As demonstrated earlier, grooves generate additional turbulence in the near-wall region that spreads to the whole boundary layer domain as we advance into the grooved area (from $x/L=0.59$ to 0.70), observed in Fig 7. Expectedly, the groove-generated turbulence marginally increases the energy dissipation rate at $0.48 \leq x/L \leq 0.70$ sections located in the grooved region as well as the last section ($x/L=0.76$), just downstream of the grooved area (see Fig. 11b to 11d). Also, the increase in energy dissipation rate tends to extend towards the boundary layer edge as the streamwise distance increases. According to this, the most quantitative influence of the grooves can be observed at the last sections closer to the end of the grooved region i.e. $x/L=0.64$.



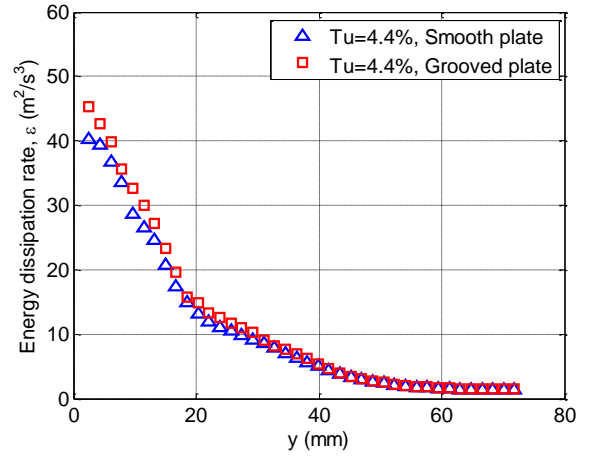
(a) $x/L=0.31$



(b) $x/L=0.53$



(c) $x/L=0.64$



(d) $x/L=0.76$

Figure 11: Energy dissipation rate variations for $Tu=4.4\%$ flow over smooth and grooved surfaces, typical error bars are shown in (b)

Kolmogorov microscale is expected to vary inversely with energy dissipation rate because of the inverse proportionality between them (Eq. 6). Figure 12 shows that for $Tu=4.4\%$ flow over the smooth plate Kolmogorov microscale has its lowest value in the vicinity of the wall and increases as distance in the wall-normal direction increases. This stands to reason, given that in higher turbulence regions, energy transfer continues to supply highly dissipative energy to smaller dissipative eddies. In other words higher dissipative energy needs smaller scales to be dissipated. Outside the boundary layer where the energy dissipation rate is next to zero the size of Kolmogorov microscale remains largely unchanged. As explained earlier, using transverse grooves on the surface introduces additional turbulence to the flow, confirmed from Fig. 7 results. This intensifies the energy dissipation rate and hence, results in a decrease in the Kolmogorov microscale. Though this decrease is small, it is worth noting again that the greatest change occurred at $x/L=0.64$, well into the grooved region.

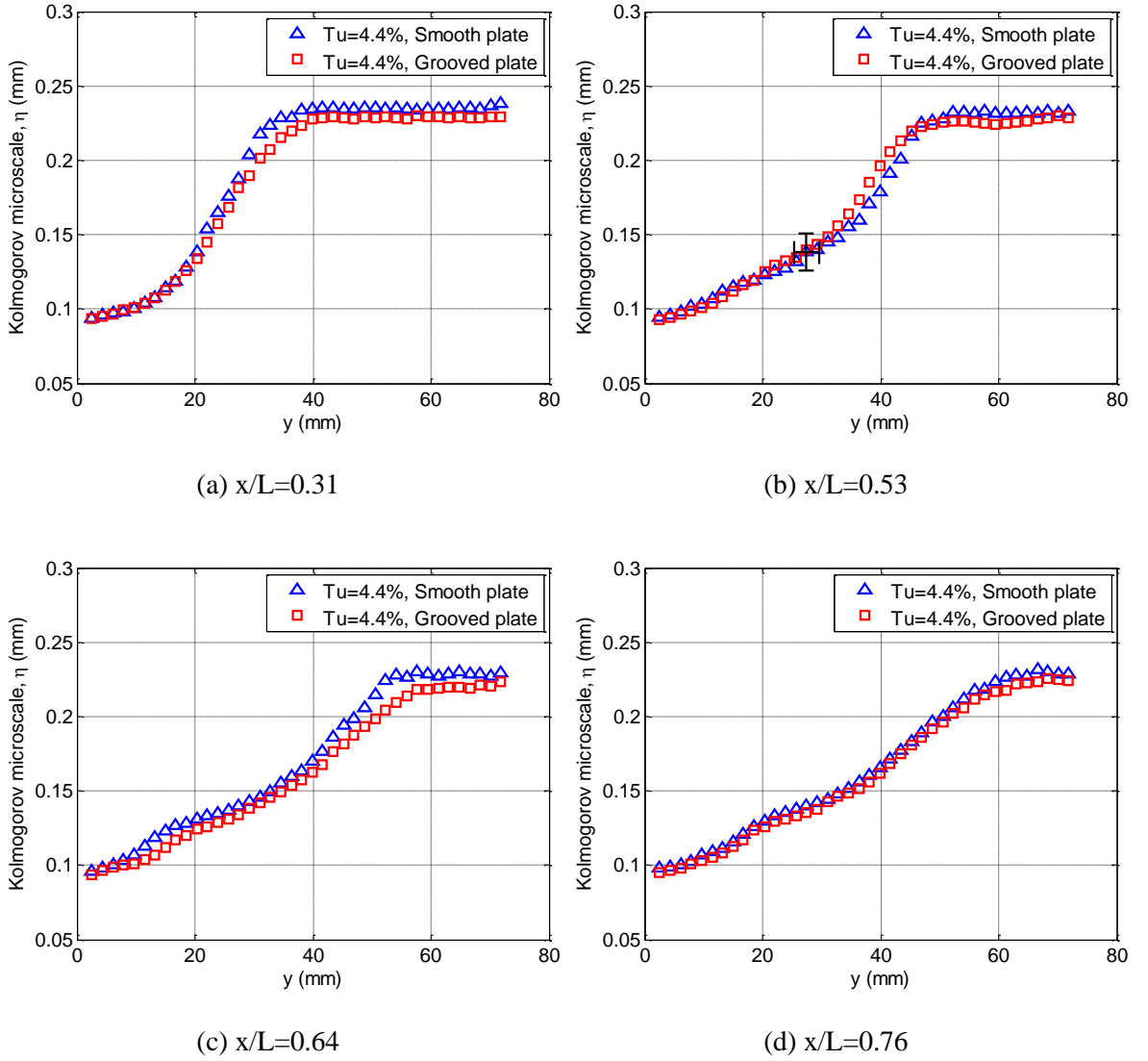


Figure 12: Kolmogorov microscale profiles for $Tu=4.4\%$ flow over smooth and grooved surfaces, typical error bars are shown in (b)

Integral length scale characterizes the energy-containing range of turbulence length scales. This scale is approximated by Taylor's hypothesis by integrating the temporal correlation function (auto-correlation function) instead of spatial correlation function (two-point correlation function) [22]. To formulate the integral length scale concept, the auto-correlation coefficient may be defined as:

$$R_u = \frac{\overline{u(t) \cdot u(t+\Delta t)}}{\sqrt{\overline{u^2(t)} \cdot \overline{u^2(t+\Delta t)}}} \quad (9)$$

whose discrete form for numerical calculation is:

$$R(m\Delta t) = \frac{\frac{1}{N-m} \sum_{i=1}^{N-m} (u_i u_{i+m})}{\frac{1}{N} \sum_{i=1}^N u_i^2}, 0 < m < N - 1 \quad (10)$$

The integral time scale can be estimated by integrating auto-correlation coefficient as:

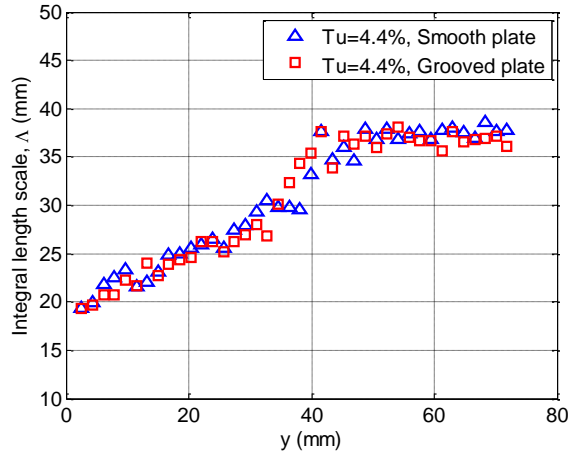
$$\tau_\Lambda = \int_0^\infty R_u dt \quad (11)$$

from which the integral length scale can be via:

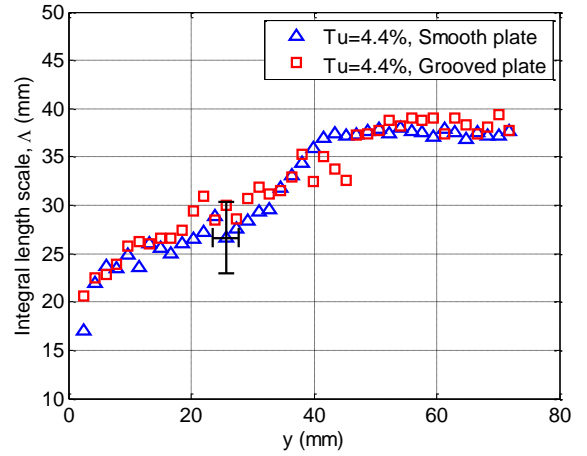
$$\Lambda = U_{mean} \cdot \tau_\Lambda \quad (12)$$

The values of integral length scale for smooth and grooved surface under 4.4% free-stream turbulence are displayed in Fig. 13. Although there are some discrepancies in the integral length scale values, it is consistently observed that the integral length scale increases within the boundary layer with moving farther in the vertical-wall direction. Integral scale has its smallest values in the near-wall region apparently because of the bounding effect of the surface. In fact, since the size of energy containing eddies is confined by the flow boundaries, so the bounding effect of the surface causes the integral length scale to be smaller near to the wall and as the distance from the wall increases the integral length scale becomes larger. It is worth noting that the integral length scale has a size range of the order of magnitude of the boundary layer thickness. This suggests that in the boundary layer flows like flow over a flat plate the dimension which confines the size of the energy containing eddies is more likely the boundary layer thickness and not the plate length. In the free-stream area, integral length scale remains roughly constant for each streamwise section. In this region, integral length scale increases as we move farther along the flow direction, for example it has value of 37.6, 37.4, 39.8, 41.7 mm at locations of $x/L=0.31, 0.53, 0.64, 0.76$ (see Table 1).

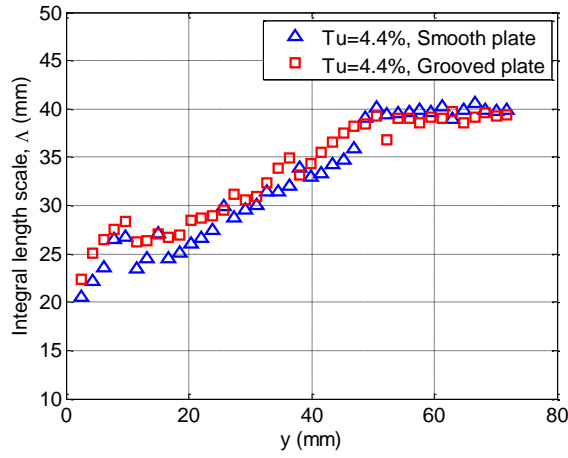
The effect of the grooves on the integral length scale is not very clear. There appears to be a marginal increase in the integral length scale in the grooved area especially in the near wall region. This would indicate some higher turbulence kinetic energy. Nonetheless, the change is non-conclusive as it is no more than the uncertainty limits. Again, groove's effect is more identifiable at $x/L=0.64$ section which is closer to the end of the grooved area.



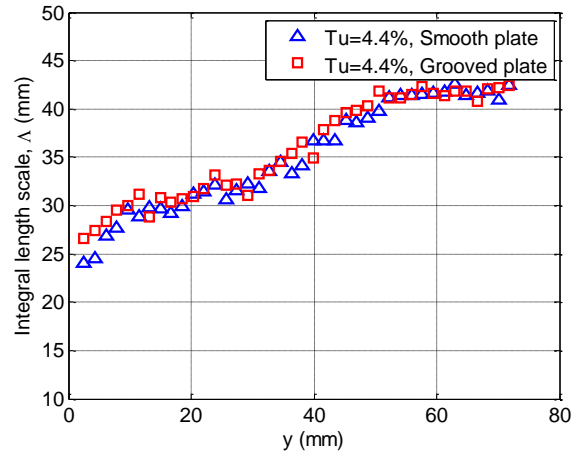
(a) $x/L=0.31$



(b) $x/L=0.53$



(c) $x/L=0.64$



(d) $x/L=0.76$

Figure 13: Integral length scale variations for $Tu=4.4\%$ flow over smooth and grooved surfaces, typical error bars are shown in (b)

The ratio of integral length scale to the Kolmogorov microscale may be a better indicator regarding the amount of kinetic energy in the turbulence energy cascade and hence, is plotted in Fig. 14. This ratio has highest value next to the wall, implying highest turbulence generation. Without the grooves ($x/L=0.31$), it dips to its lowest value before the edge of the boundary layer, at which point the free-stream turbulence brings it up to the OPP generated level. With the groove-generated extra energy the ratio of integral scale to the Kolmogorov microscale increases inside the boundary layer as we move downstream in the grooved region and it peaks around the

end of the grooved region ($x/L=0.64$); where grooved enhancement in Λ/η can be seen throughout the boundary layer. The influence even penetrates slightly beyond the edge of the boundary layer.

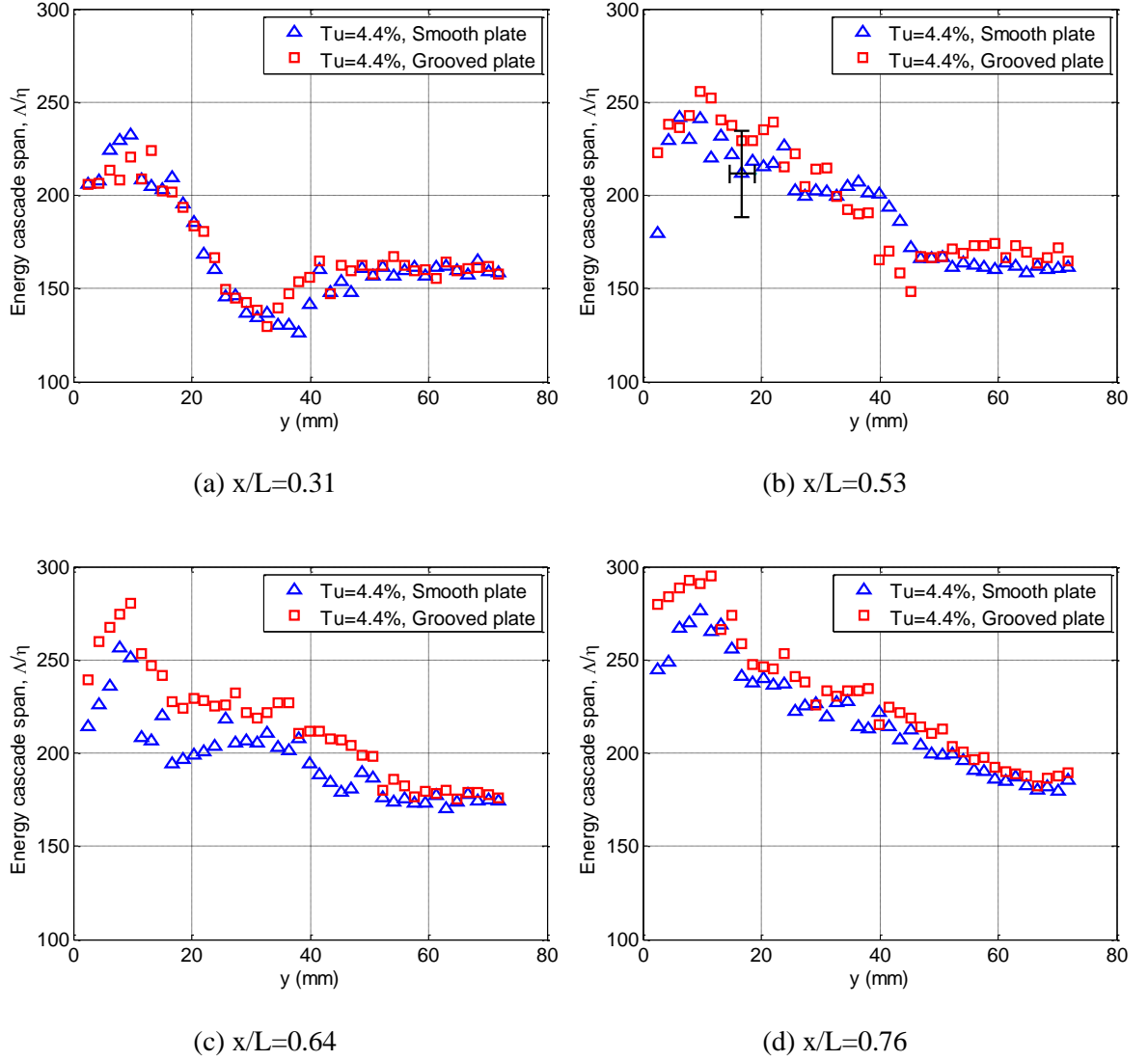


Figure 14: Energy cascade span (Λ/η) for $Tu=4.4\%$ flow over smooth and grooved surfaces, typical error bars are shown in (b).

A.4 Conclusion

The effect of free-stream turbulence on flow over a flat plate with transverse grooves has been studied experimentally. Both smooth and grooved surfaces were tested in free-stream turbulence of 0.5% and 4.4% under a free-stream velocity of 8.1 m/s.

Nearly-isotropic free-stream turbulence ($Tu=4.4\%$) makes velocity profiles fuller while increases the boundary layer thickness. Moreover, free-stream turbulence causes notable growth of the streamwise turbulence intensity throughout the entire boundary layer. PDF analysis revealed that interaction of quasi-isotropic free-stream turbulence with wall turbulence resulted in a nearly-isotropic turbulence in a small region in the vicinity of the solid surface while anisotropic turbulence prevailed in the rest area of the boundary layer.

Spanwise grooves enhance the velocity profiles especially under free-stream turbulence which the new-formed fuller profiles with larger curvature have more resistance to flow separation. They also have larger boundary layer thickness due to the roughness effect of the grooves on the surface. Energizing of the fluid by grooves was confirmed by the increase in turbulence intensity and energy dissipation rate. The higher-order moments of the turbulence signal showed that the groove-generated turbulence tends to skew the velocity fluctuation distribution especially in the near-wall region. Moreover, a positive peak of flatness factor with a negative peak of skewness factor was detected near the boundary layer's edge. These peaks are an indication of the notable role the boundary layer plays in the mixing process with the free-stream region. It has also been shown that the grooves widened the energy cascade, i.e. they increase the integral to Kolmogorov ratio. The influence of the grooves on the flow domain is significantly identifiable in the vicinity of the wall for the streamwise locations inside and immediately downstream of the grooved region. Moreover, groove effects propagate throughout the boundary layer to its edge at locations close to the end of grooved area.

A.5 References

- [1]. Gad-El-Hak, M., Flow control: Passive, active and reactive flow management, Cambridge University Press, London, 2000.
- [2]. Wahidi, R., Chakroun, W., Al-Fahed, S., The behavior of the skin-friction coefficient of a turbulent boundary layer flow over a flat plate with differently configured transverse square grooves, *Experimental Thermal and Fluid Science*, 2005; 30: 141–152.
- [3]. Lin, J.C., Howard, F.G., Turbulent flow separation control through passive techniques, AIAA paper No. 1989-976.
- [4]. Walsh, M.J., Riblets, in: Bushnell, D.M., Hefner, J.N., Viscous drag reduction in boundary layers, by *Progress in Astronautics and Aeronautics*, 1990; 123: 203-262.
- [5]. Walsh, M.J., Effect of detailed surface geometry on riblet drag reduction performance, *Journal of Aircraft*, 1990; 27: 572-573.

- [6]. Sutardi, Ching, C.Y., Effect of a transverse square groove on a turbulent boundary layer, *Experimental Thermal and Fluid Science*, 1999; 20: 1-10.
- [7]. Sutardi, Ching, C.Y., Effect of different sized transverse square grooves on a turbulent boundary layer, *Experiments in Fluids*, 2003; 34(2): 261-274.
- [8]. Sutardi, Ching, C.Y., The response of a turbulent boundary layer to different shaped transverse grooves, *Experiments in Fluids*, 2003; 35: 325-337.
- [9]. Choi, K.S., Fujisawa, N., Possibility of drag reduction using d-type roughness, *Applied Scientific Research*, 1993; 50(3-4): 315–324.
- [10]. Elavarasan, R., Ching, C.Y., Antonia, R.A., Turbulent boundary layer over a smooth wall with widely separated transverse square cavities, *Applied Scientific Research*, 1995; 55(3): 227–243.
- [11]. Pearson, B.R., Elavarasan, R., Antonia, R.A., The response of a turbulent boundary layer to a square groove, *Journal of Fluids Engineering, Transaction of the ASME*, 1997; 119: 466–469.
- [12]. Robarge, T.W., Stark, A.M., Min, S.K., Khalatov, A.A., Byerley, A.R., Design considerations for using indented surface treatments to control boundary layer separation, *AIAA paper No. 2004-425*.
- [13]. Tantirige, S.C., Iribarne, A.P., Ojha, M., Trass, O., The turbulent boundary layer over single V-shaped grooves, *International Journal of Heat and Mass Transfer*, 1994; 37(15): 2261-2271.
- [14]. Dubief, Y., Comte, P., Lesieur, M., Effect of a groove on the near-wall structure of turbulent boundary layer flows, *13th Australian Fluid Mechanics Conference, Melbourne*, 1998.
- [15]. Luo, H., Qiao, W., Xu, K., Passive control of laminar separation bubble with spanwise groove on a low speed highly loaded low-pressure turbine blade, *Journal of Thermal Science*, 2009; 18(3): 193–201.
- [16]. Liu, R., Ting, D.S-K., Checkel, M.D., Constant Reynolds number turbulence downstream of an orificed perforated plate, *Experimental Thermal and Fluid Science*, 2007; 31: 897-908.
- [17]. *Streamline streamware installation and users guide*, Dantec Dynamics, Denmark, 2000.
- [18]. Yavuzkurt, S., A guide to uncertainty analysis of hot-wire data, *Journal of Fluids Engineering, Transaction of the ASME*, 1984; 106: 181–186.
- [19]. Benedict, L.H., Gould, R.D., Towards better uncertainty estimates for turbulence statistics, *Experiments in Fluids*, 1996; 22: 129-136.
- [20]. Moffat, R.J., Describing the uncertainties in experimental results, *Experimental Thermal and Fluid Science*, 1988; 1(1): 3-17.

- [21]. Van Ingen, J.L., The e^N method for transition prediction, Historical review of work at TU Delft, 38th AIAA Fluid Dynamics Conference and Exhibit, Seattle, Washington, AIAA paper No. 2008-3830.
- [22]. Hinze, J.O., Turbulence, 2nd Ed, McGraw-Hill, New York, 1975.
- [23]. Alving, A.E., Fernholz, H.H., Turbulence measurements around a mild separation bubble and downstream of reattachment, Journal of Fluid Mechanics, 1996; 322: 297-328.
- [24]. Carlotti, P., Drobinski, P., Length scales in wall-bounded high-Reynolds-number turbulence, Journal of Fluid Mechanics, 2004; 516: 239–264.
- [25]. Mallinson, S.G., Reizes, J.A., Hong, G., Westbury, P.S., Analysis of hot-wire anemometry data obtained in a synthetic jet flow, Experimental Thermal and Fluid Science, 2004; 28: 265–272.

Appendix B: Uncertainty analysis

This appendix documents the procedure used to estimate the uncertainty in several parameters reported in this thesis. The procedure explained in Refs. [1,2] was used here. The total uncertainty of a measured parameter is a combination of bias and precision uncertainties.

$$W_{tot} = \sqrt{W_B^2 + W_P^2} \quad (1)$$

The bias uncertainty in a measured parameter was deduced based on the accuracy of instrumentation used to measure that parameter and other influencing parameters in the measurement process. In addition to bias uncertainty, the precision uncertainty of independent repeated measurements has been determined from the student's t distribution. The precision uncertainty from N independent measurement for a student's t distribution with 95% confidence interval is

$$W_P = t_{v,95} S_{\bar{X}} \quad (2)$$

where $t_{v,95}$ is the confidence interval with 95% level, $v=N-1$ is degree of freedom and $S_{\bar{X}}$ is standard deviation of the mean values of N measurements.

In order to determine the uncertainty in a dependent variable the Kline-McClintock equation was used. This equation states that if all the uncertainties of the independent variables are at the same probability level (e.g. 95%) and each of the measured variables are independent of each other, the most probable value of the result variable is given by the root of the sum of the squares of uncertainty values in dependent variables. So, if it is assumed that the result variable R is a given function of the independent variables $x_1, x_2, x_3, \dots, x_n$, Thus;

$$R = f(x_1, x_2, x_3, \dots, x_n) \quad (3)$$

Then W_R , the uncertainty in the result is given as:

$$W_R = \left\{ \left(\frac{\partial R}{\partial x_1} w_{x_1} \right)^2 + \left(\frac{\partial R}{\partial x_2} w_{x_2} \right)^2 + \dots + \left(\frac{\partial R}{\partial x_n} w_{x_n} \right)^2 \right\}^{0.5} \quad (4)$$

References

- [1]. Figliola, R.S., Beasley, D.E., Theory and design for mechanical measurements, 5th Ed., John Wiley & Sons, Inc. 2011.
- [2]. Moffat, R.J., Describing the uncertainties in experimental results, Experimental Thermal and Fluid Science, 1988; 1(1): 3-17.

Appendix C: Scaling analysis

C.1 Flow similarity

This appendix discusses the scaling effects on the experiments conducted on the test models in this research. For any experimental study, the most important variables that affect the flow conditions should be listed and analyzed. After selecting the important variables, the dimensionless parameters between variables should be determined to achieve similarity between the test model and the prototype. The similarity function is often stated as [1]

$$\Pi_1 = f(\Pi_2, \Pi_3, \dots, \Pi_n) \quad (1)$$

Having determined the dimensionless parameters according to Eq. 1, the complete similarity between model and prototype should be analyzed. Flow conditions for a model test are completely similar if all relevant dimensionless parameters have the same corresponding values for the model and the prototype [1]. In most of engineering applications it is very difficult to satisfy the complete similarity, and therefore, it is recommended to ensure the most common similarity criteria, namely geometric, kinematic, dynamic, and thermal.

Geometric similarity concerns the length dimension and is satisfied between a model and prototype when all body dimensions in all three coordinates have the same linear scale ratio. Additionally, all angles and all flow directions are preserved in geometric similarity and the orientations of model and prototype with respect to the surroundings must be identical. Kinematic similarity requires that the model and prototype have the same length scale ratio and the same time scale ratio. The result is that the velocity scale ratio will be the same for both. In other words, the motions of two systems are kinematically similar if homologous particles lie at homologous points at homologous times. Length scale equivalence simply implies geometric similarity, but time scale equivalence may require additional dynamic considerations such as equivalence of the Reynolds and Mach numbers for external flows. Dynamic similarity exists when the model and the prototype have the same length scale ratio, time scale ratio, and force scale (or mass scale) ratio [1].

C.2 Flow around a single blade

The aerodynamic forces, lift and drag, acting on a single blade depend on several parameters. The literature suggests that the most important parameters affecting the aerodynamic forces of a single blade include [2]

$$F = f(U, \rho, \mu, c, H, \epsilon, u', \Lambda) \quad (2)$$

where $F, U, \rho, \mu, c, H, \epsilon, u', \Lambda$ are aerodynamic force, air velocity, air density, air viscosity, blade chord length, blade height, blade surface roughness, air velocity fluctuations, and turbulence length scale. Dimensional analysis results in the dimensionless parameters as

$$\frac{F}{0.5\rho c H U^2} = f\left(\frac{\rho U c}{\mu}, \frac{u'}{U}, \frac{H}{c}, \frac{\Lambda}{c}, \frac{\epsilon}{c}\right) \quad (3)$$

where the geometrical scale ratios including $\frac{H}{c}, \frac{\Lambda}{c}, \frac{\epsilon}{c}$ were included in this equation as well. Using the definition of lift or drag coefficient, Reynolds number and turbulence intensity Eq. 3 can be rewritten as

$$C_F = f\left(Re, Tu, \frac{H}{c}, \frac{\Lambda}{c}, \frac{\epsilon}{c}\right) \quad (4)$$

C.3 Flow over a VAWT

In order to conduct scaling analysis for the flow over a VAWT, the most important parameters affecting the output power of the wind turbine can be listed as [3]

$$P = f(U, \rho, \omega, c, H, D, N, u', \delta) \quad (5)$$

where $P, U, \rho, \omega, c, H, D, N, u', \delta$ are turbine output power, air velocity, air density, turbine rotational speed, blade chord length, blade height, turbine rotor diameter, number of blades, air velocity fluctuations, and atmospheric boundary layer thickness. Dimensional analysis results in the dimensionless parameters as

$$\frac{P}{0.5\rho D H U^3} = f\left(\frac{R\omega}{U}, \frac{u'}{U}, N, \frac{H}{c}, \frac{H}{D}, \frac{Nc}{R}, \frac{\delta}{H}\right) \quad (6)$$

where the geometrical scale ratios including $\frac{H}{c}, \frac{H}{D}, \frac{Nc}{R}, \frac{\delta}{H}$ were included in this equation as well. Using the definition of wind turbine power coefficient, tip speed ratio, and turbulence intensity Eq. 6 can be rewritten as

$$C_P = f\left(\lambda, Tu, N, \frac{H}{c}, \frac{H}{D}, \frac{Nc}{R}, \frac{\delta}{H}\right) \quad (7)$$

References

- [1]. White, F.M., Fluid mechanics, 7th Ed., McGraw-Hill, 2009.
- [2]. Pope, A., Harper, J.J., Low speed wind tunnel testing, John Wiley and Sons, 1966.
- [3]. Paraschivoiu, I., Wind turbine design - with emphasis on Darrieus concept, Polytechnic International Press, Montreal, 2002.

Appendix D: Wind turbine generator electrical losses

The procedure of determining the electrical losses of the VAWT's generator discussed in Chapter 5 is presented in this appendix. The electrical generator of the wind turbine is an AC PMG 3 phase unit. The winding resistance of this generator was determined to be 40 ohms. The wind turbine generator was connected to a 1N5399 MIC rectifier that was used to convert the generator AC current to a DC one. This rectifier has a variable resistance changing by the rotational speed of the shaft as discussed in the manufacturer datasheet [1]. The electrical losses of the wind turbine generator were estimated by adding up the losses due to the generator winding and the rectifier. These components of losses were determined and plotted in Fig. 1 versus wind speed for different free-stream turbulence levels.

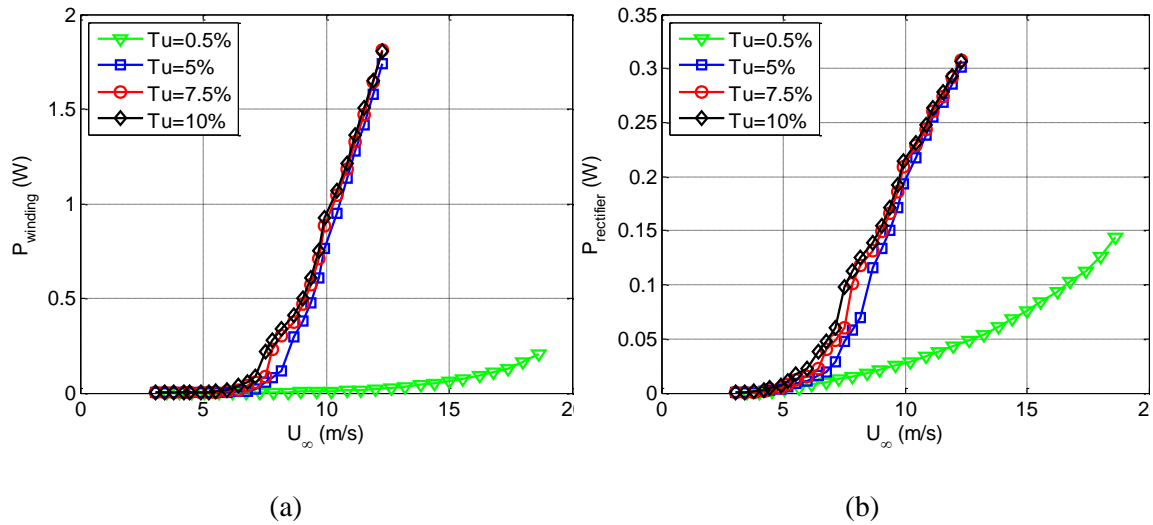


Figure 1: Wind turbine generator electrical losses due to (a) generator winding and (b) rectifier.

References

- [1]. <<http://www.cnmic.com>> Accessed Nov. 18, 2015.

Appendix E: Permissions for previously published works

Chapter 2: Straight bladed vertical axis wind turbine rotor design guide based on aerodynamic performance and loading analysis

As specified by the SAGE Publication's Copyright and Permissions [1], the publication's author retains the right to include an article in a thesis, provided that acknowledgement to journal publication is made explicit.

Chapter 3: The role of free-stream turbulence on flow evolution in the wake of a VAWT blade

Permissions obtained through correspondence with the editor. Required to reference initial source of publication as done after the title in Chapter 3.

Chapter 4: An experimental study on the interaction between free-stream turbulence and a wing-tip vortex in the near-field

As specified by the Elsevier's Author Rights [2], the publication's author retains the right to include an article in a thesis, provided that acknowledgement to journal publication is made explicit.

Chapter 5: Performance of a vertical axis wind turbine in grid generated turbulence

As specified by the Elsevier's Author Rights [2], the publication's author retains the right to include an article in a thesis, provided that acknowledgement to journal publication is made explicit.

Chapter 6: A wind tunnel study on the aerodynamic interaction of vertical axis wind turbines in array configurations

As the article has yet to be accepted, no permissions are required. Upon acceptance of article, the author retains the right to include article in a thesis in accordance to Elsevier's Author Rights [2].

Appendix A: Effect of free-stream turbulence on flow characteristics over a transversely-grooved surface

As specified by the Elsevier's Author Rights [2], the publication's author retains the right to include an article in a thesis, provided that acknowledgement to journal publication is made explicit.

References

- [1]. <https://us.sagepub.com/en-us/nam/copyright-and-permissions>, Accessed Oct. 4, 2015.
- [2]. <https://www.elsevier.com/about/company-information/policies/copyright>, Accessed Oct. 4, 2015.

Vita Auctoris

Name:	Mojtaba Ahmadi-Baloutaki
Place of Birth:	Izeh, Khouseztan, Iran
Year of Birth:	1982
Education:	B.Sc. in Mechanical Engineering, 2005, Shahid Chamran University of Ahvaz, Ahvaz, Iran. M.Sc. in Mechanical Engineering, 2009, Isfahan University of Technology, Isfahan, Iran.